Fluid Dynamics of Rotor-Stator Cavities

Bothalage Desanga Rajika Fernando

Department of Engineering

University of Leicester

This thesis is submitted for the degree of

Doctor of Philosophy

November 2017

I would like to dedicate this thesis to my loving parents ...

Acknowledgements

I would like to convey my heartfelt gratitude to Dr Shian Gao for his support and guidance throughout this work and to Professor Stephen Garrett for his continuous support and assistance throughout these years. Your guidance has excelled me in completing this research.

Next, I would like to convey my appreciation to my family for encouraging me to perceive my goal and for the endless support and commitment provided. I do not have enough words to thank you both for your hard work and patience and a huge thank you to all my family members who have supported me throughout my years of studies.

Finally, to my colleagues at the University of Leicester for making my stay an unforgettable experience.

Fluid Dynamics of Rotor-Stator Cavities

Bothalage Desanga Rajika Fernando

Abstract

This investigation is of mass, momentum and heat transfer applications of the idealised rotor-stator cavities using Computational Fluid Dynamics (CFD). This approach is based on previous literature that provides a fundamental view of the subject. However, this research is more focused on the development and simulation of high-fidelity computational models to refine the understanding of rotor-stator flow problems in engineering.

An open source CFD toolbox, OpenFOAM, is used to solve Navier-Stokes equations and turbulence is modelled using Large eddy simulation (LES) approaches.

The rotor boundary layer roughness is modelled by the parametric force approach, which is an ideal method to represent real-world roughness. Different types of rough wall conditions are imposed on the rotor. The roughness of the rotor wall affected the mean velocity profiles and turbulence intensity at the rotor. Increasing the roughness height transmits these effects to the stator wall. The outer wall of the rotor-stator cavity provides a passage to transport the roughness induced disturbances to the stator side, which tends to an unsteady flow even at minor roughness levels.

The nanofluid heat transfer in the rotor-stator cavities is investigated using single-phase and two-phase transport models. Both models result in enhanced heat transfer rate by using different volume fractions of nanoparticles. The two-phase models provide additional information on the relative slip in the nanoparticle phase due to the Brownian and thermophoresis effects. Near the hot stator, particles are displaced away from the surface, which results in a mild reduction of heat transfer rates.

The final section studies the Lagrangian particle dynamics and deposition in a Rotating Disk Chemical Vapour Deposition (RCVD) chamber. Here, the rotating effects of the disk highly agitate the particle phase, which enhances the deposition efficiencies on the rotor. Apart from that, carrier phase turbulence and thermophoretic forces are important factors in particle dynamics.

Table of contents

Nomenclature

Roman Symbols

ΔT $T_{hot} - T_{cold}$

Δt time step size of Eular or Lagrangian simulations

Δd_{mean} reduction of mean diameter due to S-I

ΔDE_{SI} reduction of particle DE% due to S-I

DE%   deposition efficency

$\overline{Nu}$ mean Nusselt number

$\boldsymbol{\Delta U^+}$ Hama roughness function

$\boldsymbol{\bar{u}}$ time-averaged velocity of the carrier phase/fluid

$\boldsymbol{d_r}$ directional random vector

$\boldsymbol{F_b}$ body forces

$\boldsymbol{F_D}$ drag force on the particle

$\boldsymbol{F_g}$ gravitational force

$\boldsymbol{F_L}$ shear induced lift force on the particle

$\boldsymbol{F_p}$ resultant force on the particle

$\boldsymbol{F_s}$ surface forces

$\boldsymbol{F_T}$ thermophoretic force

$\boldsymbol{g}$ gravitational acceleration [9.81 N/kg]

I_{dir} directional unit tensor

I unit tensor

j_B mass flux due to the Brownian force

j_P mass flux due to the nanoparticles

j_T mass flux due to the thermophoresis force

L_{str} Leonard stresses

n outward unit vector normal to a surface

q_e heat flux vector

r_p position vector

S^d deviatoric part of S

S strain rate

T_{str} test grid scale stresses

u_{avg} average velocity

u_{rms} RMS velocity

u_{rotor} velocity on the rotating disk

u instantanious velocity of the carrier phase/fluid

u' velocity fluctuation around time-averaged velocity

V_i relative impact velocity

V_r relative rebound velocity

V_{cr} critical impact velocity

Vy elastic limiting velocity

x_p position vector of the particle

$\widetilde{u}$ filtered instantanious velocity

A_1 Townsend's structure parameter

A_H Hamaker constant

A_p surface area of a particle

a_p radius of a particle

A_{disk} total surface area of the disk

B intersection of the turbulent velocity profile

$B_{thermal}$ thermal Rossby number

C_c Cunningham correction factor

C_D drag coeffcient

C_L lift coeffcient

C_l, C_d model constants of dynamic Smagorinsky model

C_w WALE constant

$c_{p,f}$ constant pressure specific heat capacity of the fluid

Co Courant number

D_B Brownian diffusion constant

d_p diameter of a particle

D_T thermophoresis diffusion constant

e internal energy

E_a adhesive energy

E_m mechanical potential energy

E_s surface energy

f_B simulations with only the Brownian force

f_T simulations with the thermophoretic and the Brownian forces

F_{bi} Brownian force component in the ith direction

G aspect ratio of the caity

G_C	contact geometry constant
G_i	zero mean unit standard deviation Gaussian random number
Gr	Grashof number
H	shape factor of a boundary layer
h	height of the cavity
h_e	specific enthalphy
h_r	roughness height of the roughness model
h_T	convective heat transfer coefficent
K	entrainment coefficent
k	turbulent kinetic energy
k_c	thermal conductivity of the carrier phase
K_e	kinetic energy of the fluid
k_p	thermal conductivity of the particle
k_r	height of a roughness element
k_s	sand grain roughness
k_T	thermal conductivity of material
K_y	a mechanical constant
k_B	Boltzmann constant [$1.38 \times 10^{-23} \mathrm{m}^2 \mathrm{kgs}^{-2} \mathrm{K}^{-1}$]
k_f	thermal conductivity of the fluid/water
k_{nf}	thermal conductivity of the nanofluid
k_{np}	thermal conductivity of the nanoparticles
k_{sgs}	subgrid-scale kinetic energy
Kn	Knudsen number
l_e	finite length of an eddy

m_p mass of the particle

n_s shape factor of the nanoparticles

Nu_r local Nusselt number

p^* normlised probability density at t=40s

Pr Prandtl number

Pr_{sgs} subgrid-scale Prandtl number

Pr_{tur} turbulent Prandtl number

Q_m ratio of resolved kinetic energy to total kinetic energy

R gas constant for air [287.06 J/kgK]

r local radius of the disk

r_1 inner radius of the annular cavity

R_2 radius of the inlet pipe of the CVD chamber

r_2 outer radius of the annular cavity

R_m curvature of an annular rotating disk cavity

R_r local radial location of the pipe plane of the CVD chamber

R_δ Reynolds number based on the local radius of the rotating disk

$R_{\theta\theta}$ resolved Reynolds stress components in tangential direction

R_{rr} resolved Reynolds stress components in radial direction

Ra Rayleigh number

Re_h Reynolds number based on the height of the cavity

Re_p particle Reynolds number

$Re_{\delta,c}$ critial transition Reynolds number based on the local radial value of the disk

$Re_{\delta,edge}$ Reynolds number based on the local radial value of the disk at the edge of the disk

$Re_{\omega,local}$ local Reynolds number based on rotation rate of the disk

Re_{Ω_c} Reynolds number based on the vorticity magnitude of the carrier phase

Re_τ Reynolds number based on the friction velocity

$Re_{h,\omega}$ Reynolds number based on the cavity height and the rotation rate of the disk

Ro Rossby number

S_P single-phase simulation model

T temparature of the fluid/water

t time

T_1 tempatrure of the rotor

T_2 tempatrure of the stator

T_C temparture of the carrier phase

t_e finite lifespan of an eddy

T_P two-phase simulation model

T_{cold} cold boundary of the CVD chamber

T_{hot} hot boundary of the CVD chamber

Tu flow disturbance level

u_p velocity of the particle

U_r time-averaged resolved velocity component in the radial direction

u'_x, u'_y, u'_z velocity fluctuation components of **u**

u_τ friction velocity

$U_{\theta,max}$ maximum tangential speed of the disk $[r_2\omega]$

$u_{\theta,r}$ time-averaged resolved relative tangential velocity

U_θ time-averaged resolved velocity component in the tangential direction

U_θ^* time-averaged resolved dimensionless velocity component in the tangential direction

u_θ^+ time-averaged resolved relative tangential velocity normalised by friction velocity

U_r^* time-averaged resolved dimensionless velocity component in the radial direction

U_z time-averaged resolved velocity component in the wall-normal direction

U_z^* time-averaged resolved dimensionless velocity component in the wall-normal direction

V_P volume of a particle

V_{PM} cell volume

$Y_{M,1}$ modulus of elasticity of the particle

$Y_{M,2}$ modulus of elasticity of the surface

z wall-normal direction to the rotating disk/plane

z^+ dimensionless wall units

N   neighbouring cell centre

P   current cell centre

Greek Symbols

α roughness factor of the roughness model

α_{eff} effective thermal diffusivity

δ_2 momentum thickness of the boundary layer

α_n normalised volume fractions for two-phase simulation model

α_p volume fraction of Lagrangian particle phase

$\beta_{thermal}$ thermal expansion coefficient

δ boundary layer thickness of the rotating disk $= \sqrt{\omega/\nu}$

δ_1 displacment thickness of a boundary layer

δ_H clearence between rotating components and stationary components in the rotor-stator cavity

Δ_{sgs} subgrid-scale filter width

Δ_w WALE model filter width

ε rate of dissipation of turbulence energy

ε_d Adhesion distance

ε_P eddy diffusivity of the particle

η_T thermophoretic coefficent

η_f a scalar property of the fluid/water

η_{nf} a scalar property of the nanofluid

η_{np} a scalar property of the nanofluid

η_r an auxilary roughness function

γ_2 rotation rate of the second disk in a rotor disk system or two-parameter family disk systems

γ_1 rotation rate of the second disk in the one-parameter family disk system

$\Delta\gamma_a$ sufrace adhesive energy per unit area

γ_g mean gradient angle

Γ generic diffusion coefficent

γ_m mean velocity angles

γ_τ turbulent shear stress angles

κ von Kármán constant of the turbulent veocity profile

λ_f mean free path of a fluid particle

λ_T thermal conductivity

μ_f dynamic visocity of the fluid/water

μ_{nf} dynamic visocity of the nanofluid

μ_{sgs} subgrid-scale dynamic viscosity

μ_{sgs} subgrid-scale dynamic visocity

μ_t turbulent dynamic viscosity

ν kinematic viscosity of the fluid

ν_{sgs} subgrid-scale kinamatic visocity

δ_{99} boundary layer thickness

ω rotation rate of the first disk

τ_w wall shear stresses

$\boldsymbol{\omega_c}$ carrier phase vorticity vector

$\boldsymbol{\Omega_C}$ rotation tensor

ϕ volume fraction of the nanoparticles

ϕ_m maximum particle packing density

ψ arbitary vector or scalar field

$\widetilde{\psi}$ filtered flow variable

$\widehat{\widetilde{\psi}}$ filtered flow variable at secondary filter

ψ_S sphericity of the nanoparticles

ϕ_{t0} inceptive volume fraction/ volume fraction at $t = 0$

ρ density of the fluid

ρ_c density of the carrier phase

ρ_p particle density

θ tangential direction of the rotor disk

τ_k Kolmogorov time scale

τ_l eddy turnover time

τ_p particle relaxation time

$\boldsymbol{\tau_{rey}}$ Reynolds tensor

$\boldsymbol{\tau_{sgs}}$ subgrid-scale stresses

τ_{eff} the effective shear stresses on the fluid

Acronyms / Abbreviations

BBO   Basset–Boussinesq–Oseen

BEK   Bödewadt-Ekman- Kármán

C-F   Cross-Flow

CFD   Computational Fluid Dynamics

CVD   Chemical Vapour Deposition

DNS   Direct Numerical Simulations

LES   Large Eddy Simulations

EIM   Eddy Interaction Model

FDM   Finite Difference Method

FEM   Finite Element Method

FVM   Finite Volume Method

IBM   Immersed boundary method

IS   Inertial Sublayer

LDV   Laser Doppler Velocimetry

LPT   Lagrangian particle tracking

MSD   Mean Square Distance

OpenFOAM Open Source Field Operation and Manipulation

PISO   Pressure Implicit with Splitting of Operators

RANS   Reynolds Averaged Navier-Stokes

RCVD   Rotating Disk Chemical Vapour Deposition

R.M.S   Root Mean Square

RS   Roughness Sublayer

S-C   Streamline-Curvature

SIMPLE Semi-Implicit Method for Pressure Linked Equation

S-I   particle-surface interactions

VANS   Volume-Averaged Navier-Stokes

WALE   Wall Adapting Local Eddy-viscosity

Chapter 1

Introduction

1.1 Context

The rotor-stator disk cavities are an exciting topic among the scientific community, not only because of rich and complicated flow structures in boundary layers but their strong influence on many engineering and real-world applications. Figure 1.1 shows some of the typical rotor-stator cavity configurations available in the literature. The most common application areas, such as turbomachinery, the internal aerodynamics of combustion engines, mixing devices, computer storages, electronic devices, crystal growth processes, spread throughout the multiple engineering disciplines. It is important to get a collective approach to understand the relations and links between the mass, momentum and heat transfer processes of the rotor-stator boundary layers. Computational Fluid Dynamics (CFD) provides the means for addressing this aim. The current investigation develops CFD models to capture the behaviour of mass, momentum and heat transfer aspects in of the cylindrical gap between a rotating disk and a stationary disk above it, at requires that have not been thoroughly investigated in previous investigations. In rotor-stator disk systems, the rotating disk is the rotor and the stationary disk lid referred to as the stator.

The structures of the rotor and stator boundary layers resemble Ekman and Bödewadt boundary layers of Bödewadt-Ekman- Kármán (BEK) family. However, the finite extent of the rotor-stator disk cavity does not lead to the same behaviour of Ekman and Bödewadt boundary layers, but much of the rotor and stator system exhibits of BEK type boundary layers.

There is a considerable number of investigations devoted to studying the fundamental mass, momentum and heat transfer aspects of the rotor-stator disk systems. Following the early experimental investigations, the first notable numerical investigation on the rotor-stator disk system is reported by Serre et al. (2001). Later, Séverac et al. (2007) and Makino et al.
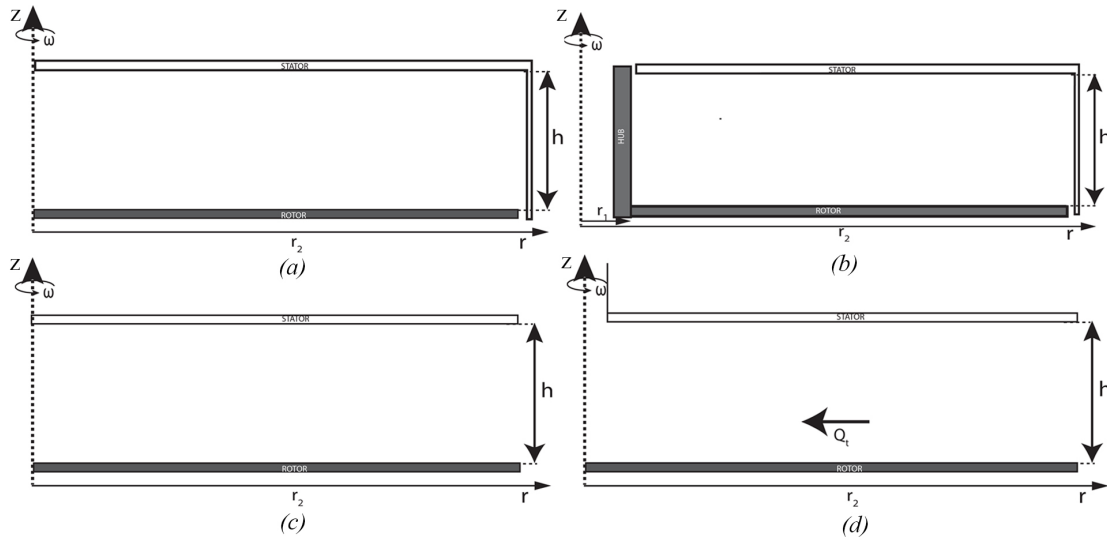
Fig. 1.1 The geometric representations of the typical rotor-stator configurations available in literature, (a) cylindrical rotor-stator cavity, (b) annular rotor-stator cavity, (c) open rotor-stator, (d) rotor-stator cavity with throughflow.

(2015) studied the transition to turbulent flow in rotor-stator cavities. Similarly, a series of investigations, including (Serre et al., 2002; Poncet and Serre, 2008; Tuliszka-Sznitko et al., 2009a; Tuliszka-Sznitko and Majchrowski, 2010; Tuliszka-Sznitko et al., 2011, 2012), studied the heat transfer characteristics of rotor-stator disk systems.

These investigations provide an understanding of the core aspects of rotor-stator disk boundary layers. The current study is based upon the groundwork of these previous investigations, but this tries to combine the previous understanding of rotor-stator disk systems with more engineering and real-world oriented aspects, which might be useful now or in the future. This thesis can be divided into three main parts based on the transport phenomena of interest and the following sections describe the current progress of these respective areas.

First part mostly concerns the momentum transport in rotor-stator cavities and on the influence of surface roughness on the behaviour of the cavity. The surface roughness is an important factor in many engineering applications. Polishing surfaces to a smooth finish can be uneconomical and sometimes surface roughness can be used to enhance specific flow features. Nikuradse (1950) did a notable study on rough wall tubes and this investigation introduced the concept of sand grain roughness, which based on the height of the roughness elements. Later, it was found that the roughness height is not the only parameter that governs the characteristics of the rough walls and Schlichting et al. (1955) introduced the concept of effective sand grain roughness, which can interpret any rough wall surface using an equivalent sand-grain roughness. After that, many investigations (Antonia and Luxton,

1971, 1972; Mulhearn, 1978; Pendergrass and Arya, 1984; Raupach et al., 1991) devoted to studying the properties of rough walls. However, most of the investigations appeared before 1990 considered the roughness as a *universal* aspect (Jiménez, 2004), but more recent investigations (Choi et al., 1993; De Angelis et al., 1997; Bhaganagar et al., 2004; Leonardi and Castro, 2010; Alveroglu et al., 2016) emphasis more on the type of roughness elements with the underlying external flow conditions. Further, the properties at the rough walls could be modified by the presence of turbulence at the near wall areas, and the levels of turbulence could influence the outcomes.

Roughness-related flow investigations are not a new concept for rotating boundary layers. The theoretical approaches on BEK boundary layers (Harris et al., 2013; Alveroglu et al., 2016), experimental investigations (Zoueshtiagh et al., 2003) and numerical investigations of the rotor-stator flows (Özkan et al., 2017) are some of the previous investigations on surface roughness effects on rotating disks. However, according to author's knowledge, currently, there is no any approach that is capable of conducting high fidelity simulation, such as Direct Numerical Simulations (DNS), Large Eddy Simulations (LES), on generalised surface roughness for rotating disk boundary layers. This could be partly due to difficulties in representing the physical roughness elements in three-dimensional computational domains.

The second part investigates the heat transfer capabilities of rotor-stator cavities. The conventional fluids, such as air, water, have weak thermal conductivities that impose a bottleneck on engineering heat transfer applications. Maxwell (1881) proposed a remedy to this problem by mixing micro-sized metallic and metal oxide particles into the working fluid. Even though the thermal conductivities are improved as expected, many practical applications of microparticle dispersions have suffered undesirable side effects (see Das et al. (2006)). The microparticles were too large to use in many industrial and engineering applications. The emergence of nanotechnology now allows the mass production of *nanoscale* particles, which are more resistant to the drawbacks experienced in microparticle dispersions. Choi and Eastman (1995) proposed metallic nanoparticle suspensions in fluid and this section addresses the enhancement of heat transfer by adding a relatively small fraction of nanoparticles to the conventional fluid. This mixture is collectively known as the *nanofluids*.

The work on nanofluids has progressed rapidly over the last couple of decades and many of the previous investigations, such as Khanafer et al. (2003); Xuan and Li (2003); Heris et al. (2007); Nguyen et al. (2007), have been based on the study of the potential heat transfer enhancement of nanofluids within different application areas. Their use has been found to be very successful in practice. Alinia et al. (2011) and Goodarzi et al. (2014) used a two-phase mixture model to study the effects of the nanoparticle slip-velocities that result in inhomogeneous volume faction distributions across the computational domain. Ghasemi

and Aminossadati (2010) studied the effects of Brownian motion on the nanoparticles in a triangular cavity using the Koo–Kleinstreuer's thermo-physical model (Koo and Kleinstreuer, 2005), and observed improvements in heat transfer rates due to Brownian slip motion.

The investigations of Bachok et al. (2011) and Turkyilmazoglu (2014) have conducted theoretical evaluations on rotating disks in a nanofluid medium, but these studies mainly concerned the effects of the nanoparticles on velocity fields rather than on the heat transfer. Later, Mustafa et al. (2015) investigated a Bödewadt boundary layer over a stationary stretching disk. More recently, Mushtaq and Mustafa (2017) studied a nanofluid flow over a stretching rotating disk with axial magnetic field using the Buongirno model (Buongiorno, 2006) for the Brownian diffusion and thermophoresis forces.

The recent investigations of nanofluid on rotating disk boundary layers motivate further investigations on this matter. However, these investigations analysed the single rotating disk boundary layers using the theoretical von Kármán transformation of steady Navier-Stokes equations, which does not give the three-dimensional time-dependent behaviours of the momentum and thermal fields. Further, unsteady simulation models can predict an instantaneous nanoparticle distribution in the computational domain, which is helpful to understand the underlying particle physics. These approaches are more suitable for getting a generalised overview of the system, and the outcomes might be useful for designing heat exchangers.

The final section considers the mass transfer aspect of rotor-stator cavities. Unlike the momentum and heat transfer cases, mass transfer related investigations are tightly coupled with a particular application area. Specifically, the particle dynamics in a Rotating Disk Chemical Vapour Deposition (RCVD) is considered. The RCVDs are technically a rotor-stator cavity with inflow and outflow streams. The process of chemical vapour deposition involves forming thin films of specific substance on a substrate, and the film formation is usually happened by allowing complex chemical reactions on the surface of the substrate. Generally, the concept is used for many industrial applications such as semiconductor manufacturing, optical devices, high-performance cutting and grinding (Jensen et al., 1991). However, purity of the film formation is essential in some applications such as semiconductor manufacturing, and contamination and their deposition on the substrate (or wafer) pose many difficulties in the manufacturing process. Hence, understanding the dynamics of these contamination particles and their deposition are very important to control the level of the purity of the substrate.

Liu and Ahn (1987) conducted a theoretical investigation to understand the micron and submicron particle deposition velocities on a semiconductor wafer. Otani et al. (1989), Pui et al. (1990) and Bae et al. (1994) did experimental investigations to supplement the

previous theoretical outcomes. Later, Ye et al. (1991) and Bae et al. (1995) investigated thermophoresis effects on particle deposition by using the heated substrate. Davis et al. (1993) and Chein and Su (2004) investigated contamination depositions inside the Rotating Chemical Vapour Deposition (RCVD) chambers using a Eulerian-Lagrangian approach and these investigations more focused on particle dynamics inside the chamber under different operational conditions. More recently, many investigations (Yook et al., 2010; Lee and Yook, 2014; Gakis et al., 2015; Lee and Yook, 2015) studied different use cases of microparticle deposition and their deposition velocity on a substrate under different operational conditions.

Currently, there are only a few investigations consider the particle dynamics near the rotating geometric configurations, and the investigation of Chein and Su (2004) limited to the axisymmetric configuration in a laminar flow field. However, the rotation effects could result in three-dimensional features of the flow field and that may eventually affect the particle dynamics. The different thermal conditions and the turbulent carrier phase can also influence the particle dynamics and these factors may significantly modify the particle deposition behaviour on a surface.

1.2 Aims and objectives of the current study

The primary motivation of this study is to investigate the mass, momentum, and heat transfer characteristics of rotor-stator cavities with the aid of high-fidelity numerical models, which are based on a second-order Finite Volume Method (FVM). These characteristics are relatively undocumented in previous literature. This research goal is pursued by the following objectives:

- Simulate the flow behaviour inside elongated rotor-stator cavities operating at the selected Reynolds numbers of 1×10^5 and 4×10^5 using second-order accurate FVM based LES methods, and then, validate and compare the capabilities of this second-order model with high-order models such as Séverac et al. (2007).

- Adept and implement the roughness model of Busse and Sandham (2012) on the validated test cases to study the effects of rough rotor surface in the rotor-stator cavity flow. Then, use this roughness model to understand the influence of roughness on the local and global flow behaviours inside the rotor-stator cavity using the time-averaged and instantaneous flow variable profiles and detailed flow visualisations.

- Implement the single-phase and the two-phase transport models coupled with an LES method to study a rotor-stator cavity, which is filled with different volume fractions of

5

Al_2O_3 nanoparticles, operating at $Re_\omega = 1 \times 10^5$. Then, use these models to understand the effects on underlying momentum and thermal fields due to nanofluid using detailed flow visualisation and different flow variable profiles.

- Use the two-phase transport model of Buongiorno (2006) to study the displacement of Al_2O_3 nanoparticles inside the rotor-stator cavity due to the thermophoresis and Brownian diffusion and determine the dominant diffusion mechanism for nanoparticle under the current conditions.

- Calculate the heat transfer rates of the Al_2O_3 based nanofluid in different volume fractions and compare them to heat transfer rate of a conventional fluid such as water. Finally, asses the suitability of nanofluid on engineering applications, based on these results.

- Conduct one-way coupled Lagrangian-Eulerian simulations to understand the particle dynamics of submicron particle phase inside a CVD Chamber operating at inlet Reynolds number of $Re_{in} \approx 1550$. Extend the study to analyse the behaviour of particles due to a rotating surface, which operates at $Re_\omega \approx 6 \times 10^4$, inside the chamber. Then, use these computational models to understand the particle depositions on a surface.

- Understand the influence of thermophoretic forces, Brownian forces on the particle dynamics and their deposition behaviour on a heated surface, and adept the Eddy Interaction Model (EIM) of Gosman and Loannides (1983) to study the effects of carrier phase turbulence on the particle phase.

- Extend the one-way coupled Lagrangian-Eulerian model to study the influence of particle-surface interactions at the surfaces in the CVD by using the particle-surface energy model of Xu and Willeke (1993).

These primary objectives of this study result in novel numerical models that have not been implemented in the context of the rotor-stator cavity. The outcomes of the research help to identify the various physical flow aspects that extend the current understanding of flow physics inside rotor-stator cavities. The following section describes the novel contributions and improvements of this investigation over the previous literature:

- The implemented roughness model of Busse and Sandham (2012) is a modified model that caters the rotating wall conditions in the rotating disk boundary layer and this is a first generation high-fidelity roughness model available to study the rough wall surfaces

of rotating disk boundary layers. The model is used to visualise the instantaneous flow behaviours inside the rough rotor-stator cavities, which can resolve the disturbance transport of rotor-stator cavities due to the roughness of the rotor. These outcomes were not possible using previous theoretical and numerical approaches. The current study only considers the relative effects of roughness, but this model can predict the flows conditions due to the real-world rough surfaces once calibrated model constants are available.

- The single-phase and two-phase transport models are alternatives to the theoretical approaches that were previously described. However, the current models coupled with an LES method can produce detailed flow visualisations inside the cavity and they can predict the time-dependent flow profiles inside the cavity. The two-phase model is capable of visualising the relative displacements of the nanoparticle phase, which can explain more realistic characteristics of the momentum and the thermal distributions that cannot be predicted by using the steady-state velocity and temperature profiles.

- The previous investigation of Chein and Su (2004) has been extended to represent more realistic real-world conditions by assuming the fully three-dimensional turbulent conditions of the flow field. The Lagrangian-Eulerian simulations are conducted under different particle forces, and the current investigation considers the carrier phase turbulence effects on the particles. These modifications show significant effects on the particle dynamics that were not documented by previous investigations. The three-dimensional particle tracks are combined with probability density plots, which can describe the bulk particle behaviour, to understand the particle dynamics and their deposition properties.

- The surface energy model of Xu and Willeke (1993) enhances the current Lagrangian-Eulerian modelling framework as this new simulation model can predict the particle-surface interactions inside the chamber. This energy model was used in many investigations to study particle-surface interactions but it has never been used on applications that involve rotating disk elements, in which the rotary motion of the disk adds extra complexity to this application. Similar to the previous section, the particle dynamics are studied, and then, the effects of particle deposition are investigated due to particle-surface interactions.

1.3   Structure of thesis

This thesis consists of nine chapters, and the subsequent chapters are organised as below.

Chapter 2 devoted to literature review. Here, early theoretical and experimental developments of the infinite rotating boundary layers (BEK family) have been discussed, followed by discussing the similar trends and development of the rotor-stator disk systems. The chapter covers plausible modelling approaches for rough wall simulations, nanofluid simulations, and the justifications are made for selecting suitable models for this investigation. The final section of the chapter discusses the theory and models in the Lagrangian Particle Tracking (LPT) framework in the context of submicron particle suspensions in a low-density fluid such as air.

Chapter 3 outlines the underlying computational methods, and turbulent models use in this investigation. The chapter starts by discussing relevant spatial and temporal discretisation methods; then the Reynolds Average Navier-Stokes (RANS), Large Eddy Simulation (LES) methods, which are used in this research, are outlined. The chapter concludes by introducing suitable transport models that can be used to study the heat transfer enhancements in rotor-stator cavities due to nanofluids.

Chapter 4 propose the suitable computational model for the rotor-stator cavities operate under two widely validated Reynolds number of $Re_\omega = 1 \times 10^5$ and 4×10^5. The time-averaged and instantaneous velocity profiles and turbulence intensity profiles of the second-order accurate FVM computational models are validated with previous literature. Then, the flow visualisations are conducted to demonstrate instantaneous flow patterns inside the cavities. Finally, a plausible mechanism of laminar-turbulent transition on the rotor boundary layer has been predicted for the higher Reynolds number test case.

Chapter 5 extends computational models of the previous chapter to evaluate the effects of rotor surface roughness on the rotor-stator cavities. The different roughness conditions on the rotor surface are simulated using a roughness model. Then the effects of the roughness on time-averaged and instantaneous velocity profiles of the rotor and the stator boundary layer profiles have been observed. Non-localised effects of the roughness on the rotor surfaces of the rotor-stator cavity are shown by the aid of instantaneous and time-averaged flow visualisations inside the cavity.

Chapter 6 uses the previously validated computational model to develop and implement transport models that are capable of studying the changes in momentum and heat transfer properties due to nanofluid. In particular, single-phase and two-phase models are used with different volume fractions of Al_2O_3 nanoparticles suspended in water. Both of these models can predict momentum and heat transfer properties of the cavity, but the latter model is capable of studying the effect of nanoparticle slip velocities relative to the carrier phase (i.e.water). Similar to the previous chapters, the analysis is carried out using time-averaged and instantaneous velocity profiles and instantaneous flow visualisations inside the cavity.

Chapter 7 describes a one-way coupled LPT framework to study the particle dynamics inside an RCVD with a heat rotor surface. The LPT model considers the different forces on the hard-spherical submicron particles (here, the Silicon particles will be considered), and the direct simulation of particle tracks can reveal the effect on the submicron particles due to the rotor motion and the thermal gradients inside the chamber. Further, this section pays particular attention to the effects of the carrier phase turbulence on the submicron particles.

Chapter 8 adepts an energy-based model to extend the capabilities of the standard LPT model by introducing particle-surface interactions near a solid surface. The selected energy model considers van der Waals energy in the particle-surface interface at which the kinetic energy of the inbound particle should be sufficient to overcome this interaction energy for a possible rebound of the particle. The consideration of these effects may affect the deposition efficiency of the particles at the rotor surface.

Chapter 9 summarises the entire throughput of the research and highlights the significance of this investigation on broader scientific and engineering context. The chapter also suggests plausible enhancements and further use cases of this research.

1.4   Publications

The contents of this thesis are published in the following journal articles.

1. Fernando, D., Gao, S. & Garrett, S.J. The effect of surface roughness on rotor-stator cavity flows, Phys. Fluids., 30, 064103.

2. Fernando, D., Gao, S. & Garrett, S.J. On the heat transfer effects of nanofluids within rotor-stator cavities, Phys. Fluids., 30, 082007.

Chapter 2

Literature Review

2.1   Introduction

This chapter discusses the relevant literature and groundwork for this investigation. The outcomes of this chapter are used at different stages of the investigation. The following synopsis describes the main focus of each subsection of this chapter.

Sections 2.2 & 2.3 discuss the rotating disk boundary layers and their instability patterns relevant to the rotor-stator flows. The outcome of this review is used to simulate and evaluate rotor-stator disk cavities in Chapter 4.

Section 2.4 describes the relevant background on the surface roughness of wall-bounded shear flows. A brief discussion is given on the general concepts of surface roughness and then the discussion is focused on previous numerical approaches to model surface roughness. The motivation for the section is to implement a roughness model in the rotor-stator cavity simulations.

Section 2.5 are on non-isothermal flows and their heat transfer. This section is more focused on heat transfer predictions in rotor-stator flows and their available Nusselt number correlations are also outlined. The following section discusses the benefits and properties of nanofluids. The correlations for determining the nanofluid thermal conductivity and viscosity are discussed. The described models in these sections are used to develop, simulate and validate the nanofluids transport models on rotor-stator cavities, which is the primary objective of Chapter 6.

Section 2.6 introduces the Lagrangian framework. The governing equations of the Lagrangian framework first stated, and then the submodels for the particles forces are outlined. The Lagrangian framework is then used to simulate particle dynamics and depositions on a rotating chemical vapour deposition chamber, which is a real-world engineering application of the rotor-stator disk setup.

2.2 Rotating disk boundary layers

The flow over a rotating disk has received extensive attention from the scientific community for over 100 years. Much of its popularity stems from early theoretical and experimental investigations of single rotating disks, such as Ekman (1905), von Kármán (1921) and Bödewadt (1940) boundary layers. The disk develops three boundary layer types that are collectively called the BEK boundary layer family. Usually, parametrisation is carried out using the Rossby number (Ro), which is the ratio of the inertial force to Coriolis force. This produces an infinite number of members to BEK family. $Ro = -1, 0, 1$ give respectively a von Kármán, an Ekman and a Bödewadt layer.

Since von Kármán (1921) derived the similarity solution for laminar flow over a single rotating disk of the infinite radius in a quiescent fluid, rotating disk boundary layers have attracted much attention, and the availability of an analytical solution for this three-dimensional boundary layer provided a standard validation approach to later numerical investigations. The similarity solution consists of three independent profiles of the stream-wise, cross-wise and wall-normal velocity components. The cross-wise velocity profile features an inflectional point that enables laminar flow instabilities to develop. The rotating disk boundary layer has become a prototype model for studying three-dimensional boundary layers. The relatively simple geometry, the absence of stream-wise pressure gradients and ease of repeatability are some of the advantages of rotating disk boundary layers over other three-dimensional boundary layers, such as backwards swept wings, which can feature a similar inflection point in the cross-wise velocity profile.

At a later stage, Smith (1947) conducted an experimental investigation with a rotating disk in laminar flow and he observed travelling sinusoidal waves, which had approximately a $14°$ inclination to the outward-drawn radius vector, in a narrow band just below the transition Reynolds number. However, the travelling nature of these vortices was later determined to be a measuring error, and the observed wave pattern is stationary, with zero phase velocity. In subsequent theoretical and experimental investigations Gregory et al. (1955) and Kobayashi et al. (1980) observed a similar set of 26–33 stationary vortices around the disk (see Fig. 2.1) and Kohama (1984) concluded that this stationary vortex pattern plays a significant role in the transition to turbulence. Wilkinson and Malik (1985) reconfirmed that the stationary vortices initiate as a result of localised surface imperfections of the disk, which was initially suggested by Gregory et al. (1955). Further, this instability pattern is an inviscid convective instability mode, which is commonly known as *Cross-Flow* (C-F) instability, hereafter denoted as Type I instability.

Apart from the C-F instability, Fedorov et al. (1976) observed another set of instability pattern, which consisted of 14–16 vortices with a $20°$ wave angle. This pattern denoted as the
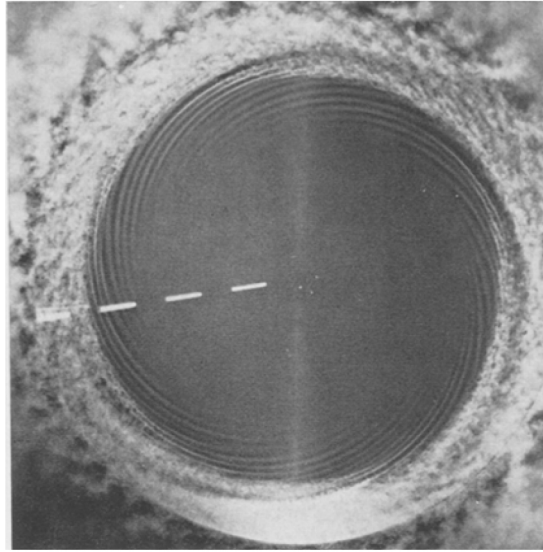
Fig. 2.1 Type I instability of the rotating disk boundary layers, where the disk rotates in a counter-clockwise sense at a rate of 1800 rpm (Kobayashi et al., 1980).

Type II instability, which is a stationary mode that was also found independently by Faller and Kaylor (1966) and Lilly (1966) in the Ekman layer. The Type II pattern is a viscous instability mode and Lilly (1966) found that the Coriolis force is the driving force of this instability in Ekman layers. Unlike Type I instabilities, Type II instabilities are sensitive to external disturbances, and by having much higher disturbance levels in the flow configuration, Type II modes can dominate Type I instability modes (MacKerrell, 1987). However, earlier investigations of Gregory et al. (1955) did not feature any Type II patterns, as they maintained the experiments at a very low disturbance level, at which Type I patterns usually dominate.

In a later investigation, Faller (1991) has further elaborated the importance of the Type II travelling mode in transition to turbulence by experiment and numerical investigation in Ekman layers. These instability patterns are similar to Type I modes, but they have characteristic negative angles compared to positive angles in the Type I mode. In this investigation, he suggested a set of plausible transition mechanisms, which involve Type I, Type II and their respective secondary instability patterns. The exact mechanism of transition is based on the level of excitation of disturbances in the external flow. Concisely, these mechanisms can be categorized in order of decreasing amplitudes of the disturbance, as *(A)* interaction of multiple modes of dominant Type II, *(B)* interaction of Type II mode with base flow to produce secondary instabilities, *(C)* interaction of Type I and Type II modes, *(D)* interaction of the Type I mode with the base flow to produce secondary instability patterns,

12

which was the most popular mechanism among previous investigations on the von Kármán single rotating disk.

Despite the different transition mechanisms purposed in literature, no possible explanation could be proposed for the very consistent and sudden transition Reynolds numbers $Re_{\delta,c}$ showed in von Kármán boundary layers. Malik et al. (1981) summarised and tabulated $Re_{\delta,c}$ values from previous investigations and they obtained a mean $Re_{\delta,c} = 513$ with less than 3% variance, regardless of the state of the external disturbances levels of the flow. This critical Reynolds number is very consistent compared to other three-dimensional boundary layers, like a flat plate or a channel flows boundary layer. Lingwood (1995, 1996) provided an explanation for the consistency of $Re_{\delta,c}$ by theory and experiment. She showed that the rotating disk boundary layers are absolutely unstable at $Re_{\delta,c} = 507$, at which impulse responses grow around the source rather than being convected away from the source. Due to the limitations of linear stability theory, her predictions are confined to the local characteristics of the flow field, but she postulated that the local absolute instability might trigger self-excited global modes in rotating disk boundary layers. More recently, Appelquist et al. (2015) have conducted linearised DNS to study the global stability behaviour of rotating disk boundary layers. They concluded that if the edge of the disk is far from the point where the absolute instability occurs (here, if absolutely instabilities initiate at $Re_{\delta,c} = 507$, then the edge of the disk should be at least $R_{\delta,edge} = 594$), rotating disk boundary layers can be globally unstable. They explained that inward disturbances generated at the edge of the disk across a pocket of an absolutely unstable region before that edge. These are the necessary conditions to achieve a global instability in rotating disk boundary layers. As suggested by Davies and Carpenter (2003), this means a hypothetical infinite rotating disk is unconditionally globally stable due to the lack of inward disturbances at the outer edge of the disk.

Lingwood (1997) studied further absolutely unstable behaviour in the BEK family of boundary layers using linear stability theory. She determined that the Ekman layer is absolutely unstable at $Re_{\delta,c} = 198$, which is an agreement with Faller and Kaylor (1966)'s prediction of turbulence transition at $Re_{\delta,c} \approx 180$–$200$. As $Ro \rightarrow 1$, both convective and absolute modes become more unstable. Unlike with a von Kármán boundary layer, in the Bödewadt boundary layers, even Type I stationary modes become absolutely unstable, at $Ro \approx 0.5$. This shows that the Bödewadt boundary layers are much more unstable than the von Kármán and Ekman boundary layers.

Many further investigations have been conducted to address different aspects of rotating boundary layers. These include a rotating sphere (Garrett and Peake, 2002), rotating cone (Garrett and Peake, 2007), fully turbulent boundary layers of rotating disk (Elkins and Eaton, 2000), global stability of rotating disks (Davies and Carpenter, 2003; Appelquist et al., 2015).

2.3   Rotor-stator cavities

As described before, in rotor-stator cavities, rotor and stator elements are similar to Ekman and Bödewadt boundary layers of the BEK family. Hence, some characteristics of these boundary layers also feature in the rotor-stator boundary layers. Nevertheless, rotor-stator cavities are more common examples of BEK boundary layers, since rotor-stator cavities have a finite outer radius at the casing and a rotor hub (for annular cavities). These radial boundaries alter the behaviour of classic BEK boundary layers. Hence, their behaviours and characterises may not match. Rather than having separate Ekman and Bödewadt boundary layers, the flow in a rotor-stator cavity is one cohesive unit, and the rotor-stator boundary layers can interact with each other by exchanging mass, momentum and heat.

For the ease of discussion, several geometrical and global parameters can be defined to identify the rotor-stator cavity. The rotor-stator cavity is a special case of a rotating disk system, which is illustrated in Fig. 2.2. The aspect ratio of a cylindrical cavity $G = h/r_2$ is based on the height of the cavity h and outer radius of the disk r_2. The aspect ratio of an annular cavity is defined as $G = h/(r_2 - r_1)$, where r_1 is the inner radius of the cavity, and the radius of curvature is another characteristic feature of the annular cavity that is defined as $R_m = (r_2 + r_1)/(r_2 - r_1)$. The Reynolds number based on the cavity height is defined as $Re_h = (\omega h^2)/\nu$, and the local Reynolds number $Re_\delta = r/\delta$ is based on the local radial value r and the characteristic length scale $\delta = \sqrt{\nu/\omega}$. For finite cavities, alternate definitions of the Reynolds number $Re_\omega = (\omega r^2)/\nu$ can be used. In general, the parameter γ_2/ω can be used to categorise two disk problems into three distinct groups, the rotor-stator ($\gamma_2/\omega = 0$), the co-rotating ($\gamma_2/\omega > 0$) and the counter-rotating ($\gamma_2/\omega < 0$) groups, where ω and γ_2 are rotating rates of first and second disks respectively (see Fig. 2.2). Often, the term "rotor disk system" will be used to identify all three groups collectively. The following descriptions mostly cover on rotor-stator cavities, but some properties of open cavities and cavities with throughflow (see Fig. 1.1) are explained, where necessary.

Following von Kármán (1921)'s similarity solution approach, Batchelor (1951) considered a more generalised method to obtain exact solutions for steady axisymmetric viscous rotating flows. As a result, he obtained one and two-parameter families of solutions. The one-parameter family consists of single infinite disks; an entire solution space is defined using the parameter, $\gamma_1/\omega_1 = (-\infty, +\infty)$, where γ_1, ω_1 are the angular velocities of the fluid at $z \to \infty$ and on the rotating plane, respectively. The von Kármán (1921) solution is a member of the one-parameter family and it is when $\gamma_1/\omega = 0$. The two-parameter family solutions represent the flow between two coaxially mounted infinite disks, with different rotation rates. Here, the governing parameters are γ_2/ω and Re_h, where γ_2 is the angular velocity of the second disk. At a given γ_2/ω and sufficiently large Re_h values, the motion
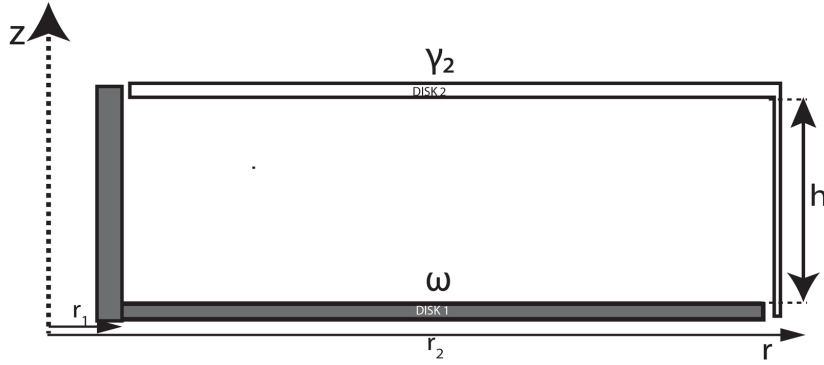
Fig. 2.2 Annular rotating disk system.

can be described as the solid body rotation at the core region (a location away from boundary layers, also known as the main body of the fluid) with zero radial and axial velocity gradient components. The boundary layer on the disks develops as the Reynolds number increases. This generalised approach covers the cases of a single rotating disk, co-rotating disks, and counter-rotating disks, in which the rotor-stator system is a member of the two-parameter family solutions with $\gamma_2/\omega = 0$.

Stewartson (1953) proposed a different concept to Batchelor (1951)'s explanation of a solid body rotation at the core region. He suggested that the rotation of the core region (or the main fluids body) was valid for co-rotating disks but not for counter-rotating disks. He also presented the experimental evidence to back his theoretical findings. At a later stage, Mellor et al. (1968) and Kreiss and Parter (1983) solved this difference by suggesting the non-uniqueness of boundary layer solutions at a given Re_h value, which validate the admissibility of solutions of both Batchelor (1951) and Stewartson (1953). In practice, the finite cavities with a closed geometry can be described by Batchelor solutions, whereas Stewartson solutions resemble cavities without an outer casing (open cavities) or cavities with either a centripetal or a centrifugal throughflow (see Fig.1.1(d)). Later, Poncet et al. (2005) conducted an experimental investigation to compare the flow structures of Batchelor and Stewartson rotor-stator cavities with throughflow.

Nevertheless, it is important to mention that finite cavities are not fully compatible with the boundary conditions of the similarity solutions due to the rotor hub and casing walls. For this reason, Dijkstra and Van Heijst (1983) conducted a numerical investigation on an enclosed rotating disk, by solving the Navier–Stokes equations using a finite difference method, which avoids the use of any similarity solution assumption. In the case of the rotor-stator flow, they obtained the stream-function of the flow field inside the cylindrical cavity and observed a radial outflow on the bottom rotor is due to the centrifugal flow. On the

other end, a radial inflow was observed along the top stator layer, and a wall jet was observed on the sidewall, which transports fluid in the upward direction to the stator. They noticed that the measured velocity profiles are self-similar up to $r/r_2 = 0.87$, regardless of the finite nature of the cavity. Finally, they concluded that a substantial part of the fluid outside the boundary layers is rotating, which agrees with Batchelor (1951). Even though the boundary conditions of the finite geometries are incompatible with similarity solutions, these solutions can still predict the qualitative behaviour of the finite rotor disk systems.

For elongated cavities ($G \ll 1$), Daily and Nece (1960) identified four regimes based on G and Re_ω as shown in Fig. 2.3. The regions I and III represent merge boundary layers, whereas region II, IV are unmerged boundary layers. As explained in Launder et al. (2010), transitions in between regions are possible and the typical transition paths can include $I \rightarrow IV \rightarrow III$, $II \rightarrow I \rightarrow III$ and $IV \rightarrow III$. This is usually a result of thickening of the boundary layers when increasing the local Reynolds number $Re_{\omega,local}$. For the current study, the regions of interest are II and IV, which can be collectively called as the *Batchelor regime*. Therefore, further discussions mostly focus on these two regions.
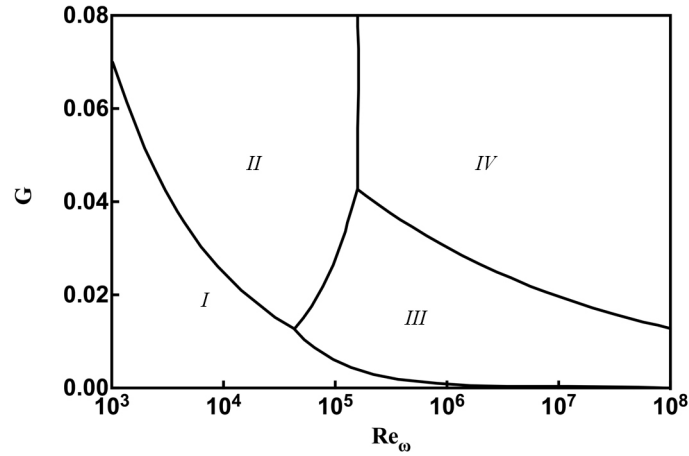
Fig. 2.3 The four regimes of elongated cylindrical cavities purposed by Daily and Nece (1960).

Later advancements in turbulence and transition predictions on single disk problems encouraged the use of similarity approaches in two disk systems to study the transition mechanisms of these systems. It is claimed that the instability patterns in Batchelor regime are similar to instability patterns in single disk investigations (Séverac et al., 2007).

Sirivat (1991) conducted an experiment to study the stability of rotor-stator cavities at different G and $1/Re_h$ values. Sirivat (1991) adds a transparent rotor located at the top, and a bottom stator disk, which was made of clear-anodised aluminium. As results, he observed three instability types at different aspect ratios. A stationary circular pattern, mode I, was

observed for $G = 0.0225$–0.0475. When the aspect ratio reduced to $G = 0.014$, another pattern, mode II appeared, which featured spiral patterns with negative wave angles. Both of these modes correspond to stationary and travelling modes of Type II instability. Then another pattern, mode III, was detected at higher rotation speeds, and this also consists of spiral patterns, but they have positive wave angles, which can be described as Type I instabilities. Further, he identified a transitional behaviour of the mode I and mode II patterns. In the mode I pattern at the higher Re_h values, turbulence at the side walls acts as the primary cause for the transition to the turbulence. For the mode II, different transitional paths have been observed, and as $Re_h \rightarrow 11.36$, clear evidence of spiral collapse was identified, which was deemed to be the plausible path to the onset of turbulence for mode II.

After Lingwood (1995, 1996), the perception of turbulent transition on rotating disk has changed significantly. The investigations of rotating disk systems were no exception, and many investigations have urged to ascertain absolute unstable behaviour of these systems, which is intuitive, as their single disk counterparts are proven to be absolutely unstable. Even though the two disk problems consist the elements of the single rotating disk setup, an absolutely unstable behaviour is not guaranteed on the two disk problems.

Gauthier et al. (1999) conducted experimental investigations on a rotor-stator cavity Their experimental arrangement is similar to the one by Sirivat (1991), which was mainly run at $G = 0.048$. In this experiment, the development of two boundary layers has been observed using a laser sheet visualisation technique. The boundary layers tend to separate after $Re_h > 56$. This technique also allowed to measure the thickness of both boundary layers. It was shown that the thickness of the Bödewadt layer gradually increases at reducing radius values, but the Ekman layer has nearly constant boundary layer thickness throughout the rotor disk. Circular instability patterns were observed over the range of $70 < Re_h < 140$, and approximately about 30 Type II spiral patterns emerged at $140 < Re_h < 200$. Eventually, beyond the Reynolds numbers of $Re_h > 200$ turbulence structures appeared. Then a similar set of experiments was conducted with periodic forcing by introducing modulation on the rotation rate of the disk, which introduces the wide spectrum of frequencies to the flow. A new set of spatiotemporal light intensity images was obtained for the propagating circular patterns and the power spectral density of the varying light intensity was captured. This revealed that the flow system acts as a large-band amplifier, at which the most unstable (or most amplified) frequency is nearly four times the rotation rate of the disk. This behaviour was observed regardless of the external disturbances on the disk. The most unstable wave-number was determined to be $k_c \delta_B = 0.5$, which is close to Lingwood (1997)'s value of $k_c \delta_B = 0.33$ for convective/absolute unstable circular waves in a Bödewadt layer. The critical Reynolds number is about $Re_{\delta,c} = 76$. This value tends to decrease as the aspect ratio increases. In

general, all the instability patterns are deemed to be convectively unstable, except some of the self-sustained patterns observed at higher radial positions.

Serre et al. (2001) investigated by DNS cylindrical rotor-stator cavities ($G = 0.2$ and 0.33) and rotor-stator annular cavities ($G = 0.2$, $R_m = 4$ and 5). Similar to the experiment of Gauthier et al. (1999) and Sirivat (1991), this numerical study also noticed the circular and spiral instabilities (Type I, and for Type II both stationary and travelling modes) at sufficiently high Reynolds numbers. This simulation was run at a Reynolds number high enough to initiate eight Type II travelling waves in the rotor boundary layer, which are similar to Type II spiral patterns that were observed in Ekman layers by Faller (1991). The importance of curvature (R_m) of the cavity is elaborated for axisymmetric structures, and a strong dependency on local curvature for the onset of turbulence has been observed. For annular cavities, the disturbances, which are initiated at the stator due to supercritical bifurcation (Morozov and van Saarloos, 2007), are transported through the rotor hub to the rotor disk at which these disturbances can lead to the subcritical bifurcation in the Ekman boundary layer. Conversely, in the cylindrical cavities, disturbances were attuned near the axis, which implies that the cylindrical cavities are more stable than their annular counterparts. Another experimental study was conducted by Schouveiler et al. (2001). They constructed detailed transition diagrams, which summarise possible instability patterns, such as circular waves, spiral waves, solitary waves and turbulent spots, at the different Reynolds numbers and disk aspect ratios.

Lygren and Andersson (2001) studied fully turbulent rotor and stator boundary layers using DNS on an annular segment. The simulations run at $Re_\omega = 4 \times 10^5$ with a cavity aspect ratio $G = 0.02$. The radial and tangential boundary conditions were set using quasi-periodic boundary conditions. Because of these boundary conditions, any effects from the hub and the sidewall were discounted and the boundary layers behaved as an infinite radius rotor-stator cavity. The mean velocity, turbulence intensity and wall shear stresses were extracted from DNS. It was observed that the turbulence intensity and shear stresses near the rotor are much higher than the turbulence intensity near the stator. Apart from that, a detailed analysis was carried out to identify any coherent structure near the two boundary layers. It was confirmed that the ensemble-averaged coherent structures near the rotor and stator are similar to each other. Séverac et al. (2007) investigated a finite rotor-stator cavity with LES and Laser Doppler Velocimetry (LDV) experiments. All the simulations and experiments used a cavity with aspect ratio $G = 0.2$, tested at Reynolds numbers, $Re_\omega = 1 \times 10^5$–$1 \times 10^6$ and $R_m = 1.8$. By comparing the two cases of $Re_\omega = 1 \times 10^5$ and 4×10^5 they confirmed that the stator boundary layer becomes turbulent at a much lower Re_ω value than the rotor boundary layer. In the rotor boundary layer of the $Re_\omega = 1 \times 10^6$ case, there are about 19 spiral arms with

an approximately $16°$ wave angle in the region $0.14 < r/r_2 < 0.61$. By this, those were identified as a Type I instability pattern. Beyond this region, flow structures become more thin and axisymmetric, indicating an incipient transition to turbulence.

More recently, Makino et al. (2015) conducted a very similar LES and experimental study to Séverac et al. (2007) 's investigation. This investigation considered the same two Reynolds numbers, $Re_\omega = 1 \times 10^5$ and 4×10^5, with a cylindrical cavity and an annular cavity $R_m = 1.8$. Both cavities had the same aspect ratio $G = 0.2$. As Séverac et al. (2007), the lower Reynolds number simulation showed a turbulent stator and a laminar rotor boundary layers, but at the higher Reynolds number of $Re_\omega = 4 \times 10^5$, a fully turbulent stator boundary layer was predicted, with rotor boundary layer in the transition-turbulent state. Unlike Séverac et al. (2007) 's simulations, here, Makino et al. (2015)'s rotor boundary layer only featured about 16 Type II modes, which was deemed to result from the *Streamline-Curvature* (S-C) Itoh (1996). Further, they proposed that the Type II instabilities are the main reason for the transition to turbulent flow that the exact transition mechanism is probably the interaction of these Type II with secondary instabilities, which was explained as *mechanism B* in Faller (1991).

These studies explain that in the rotor-stator cavities, circular and spiral waves are common in the stator boundary layer and that the stator boundary layer is relatively more unstable compared to the rotor boundary layer. The presence of a rotor hub promotes instabilities in the rotor boundary layer. In contrast to the single disk Ekman layers, instabilities in the rotor-stator cavities are mostly convectively unstable.

2.4 Surface roughness

Surface roughness is an important property for many wall bounded industrial, engineering and geophysical flows. The manufacturing processes of hydraulically smooth surfaces add significant cost to their production cycle. Else, in some applications, surfaces are deliberately rough to enhance the heat transfer rate. For example, in the case of atmospheric boundary layers, surface roughness elements of different heights are unavoidable, as plant canopies, human made structures and ocean waves are integral parts of typical atmospheric boundary layers.

The earliest investigations of surface roughness in hydrodynamics date back to the mid-nineteenth century, when Darcy (1857) studied the pressure loss in liquid conduits. Then, the most notable investigation was conducted by Nikuradse (1950), who studied the turbulent flows in rough tubes. In this study, pipes were roughened by cementing sand grains in

the walls of the pipes. He identified three key regimes, based on the average height of the roughness elements (or the elongations of the sand grains toward the flow field).

- A smooth regime: Roughness elements are entirely confined inside the viscous sublayer and the friction factor is the same as the smooth pipes.

- A transitionally rough regime: This is an intermediate region, in which the heights of the roughness elements are of the same order as the viscous sublayer thickness. The friction factor increases with the Reynolds number of the flow and both viscous and pressure drag contribute toward the friction factor.

- A fully rough regime: The friction factor is independent of the Reynolds number of the flow. The viscous drag is negligible compared to the pressure drag due to the roughness elements, which are the primary contributor to the friction factor.

It was soon realised that the height of the roughness element is not the only parameter which defines the properties of the roughness, but the shape and density of the roughness elements also play a crucial role. To address this point, Schlichting et al. (1955) suggested the concept of effective sand grain roughness (k_s), which is the roughness height that produces an equivalent drag penalty to the sand grain drag penalty in the fully rough regime in Nikuradse (1950)'s experiment. Further, the non-dimensioned roughness height defined as $k_s^+ = (k_s u_\tau)/\nu$, where $u_\tau = \sqrt{\frac{\tau_w}{\rho}}$. The transition regime in Nikuradse (1950)'s experiment falls between $3.5 < k_s^+ < 68$. Any value outside is range belongs to either the smooth or the fully rough regime. However, this interval is not universally constant, as later, some investigations have found different roughness height ranges depending on the nature of the surface and of the roughness.

If the roughness element height (k_r) is marginally taller than the viscous sublayer, there is a good chance that the system is in the transition roughness regime. At smooth laminar flow conditions, the viscosity is the dominant source of wall shear stresses near the viscous sublayer, but with the presence of the roughness elements, the drag forces, due to these roughness elements, become the dominant contributor to the wall shear stress. In the vicinity of the roughness elements, horizontal shear stresses are inhomogeneous and this behaviour does not vanish immediately above the roughness element, but the effect could extend up to 2 to 5 times the roughness element height above the roughness elements. This entire region is called the Roughness Sublayer (RS). The Inertial Sublayer (IS), in which the horizontal shear stresses are homogeneous, is at the top of the RS region. Figure 2.4 illustrates these two regions concerning the k_r.

Townsend (1976) proposed a Reynolds number similarity hypothesis. This hypothesis can be best explained in the context of a turbulent rough wall, as this could be one of the most useful applications of the hypothesis. Townsend (1976) proposed to assume that, if the height of roughness element k_r is sufficiently small enough compared to the boundary layer thickness (δ_{99}), then the effects of the roughness, such as mean velocity changes and changes to statistical moments of the turbulent fluctuations, do not propagate to the outer layer. It is suggested that the threshold ratio, k_r/δ_{99}, should be higher than 40 to achieve this, but on some occasions, the threshold ratio may go up to 80 (Jiménez, 2004).
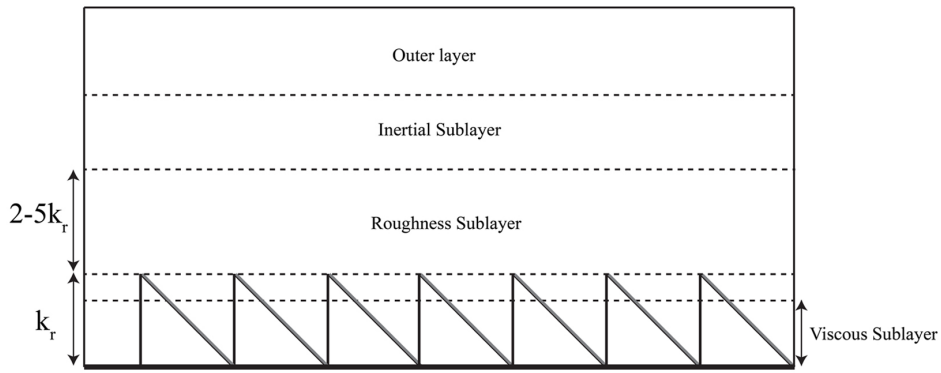
Fig. 2.4 Possible regimes of a rough boundary layer.

Early investigations of rough surface boundary layers are predominantly experimental investigations, but on some occasions, physical experiments are difficult to conduct as the roughness length scales are very small compared to the boundary layer length scales. With the advancement of computational resources, numerical investigations have become a good supplement to experimental investigations.

However, the numerical simulations of rough walls impose a significantly high computational burden over their smooth wall counterparts, as it is always cumbersome to resolve small roughness elements near the wall surface. Hence, early numerical studies on wall resolved surface roughness are mostly confined to simple geometrical configurations, such as flat plate boundary layers and channel flows.

2.4.1 Rough rotating disk boundary layers

The investigations of surface roughness on a rotating disk is not a new topic, as many authors have previously investigated this topic through different approaches. Zoueshtiagh et al. (2003) conducted an experimental investigation to study the boundary layer transition over a rough wall rotating disk spinning under water. They reported the transition Reynolds numbers (Re_c)

and boundary layer velocity profiles for the different roughness levels. It was found that the boundary layer roughness has a minor influence on transition and that transition occurs similarly to the smooth boundary layers, by which rough boundary layers are also absolutely unstable. However, after a certain threshold roughness level, Re_c tends to decrease sharply. Finally, they determined that the absolute instability may continue to play a significant role even for the transition over the large roughness elements.

Harris et al. (2013) conducted a theoretical and experimental investigation of the stability of rotating disk boundary layers. A smooth surface was replaced by a surface function that modelled a rough surface. The corresponding stability curves of these configurations show a decrease in the number of spiral vortices, which was interpreted as a switch in the dominant transition mechanism to Cross-Flow instability to Streamline-Curvature instability. As a result, the slight increase in $Re_{\delta,c}$ results in a small increase in roughness effects, but a further increase in roughness effects start to reduce the $Re_{\delta,c}$. The subsequent experiments also confirm this fact.

Alveroglu et al. (2016) conducted a theoretical investigation, and here, they studied the influence of different types of roughness on the convective instability in the BEK family boundary layers. They found that all types of roughness have a stabilising effect on the Type I instability on all the BEK boundary layers, except the radial groove type roughness in the Bödewadt layers. The Type II instabilities are unstable to concentric grooves for all types of boundary layers, whereas radial grooves and isotropic roughness types stabilise the Type II structures on Ekman and von Kármán boundary layers.

Özkan et al. (2017) conducted an experimental and numerical study on rotor-stator cavities. Here, more attention was paid to comparing roughness induced effects and geometric induced effects. It was determined that the geometric and roughness effects impose similar effects on the rotor-stator flow.

These investigations provide a profound understanding of the behaviour of rough rotating disk boundary layers. However, most of these investigations are based on the effects of roughness on the rotating boundary layer stability and their approaches were fine tuned to tackle this purpose. None of these methods are suitable for adept as a roughness model for high-fidelity simulations models, which is one of the aims of the current study.

The following sections discuss some of the roughness models used in high fidelity simulation models. However, the discussion is more focused on the selection of a suitable roughness model for rotor-stator cavities by considering their relative computational cost, accuracy, and their ability to represent generalised rough wall surfaces available in the real world.

2.4.2   Fully resolved rough wall simulations

As mentioned earlier, fully resolved rough wall simulations are computationally expensive simulations, but they can mimic the actual conditions present in rough walls. There are two principal techniques available for such simulations, which are body-fitted grids and immersed boundary methods. The following sections review their approach with relevant examples. *The body-fitted methods* use a body-fitted mesh (or grid), in which the mesh conforms to the surface of the geometry. In the context of rough walls, the irregular wall boundaries are covered by the mesh that tends to be unstructured. Figure 2.5 shows an example of the body-fitted mesh over a wavy and a smooth wall. The body-fitted methods are suitable for simple geometries, like flat plate boundary layers, channel flows. Even for these simplified geometries, if the roughness elements are too small, the number of mesh elements in the near wall regions can increase significantly, which may make the computation not affordable.

(a)

(b)
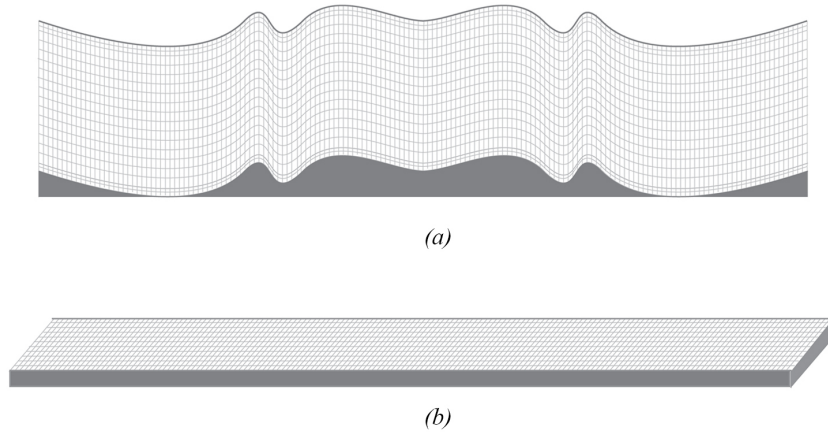
Fig. 2.5 An illustration of body-fitted mesh on, (a) a wavy wall, (b) a flat wall.

Choi et al. (1993) studied drag reduction mechanisms in turbulent flow over a riblet mounted surface using a body-fitted mesh. They observed increments and decrements in mean velocity in the log law region for drag decreasing and drag increasing scenarios, respectively. The reductions in velocity, in vorticity fluctuation components, and in Reynolds shear stresses above the riblets were predicted for the case of drag reduction.

Later, De Angelis et al. (1997) used a body-fitted mesh to simulate a pressure driven flow between a no-slip wavy wall and a slip flat wall (a wall without wall shear stresses). The mean velocity fields and turbulent statistics near the wavy wall showed significant changes when they compared to the flat wall case. The buffer zone was the most affected area. Further,

they observed a thin layer closer to the boundary where most of the energy in the stream-wise direction eventually convert into the span-wise and wall-normal directions.

The immersed boundary method (IBM) is an alternative to the body-fitted method. It uses a force field to mimic the effects of a rough wall instead of following the rough wall contours with the computational mesh boundary. This method is used by Peskin (1977), who investigated blood flow patterns in the human heart.

For the simulations that are performed in a Eulerian mesh, the immersed boundary is treated by a Lagrangian approach. The immersed boundary is independent of the underlying mesh, and it can freely move relative to it. Figure 2.6 shows an example of an immersed boundary in the fluid. At the intersection between the Eulerian mesh and the immersed boundary, a force term is added to the discretised governing equations. To model the effects of the boundary various models have been purposed for calculating the force field, but those details are beyond the scope of this study, and interested readers are referred to the reviews of Silva et al. (2003) and Mittal and Iaccarino (2005) for more details.
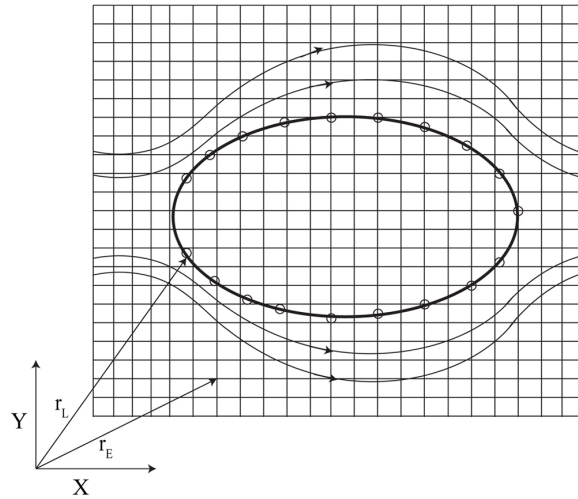
Fig. 2.6 An illustration of an immersed boundary mesh.

Bhaganagar et al. (2004) performed immersed boundary DNS simulations the flow between a smooth wall and a rough wall covered by regular three-dimensional roughness elements. The simulations were performed for various roughness element heights, $k_r^+ = 5.4$, 10.8, 21.6 at $Re_\tau = 400$. The simulations revealed that the roughness tends to increase the velocity and the vorticity fluctuations in the inner layer, but in the outer layer effects can only be observed in velocity fluctuations fields. The roughness effects on high-order moments and on the energy budget were also considered. They concluded that the size of the roughness elements has a significant impact on the inner and outer layer interactions with the boundary.

Breugem and Boersma (2005) performed DNS simulations on a permeable turbulent channel flow. The permeability was achieved through a grid of cubes, which were modelled by an immersed boundary. In parallel to these immersed boundary simulations, Breugem and Boersma (2005) performed a second set of simulations using Volume-Averaged Navier-Stokes equations (VANS) (Whitaker, 1996). VANS are more computationally affordable than the DNS, but they require the use of a turbulence closure model. Both approaches were implemented with similar flow and boundary conditions for comparison purposes. Breugem and Boersma (2005) found that these two approaches produce similar predictions, and in general, elevated levels of R.M.S (Root Mean Square) values of velocity are observed in the wall permeable regions. Further, the study provided indirect evidence that permeability effects have more intense effects than surface roughness effects.

Leonardi and Castro (2010) performed DNS simulations of rough channel flow, in which the wall had a staggered array of cubes with various plane area densities. These cubes were modelled by the immersed boundary approach. It was determined that the form drag be the dominant component of the total surface drag. As the roughness of the surface increased, the significant effects on the turbulent flow quantities near the wall have been observed, but there were no significant effects observed in the outer part of the boundary layer. Increasing the area density led to a monotonic decrease in normalised vertical shear stress around the top of roughness elements. This is in contrast to observations by Orlandi et al. (2006) work on two-dimensional roughness elements.

2.4.3   Modelled rough wall simulations

The previous section focused on high fidelity methods for simulating roughness effects on wall-bounded flow. However, almost all the literature that was reviewed in the previous section describes simple geometric arrangements such as channel flows. Modelling the effect of roughness is a more viable option for simulating rough wall-bounded flows in more complex geometries. Modelling the roughness requires no modification to the computational mesh of the equivalent smooth wall simulation, but it may require modifications to the boundary conditions or to the governing equations. None of these techniques are recommended for studying the detailed flow features inside the roughness sublayer or near the roughness elements. The following sections will explain some of the common surface roughness modelling approaches used in the literature.

RANS simulations make use of rough wall functions, which are sufficiently accurate for a good range of industrial and engineering simulations. Here the effects of roughness are accounted for through the equivalent sand grain approach. The roughness height and the shape of the rough wall are transformed into a Nikitenko (1963)'s roughness scale value.

Then the effects of surface roughness are simulated by increasing the wall skin friction by adjusting the turbulent eddy viscosity at the wall boundary.

Taylor et al. (1985) proposed a discrete element method approach that accounts for the surface roughness of the wall region. Taylor et al. (1985) modelled the roughness effects through a pressure drag term with the aid of a parameter, the blockage coefficients (β_B), for which a spatial distribution is determined by solving an additional transport equation for β_B. The original model was developed to handle identical roughness elements, but later a new model was introduced that can cater for a mixture of different roughness elements. However, the original model has the drawback of being only compatible with turbulent boundary layer flows computed by a mixing length model, which prevents its direct use with sophisticated turbulence closure methods. Recently, Aupoix (2016) addressed this issue by formulating a revised discrete element method that is compatible with more sophisticated turbulence closure RANS models, which are the primary methods of solving many engineering and industrial related flows problems.

Another effective strategy that is common in DNS and LES simulations is modifying the boundary conditions near the rough wall to model the roughness effects. Tuck and Kouzoubov (1995) proposed steady laminar flow simulations on a flat wall. They imposed a partial slip boundary condition on a wall to achieve roughness-like perturbations in the near wall region. Later, Orlandi et al. (2003) simulated a series of slip conditions on turbulent channel flows. The initial simulation is conducted using no-slip boundary conditions; then slip boundary conditions are introduced in a the component-wise manner in the steam-wise (u_1), span-wise (u_2) and wall-normal (u_3) directions, respectively. The slip conditions on u_2 result in similar outcomes to the unperturbed case (smooth wall), whereas the slip conditions on u_1 and u_3 result in drag reductions and structural changes in velocity fields (both mean and turbulent), respectively. Similar structural changes were previously observed in rough wall DNS.

Flores and Jimenez (2006) investigated a turbulent channel flow under the perturbed wall boundary conditions. Even though the investigation is not explicitly focused on modelling wall roughness effects, the outcomes of near wall perturbations resemble rough wall effects. In this investigation, the smooth wall conditions are removed from near wall regions, and non-zero Reynolds stresses have introduced to perturb the velocity field. They observed some effect in the first and second moments of velocity, which are similar in trend to the ones observed in rough wall layer. The effects of the boundary conditions on the mean velocity fields are described using equivalent sand grain roughness. Here, no structures and effects of turbulent quantities penetrate to the outer layer and all the effects are confined to the roughness sublayer.

Miyake et al. (2000) proposed a concept of roughness elements. These are zero volume wall-normal lines extending 15–30 wall units from the wall surface. The profile drag due to these roughness elements are calculated and they are represented as an additional force in the momentum equation. The model has been tested with a channel flow bounded with rough and smooth walls and the mean velocity and turbulent quantities were calibrated with experimental results.

Cui et al. (2003) investigated by LES turbulent flow over arbitrary rough surfaces. Surface roughness was introduced by introducing a body force term in the momentum equation. The roughness was split between resolved roughness and subgrid-scale roughness, which is the similar concept to LES. Here, Verzicco et al. (2000)'s body force approach was used to resolve the large-scale wavy elements. Roughness elements smaller than the grid scale were modelled with Miyake et al. (2000)'s roughness element model. The outcomes of the simulations were validated against a simulation, in which all roughness scales were resolved by a body-fitted grid. The method is very robust and does not rely on any empirical input from experiments, but a complex modification to the momentum equation is a drawback.

Scotti (2006) proposed a body force method to model the effects of roughness. The method is simple to implement and requires no extra computational overheads to simulate. The body force is steady and uniform and based on a single parameter, the roughness height, which is a physical parameter rather than a modelling constant. The model was tested with turbulent channel flow with a rough wall, over which the roughness heights were in the transitional regime (based on the Nikuradse (1950)'s scale), and the outcomes were validated with experimental results.

Busse and Sandham (2012) developed a parametric force model that accepts multiple parameters, the roughness factor (α), the model roughness height (h_r), and the roughness shape $\big(G(z,h_r)\big)$ function. These multiple parameters may complicate the modelling process, but the different combinations can give more flexibility and controllability for representing many kinds of rough walls available in industrial and engineering applications. These parameters have physical significance, but the values used in the model are not directly linked with physical parameters, such as roughness height, and suitable values for these model parameters can be determined with the aid of fully resolved DNS or experimental investigations. As test cases, a set of turbulent channel flow simulations were conducted with different parameter values. The roughness factor (α) and roughness height (h_r), were found to mostly affect the mean velocity profiles and the Reynolds stress profiles, whereas the shape functions are more affected the Reynolds stress profiles more than the mean velocity profiles.

2.5 Non-isothermal flows in rotor-stator cavities

Heat transfer of rotating disks is relevant to many practical applications, such as rotating machinery, combustion chambers and mixing vessels. Early investigation of the subject dates back to the 1950s when important properties of isothermal rotating boundary layers were investigated. By assuming von Kármán (1921)'s similarity solutions, Millsaps (1951) investigated laminar heat transfer coefficients (or the Nusselt numbers) on the rotating disk. Later, Cobb and Saunders (1956) obtained the previously determined laminar heat transfer coefficients to turbulent flow by conducting a series of experimental investigations. They found that the turbulent flow significantly increases heat transfer coefficients of the rotating disk.

Early investigations on heat transfer of rotor-stator cavities were conducted by Nikitenko (1963). He investigated a range of cavities with different aspect ratios, $0.018 < G < 0.085$ at $Re_\omega < 1 \times 10^6$, where both disks were maintained at isothermal conditions. The aim was to obtain generalised correlations for local Nusselt number (Nu_r) distributions for laminar and turbulent flows in the form of, $Nu_r = h_T r / k_f$, where h_T and k_f are the convective heat transfer coefficient and the thermal conductivity of the fluid. The resulting local Nusselt number correlations on the rotor have the form of $Nu_r = 0.675 Re_\omega^{0.5}$ for laminar flow, $Nu_r = 0.02175 Re_\omega^{0.8}$ for the turbulent flow, but none of these correlations includes the effects of the aspect ratio.

Owen et al. (1974) conducted a combined theoretical and experimental investigation of heat transfer over rotating disks. This investigation consisted the cases of a free disk (case equivalent to single disk), of a rotor-stator cavity and of a rotor-stator cavity with throughflow. For the rotor-stator cases, the various aspect ratios within the range $G = 0.0067$–0.18 were tested over Reynolds number range, $2 \times 10^5 \leq Re_\omega \leq 4 \times 10^6$. In the rotor-stator cavities with throughflow, coolant fluid was introduced through a hole on an adiabatic stator. Here, the rotor was the heat source of all the cases in this experiment. The results showed that the dependency of the mean Nusselt numbers ($\overline{Nu_r}$) on the aspect ratio of the cavity, with $G \to \infty$ giving the mean Nusselt number of the free disk ($\overline{Nu_{r,d}} = 0.017 Re_\omega^{0.814}$). At aspect ratios $G < 0.01$, the flow is Couette type (Regions I, III in Fig. 2.3) and ($\overline{Nu_r} > \overline{Nu_{r,d}}$). The Batchelor regime (Regions III, IV in Fig. 2.3) is observed in the range of $0.01 \leq G \leq 0.06$ and the core rotation of the cavity is observed. In this region, the mean Nusselt number is less than the case of the free rotating disk ($\overline{Nu_r} < \overline{Nu_{r,d}}$). At any aspect ratio higher than $G = 0.06$, the mean Nusselt number becomes independent of the aspect ratio of the cavity and ($\overline{Nu_r} = \overline{Nu_{r,d}}$). These results imply that the mean Nusselt number decreases as the aspect ratio increases. At $G > 0.06$, the convective heat transfer coefficient over the rotor becomes decoupled from that over the stator, and the rotor heat transfer process essentially becomes

that of a single disk. Further, they showed that the throughflow has a great influence on heat transfer rates and that the average Nusselt number tends to increase with the throughflow.

Shchukin and Olimpiev (1975) performed heat transfer experiments on a rotor-stator cavity of aspect ratio $G = 0.0645$. They imposed radial temperature distribution over the rotor was found to vary in a fashion of r^n, where usually $n = 0.25$. In the turbulent regime, the average Nusselt number was $\overline{Nu_r} = 0.0168Re_\omega^{0.8}$, which is approximately 11% higher than the free disk value.

These early-stage investigations were more focused on determining the bulk heat transfer properties under laminar and turbulent conditions and their geometrical dependency. Different correlations of local and average Nusselt numbers were proposed to reflect these changes. Many of the pre-1990 investigations are described in (Owen and Roger, 1989; Owen, 1994). The advancements in rotating disk boundary layer models during the 1990s had a significant influence on heat transfer studies in both single and two-disk systems. Henceforth, much of the attention is paid to the more recent investigations.

Elkins and Eaton (2000) conducted a detailed experimental investigation on a heated single rotating disk for Reynolds numbers up to $Re_\omega = 1 \times 10^6$. Due to the low temperature difference maintained during the investigations, the thermal transport was treated as a mere passive scalar and it had a less significant effect on the velocity fields of the flow. It was found that the convective heat transfer coefficient (h_T) is fairly constant in the laminar flow region, but it varies as $h_T \propto r^7$ and $h_T \propto r^{0.6}$ in the transition and turbulent regions respectively. This investigation also compared the outcomes of momentum and thermal transport properties with their respective two-dimensional boundary layer counterparts. At the selected conditions, the boundary layer separated into two regions, the inner and the outer regions, where the demarcation height was defined as $z/\delta \approx 3$. In inner region, Townsend's structure parameter (A_1) and correlation coefficients, $R_{u\theta}$, $R_{v\theta}$ are reduced compared to their corresponding values in two-dimensional boundary layers. This suggests that the three-dimensionality of the boundary layer affects both turbulent shear stresses and heat flux. The outer region of the boundary layer, $z/\delta > 3$, is also different from two-dimensional boundary layers. In this region, the turbulent Prandtl number (Pr_{tur}) reduces below the two-dimensional boundary layers (Subramanian and Antonia, 1981; Gibson et al., 1984) in either side of the three-dimensional boundary layers of the rotor-stator cavity. The quadrant analysis (Rajagopalan and Antonia, 1982; Wallace, 2016) was done on instantaneous turbulent fluctuation components to understand the contribution of the sweeps and the ejections in the rotating boundary layer and it revealed that there is a huge deficit in sweeps contributions on turbulent shear stresses, whereas both ejections and sweeps contribute to vertical turbulent

heat flux. This explains the reduction observed in the turbulent Prandtl numbers of rotating boundary layers.

The first noticeable numerical investigation of the heat transfer of a rotor-stator cavity was conducted by Serre et al. (2004) using a DNS for a rotor-stator cavity with an aspect ratio of $G = 0.426$, $Re_\omega = 1.1 \times 10^5$. This study visualised instantaneous temperature distributions inside the cavity. The hot large-scale structures were elongated toward the upper rotor layer, which is a result of Ekman pumping. A region of hot flow also spreads from the rotor hub to one third of the $\Delta r = (r_2 - r_1)$. The buoyancy effects on the flow were tested using different Rayleigh numbers of $Ra = 0$, 2×10^4, 2×10^6. As described in the Elkins and Eaton (2000), buoyancy effects were less sensitive to the velocity fields but more sensitive to the mean temperature gradients. At the higher Rayleigh numbers of $Ra = 2 \times 10^4$ and 2×10^6 a significant decrease in temperature was noticed in both boundary layers and, in both cases, the temperature distributions of the core region was also reasonably constant compared to the $Ra = 0$ case. Later, Poncet and Serre (2008) extended this investigation with a cavity of aspect ratio $G = 0.2$ over a range of Reynolds and Rayleigh numbers up to $Re_\omega = 1 \times 10^5$ and $Ra = 1 \times 10^8$.

Tuliszka-Sznitko et al. (2009b) investigated the heat transfer properties in rotor-stator cavities using LES. For this numerical investigation, cavities of two different configurations of $G = 0.2$, $Re_\omega = 3 \times 10^5$ and $G = 0.11$, $Re_\omega = 1.5 \times 10^5$, were used. The thermal Rossby numbers of their simulations were $B_{thermal} = \beta_{thermal}(T_2 - T_1) = 0.01$ and 0.4, where T_2, T_1, and $\beta_{thermal}$ are the temperatures of the stator and of the rotor, and the thermal expansion coefficient of fluid respectively. Local Nusselt number distributions were obtained for the rotor and stator. It was observed that an increase in Reynolds number increases the local Nusselt number, which implies a higher heat transfer rate. The influence on the thermal Rossby number on the local Nusselt numbers is shown to be comparatively negligible. Later, Tuliszka-Sznitko and Majchrowski (2010) conducted a similar investigation for co-and counter-rotating cavities.

Tuliszka-Sznitko et al. (2012) proposed rotor-stator DNS and LES over the aspect ratio range $G \approx 0.02$–0.5 and Reynolds number range, $Re_\omega = 1.0 \times 10^5$–$2.9 \times 10^5$. The axial distributions of Reynolds stress components, and temperature fluctuations, turbulent heat flux were validated against previous experiments by of Elkins and Eaton (2000). It was determined that the structural parameters are less sensitive than the Reynolds stress components and turbulent heat fluxes on the changes to the geometric parameters, such as G and R_m.

2.5.1 Heat transfer and nanofluid flows

High performance devices are ubiquitous in modern society, because of the rapid development of technological and industrial sectors. Effective heat management is a key to the operation of these devices, failure to remove the excess heat may severely affect the lifespan and the performance of these devices. As an example, Sulaiman (2011) investigated thermal throttling of microprocessors, which is one of the major bottlenecks in today's semiconductor industry. The issue is not limited to the semiconductor industry but also affects the automobile, space, defence, medical, and industrial sectors.

The thermo-physical properties of the coolant fluid are another vital factor that affects the heat transfer of a process. The gases and liquids are the most common types of coolants used in modern applications. Even though liquids have better heat transfer capabilities than the gases, they also have a low thermal conductivity, which may be not ideal for high performance applications. However, the liquid state enables to enhance the thermal properties of a liquid by mixing it with another substance. As an example, in many applications, a small increase in performance can be achieved by mixing water with ethylene-glycol. The specific heat capacity of metallic substance and their oxides are far superior to liquids. Therefore, a suspension of solid particles in a liquid may impose the heat transfer rate than the pure liquid. However, producing suspensions to fit a wide variety of heat transfer applications is challenging.

The first attempt to characterise a spherical particle suspension in a liquid was reported back to Maxwell (1881). Following Maxwell's investigation, Hamilton and Crosser (1962) studied the effective thermal conductivity of heterogeneous two-component mixtures, which consist of continuous and disperse phases. In these cases, the thermal conductivity of the mixture is obtained as a function of the conductivity of the pure materials which are mixed to compose the mixture.

These stage investigations that are described above considered a micro-sized particle phase, which introduced additional complexities in fluid and heat transport processes. Das et al. (2006) reviewed several reasons for the failure of the micro-sized particle suspensions as a potential heat transfer enhancement solution.

- Micro-sized particles promote quick sedimentation. This might form an insulation layer, which prevents further efficient heat transfer.

- High flow rates and fluid circulation may increase erosion of the internal parts of the equipment.

- Microparticles may cause clogging in narrow channels or pipes.

- The suspension can be subjected to considerable pressure drops, which increase pumping power.

In micro-fluids, heat transfer capabilities are proportional to particle concentration in the mixture, but increased concentrations may result in more significant exposure to the above drawbacks. Despite the failure to deliver the expected results, there is no fundamental misconception in the idea of liquid-solid hybrid solutions enhancing the heat transfer in a system. If the microparticles are too bulky to achieve desired results, further reduction in the size of the particles may mitigate some of the complications that may be experienced during preliminary tests.

The emergence of nanotechnology allows the new suspension to be made. It is capable of manipulating and modifying the nanoscale structures, which add an extra layer of versatility to product design and to the manufacturing processes. Nanotechnology enables the production of nanoscale particles that have different electrical, thermal, and mechanical properties of their parent materials (Das et al., 2006). The first notable heat transfer application in nanoparticles reported by Choi and Eastman (1995). They investigated the possibility of enhancing the heat transfer rates by adding copper a nanoparticle phase to the liquid phase, which showed a considerable improvement in heat transfer over using just pure liquid. At the same time, they noticed that there is no significant increase in pressure loss through the heat exchanger, which is significant progress over microparticle suspensions.

Eastman et al. (1999) studied copper nanoparticles with the volume fraction of 5% suspended in water. They have confirmed excellent suspension properties of the particle phase, which increased the heat transfer by 60% compared to pure water. The suspensions of nanoparticles in a liquid are collectively termed as nanofluids. This has developed into a highly regarded research topic during the past decades (Murshed and Estellé, 2017). The success of nanofluids reflects their ability to overcome the issues that were encountered with microparticle suspension.

Lee et al. (1999) conducted experiments about nanosized metal oxides suspended in liquids unlike with micro-sized particles, the nanofluid heat transfer not only depends on the nanoparticle concentration (or volume fraction), but also on the particle size. In general, smaller particles tend to give a higher heat transfer, because of their specific surface area contribution to the heat transfer is higher than the larger particles, at the same volume fraction. Using low volume fractions of the dispersed phase enables to maintain the Newtonian behaviour of the flow, which eases the analysis and the design process.

For conventional fluid flow problems, the conduction and convection are the prominent heat transfer mechanisms and the nanofluids heat transfer is not an exception, but these mechanisms are often complicated by the presence of multiple phases, multiple components,

and the effects that are only significant to nanoscale structures. The following sections present thermal conductivity and viscosity prediction models for nanofluids. Many of these models have evolved from micro and macro scale particle dynamics.

2.5.1.1 Thermal conductivity of nanofluids

Maxwell (1881)'s original model, which was developed for macro scale particle, can be adapted to estimate the thermal conductivity of the nanofluids. The effective thermal conductivity of the nanofluid is a function of the conductivities of each constituent of the mixture and the corresponding expression reads as

$$k_{nf} = \frac{k_{np} + k_f - 2\phi(k_f - k_{nf})}{k_{np} + k_f + 2\phi(k_f - k_{nf})} k_f, \tag{2.1}$$

where
k_{nf} = thermal conductivity of the nanofluid [W/mK].
k_{np} = thermal conductivity of the nanoparticles [W/mK].
k_f = thermal conductivity of the fluid [W/mK].
ϕ = volume fraction of the nanoparticles.

Bruggeman (1935) suggested a new model that accounts for the interactions among randomly distributed particles. The model assumes a binary mixture of homogeneous spherical particles from which the effective thermal conductivity of the nanofluids k_{nf} is determined by the solution of

$$\phi\left(\frac{k_{np} - k_f}{k_{np} + 2k_f}\right) + (1.0 - \phi)\left(\frac{k_f - k_{nf}}{k_f + k_{nf}}\right) = 0. \tag{2.2}$$

Maxwell's model is only applicable to spherical particles. Hamilton and Crosser (1962) extended the model to non-spherical particles by adding an empirical parameter, the spherical shape factor (n) by which

$$k_{nf} = \left(\frac{k_{np} + (n_s - 1)k_f - (n_s - 1)\phi(k_f - k_{np})}{k_{np} + (n_s - 1)k_f + \phi(k_f - k_{np})}\right) k_f. \tag{2.3}$$

The shape factor (n_s) is defined as $n_s = 3/\psi_S$ and ψ_S is the sphericity of the nanoparticles, which is defined as the ratio of the surface area of a sphere with the same volume of the particle, to the surface area of the particle. Maxwell's equation is a special case of Eq. (2.3), where $n_s = 1$.

Bhattacharya et al. (2004) suggested the idea of modelling the motion of small-scale nanoparticles in a suspension as a *Brownian motion* (see Section 2.6.4 to Brownian motion in

submicron Lagrangian particles). The Brownian motion is a random motion that may occur in particles suspended in fluids, and the magnitude of the force exerted on the particles is inversely proportional to the size of the particles (usually diameter of the particle). Hence, the Brownian motion may be very much significant for nanoparticle suspensions in liquids. Koo and Kleinstreuer (2004) proposed the effective thermal conductivity model as a linear combination of static and Brownian portions of thermal conductivities:

$$k_{nf} = k_{static} + k_{Brownian}. \tag{2.4}$$

The static contribution of the thermal conductivity is the non-Brownian portion of the thermal conductivity, which can be defined by Eqs. (2.1) & (2.3). The second term on the right-hand side represents the addition of the thermal conductivity due to Brownian motion, which is defined as

$$k_{Brownian} = 5 \times 10^4 \beta_1 \phi \rho_f c_{p,f} \sqrt{\frac{k_B T}{\rho_{np} d_{np}}} f(T, \phi), \tag{2.5}$$

where
$k_B =$ Boltzmann constant [$1.38 \times 10^{-23} \mathrm{m^2 kg/s^2 K}$].
$c_{p,f} =$ constant pressure specific heat capacity of the fluid [J/kgK].
Here, β_1 and $f(T, \phi)$ are determined from experiments and Koo and Kleinstreuer (2004) specified the corresponding values for CuO nanoparticles as

$$\beta_1 = \begin{cases} 0.0137(100\phi)^{-0.8229} & \text{if } \phi < 1\%, \\ 0.0011(100\phi)^{-0.7272} & \text{if } \phi > 1\%, \end{cases} \tag{2.6}$$

$$f(T, \phi) = (-6.04\phi + 0.4705)T + (1722.3\phi - 134.63). \tag{2.7}$$

Equation (2.7) is valid for the specific volume fraction and temperature ranges of 1%$< \phi <$4%, and 300 K$< T <$325 K.

2.5.1.2 Viscosity models for nanofluids

The viscosity models of nanofluids are as important as the thermal conductivity models. The presence of a secondary phase increases the nanofluid viscosity and a proper estimate of the effective viscosity of the mixture is very important to predict the outcomes of the system. Viscosity is an important fluid property, and it describes the resistance to flow. The pressure drop in a laminar pipe flow is directly proportional to viscosity and turbulent flow

characteristics and transition to turbulence very much depend on the viscosity of the fluid. Further, in most flows, the temperature has a significant influence on the viscosity of the fluid.

Several theoretical models are available, but none of them is universally accepted, to evaluate nanofluid viscosity, still, these models are often used in analytical and numerical investigations. A most popular model was proposed by Einstein (1906) by which the effective viscosity:

$$\mu_{nf} = \mu_f(1 + 2.5\phi). \tag{2.8}$$

The model is acceptable for nanoparticles concentrations below 1%vol, and many investigators proposed different modifications to the original model.

Hatschek (1913) revised the model of Eq. (2.8) as

$$\mu_{nf} = \mu_f(1 + 4.5\phi), \tag{2.9}$$

which extends its validity of particle concentrations up to 40%.

Brinkman (1952) modified Einstein (1906)'s model to improve its validity at moderate concentrations (< 4 %vol) of particles and the expression reads as

$$\mu_{nf} = \frac{\mu_f}{(1 - \phi)^{2.5}}. \tag{2.10}$$

Roscoe (1952) proposed Eq. (2.11), which is valid for a mixture of any concentration, with rigid spherical particles. The model is capable of accepting different packing fractions of particles to determine the effective viscosity of particle mixture:

$$\mu_{nf} = \mu_f\left(1 - \frac{\phi}{\phi_m}\right)^{2.5}, \tag{2.11}$$

where ϕ_m is the maximum particle packing density. For mono-sized particles, the maximum packing density is $\phi_m = 0.74$ and in mixtures with random loose packing, $\phi_m \approx 0.6$.

Krieger and Dougherty (1959) studied the non Newtonian behaviour of hard-spherical particle suspensions. They proposed the semi-empirical Eq. (2.12) for estimating the effective viscosity based on ϕ_m:

$$\mu_{nf} = \mu_f\left(1 - \frac{\phi}{\phi_m}\right)^{-n\phi_m}. \tag{2.12}$$

Even though the dependency of viscosity on temperature is well known, none of above models reflects that dependence of viscosity on the temperature of the nanofluid. Kulkarni et al. (2006) studied the rheological properties of CuO nanoparticles suspensions, and correlated the nanofluid viscosity to the fluid temperature T over the range of 5–50°C. They

found that

$$ln(\mu_{nf}) = -(2.8751 + 53.538\phi - 107.12\phi^2) + \frac{(1078.3 + 15857\phi + 20587\phi^2)}{T}. \quad (2.13)$$

As mentioned before, the Brownian motion of nanoparticles has a significant influence on the nanofluid properties. Batchelor (1977) investigated the effects of Brownian motion on a statistically homogeneous spherical particle suspension on liquids and modified Einstein's viscosity model to represent the Brownian motion as

$$\mu_{nf} = \mu_f(1 + 2.5\phi + 6.5\phi^2). \quad (2.14)$$

Koo and Kleinstreuer (2004) followed the approach of Eq. (2.5), by which nanofluid viscosity is written as a linear combination of the static nanofluid viscosity and the viscosity contribution from Brownian motion as

$$\mu_{nf} = \mu_{static} + \mu_{Brownian}. \quad (2.15)$$

Here, μ_{static} can be estimated by any one equation from Eqs. (2.8) & (2.14) and $\mu_{brownian}$ is defined as

$$\mu_{Brownian} = 5 \times 10^4 \beta_1 \phi \rho_f c_{p,f} \sqrt{\frac{k_B T}{\rho_{np} d_{np}}} f(T, \phi), \quad (2.16)$$

where all the parameters have the same meaning as in Eq. (2.5).

This section outlined only a few of the viscosity models that are available in the literature to evaluate the viscosity of nanofluids. However, a significant number of additional models that have been reviewed in literature and the majority of them are extensions or modifications of the models which have been presented here. Interested readers are referred to the detailed review by Murshed and Estellé (2017).

2.5.1.3   Other properties of nanofluids

The thermal conductivity and viscosity are the main fluid properties that affect the nanofluid heat transfer. The equivalent nanofluid mixture value of density, specific heat capacity, thermal expansion coefficient, etc., can be obtained by the weighted average defined as

$$\eta_{nf} = (1 - \phi)\eta_f + \phi\eta_{np}, \quad (2.17)$$

where η represents a scalar fluid property and the subscripts f and np denote the fluid and nanoparticles values respectively.

2.5.2 Heat transfer in rotating disk boundary layers due to nanofluids

The conventional heat transfer of rotating disk boundary layers is a well researched topic, and much of the previous literature was reviewed in Section 2.5. However, this section focuses more on the available literature related to rotating disk boundary layer flows in nanofluid context.

Nanofluid heat transfer is not a highly investigated topic in rotating disk boundary layer flow domain, but there are a few investigations that concern the nanofluid heat transfer enhancement in single rotating disk boundary layers, which closely resemble with rotor-stator flow systems. Bachok et al. (2011) studied nanofluid heat transfer in a porous rotating disk. They conducted a numerical simulation by solving the transformed boundary layer equation using a finite difference method. In this study, nanofluid made of nanoparticles of Al_2O_3, CuO, TiO_2, and water was used as the base fluid. The mixture thermal conductivities are calculated based on Maxwell's model and Patel et al. (2006)'s model. As the nanoparticle concentration increases (particle concentrations can increase up to 20% vol), the latter model predicts increased heat transfer rates on both suction and injection (to simulate porosity) at the rotor surface, whereas the former model only predicts increased heat transfer rates under injection.

More recently, Turkyilmazoglu (2014) carried out an investigation to evaluate the flow and heat transfer rates over a rotating disk with nanofluids, which consist with various concentrations of nanoparticles of Al_2O_3, CuO, Cu, TiO_2, suspended in water. This study was more concerned with the variation in the momentum boundary layers under increased nanoparticle concentrations. The boundary layer velocity plots evidenced that increasing the concentration of nanoparticles, such as Al_2O_3, TiO_2, increases the amount of fluid pumped into the rotor boundary layer, but nanoparticles of CuO, Cu behaved oppositely. Regardless of the type of the nanoparticle, an increase in particle concentration increases the Nusselt number, which is an indication of enhancement in heat transfer rate at the same temperature difference.

Bachok et al. (2011) and Turkyilmazoglu (2014) investigations are based on von Kármán similarity solutions, which are very accurate, but their underlying assumptions are restrictive compared to numerical solutions for applications to rotor-stator systems. Another drawback is that the flow fields are assumed to be fully laminar, so these approaches are unusable for the turbulent flow regime. The current study tries to mitigate these drawbacks, by developing and simulating nanofluid based FVM computational models for the rotor-stator flow, and turbulence in the flow is handled using LES. The operational Reynolds number (Re_ω) is 1.0×10^5, which is sufficient for obtaining a turbulent stator boundary layer, but a considerable portion of the rotor boundary exhibits laminar behaviour.

2.6   Lagrangian particle tracking framework

In mechanics, the motion of a system is described either by a *Eulerian* or a *Lagrangian* approach. The Lagrangian approach tracks individual fluid particles in the system, and the particle properties are defined in the frame of reference of the particles. The fluid particles can be either individual molecules or fluid parcels, which are a collection of particles with the same properties. In a Lagrangian simulation, these particles are initially injected at a fixed position (x_0) in computational space and are initialised with properties such as volume, density, velocity, temperature, etc. As the time advances, the particles are free to change their spatial locations and properties according to the laws of mechanics. At any particular i^{th} time frame ($i\Delta t$), one can observe and track the trajectories of the particles and the loci of these particles are often called particle path lines or particle trajectories.

Since the volume fraction (or the concentration) of the carrier fluid is high, it is computationally expensive to use the pure Lagrangian approach to simulate fluid phase, because of the high number of fluid particles. Hence, past investigations have used a hybrid approach by which the Eulerian framework is used to solve the continuum phase (fluid phase), and the Lagrangian method is used to solve diluted dispersed phase within it. This Eulerian-Lagrangian hybrid approach has been used quite extensively in various engineering and industrial applications, which include industrial piping (Ingham, 1975; Fan and Ahmadi, 1993; Li et al., 1994; Inthavong et al., 2016), outdoor air quality and ventilation (Zhao et al., 2004; Zhao and Chen, 2006; Yan et al., 2016), the human respiration system (Nazridoust and Asgharian, 2008; Inthavong, Tu and Ahmadi, 2009; Inthavong, Wen, Tu and Tian, 2009; Inthavong et al., 2010, 2013) and Chemical Vapour Deposition (CVD) systems (Burns et al., 1997; Chein and Su, 2004).

Dispersed solid particles in a fluid can be subjected to different forces, depending on the application, external environmental factors, or particle properties themselves (e.g., shape, size, density ratio, heat capacity, etc.). These factors can significantly influence the outcomes of any particle tracking method, and it is essential to embed relevant information on the core particle tracking framework. The following sections are devoted to outlining a basic particle tracking framework and to introducing its corresponding submodel, which is of particular importance in CVD systems.

The fundamental principle that governs the motion of the particles is Newton's second law of motion. Given a starting Lagrangian particle position vector ($\boldsymbol{x_p}$), the particle track can be obtained by integrating the following equations of motion:

$$\frac{dm_p\boldsymbol{u_p}}{dt} = \sum \boldsymbol{F_p},\qquad(2.18)$$

$$\frac{d\boldsymbol{x_p}}{dt} = \boldsymbol{u_p},$$ (2.19)

where

m_p = particle mass.

$\boldsymbol{u_p}$ = particle velocity.

$\boldsymbol{F_p}$ = the resultant force acting on particles.

The subscript p indicating the pth particle in the set.

The Basset–Boussinesq–Oseen (BBO) equation provides a general framework for estimate the forces on small dispersed particles suspended in a fluid at low Reynolds numbers (Fan and Zhu, 2005). The Reynolds number of a particle is based on the relative velocity between particles and the size of the particles is assumed as comparable with the Kolmogorov length scale of the continuous phase. According to Amiri et al. (2006), these forces on particles can be categorised into four distinct groups:

- The forces due to the motion of the particles. E.g., Basset force, virtual mass, Magnus force.

- The forces due to the motion of the surrounding fluid. E.g., drag and lift forces.

- The forces that arise due to external fields which are independent of the motion of particles or fluid (e.g. gravitational forces, magnetic forces, electrical forces).

- The forces that result in objects which are immersed in a fluid. E.g., buoyancy force.

Even though the BBO equation provides a generic framework for estimating the forces on the particles in fluids, all the terms in the BBO equation may not be significant under specific conditions. For some hard-submicron particles suspended in a gas medium, the Basset force, and the virtual mass can be neglected, due to the high-density ratio between particles and fluid (Burry and Bergeles, 1993). The drag and gravitational forces are then the most significant forces on the particles. For particles well beyond the Strokes regime, lift force can take place due, to the uneven flow distributions around the particles (Amiri et al., 2006).

Apart from the basic forces which are described above, other factors may influence the motion of dispersed particles. These factors may be more significant when the particles are subjected to more complicated flow conditions, such as the presence of thermal gradients, particle diffusion and turbulence in the carrier phase. The development of the Lagrangian framework is typically supplemented by various submodels of the behaviour under these conditions. The next sections are devoted to understanding and formulate the basic forces and submodels, which have been used in this investigation.

2.6.1 Drag force

The drag force on a particle in a fluid medium is unavoidable when there is a relative motion between the particle and the fluid. The early theoretical development was initiated by Stokes (1851), who assumed that the convective effects are negligible compared to the diffusion effects. This assumption limits the applicability of the Stokes theory creeping flows. Later, Oseen (1927) improved the theory by adding linearised convective terms that relax some of the restrictions in the Stokes model. As the velocity of the flow with respect to the particle increases, the flow pattern near the particle becomes more coupled and an analytical estimate of the drag is not possible. This requires reordering to a correlation-based approach in forced by experiments. Achenbach (1974) and Clift and Gauvin (1971) studied drag forces on spherical particles in turbulent flows. They, established that the drag force depends on the particle Reynolds number ($Re_p = \rho_c |\boldsymbol{u} - \boldsymbol{u_p}| d_p / \mu$). For the sake of generality, the drag force is presented in, drag coefficient (C_D), which is

$$C_D = \frac{\boldsymbol{F_D}}{0.5 \rho_c A_p |\boldsymbol{u} - \boldsymbol{u_p}| (\boldsymbol{u} - \boldsymbol{u_p})}, \tag{2.20}$$

where
$\boldsymbol{F_D}$ = drag force .
$\boldsymbol{u}$ = velocity of the carrier phase.
$\boldsymbol{u_p}$ = velocity of the particle.
A_p = surface area of the fluid particle.
ρ_c = density of carrier phase.
The denominator is often referred to as the dynamic pressure. The term $(\boldsymbol{u} - \boldsymbol{u_p})$ is the relative velocity between the continuum phase and particles.

Morsi and Alexander (1972) suggested the following empirical relation for the drag coefficient for smooth spherical particles:

$$C_D = a_{11} + \frac{a_{22}}{Re_p} + \frac{a_{33}}{Re_p^2} + a_{44}. \tag{2.21}$$

The model constants a_{11}, a_{22}, a_{33}, a_{44} are specified in original literature of Morsi and Alexander (1972) for a range of Re_p values.

Clift and Gauvin (1971) used a different empirical correlation for the drag coefficients. This model is capable of tracking liquid droplets that are susceptible to shape distortion at

high Weber numbers (Liu et al., 1993). The expressions for the drag coefficient are given as

$$C_D = \begin{cases} \frac{24}{Re_p} + \left(1 + \frac{1}{6}Re_p^{2/3}\right) & 1 < Re_p < 1000, \\ 0.44 & Re_p > 1000. \end{cases} \tag{2.22}$$

Droplet distortion function is given as follows:

$$C_{DD} = C_D(1 + 2.632y_{dis}). \tag{2.23}$$

The distortion parameter is between ($0 \leq y_{dis} \leq 1$), and for hard-spherical particles $y_{dis} = 0$. Alongside the development of spherical drag models, non-spherical drag force models gained a much of attraction because of their relevance to many industrial and engineering applications. The details about non-spherical drag laws will not be discussed here but interested readers are referred to Haider and Levenspiel (1989). Figure 2.7 shows a comparison of drag models, which have discussed in this section.
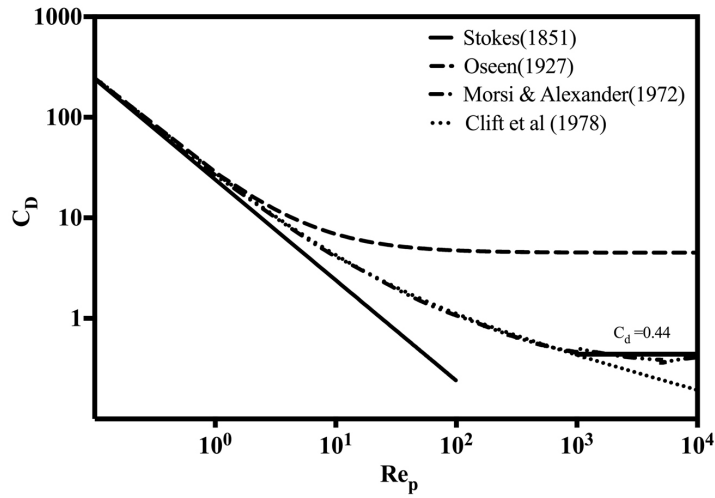
Fig. 2.7 A comparison of drag models with particle Reynolds number (Re_p).

2.6.2 Gravitational force

The gravitational force is a body force that affects mass in a gravitational field. The direction of the force is in the same direction as the gravitational acceleration (**g**). In particle dynamics, the gravitational force becomes significant in particles with diameters larger than 2 μm (Li and Ahmadi, 1993), and the magnitude of the buoyancy effects are calculated according to the Archimedes principle. The resulting net gravitational force per unit mass can be expressed as

below:

$$F_G = g\left(1 - \frac{\rho_c}{\rho_p}\right), \tag{2.24}$$

where

ρ_c = density of the carrier phase.

ρ_p = density of the the particles.

2.6.3 Lift force

The lift force on a particle is defined as the lateral force, which is the in-plane components of the total force acting on the particles, normal to the particle velocity. As such, lift is different from the conventional aerodynamic lift force. Poiseuille (1841) observed a lateral force on blood cells in capillary but the proper causes of these observations remained undiscovered until the later discovery of Segré (1961) and Segré and Silberberg (1962). They observed that particles drift away from the tube axis in a Poiseuille flow experiment. This confirmed the existence of a lateral force on particles suspended in a fluid. Oliver (1962) investigated the particle dynamics in a flow moving in the downward direction. If the particles moved in the same direction as the fluid flow, they drifted away from central axis of the tube; otherwise, particles tended to move toward the central axis of the tube.

The lateral lift force can be caused by shear and wake effects of the carrier phase, by the rotation of particles, or by shape deformation of particles. These factors may not need to contribute in equal magnitudes to the resulting lift force. For hard-spherical particles, the lift due to the shape deformation can be neglected. The rotation of particles is a localised effect and this component is often referred to as the Magnus force (Magnus, 1861). Particle rotation can be initiated by collision with boundaries, inter particle collisions, or carrier phase shear stresses (Rusche, 2003). Rubinow and Keller (1961) derived a low Re_p model for the Magnus force. Later, Crowe et al. (1998) extended this model to higher Re_p numbers.

Apart from particle rotation, the carrier phase shear can impart a lift force on particles. The shear of the carrier phase can generate an uneven pressure distribution over the particle, due to the uneven relative velocity around the particle. As shown in Fig. 2.8, direction of this shear induced lift force is determined by direction of the shear rate of the carrier phase $\left(\frac{d\boldsymbol{u}}{dy}\right)$ and the slip velocity $(\boldsymbol{u} - \boldsymbol{u_p})$. The resulting lift force is identified as the shear induced lift force $\boldsymbol{F_L}$.

Saffman (1965) produced a shear induced lift force model, which is often referred to as the Saffman lift force ($\boldsymbol{F_L}$), which is

$$\boldsymbol{F_L} = 6.46\rho_c a_p^2 \nu^{1/2}(\boldsymbol{u} - \boldsymbol{u_p})|\frac{d\boldsymbol{u}}{dy}|^{1/2}\boldsymbol{sgn}\left(\frac{d\boldsymbol{u}}{dy}\right), \tag{2.25}$$

where $\boldsymbol{u}$, a_p and ν are the carrier phase velocity, particle radius and the kinematic viscosity of the carrier phase fluid. The notation $\boldsymbol{sgn}\left(\frac{d\boldsymbol{u}}{dy}\right)$ denotes the sign of the derivative.

Auton (1987) derived an alternative form of the above equation in terms of the lift coefficient (C_L) and of the vorticity ($\boldsymbol{\omega_c}$) of the carrier phase, and it reads as
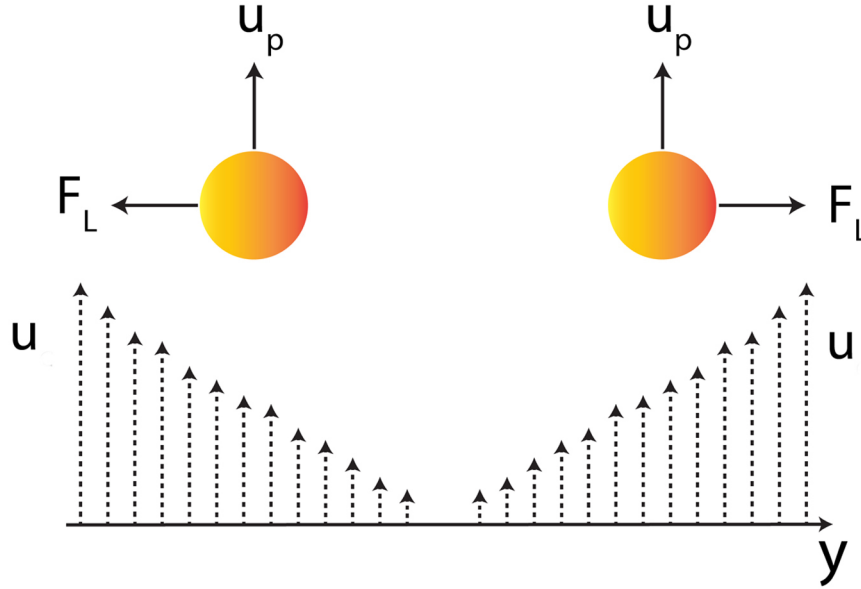

Fig. 2.8 An illustration of carrier phase velocity profiles and the directions of the shear-induced lift force on the particles.

$$\boldsymbol{F_L} = -\rho_c \alpha_p C_L (\boldsymbol{u} - \boldsymbol{u_p}) \times \boldsymbol{\omega_c}, \tag{2.26}$$

where $\boldsymbol{\omega_c} = \nabla \times \boldsymbol{u}$.

The Saffman lift coefficient C_L is defined as

$$C_L = \frac{3}{2\pi\sqrt{Re_{\Omega c}}} C_L', \tag{2.27}$$

where

C_L' = A constant value of 6.46.

$Re_{\Omega c}$ = Reynolds number based on the vorticity magnitude of the carrier phase ($\Omega c = |\boldsymbol{\omega_c}|$).

Equation (2.27) only valid for $0 \leq Re_p \leq Re_{\Omega c} \leq 1$. To mitigate this Mei and Klausner (1994) proposed the following model that is valid over a broader Re_p range:

$$C_{L,M}' = \begin{cases} C_L'(1 - \alpha_{L,M}\beta_{L,M}^{0.5}e^{-0.1Re_p} + \alpha_{L,M}\beta_{L,M}^{0.5}) & 1 < Re_p < 40, \\ C_L'0.0524(\beta_{L,M}Re_p)^{0.5} & 40 < Re_p < 100, \end{cases} \tag{2.28}$$

$$\alpha_{L,M} = 0.3314, \quad \beta_{L,M} = \frac{Re_{\Omega_c}}{Re_p}. \tag{2.29}$$

The model is known as the *Saffman-Mei lift* force model and it can be used to $Re_p = 100$. Nevertheless, the Saffman (1965) model was developed for unbounded shear flows and the presence of wall boundaries may deteriorate the accuracy of the model in near wall regions. McLaughlin (1993) proposed a correction for near wall regions in the Saffman lift model, but this correction was initially verified only for linear sheared flows and the model is unproven for more complicated flow scenarios.

In this section, the main contributions to the lateral lift forces have been discussed. For hard-spherical particles at a low rotation rate, deformation and Magnus effects can be neglected. All models are one-way coupled, and no force feedback is assumed for the dispersed phase to carrier phase. Hence, only the shear induced lift is considered, which is evaluated using the Saffman-Mei lift model. Even though the wall effects may have a significant impact on the near wall calculation, the implementation of wall corrections was not considered, which could be a drawback in the current simulation work.

2.6.4 Brownian Force

A particle suspended in a fluid continuously collides with the surrounding gas or liquid molecules of the carrier phase. These instantaneous collisions affect the momentum of the particle and they can make the particle to move in a random path, which is known as the Brownian motion. Brownian motion generates particle diffusion even in a stagnant fluid and the Brownian diffusion constant D_B by (Buongiorno, 2006)

$$D_B = \frac{k_B T_c C_c}{3\pi\mu d_p}, \tag{2.30}$$

where T_c is the absolute temperature of the carrier phase and the term C_c in Eq. (2.30) is the Cunningham correction factor, which can be estimated as (Davies, 1945)

$$C_c = 1 + 2Kn(1.247 + 0.4e^{-1.1/Kn}), \tag{2.31}$$

where $Kn = \lambda_f/d_p$ is the Knudsen number which is defined as the ratio of the mean free path of the molecules forming the continuous phase (λ_f) to the diameter of dispersed phase particles (d_p). For $\lambda_f = 65$nm, the variation of the Cunningham correction (C_c) factor with Knudsen numbers is shown in Fig. 2.9.
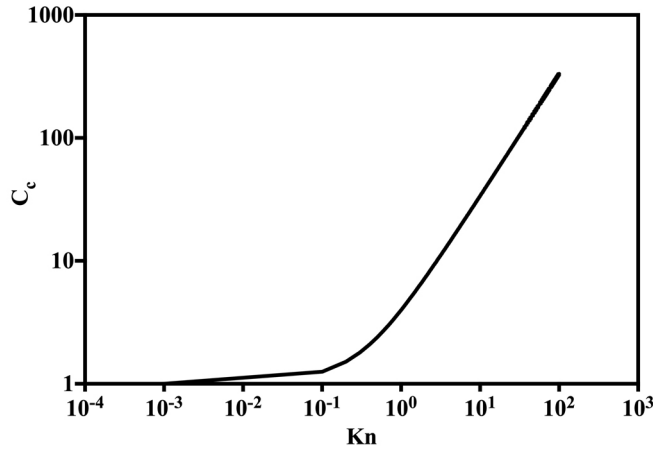
Fig. 2.9 Variation of Cunningham correction (C_c) factor with Knudsen number (*Kn*).

According to Eq. (2.31) and Fig. 2.9, particles with a smaller diameter (or higher Knudsen numbers) are subjected to higher Brownian diffusion rates. An expression for the Brownian force is reported in Guha (2008) and in Inthavong et al. (2010), and amplitude of the Brownian force component states as

$$F_{bi} = \frac{G_i}{m_p} \sqrt{\frac{2k_b^2 T_c^2}{D_B \Delta t}},$$
(2.32)

where G_i is a zero mean, unit standard deviation Gaussian random number (standard normal distribution) and the force amplitude is calculated in each time step Δt. On submicron particles suspended in a fluid, Brownian effects may be significant, but many investigations suggest that the presence of turbulence may overshadow the Brownian effects. Ounis and Ahmadi (1990) did an extensive review of this topic, and their conclusions suggest that the Brownian effects may become substantial in near-wall areas, where laminar flow dominates.

2.6.5 Turbulent dispersion of submicron particles

The turbulent structures in the carrier phase could be highly influential on dispersed phase dynamics. It is recommended to use the instantaneous carrier phase velocity (**u**) for dispersed phase calculations to capture the carrier phase turbulence effects on the dispersed phase. The Reynolds decomposition of instantaneous carrier phase velocity in terms of the mean velocity ($\bar{\boldsymbol{u}}$) and of the velocity fluctuation ($\boldsymbol{u}'$) is given by

$$\boldsymbol{u} = \bar{\boldsymbol{u}} + \boldsymbol{u}'.$$
(2.33)

DNS or high fidelity LES are the most suitable methods to capture these instantaneous velocities. However, their demand on the computing resources is too high to simulate

45

the most flow of industrial interest. The RANS methods can simulate a complex flow with less computing resources, but the resolved carrier phase velocity fields are limited to time-averaged values ($\bar{u}$), which are insufficient for determining $\boldsymbol{u} = \bar{\boldsymbol{u}} + \boldsymbol{u}'$. To estimate $\boldsymbol{u}'$, the Monte Carlo method could be adapted to the underlying RANS model. Gosman and Loannides (1983) used the Eddy Interaction Model (EIM) alongside the RANS k-ε model to study the turbulent dispersed liquid droplets during a combustion process. Later, many investigators, including Wang and Stock (1992), MacInnes and Bracco (1992), and Stapleton et al. (2000), adapted this method to simulate the effects of turbulence on the particle phase. In these approaches, the velocity fluctuation of the carrier phase ($\boldsymbol{u}'$) is made up with the aid of stochastic methods. The unsteady flow of the carrier phase is modelled as a number of eddies, each of which has a finite lifespan (t_e) and a length (l_e). During the motion of a particle, it may interact with several of these eddies in the carrier phase. Once a particle enters into an eddy, $\boldsymbol{u}'$ is assumed constant over the t_e of the eddy and the particle path line is calculated by solving the Eqs. (2.18) & (2.19) at the end of particle residence time (t_r). Small particles tend to attach to the eddies during the life of the eddy ($t_e = t_r$), whereas particles with large inertia may prematurely exit from the eddy ($t_e < t_r$) (Guha, 2008). Whatever the outcome, when the particle crosses into a new eddy, the particle path line is extended using the information from the new eddy. The local eddy generation and its properties (t_e, l_e) can be generated from the pre-calculated mean carrier phase velocity and k and ε fields as in

$$l_e = C_\mu^{0.5} \frac{k^{3/2}}{\varepsilon}, \tag{2.34}$$

$$t_e = \frac{l_e}{|\boldsymbol{u}'|}. \tag{2.35}$$

The EIM method assumes isentropic turbulence. Hence, the Root Mean Square (RMS) velocity components attain the following form:

$$\sqrt{\overline{u_x'}} = \sqrt{\overline{u_y'}} = \sqrt{\overline{u_z'}} = \sqrt{\frac{2}{3}k}. \tag{2.36}$$

The fluctuation velocity components of $\boldsymbol{u}'$, can be obtained as follows:

$$u_x' = G_1 d_{r,x} \sqrt{u_x'^2}, \tag{2.37a}$$

$$u_y' = G_2 d_{r,y} \sqrt{u_y'^2}, \tag{2.37b}$$

$$u_z' = G_3 d_{r,z} \sqrt{u_z'^2}, \tag{2.37c}$$

where G_1, G_2 and G_3 are the random numbers from a Gaussian distribution of zero mean and unit standard deviation. This implementation uses a directional random vector $\boldsymbol{d_r} = (d_{r,x}, d_{r,y}, d_{r,z})$, to generate additional spatial randomness in the fluctuation components.

2.6.6 Thermophoretic force

A Thermophoretic force is generated by the presence of a temperature gradient ($\boldsymbol{\nabla} T_c$) in the carrier phase, by which particles move in the direction of decreasing temperature (a direction opposite to the $\boldsymbol{\nabla} T_c$. Talbot et al. (1980) derived an expression for the thermophoretic force per unit mass as

$$\boldsymbol{F_T} = \frac{-\eta_T}{m_p T_c} \boldsymbol{\nabla} T_c, \tag{2.38}$$

where the thermophoretic coefficient, (η_T) is defined as

$$\eta_T = \frac{6\pi d_p \mu^2 C_s (K_{ther} + C_t Kn)}{\rho_c (1 + 3C_m Kn)(1 + 2K_{ther} + 2C_t Kn)}, \tag{2.39}$$

where K_{ther} is defined as $\frac{k_c}{k_p}$, and k_c, k_p are thermal conductivities of carrier phase and particle phase respectively. The values of the constants in Eq. (2.39) are taken as $C_s = 1.17$, $C_t = 2.18$, $C_m = 1.14$.

2.6.7 Interphase coupling

In two-phase particle laden flows, the coupling, between the dispersed phase and the carrier phase mostly depends on the volume fraction of the dispersed phase. The Lagrangian particle volume fractions are denoted as $\alpha_p = V_p/V_F$, where V_p, V_F are volumes occupied by the particle phase and fluid, respectively. Elghobashi (1994) reviewed the dependence of α_p with the degree of coupling. Figure 2.10 illustrates the dependency of the interphase coupling on α_p. In Fig. 2.10, τ_p is scaled by the Kolmogorov time scales (τ_k) and by the eddy turnover time (τ_l).

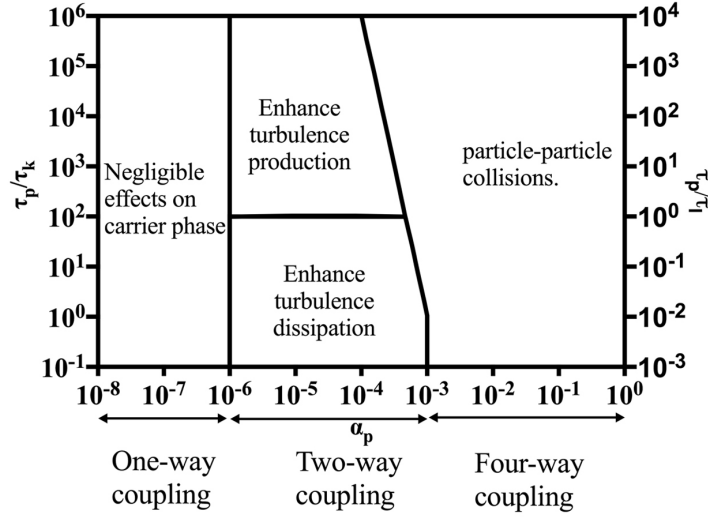Fig. 2.10 Interphase coupling with particle volume fractions (α_p) (Elghobashi, 1994).

The one-way coupling is valid for highly diluted volume fractions of $\alpha_p < 10^{-6}$. Hence, the particle (disperse phase) dynamics is depended on the carrier phase, but the particle feedback on the carrier phase is too weak to have a significant effect on the carrier phase. A two-way coupling occurs at moderate diluted volume fractions, $10^{-6} < \alpha_p < 10^{-3}$, which enable the feedback of individual particles on the carrier phase. In this regime, Elghobashi (1994) introduced a secondary classification, which describes the variation of the modulation of the carrier phase turbulence with different particle relaxation times (τ_p). For a given α_p in the two-way coupling region, a cluster of small particles (or particles with low values of τ_p) could result in increased exposure of their surface area to the surrounding carrier phase fluid than a similar cluster consisting of relatively larger particles. Hence, smaller particles tend to enhance the turbulence dissipation of the carrier phase. Whereas, large particles (higher values of τ_p) implies high Re_p, which enhances the turbulent production of the carrier phase. For much denser suspensions with $\alpha_p > 10^{-3}$, particle-particle collisions become effective, and the term four-way coupling is used to describe this region.

2.6.8 Particle-surface interactions

So far, the contents of Section 2.6 explained the dynamics of particles and their interactions with surround fluid. However, particles behaviour near a solid surface could be an important factor to consider as it could modify the particle deposition behaviour near that surface. The following section discusses the progress on this topic and this study will adept some of these methods in investigating the effects of particle-surface interactions inside a Rotating Chemical Vapour Deposition (RCVD) chamber.

The particle-surface interaction near a solid surface is not only relevant to particles with solid mechanical properties, but it is very much observable in deformable particles, such as liquid droplets. Early stage investigators have observed a reduction in particles and filtration efficiencies on the particles with a certain velocity and inertia. Jordan (1954) did the first notable study about near surface interactions. This investigation provides a quantitative analysis to understand the adhesive energy on the surfaces, but it did not have any experimental evidence to support the idea.

Gallily and La Mer (1958) conducted experiments to supplement Jordan (1954)'s idea of particle-surface interactions, and a two-dimensional jet of glycerol aerosol impacting on inclined Desicote-coated glass slides was observed for different jet stream velocities. They observed a spread in the collection area of the particles as the jet velocity increases, which can be described by possible bounce effects on the surface. In this case, they firmly assumed no sliding effects due to the nature of the application. Further, they assumed that the particle bounce off is affected by the drag force of the air (continuum phase), and subsequently, particles move in a curved trajectory to re-impinge (either re-bounce or deposit) on the surface. Fuchs (1964) provided a comprehensive review of the subject. Even though these investigations have given a useful insight into particle-surface interactions, the results are merely qualitative and lack quantitative descriptions, which require getting a further understanding of the subject.

Rao and Whitby (1977, 1978) conducted a series of experiments to clarify the effects of particle-surface interactions on the particle deposition efficiency. They observed the impact of dry particles on dry surfaces and concluded that particle bounce effects have a substantial influence on particle deposition. In this investigation, they not only determined the causes but identified some remedies to improve the particles deposition. These techniques, such as oil coating the particle surface and the collector surface, selecting different materials for the collector surface (e.g. glass fibre), have improved the depositions efficiencies in their investigations. At a later stage, Esmen et al. (1978) determined that particle flattening is an essential element in improving the particle deposition efficiencies.

Dahneke (1971, 1975) did a thorough investigation of the particle-surface interactions. As a result, he was able to present a particle rebound theory, which is based on particle-surface energy (or adhesion energy) and particle restitution coefficients. This theory provides a generalised approach to predicting the critical values of particle diameters, and of particle velocities, in which particle deposition may occur. Later, Paw and Tha (1983) provided further experimental validation of the rebound theory. With the understanding of the rebound theory, Cheng and Yeh (1979) semi-empirical model using the particle equations of motion and experimental results. They have deduced the critical values of the product of impact

49

velocity, particle diameter, the square root of specific gravity at which the inception of bounce occurs of the particles. Empirical model using the particle equations of motion and experiment results. They have deduced the critical values of the product of impact velocity, particle diameter, the square root of specific gravity at which inception of particle bounce occurs.

Rogers and Reed (1984) broadened the existing rebound theory by incorporating elastic-plastic deformation properties in the particles, in which initial inbound energy should overcome this extra plastic deformation energy to bounce off at the surface. Their study further confirms that the particle deformation is more likely to take place in the particles rather than in the contact surface. Tsai et al. (1990) proposed a new theoretical model by considering contact deformation mechanics and contact surface energy (or adhesive energy on the surface). The investigation pays emphasis on the extra energy needed for surface aspirations, such as surface roughness.

The plastic deformation is an irreversible process, which causes permanent energy loss, and the energy loss can be a significant portion of the initial kinetic energy. Apart from the energy loss, the outer layer of the particles can undergo permanent deformation, in which this plastically deformed layer can show different material properties from its original properties before the impact. Xu and Willeke (1993) studied the right-angle impact and rebound of particles. Consideration is paid on the secondary elastic deformation of previously deformed particles under an impact. The study revealed that the 50% of the initial kinetic energy is stored as secondary elastic deformation energy, while up to 40% is dissipated as the plastic deformation energy, in which energy portions exclusive to secondary deformations phase are significant to determine the subsequent rebound and deposition characteristics of the particles. At a later stage, Xu et al. (1993) have extended this theory to model the impact of incident angles less than 90°. They concluded that the only the normal component is viable for the plastic deformation, whereas the tangential component to the surface contribute toward the particle rotation (or rolling) and rebound. Later, Fergus (2010) has developed a numerical model to study the right-angle particle impact and resuspension of aerosol.

Chapter 3

Computational methods

3.1 Introduction

This chapter describes the all the necessary numerical methods used in the current investigation. The discretisation of partial differential equations using Finite Volume Methods (FVM) is described first. Followed by an introduction to turbulent models use throughout this investigation. The chapter concludes by discussing the suitable transport models used to study the heat transfer in rotor-stator cavities due to nanofluids.

3.2 Computational methods in fluid dynamics

Modern computational methods are capable of replicating a complex physical phenomenon in a digital computer. They can refine knowledge obtained from experiments and theoretical investigations, or produce new insights that are not accessible by classical experimental and theoretical techniques. These gains have a computational cost, and even today's supercomputers may not guarantee to represent the space and time-dependent physical processes under certain conditions. Hence, a careful selection of the most efficient and suitable numerical methods and algorithms is crucial in a successful numerical investigation.

The Navier-Stokes equations are a set of partial differential equations that govern the fluid motion. For some simplified physical applications, exact solutions are available for the Navier-Stokes equation (e.g. von Kármán (1921)), but, in general, it is difficult to find exact solutions for the full Navier-Stokes equation. The numerical and computational approximations are the only viable option in the most of the real-world engineering fluid flows.

Computational Fluid Dynamics (CFD) provides the algorithms, tools, and practices to obtain approximate solutions for the Navier-Stokes equations. This framework can model many engineering flows of practical interest. Still, the selection of appropriate algorithms and tools can significantly improve the efficiency of the solution process.

The selection of a discretisation scheme is the practical first step for solving partial differential equations. This scheme determines how the differential governing equations are converted into a set of algebraic equations. For example, the Finite Difference Method (FDM), the Finite Element Method (FEM), the Spectral Method and the Finite Volume Methods (FVM) are the main discretisation schemes used in fluid flow problems. In each one of these schemes, the discretised set of algebraic equations can be solved using a suitable equations solver for linear systems. However, for this study, FVM is selected as the method of discretisation.

3.3 Governing equations

As described in Chapter 1 & 2, this study investigates on different physical aspects of rotor-stator cavities and the flow field inside these cavities are governed by the Navier-Stokes equations. For an unsteady incompressible flow, the incompressible form of the governing equations are

$$\boldsymbol{\nabla}.\boldsymbol{u} = 0, \tag{3.1a}$$

$$\frac{\partial \boldsymbol{u}}{\partial t} + \nabla.\boldsymbol{uu} = -\boldsymbol{\nabla}p + \boldsymbol{\nabla}.\boldsymbol{\tau} + \boldsymbol{F_b}, \tag{3.1b}$$

where p is the specific pressure defined as $p = \frac{P}{\rho}$ and P is the static pressure. $\boldsymbol{\tau}$ and $\boldsymbol{F_b}$ are the shear stresses and the specific body forces respectively. Incompressibility condition of the flow field assumes constant density (ρ = constant) throughout the entire domain and Eq. (3.1) are normalised by the given ρ of the working fluid.

In general, local variations of the fluid density due to strong buoyancy effects or changes in volume fractions of a disperse phase can be studied using the conservative form of the governing equations which are given by

$$\frac{\partial \rho}{\partial t} + \boldsymbol{\nabla}.\rho\boldsymbol{u} = 0, \tag{3.2a}$$

$$\frac{\partial \rho\boldsymbol{u}}{\partial t} + \boldsymbol{\nabla}.\rho\boldsymbol{uu} = -\nabla P + \boldsymbol{\nabla}.\boldsymbol{\tau} + \rho\boldsymbol{g} + \boldsymbol{F_b}. \tag{3.2b}$$

The pressure distribution of the flow domain can be calculated by considering the equation of state:

$$P = \rho R T, \tag{3.3}$$

where R is the gas constant and the particular value for air is 287.058 $\text{Jkg}^{-1}\text{K}^{-1}$.

These two forms of governing equations are suitable for studying all the application aspects of the current study. Equations (3.1) & (3.2) solve the mass and momentum balance of a flow domain, but a study that involves a heat transfer process should be supplemented with a transport equation for the total energy (E_t) balance of the flow domain. Total energy balance in terms of mechanical energy and thermodynamic energy can be expressed as

$$\underbrace{\rho \frac{De}{Dt}}_{Thermo} + \underbrace{\rho \frac{DK_e}{Dt}}_{Mechnical} = \underbrace{-\boldsymbol{\nabla}.\boldsymbol{q_e}}_{Thermo} + \underbrace{\boldsymbol{\nabla}.(\boldsymbol{\sigma}.\boldsymbol{u}) + \rho\Phi + \rho(\boldsymbol{g}.\boldsymbol{u})}_{Mechnical}, \tag{3.4}$$

where e, $K_e = \frac{1}{2}\boldsymbol{u}^2$ and $\boldsymbol{q_e}$ are internal energy, kinetic energy and the heat flux vector defined positive for the inward direction, respectively. $\frac{D}{Dt} = \frac{\partial}{\partial t} + \boldsymbol{\nabla}.\boldsymbol{u}$ is the material derivative. $\boldsymbol{\sigma}$ is the mechanical stress component that can be represented as $\boldsymbol{\sigma} = \boldsymbol{\tau} - P\boldsymbol{I}$. The heat generation or absorption inside the domain can be represented by the specific heat source or the specific heat sink Φ term.

According to Tu et al. (2007), specific enthalpy (h_e) can be defined as the sum of internal energy and specific pressure, $h_e = e + \frac{P}{\rho}$. By combining this definition with Eq. (3.4), a transport equation for h_e can be derived as

$$\frac{\partial \rho h_e}{\partial t} + \boldsymbol{\nabla}.\rho h_e \boldsymbol{u} + \frac{\partial \rho K_e}{\partial t} + \boldsymbol{\nabla}\rho \boldsymbol{u} K_e - \frac{\partial P}{\partial t} = -\boldsymbol{\nabla}.\boldsymbol{q_e} + \boldsymbol{\nabla}.(\boldsymbol{\tau}.\boldsymbol{u}) + \rho\Phi + \rho(\boldsymbol{g}.\boldsymbol{u}). \tag{3.5}$$

Equation (3.5) is usually combined with mass and momentum conservation equations described in Eqs. (3.2), which are suitable for the flow problems with strong variations in local fluid density. If the fluid is incompressible and the density variation throughout the domain is negligible, specific enthalpy can be expressed as $h_e = c_p T$ where c_p is the specific heat at constant pressure (Tu et al., 2007). Further, by neglecting kinetic energy, and assuming that the work done by the buoyancy forces and the shear stresses are negligible, Eq. (3.5) can be reduced to

$$\rho c_p \left[\frac{\partial T}{\partial t} + \boldsymbol{u}.\boldsymbol{\nabla}T \right] = -\boldsymbol{\nabla}.\boldsymbol{q_e} + \rho\Phi. \tag{3.6}$$

Here, the value of c_p is also assumed to be a constant value, and in most engineering flow applications, $\frac{\partial P}{\partial t} = 0$ (Tu et al., 2007). If there is no heat generation or absorption inside the domain of interest, then $\Phi = 0$. By considering *Fourier's law of heat conduction*, heat flux

vector can be expressed as $\boldsymbol{q_e} = -\boldsymbol{\nabla} k_f T$ and the simplified form of Eq. (3.6) is written as

$$\rho c_p \left[\frac{\partial T}{\partial t} + \boldsymbol{u}.\boldsymbol{\nabla} T \right] = \boldsymbol{\nabla}.(\boldsymbol{\nabla} k_f T), \tag{3.7}$$

where k_f is the thermal conductivity of the fluid.

Apart from the mass, momentum and energy transport equations, which described in this section, a generic transport equation for a scalar field ψ can be expressed as follows:

$$\frac{\partial \psi}{\partial t} + \boldsymbol{u}.\boldsymbol{\nabla} \psi = \boldsymbol{\nabla}.(\Gamma \psi), \tag{3.8}$$

where Γ is the diffusion term in the transport equation. The next section describes the FVM discretisation procedure for the spatial and the temporal terms in Eqs. (3.1)–(3.8).

3.4   Finite Volume Method

In this method, the computational domain is subdivided into a finite number of subdomains that are often referred to as finite volumes or control volumes. The vector variables (e.g. velocity) are either stored in the cell centre or on face centres, and scalar variables (e.g. pressure) are always stored in the cell centre of the volume element. Any cell centre value can be translated into cell faces using a suitable interpolation method. The interpolation process ensures the conservation of mass, momentum and energy.

The FVM has certain advantages over other discretisation schemes for engineering applications. The FVM supports unstructured meshes, which are suitable for modelling complicated geometries. It can also handle a good range of physical boundary conditions. For this reason, the majority of commercial and open source general-purpose CFD codes are based on the FVM. The FVM is the discretisation approach used by the Open Source Field Operation and Manipulation software (OpenFOAM®). OpenFOAM is an open source general-purpose CFD library which is based on C++, and it is publicly available through the GNU public licence.

For the sake of clarity, further discussions are divided into two sections, spatial discretisation and temporal discretisation, which are applied in space and time-dependent applications. Initially, these discretisation methods are demonstrated in an unsteady scalar transport equation with the convective and the diffusive terms (see Eq. (3.8)) and then, the possible extension is discussed for the Navier-Stokes equations.

3.4.1 Spatial discretization

The FVM can be regarded as a special case of the weighted residual method with a unit weight function (Fallah et al., 2000). The inner product of a typical transport equation with the unit function can be written as

$$\int_{V_d} \left(\boldsymbol{\nabla u}.\psi + \boldsymbol{\nabla}\Gamma.\boldsymbol{\nabla}\psi \right) dV = 0, \tag{3.9}$$

where

ψ = an arbitrary vector or scaler field.

V_d = the volume of the computational domain.

$\boldsymbol{u}$ = the velocity field.

Γ = the diffusion term.

In CFD, Eq. (3.9) is a volume integral over the domain (V_d), and (.) denotes scalar product. The domain can be subdivided into a collection of finite number subdomains, often referred to as the unit control volumes (or cells). The typical structure of a cell arrangement is shown in Fig. 3.1. Even though the cells are hexahedrons, OpenFOAM is capable of handling unstructured meshes which consist of cells with an arbitrary number of faces. The point **P** identifies the cell centre, and **N** is the neighbouring cell centre.

The continuous volume integrals in Eq. (3.9) can be transformed into surface integrals using Gauss's divergence theorem by

$$\int_V \boldsymbol{\nabla} \star \psi \, dV = \int_S \boldsymbol{n}.\psi \, dS = 0, \tag{3.10}$$

where ($\boldsymbol{\nabla}\star$), V, and S are an arbitrary vector or tensor operation such as the divergence operator or the gradient operator, the surface area of a control volume, and the volume of a control volume, respectively. The outward unit vector normal to the infinitesimal surface area dS is denoted as $\boldsymbol{n}$, and the directional distance (or the vector) between the cell centre **P** and the directional distance to an adjacent face centre is denoted as $\boldsymbol{d}$.

Equation (3.11) is the surface integral representation of the volume integrals in Eq. (3.9). By averaging a piecewise linear discrete domain, the surface integrals can be replaced with summations as shown in Eq. (3.12).
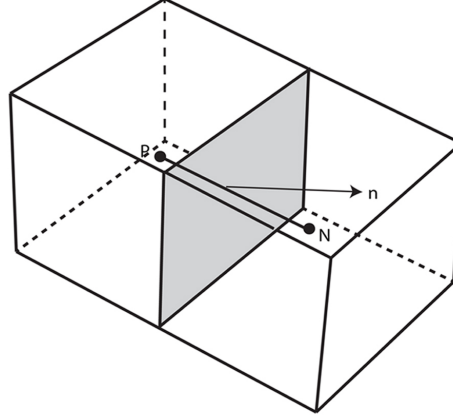
Fig. 3.1 A Typical arrangement of **P** and **N** cells in computational mesh with hexahedral cells.

$$\int_S \psi \boldsymbol{u}.\boldsymbol{n} \, dS + \int_S \Gamma \boldsymbol{\nabla} \psi.\boldsymbol{n} \, dS = 0, \tag{3.11}$$

$$\sum_{cf} \psi_f \boldsymbol{\phi_f} + \sum_{cf} \Gamma_f \boldsymbol{\nabla} \psi_f.\boldsymbol{S_f} = 0. \tag{3.12}$$

The first and the second terms of the right-hand side of the Eq. (3.12) are the convective and diffusion terms respectively. the symbol $\boldsymbol{\phi_f}$ represents the flux through the cell faces, and face area vector is defined as $\boldsymbol{S_f} = \boldsymbol{n} \cdot S_f$. The second term on right-hand side of Eq. (3.12) contains a gradient term and for non-orthogonal cells, this can be defined by (Jasak, 1996)

$$\boldsymbol{S_f}.(\boldsymbol{\nabla}\psi)_f = \boldsymbol{\Delta_{orth}} \frac{(\psi)_N - (\psi)_P}{|\boldsymbol{d}|} + \boldsymbol{k_{orth}}.(\boldsymbol{\nabla}\psi)_f. \tag{3.13}$$

Equation (3.13) is a generalised expression for the gradient that considers non-orthogonal computational cells, which arise as a result of non-parallel $\boldsymbol{S_f}$ and $\boldsymbol{d}$ vectors in the cells of the computational mesh. The orthogonal vector $\boldsymbol{\Delta_{orth}} = \frac{\boldsymbol{d}}{\boldsymbol{d}\cdot\boldsymbol{S_f}}|\boldsymbol{S_f}|^2$ is parallel to the directional vector $\boldsymbol{d}$ and the magnitude is estimated using the *over-relaxed approach* (Jasak, 1996). The non-orthogonal correction vector $\boldsymbol{k_{orth}}$ is estimated from the relation $\boldsymbol{S_f} = \boldsymbol{\Delta_{orth}} + \boldsymbol{k_{orth}}$.

3.4.2 Interpolation Schemes

Collocated solvers, such as OpenFOAM, store the vector variables at the cell centres. The evaluation of Eq. (3.12) requires face-centred values, which require an interpolation method

to transfer cell-centred information to the face centres. The upwind interpolation and linear interpolations are the most frequent methods in FVM based investigations.

3.4.2.1 Upwind Interpolation

This is a bounded first-order accurate method, in which the interpolations are based on the direction of the flow. Since this is a first-order method, solutions tend to more diffusive. The upwind interpolation is formulated as

$$\psi_f = \begin{cases} \psi_P & (\boldsymbol{S}.\psi)_n > 0, \\ \psi_N & (\boldsymbol{S}.\psi)_n < 0. \end{cases} \tag{3.14}$$

3.4.2.2 Linear Interpolation

This is an unbounded second-order accurate method and it is referred to as the Central Difference Scheme (CDS). The method is insensitive to the flow directions, and this leads to oscillations at high Peclet numbers (Pe). The linear interpolation is formulated as

$$\psi_f = x_{PN}\psi_P + (1 - x_{PN}\psi_N), \tag{3.15}$$

where $x_{PN} = \frac{\text{distance(f-}\boldsymbol{N})}{\text{distance(}\boldsymbol{P}\text{-}\boldsymbol{N})}$.

3.4.3 Discretization of time derivatives

The time-dependent transport equations have time derivative term in their governing equations. The discretisation of this term follows a different approach than the spatial discretisation. The time derivative can be represented by a Taylor series expansion of the previous time step values, and the accuracy of the scheme is related to the truncation error of this infinite series.

If the calculation of the current time step value is purely based on previous time step values, these schemes are called explicit schemes, whereas implicit schemes involve the current time step value in their calculations. OpenFOAM only accommodates fully implicit temporal schemes, which are more stable but computationally expensive than explicit schemes. Equations (3.16) & (3.17) represent the first-order Euler method and seconder order backward difference methods that are used to integrate a time derivate over control volumes.

First-order Euler method:

$$\frac{\partial}{\partial t} \int_V \psi \, dV = \frac{(\psi_P V)^n - (\psi_P V)^{n-1}}{\Delta t}. \tag{3.16}$$

Second-order backward difference:

$$\frac{\partial}{\partial t} \int_V \psi \, dV = \frac{3(\psi_P \, V)^n - 4(\psi_P \, V)^{n-1} + (\psi_P \, V)^{n-2}}{2\Delta t}, \tag{3.17}$$

where n, $n-1$ and $n-2$ are the current time step, the old time step, and the old-old time step, respectively.

3.4.4 The Spatial and the temporal discretization of an unsteady generic scalar transport equation with convective and diffusion terms

A unsteady transport equation (e.g. Eq. (3.8)) contains both spatial and temporal derivatives which need to be solved using discretization methods described in Sections 3.4.1–3.4.3. The integral form of a transport equation with a convective term and a diffusive term can be described as

$$\int_t^{t+\Delta t} \left[\frac{\partial}{\partial t} \int_V \psi \, dV + \int_V \boldsymbol{\nabla} \cdot (\boldsymbol{u}\psi) \, dV + \int_V \boldsymbol{\nabla} \cdot (\Gamma \boldsymbol{\nabla}\psi) \, dV \right] dt = 0. \tag{3.18}$$

By considering the spatial discretization procedure described in Eq. (3.12), the *semi-discretized* form (Hirsch, 1990) of the Eq. (3.18) and the expression for a time independent control volume can be written as

$$\int_t^{t+\Delta t} \left[\left(\frac{\partial \psi}{\partial t} \right)_P V_{PM} + \sum_{cf} \psi_f \boldsymbol{\phi_f} - \sum_{cf} \Gamma_f \boldsymbol{\nabla}\psi_f . \boldsymbol{S_f} \right] dt = 0, \tag{3.19}$$

where V_{PM} is the volume of the control volume, which was assumed to be a time independent. In convective and diffusion terms, the relation between the face-centred values and their cell-centred value can be estimated either implicitly or explicitly (Jasak, 1996; De Villiers, 2006). The explicit approach is easier to implement in parallel computer code but simulations are restricted by the Courant–Friedrichs–Lewy (CFL) condition. The CFL condition limits the size of the computational time steps by imposing the condition $Co_{max} = \Delta t \sum_{i=1}^{n_d} \frac{u_i}{\Delta x_i}$ where $Co_{max} = 1.0$ is the maximum Courant number for a typical CFD simulation and $n_d = 3$ is taken for a three-dimensional case. The u_i and Δx_i are the velocity component and the length interval in the respective i directions. While the implicit approach is suitable for simulations that use a higher Co numbers but the approach is more computationally expensive.

Equations (3.20) presents first-order Euler implicit method used in the current implementation of OpenFOAM is given by

$$\frac{(\psi_P)^n - (\psi_P)^{n-1}}{\Delta t}V_{PM} + \sum_{cf}\psi_f^n\phi_f - \sum_{cf}\Gamma_f(\nabla\psi_f)^n.S_f = 0. \tag{3.20}$$

Here, the face values of the current time step ψ_f^n of the equation are estimated by interpolating the current time step values of **P** and **N** control volumes, and they are given by

$$\psi_f^n = x_{PN}\psi_P^n + (1 - x_{PN})\psi_N^n. \tag{3.21}$$

Equation (3.22) shows the implementation of the second-order implicit backward difference method. Unlike in the Euler implicit method described above, this method assumed that there are no temporal variations in the face values:

$$\frac{3(\psi_P)^n - 4(\psi_P)^{n-1} + (\psi_P)^{n-2}}{2\Delta t}V_{PM} + \sum_{cf}\psi_f^n\phi_f - \sum_{cf}\Gamma_f(\nabla\psi_f)^n.S_f = 0. \tag{3.22}$$

3.4.5 Solutions to the Navier-Strokes Equations using FVM

The solutions to the Navier-Strokes equations, which described in Section 3.3, can be obtained using the spatial and temporal discretisation process described in Sections 3.4.1 & 3.4.3. However, substituting the velocity to Eq. (3.18) encounters nonlinearity in the momentum equation.

This issue can be overcome by using a nonlinear system of solvers (Ferziger and Perić, 2002), but the drawback of this approach is the high computational overhead. Equations (3.23a) & (3.23b) show the velocity lagging method, which is a computationally inexpensive approach, and it can linearise the nonlinear terms by lagging the face flux field using the previous iteration or time step value and this can be represented as

$$\int_S dS.n\,uu = \sum S_f.u_f^{n-1}u_f^n, \tag{3.23a}$$

$$= \sum \phi_f^{n-1}.u_f^n. \tag{3.23b}$$

For the incompressible Navier-Strokes equations (see Eqs. (3.1a) & (3.1b)), the unavailability of an explicit pressure equation poses another issue, as the calculation of velocity requires the pressure gradients in the flow field. Patankar and Spalding" (1972) purposed the Semi-Implicit Method for Pressure-Linked Equation (SIMPLE), which is an iterative pressure-velocity coupling algorithm. Later, Issa (1986) introduced a non-iterative algorithm,

the Pressure Implicit with Splitting of Operators (PISO), which is more suitable for time-dependent flow problems. The conventional *pressure-velocity coupling* methods that used in the incompressible Navier-Stokes equations are extended as *"pressure-velocity-density coupling"* methods. These coupling methods can be used to solve the conservative form of governing equations that are used to predict the local variation of the fluid density in a flow field (Ferziger and Perić, 2002; Demirdžić et al., 1993).

3.5 Turbulence modelling

Turbulence in a fluid flow is a naturally occurring phenomenon that may initiate at high Reynolds numbers, as the fluid particles deviate from mean flow path by random motion. The turbulence characteristics in a flow are not properties of the fluid, but they are properties of the flow. Hence, each turbulent flow is unique and dependent on external factors and boundary conditions. This makes the investigation and evaluation of turbulent flow more complicated than laminar flows. Instability mechanisms, such as the Tollmien-Schlichting waves in two-dimensional boundary layers, and Type I, II, III instabilities in three-dimensional boundary layers, can initiate a turbulent flow, but the transition from laminar to turbulent flow is not an abrupt process but evolves through a transition region. This transition region may have large-scale coherent structures, which are not entirely random. Further insights into turbulence can be obtained from Pope (2000).

In the context of turbulent flow predictions, early-stage investigations used strong simplifying assumptions calibrated by experiment, but the recent developments in computing technology enable more advanced computational and numeral techniques in modelling turbulent flows. The Reynolds Average Navier-Stokes Equations (RANS), the Large Eddy Simulations (LES) and the Direct Numerical methods (DNS) are the prominent turbulent flow modelling techniques available. All three techniques can blend with the numerical methods that have been discussed in Section 3.4.

Each method has its pros and cons, and the selection of the most suitable method depends on the purpose of the investigation and on the availability of computational resources. The capabilities of RANS methods are good enough for the most industrial fluid flows. To simulate and visualise turbulent transition or instantaneous turbulent structures, it is better to use DNS or high fidelity LES.

The current study uses RANS and LES models at different stages. The momentum and heat transfer of the rotor-stator cavities will be studied using LES. An extended version of the dynamic Smagorinsky model is used to evaluate turbulent properties, and structures of the rotor-stator cavities operating at $Re_\omega = 1 \times 10^5$ and 4×10^5. However, the heat transfer

effects of the rotor-stator cavity due to nanofluid are simulated using Wall Adapting Local Eddy-viscosity (WALE) subgrid-scale model. This model is more stable than the extended dynamic subgrid-scale model for heat transfer simulations.

Finally, Lagrangian particle tracking (LPT) simulations in the Chemical Vapour Chamber (CVD) are conducted with a RANS turbulent model. Poncet et al. (2010) studied the suitability of RANS models in the context of rotating disk boundary layer flows. In general, the simulations that used the Reynolds Stress Model (Elena and Schiestel, 1996) showed a close agreement with experimental outcomes when they compared to two equation RANS closure models, such as k-ε model and k-ω model. In rotor-stator cavity simulations (i.e. test cases with or without an axial inward flow), all the turbulent models, which including the two equation turbulent models, provided very satisfactory results. However, the the Eddy Interaction model (EIM) of Gosman and Loannides (1983) *strictly* assumed k-ε model in its formulations (see the description and the references within Section 2.6.5). Hence, the k-ε model is selected to ensure compatibility with the EIM model that is used in this work. The DNS or LES methods, which can simulate unsteady eddy structures in the flow, are the alternatives to EIM and they can provide improved accuracy over standard EIM (Stapleton et al., 2000). Nevertheless, the EIM is still used to impose carrier phase turbulence effects on the disperse phase as DNS and LES methods are computationally expensive to use in the current fully three-dimensional CVD configuration. The following sections describe the underlying principles of all these turbulent models outlined above.

3.5.1   Reynolds Averaged Navier-Stokes equation (RANS)

The Reynolds Averaged Navier-Stokes (RANS) models are the most used types of turbulent models, and it applies most industrial fluid flows at high Reynolds numbers. In the current investigation, RANS methods are not suitable for resolving the flow inside rotor-stator cavities but can be used to calculate time-averaged velocity fields in a rotating vapour deposition chambers in Chapter 7.

These methods assume the Reynolds decomposition of Eq. (2.33) and substituting Eq. (2.33) to the Navier-Strokes equations and time averaging the entire equations results in a non-zero term, $\boldsymbol{\tau_{rey}} = -\boldsymbol{\nabla}.((\overline{\boldsymbol{u'u'}})$, which is known as the Reynolds stress tensor. Various models are available to estimate the Reynolds stress tensor, but for this investigation the k-epsilon (k-ε) method is used.

3.5.1.1   k-ε method

The k-ε turbulence model is one of the most commonly used RANS methods. As the name implies, this model considers the budgets of turbulent kinetic energy (k) and turbulent dissipation rate (ε) to determine the turbulent viscosity (μ_t), which can be used to calculate the Reynolds stress tensor by the Boussinesq approximation (Boussinesq, 1877; Schmitt, 2007) and assuming the eddy viscosity model. The spatial and time variations of k and ε can be obtained using the transport equations describe in Eqs. (3.24) & (3.25) by Launder and Spalding (1974) and El Tahry (1983):

$$\frac{\partial}{\partial t}(\rho k) + \boldsymbol{\nabla}.(\rho k \boldsymbol{u}) = \boldsymbol{\nabla}^2 \left[(\mu + \frac{\mu_t}{\sigma_k})k \right] + P_k - \frac{2}{3}\rho(\boldsymbol{\nabla}.\boldsymbol{u})k - \rho\varepsilon + S_k, \qquad (3.24)$$

$$\frac{\partial}{\partial t}(\rho\varepsilon) + \boldsymbol{\nabla}.(\rho\varepsilon\boldsymbol{u}) = \boldsymbol{\nabla}^2\left[(\mu + \frac{\mu_t}{\sigma_\varepsilon})\varepsilon\right] + \frac{C_{1\varepsilon}\varepsilon P_k}{k} -$$
$$\left(\frac{2}{3}C_{1\varepsilon} + C_{3,\text{RDT}}\right)\rho(\boldsymbol{\nabla}.\boldsymbol{u})\varepsilon - C_{2\varepsilon}\rho\frac{\varepsilon^2}{k} + S_\varepsilon, \qquad (3.25)$$

where P_k models the generation of kinetic energy due to the mean velocity gradient. $\sigma_k = 1.0$ and $\sigma_\varepsilon = 1.3$ are the values used as the turbulent Prandtl numbers of k and ε, and the model constant have the values of $C_{1\varepsilon} = 1.44$, $C_{2\varepsilon} = 1.92$ and $C_{3,\text{RDT}} = -0.33$, where RDT stands for Rapid Distortion Theory (El Tahry, 1983). Finally, the turbulent viscosity can be calculated by

$$\mu_t = \rho C_\mu \frac{k^2}{\varepsilon}. \qquad (3.26)$$

The model constant $C_\mu = 0.09$ is used for the majority of flow conditions.

3.5.2   Large eddy simulations (LES)

In a typical turbulent flow, the large eddies are the most energetic portion of the unsteady flow. These large eddies are non homogeneous, anisotropic and susceptible to boundary effects, while the small eddies can be considered to be more homogeneous and universal. LES use a spatial filtering approach to separate the small eddies from large eddies (Leonard, 1975). The large eddies are solved directly using the filtered Navier-Stokes equations whereas the flow components corresponding to the small eddies are modelled. Because of this selective scale filtering, the computational cost of LES is less than the equivalent DNS. Still, LES are computationally more expensive than the equivalent RANS simulations. As defined in Sagaut (2006) and Pope (2000), a typical spatial filtering operation on a total flow variable

$\psi(\boldsymbol{r_p},t)$ is

$$\widetilde{\psi}(\boldsymbol{r_p},t) = \int_{-\infty}^{+\infty} \int_{-\infty}^{+\infty} \psi(\boldsymbol{r}',t')\, G\Big(\boldsymbol{r_p}-\boldsymbol{r}',t-t'\Big)\, d\boldsymbol{r}'dt'. \tag{3.27}$$

This represents total flow variable $\psi(\boldsymbol{r_p},t)$ as

$$\psi(\boldsymbol{r_p},t) = \widetilde{\psi}(\boldsymbol{r_p},t) + \psi'(\boldsymbol{r_p},t), \tag{3.28}$$

and the filter kernel in Eq. (3.27) satisfies the following property:

$$\int_{-\infty}^{+\infty} G(\boldsymbol{r}',t')\, d\boldsymbol{r}'dt' = 1, \tag{3.29}$$

where

$\boldsymbol{r_p}$ = spatial variable.

t = temporal variable.

$\psi(\boldsymbol{r_p},t)$ = total flow variable.

$\widetilde{\psi}(\boldsymbol{r_p},t)$ = filtered flow variable.

$\psi'(\boldsymbol{r_p},t)$ = small-scale spatial fluctuation about $\widetilde{\psi}(\boldsymbol{r_p},t)$.

$G(\boldsymbol{r}',t')$ = filter kernel.

The commonly used filter kernels are the top-hat (box filter), the Gaussian filter and spectral cut-off filters. The filter kernel is defined utilising a filter length (Δ_{sgs}) which can be of arbitrary size, but in LES, it is selected as the boundary scale between the large eddies and small eddies. The filter length scale is usually set in the inertial subrange, and in an FVM code, like OpenFOAM, the filter length is matched to the local cell size of the mesh. According to Versteeg and Malalasekera (2007), the implicit filter length is defined as $\Delta_{sgs} = \sqrt{\Delta x \Delta y \Delta z}$.

As described previously, the filtering process divides the flow into two portions. The flow field now consists of large eddies (grid-scale structures) and small eddies (subgrid-scale structures). A more profound view can be obtained by filtering Navier-Stokes equations with the filter operation in Eq. (3.27). The filtered incompressible Navier-Stokes equations can be expressed as

$$\boldsymbol{\nabla}.\widetilde{\boldsymbol{u}} = 0, \tag{3.30a}$$

$$\frac{\partial \widetilde{\boldsymbol{u}}}{\partial t} + \boldsymbol{\nabla}.\widetilde{\boldsymbol{uu}} = -\boldsymbol{\nabla}\widetilde{p} + \boldsymbol{\nabla}.\widetilde{\boldsymbol{\tau}} + \widetilde{\boldsymbol{F_b}}. \tag{3.30b}$$

The second term on the left-hand side of Eq. (3.30b) is non-commutable, which implies $\widetilde{uu} \neq \widetilde{\widetilde{u}}\widetilde{\widetilde{u}}$. As a remedy, the subgrid-scale stresses ($\boldsymbol{\tau_{sgs}}$) are defined as

$$\boldsymbol{\tau_{sgs}} = \widetilde{\boldsymbol{u}\boldsymbol{u}} - \widetilde{\widetilde{\boldsymbol{u}}}\widetilde{\widetilde{\boldsymbol{u}}}, \tag{3.31a}$$

$$= \widetilde{(\widetilde{\boldsymbol{u}} + \boldsymbol{u}')}\widetilde{(\widetilde{\boldsymbol{u}} + \boldsymbol{u}')}, \tag{3.31b}$$

$$= \underbrace{(\widetilde{\widetilde{\boldsymbol{u}}\widetilde{\boldsymbol{u}}} - \widetilde{\widetilde{\boldsymbol{u}}}\widetilde{\widetilde{\boldsymbol{u}}})}_{I} + \underbrace{(\widetilde{\widetilde{\boldsymbol{u}}\boldsymbol{u}'})}_{II} + \underbrace{(\widetilde{\boldsymbol{u}'\widetilde{\boldsymbol{u}}})}_{} + \underbrace{(\widetilde{\boldsymbol{u}'\boldsymbol{u}'})}_{III}, \tag{3.31c}$$

where

$I = $ Lenord stresses ($\boldsymbol{L_{str}}$).

$II = $ cross stresses.

$III = $subgrid-scale (SGS) eddy interactions.

The Lenord term represents the stresses at resolved-scales (large scales), and the SGS eddy interactions represent the stresses at the subgrid-scale level. The cross-stresses represent the interaction between the resolved-scales and the subgrid-scale stresses. A successful subgrid-scale model should be able to get an accurate estimate of these quantities, and the next section will describe the subgrid-scale models that are used in the current investigation.

3.5.2.1 Dynamic Smagorinsky model

Smagorinsky (1963) provided the first subgrid-scale model for LES, based on *Prandtl's mixing length theory*. Deardorff (1970) used LES to investigate the turbulence in a channel flow, which might be regarded as the first engineering application of LES. A successful LES model should be able to mimic the energy transfer from the resolved-scales to the subgrid-scales. The zero equations subgrid-scale models (equivalent to Prandtl mixing length model in RANS) are the simplest models, yet they are very popular among the research community, and the Smagorinsky model is an example for this category. The following section outlines the particular implementation of Fureby et al. (1997). Following Prandtl's mixing length approach, the subgrid-scale viscosity can be estimated as

$$\boldsymbol{\tau_{sgs}} = -2\nu_{sgs}\widetilde{\boldsymbol{S}} + \frac{2}{3}k_{sgs}\boldsymbol{I}, \tag{3.32}$$

where

$\nu_{sgs} = $ subgrid-scale viscosity.

$\widetilde{\boldsymbol{S}} = \frac{1}{2}(\boldsymbol{\nabla}\widetilde{\boldsymbol{u}} + \boldsymbol{\nabla}\widetilde{\boldsymbol{u}}^T)$ is the strain rate of the resolved-scale.

k_{sgs} = subgrid-scale kinetic energy.

$\boldsymbol{I}$ = unit tensor.

The corresponding values for k_{sgs} and ν_{sgs} are given as below:

$$k_{sgs} = C_l \Delta_{sgs}^2 |\widetilde{\boldsymbol{S}}|^2, \quad \nu_{sgs} = C_d \Delta_{sgs}^2 |\widetilde{\boldsymbol{S}}|^2, \tag{3.33}$$

where C_l and C_d are the model constants, the values of which are user defined and flow dependent. The typical values are $C_l = 0.202$ and $C_d = 0.042$, but these are not universal.

A better approach would be obtaining these values from the resolved-flow, dynamically. Germano et al. (1991) proposed a dynamic version of the Smagorinsky model that calculates the model constants as a part of the simulation process. The dynamic model uses information from the smallest resolved-scales to achieve this. Specifically, an additional coarser spatial filter "$\widehat{(.)}$" is used to identify the smallest resolved-scales in the LES. A scale similarity between the largest eddies in the subgrid-scale and the smallest scales in the resolved-scales is assumed (Meneveau and Katz, 2000). If the secondary filter (or the test filter) is applied to filtered Navier-Stokes equations (see Eqs. (3.30a) & (3.30b)), the stresses at the test filter level can be defined as

$$\boldsymbol{T_{test,str}} = \widehat{\widetilde{\boldsymbol{u}}\widetilde{\boldsymbol{u}}} - \widetilde{\widehat{\boldsymbol{u}}}\widetilde{\widehat{\boldsymbol{u}}}. \tag{3.34}$$

The Leonard stresses ($\boldsymbol{L_{str}}$) for the test filter level is

$$\boldsymbol{L_{str}} = \boldsymbol{T_{test,str}} - \widehat{\boldsymbol{\tau}_{sgs}}. \tag{3.35}$$

The model constants C_l and C_d are computed as (Fureby et al., 1997)

$$C_l = \frac{\langle \frac{1}{2} tr(\boldsymbol{L_{str}})m \rangle}{\langle mm \rangle}, \quad C_d = \frac{\langle \boldsymbol{L_{str}^D}.\boldsymbol{M} \rangle}{\langle \boldsymbol{M}.\boldsymbol{M} \rangle}, \tag{3.36}$$

where $\boldsymbol{L_{str}^D}$ is the deviatoric component of the $\boldsymbol{L_{str}}$. The expressions for the $\boldsymbol{M}$ and m is defined as follows:

$$\boldsymbol{M} = \widehat{\Delta_{sgs}^2 |\widetilde{\boldsymbol{S}}|\widetilde{\boldsymbol{S}}} - \widetilde{\Delta_{sgs}^2}|\widehat{\widetilde{\boldsymbol{S}}}|\widehat{\widetilde{\boldsymbol{S}}}, \quad m = \widehat{\Delta_{sgs}^2 |\widetilde{\boldsymbol{S}}|^2} - \widetilde{\Delta_{sgs}^2}|\widehat{\widetilde{\boldsymbol{S}}}|^2. \tag{3.37}$$

The angle brackets in Eqs. (3.36) represents averaging along a homogeneous direction. This is used to avoid singularities in the model. However, this approach is not suitable for the rotor-stator cavities, due to the unavailability of a homogeneous direction. Hence, for the current investigation, averages over the local cells faces have been considered and this method allows long simulation times without any numerical or physical anomalies. Further, energy backscattering could be as important as energy forwardscattering for the wall bounded flows (Mason and Thomson, 1992; Blackman et al., 2017), therefore, the backscattering was

allowed by enabling negative values in Eq. (3.33) which permits energy propagation from small scales to the large scales. Here, the minimum value of the effective viscosity of the simulation is limited to zero.

3.5.2.2   Wall Adapting Local Eddy-viscosity model (WALE model)

This is an eddy viscosity model purposed by Nicoud and Ducros (1999). The subgrid-scale viscosity is calculated by considering the traceless symmetric part of the square of the velocity gradients tensor ($\boldsymbol{S^d}$), and the expression for μ_t reads as follows:

$$\mu_{sgs} = \rho \widetilde{\Delta_w} \, \frac{(\boldsymbol{S^d S^d})^{3/2}}{(\widetilde{\boldsymbol{SS}})^{5/2} + (\boldsymbol{S^d S^d})^{5/4}}, \tag{3.38}$$

where $\widetilde{\boldsymbol{S}}$ and $\boldsymbol{S^d}$ are the filtered and deviatoric parts of $\boldsymbol{S}$ respectively, and the ρ is the density of the fluid. The quantity $\Delta_w = C_w V_{PM}^{1/3}$ is the filter width of the WALE model parametrised by a constant $C_w = 0.325$, and the volume of cells ($V_{PM} = \Delta x \Delta y \Delta z$).

3.5.3   Direct Numerical Simulations (DNS)

Direct Numerical Simulations (DNS) are a simple but computationally expensive approach that resolves every length and timescale in the flow without any aid of any turbulence model. Due to high demand on computational resources, the DNS approach was unrealistic until the early 1970s. Lilly (1971) conducted the first notable work in DNS. At that time the majority of the investigations were limited to homogeneous low Reynolds number flows. Recent advancement in computing resources allows DNS to inhomogeneous flow fields. However, at high Reynolds numbers, DNS are susceptible to numerical instabilities, which can be avoided by using a suitable stabilisation method (Tadmor, 1989).

3.6   Single and two-phase transport models of nanofluid heat transfer

There are two main approaches to modelling nanofluid related flow problems, and Fig. 3.2 illustrates a hierarchical view of these approaches.

The current study adopts both single-phase and two-phase approaches, in which the former is computationally less demanding, whereas the latter provides more information about the behaviour of the nanofluid flows. The scope of this study is limited to Eulerian-Eulerian approximations, and no attempts have been made to use Eulerian-Lagrangian

Fig. 3.2 A summary of available numerical approaches to model nanofluid flows.

approaches, as the computation was estimated to be unaffordable even for moderate particle concentrations (1–5% vol). Chapter 7 performs simulations by a Eulerian-Lagrangian method and shows its application to rotor-stator flows for relatively large particles (i.e. micron and submicron particles) at very low volume fractions ($\alpha_p < 10^{-6}$).

3.6.1   Single-phase models

As the name implies, a single phase flow model assumes that any number of phases in the real flow are thermally in equilibrium and have zero relative velocity between the phases. In continuous phase case, water and solid phase nanoparticles are modelled as a continuous liquid. The thermo-physical properties of the mixture can be calculated from correlation models, which were described in Section 2.5.1.1. Then, these thermo-physical values feed into the conservative form of the mass and momentum equations (see Eqs. (3.2)), and the energy equation (see Eq. (3.7)) described in Section 3.3, and they read as

$$\frac{\partial \rho_{nf}}{\partial t} + \boldsymbol{\nabla}.\rho_{nf}\boldsymbol{u} = 0, \tag{3.39}$$

$$\frac{\partial \rho_{nf}\boldsymbol{u}}{\partial t} + \boldsymbol{\nabla}.\rho_{nf}.\boldsymbol{uu} = -\nabla P + \boldsymbol{\nabla}.\boldsymbol{\tau_{eff}} + \rho_{nf}\boldsymbol{g_b}, \tag{3.40}$$

$$(\rho c)_{nf}\left[\frac{\partial T}{\partial t} + \boldsymbol{u}.\boldsymbol{\nabla} T\right] = \boldsymbol{\nabla}.(k_{eff}\boldsymbol{\nabla} T). \tag{3.41}$$

Here, $\mathbf{u}$ is the resultant nanofluid velocity, and ρ and c are density and heat capacity at constant pressure, and the subscript nf in each parameter represents the equivalent nanofluid properties. $\boldsymbol{g_b} = \left[1 - \beta_{nf}(T - T_{ref})\right]\boldsymbol{g}$ is the Boussinseq gravity calculated using the Boussinesq approximation (Gray and Giorgini, 1976), and β_{nf}, T_{ref} and $\boldsymbol{g}$ are thermal expansion coefficient of the nanofluid, reference temperature and gravitational acceleration, respectively. Since the volume fraction of nanoparticles is assumed homogeneous throughout the domain, the single-phase model has the form of the standard incompressible Navier-Stokes equations, but still, the density of nanofluid is coupled with the fixed volume fraction defined in the problem. The effective shear stresses (μ_{eff}) and thermal conductivities (k_{eff}) of the equation read as follows:

$$\mu_{eff} = \mu_{nf} + \mu_{sgs}, \tag{3.42}$$

$$k_{eff} = k_{nf} + (\rho c)_{nf}\frac{\mu_{sgs}}{Pr_{sgs}}, \tag{3.43}$$

where μ_{sgs} and Pr_{sgs} are subgrid-scale viscosity and Prandtl number. As described in Section 2.5.1.3, the equivalent nanofluid values for ρ_{nf}, $(\rho c)_{nf}$ and β_{nf} can be calculated as

$$\rho_{nf} = (1 - \phi)\rho_f + \phi\rho_{np}, \tag{3.44}$$

$$(\rho c)_{nf} = (1 - \phi)(\rho c)_f + \phi(\rho c)_{np}, \tag{3.45}$$

$$(\beta)_{nf} = (1 - \phi)(\beta)_f + \phi(\beta)_{np}. \tag{3.46}$$

For a nanofluid with ϕ % vol of nanoparticles.

3.6.2 Two-phase models

The Eulerian-Eulerian approach treats the dispersed phase as another continuous phase. Hence, the computational load does not depend on the particle volume fraction, which is a significant advantage of the fully Eulerian approach in two-phase flows compared to the Eulerian-Lagrangian approach. Subsequent sections briefly explain the three Eulerian-Eulerian methods,

The Volume of fluid (VOF) method is ideal for modelling the behaviour of two or more immiscible fluids with fluid interface tracking algorithms (van Sint Annaland et al., 2005; Renardy et al., 2001). Usually, the mixture has common momentum and energy equations, and the secondary phases have individual volume fraction equations. The typical problems that are suitable for the VOF include the motion of gas bubbles inside a liquid and the motion of liquid after breaking of a dam.

The mixture model is suitable for modelling a multiphase flow with non-zero slip velocities between each phase, which means that one phase may have relative motion respect to the other phases, due to an external force, such as gravity, centrifugal forces, etc. As in the VOF method, the mixture model has a common continuity, momentum and energy equations, but secondary phases have individual volume fraction equations.

The Eulerian models are more general than the mixture model and VOF model and allow to model any number of independent, yet interacting phases. Each phase has own continuity, momentum, and energy and equations, but in practice, the number of phases can be quickly constrained by computational memory available. This model is the least restrictive model in Eulerian-Eulerian modelling approach, and it can handle problems involving interphase mass, momentum and energy transfer through interphase exchange coefficients.

After discussing the advantageous and disadvantageous of each Eulerian-Eulerian modelling approach, the mixture model and the Eulerian model are deemed to be more suitable than the VOF method. Further, by considering the computational cost, the complexity of the modelling, and higher adapting from of previous literature, the mixture model is chosen for this study.

As described earlier, in the traditional mixture model, a slip velocity can arise due to the imbalance in local forces of nanoparticles, such as gravity, centrifugal forces, etc. The slip velocity can be presented as a function of the particle relaxation time, particle drag forces, and advection due to the local mixture velocity (Rebay et al., 2016). The current investigation adepts a different approach to calculating the slip velocities and the calculation of these slip velocities are based on the slip mechanisms, described by Buongiorno (2006). This is an alternative approach to the traditional mixture model.

According to Buongiorno (2006), inertia, Brownian diffusion, thermophoresis, diffusiophoresis, Magnus effects, fluid drainage, and gravity are the seven slip mechanism that might be important in nanoparticle dispersion. Further, he explains that the Brownian diffusion and thermophoresis are relatively important than the other slip mechanism in nanoparticle dispersion. However, the presence of turbulence can significantly suppress the Brownian and thermophoresis effect, but still, these effects may play a significant role in near-wall regions, where laminar flow dominates. By considering Brownian and thermophoresis effects, the

governing Eqs. (3.39) & (3.41) can be rewritten as

$$\frac{\partial \rho_{nf}}{\partial t} + \nabla.\rho_{nf}\boldsymbol{u} = 0, \tag{3.47}$$

$$\frac{\partial \rho_{nf}\boldsymbol{u}}{\partial t} + \nabla.\rho_{nf}\boldsymbol{uu} = -\nabla P + \nabla.\boldsymbol{\tau_{eff}} + \rho_{nf}\boldsymbol{g_b}, \tag{3.48}$$

$$(\rho c)_{nf}\left[\frac{\partial T}{\partial t} + \boldsymbol{u}.\nabla.T\right] = \nabla.(k_{eff}\nabla T) + (\rho_p c_p)\left[D_B\nabla\phi.\nabla T + D_T\frac{\nabla T.\nabla T}{T}\right], \tag{3.49}$$

$$\left[\frac{\partial \phi}{\partial t} + \boldsymbol{u}\nabla.\phi\right] = \nabla.\left[(D_B + \varepsilon_P)\nabla\phi + D_T\frac{\nabla T}{T}\right], \tag{3.50}$$

where ϕ is the volume fraction of the nanoparticles and D_B, D_T are Brownian and thermophoresis diffusion respectively. Buongiorno (2006) made following assumptions for nanofluid mixture (both base fluid and nanoparticles):

- No chemical reactions.

- Negligible external forces.

- The mixture is diluted $\phi \ll 1$.

- Viscous dissipations are negligible.

- Radiative heat transfer is negligible.

- Base fluid and nanoparticles are locally in thermal equilibrium.

The continuity and momentum equations (see Eqs. (3.47) & (3.48) are in the same form as the single-phase equations but the energy equation (see Eq. (3.49) is modified with added nanoparticle diffusion because of Brownian and thermophoresis effects, in which these additional terms account for the nanoparticle slip velocity relative to the base fluid. The final equation is the volume fraction equation (see Eq. (3.50), which models the homogeneous portion (advection term in Eq. (3.50) and slip velocities (diffusion term in Eq. (3.50)) of the nanoparticle transport. In the same investigation, Buongiorno (2006) provided the expression for the diffusion constants of Brownian and thermophoresis effects that also used in this study and they can be read as follows:

$$D_B = \frac{k_B T}{3\pi\mu d_{np}}, \tag{3.51}$$

$$D_T = \beta_p \frac{\mu}{\rho} \phi, \tag{3.52}$$

where $k_B = 1.38^{-23} \text{m}^2/\text{kgs}^2\text{K}$ is the Boltzmann constant, and $\beta_p = 0.26 \frac{k_f}{2k_f + k_{np}}$ is the proportionality factor.

The effective shear stresses and thermal conductivity are calculated following a similar procedure to Section 3.6.1. As suggested by Buongiorno (2006), the eddy diffusivity of particles (ε_p) is set equal to the eddy diffusivity of momentum (μ_{sgs}) and the nanoparticles are taken as homogeneously entertained by the turbulent eddies of the continues phase.

3.7   Summery

This chapter explained the numerical and computational methods relevant to the current investigation. The FVM discretisation method was introduced, followed by a general introduction to turbulence. The three main approaches to the turbulent modelling, RANS, LES, and DNS, were discussed and a brief explanation was given on RANS and LES methods, which are used at the different stages of this investigation. Finally, more details on three turbulent models, the k-ε method, the dynamic Smagorinsky model, and the WALE model, were given. Two transport models were discussed to simulate the rotor-stator cavities filled with nanofluids, and the future considerations were paid on their the operational limitations, relative advantages and disadvantages.

Chapter 4

A computational validation for the rotor-stator cavities

4.1 Introduction

This chapter is devoted to the implementation of an LES model to simulate rotor-stator cavities. Previous numerical models of rotating disk boundary layers mainly used high-order numerical methods with DNS or LES. The single rotating disk investigations by (Wu and Squires, 2000; Davies and Carpenter, 2003; Appelquist et al., 2015, 2016), rotor-stator flows investigations by (Serre et al., 2004; Lygren and Andersson, 2001; Séverac et al., 2007; Tuliszka-Sznitko et al., 2009a) are some of the examples where these high-order methods were used. The recent investigation of Makino et al. (2015) is the only second-order based numerical investigation on rotor-stator flows. They used a collocated grid-based solver with the Crank-Nicolson scheme to solve the flow governing equations. The large-scale turbulent components were resolved with a mixed-timescale SGS model based LES method.

The current simulations were set up under the similar physical conditions to the ones in Makino et al. (2015). Elongated annular cavities of $G < 1$ are simulated for two different operational Reynolds numbers $Re_\omega = \frac{\omega r_2^2}{\nu} = 1 \times 10^5$ and 4×10^5. The lower Re_ω case attains only a turbulent stator flow, whereas the higher Re_ω case results in turbulence both at the rotor and stator.

The objective of this chapter is to ascertain the suitability of FVM methods and general purpose CFD tools, such as OpenFOAM, to simulate rotor-stator flows. For this, the OpenFOAM results are compared with previous investigations of Séverac et al. (2007) and Makino et al. (2015).

4.2 Problem definition

4.2.1 Geometric modelling

The rotor-stator cavities, which are modelled in this section, consisting of the two concentric disks. The inter-disk spacing (h) between these two disks is large enough to avoid merged boundary layers. Figures 4.1 & 4.2 illustrate the top and side views of the rotor-stator cavity. The geometry is defined in the cylindrical coordinate system (r, θ, z). The inner radius (r_1) is the radius of the hub that this is directly connected to the rotating disk. The distance between the origin and the periphery of the rotating disk is the outer radius (r_2). For an annular cavity, the radial extent is $\Delta r = r_2 - r_1$ and, if $r_1 = 0$, the cavity becomes a cylindrical cavity. The operational Reynolds number based on the rotating disk periphery is $Re_\omega = \frac{\omega r_2^2}{\nu}$ and the local Reynolds number at any given point (p) is $Re_{\omega,local} = \frac{\omega r^2}{\nu}$ where r is the radial distance between the point and the origin.
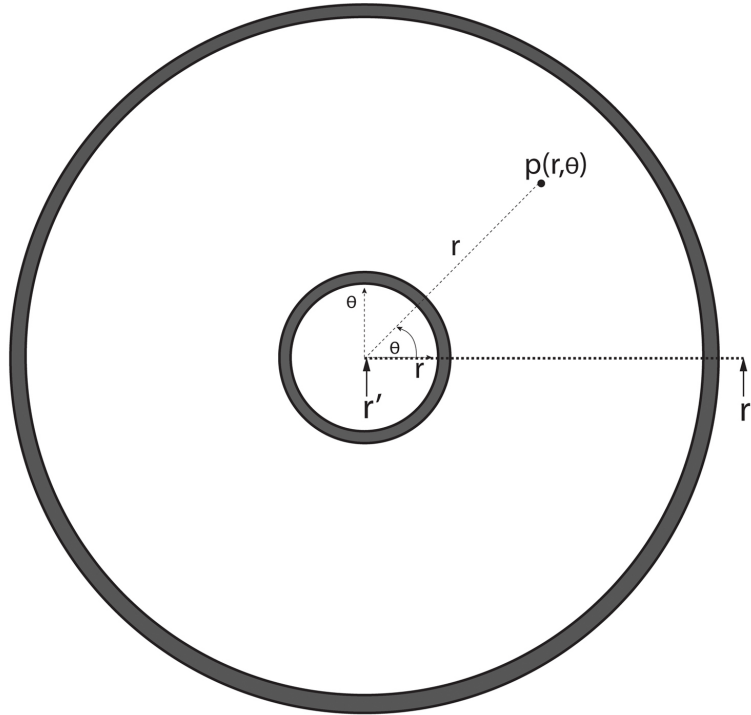
Fig. 4.1 Top view of the rotor-stator cavity and the grey areas represent finite gaps ($\delta_{H-rotor}$ and $\delta_{H-stator}$) in the geometry.

The physical assembling and machining processes of a cavity require small clearances between rotating components and stationary components ($\delta_{H-rotor}$ and $\delta_{H-stator}$ in Fig. 4.2), whereas numerical models require capturing this information to avoid any potential numerical

disorders. For Taylor-Couette flow problems, the clearances were maintained under a certain threshold value $\delta_H/h < 0.2$ at which these gaps have negligible effects on the flow field away from the clearances (Tavener et al., 1991). Later, Séverac et al. (2007) have followed this approach to model the clearances in their rotor-stator cavity simulations and they used boundary vanishing functions to regularise the tangential velocity component near the rotor and the stator boundary surfaces. The current investigation uses the clearance values $\delta_H/h \ll 0.2$, and these clearances are implemented by geometrical modelling. The aspect ratio G and the curvature R_m are two important geometric parameters of the cavity, which have a significant influence on flow properties and characteristics. During this entire investigation, the G and R_m are kept as constant values, and they are defined in Eq. (4.1):

$$G = \frac{h}{r_2 - r_1} = 0.2, \quad R_m = \frac{r_2 - r_1}{r_2 - r_1} = 1.8. \tag{4.1}$$
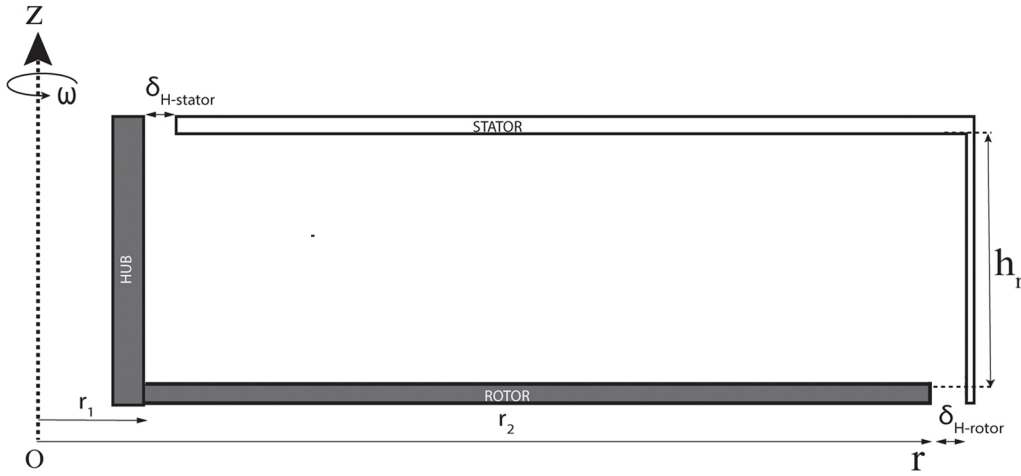
Fig. 4.2 The side view of the rotor-stator cavity cross section r'–r' as shown in Fig. 4.1.

A commercial mesh generation software, ANSYS ICEM CFD®, is used to generate a hexahedral computation mesh. The number of elements, which are used to construct high and low Reynolds number cases, are shown in Table 4.1, and the final mesh configuration for the case of $Re_\omega = 4 \times 10^5$ is shown in Fig. 4.3.

Re_ω	r_1	r_2	h	$r \times \theta \times z$
1×10^5	140	40	20	$220 \times 180 \times 140$
4×10^5	280	80	40	$256 \times 600 \times 180$

Table 4.1 The mesh configurations use in LES simulations.

(a) *(b)*
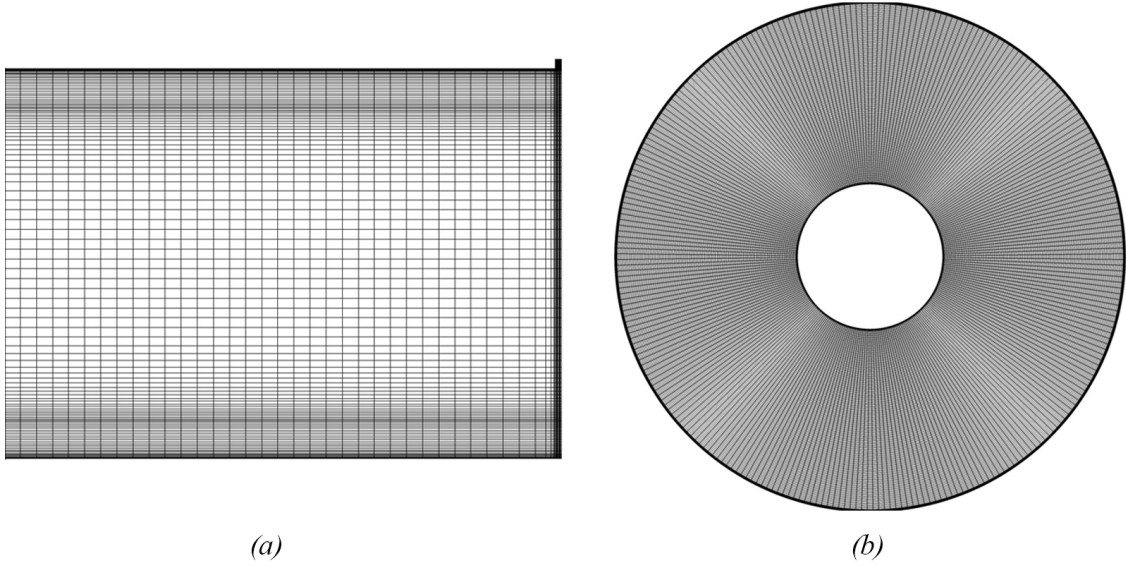
Fig. 4.3 The computational mesh used in $Re_\omega = 4 \times 10^5$, (a) side view, (b) top view.

4.2.2 Numerical modelling

All simulations are conducted using OpenFOAM®, which uses a second-order accurate FVM based segregated solver, and the non-iterative PISO algorithm provides the pressure-velocity coupling solutions to the governing equations. All the simulations satisfy the conditions $z_{max}^+ \leq 1.0$ and the maximum value of Courant number is maintained at $Co_{max} \leq 0.325$.

4.2.3 Governing equations and turbulence modelling

The governing equations for a Newtonian single-phase isothermal incompressible flow can be described by three-dimensional Navier-Stokes equations as described in Eqs. (3.1), and the current study uses the incompressible filtered Navier-Stokes equations (see Eqs. (3.30)), which are a result of spatial filtering of Eqs. (3.1) due to the LES turbulent modelling.

75

A collocated FVM has been used to discretise the governing equations, and a second-order accurate central difference scheme and the implicit backward difference method are used to perform the spatial differentiation and the temporal integration of Navier-Stokes equations. The dynamic Smagorinsky model (see Section 3.5.2.1) is used to calculate the subgrid-scale turbulent stresses on the flow field.

All the walls are treated with no-slip boundary conditions. The rotating motion of the rotating disk set is through the boundary condition on the disk surface and rotation rate (ω) is adjusted to satisfy the required Re_ω conditions by

$$\boldsymbol{u_{rotor}} = \omega \boldsymbol{r_p} \times \boldsymbol{I_{dir}}, \tag{4.2}$$

where $\boldsymbol{r_p}$ is the position vectors to a given point (p) on the rotor surface and $\boldsymbol{I_{dir}} = (0,0,1)$ is the axial directional vector.

4.3   Results and discussion

This section discusses the validation of the computational model against rotor-stator cavities with $Re_\omega = 1 \times 10^5$ and 4×10^5. All the simulations are initialised with the zero velocity everywhere in the internal computational domain (except at the boundary surfaces). The reference pressure of the flow field set to zero and the zero-gradient pressure conditions are applied at all the boundaries of the computational domain.

As discussed in Section 3.5.2, resolution and the quality of the mesh is an important factor for a successful LES approach. A finer mesh can directly resolve higher frequency structures, and the finest mesh can resolve the smallest structures of the problem, i.e. the Kolmogorov scales, in which LES is almost in line with DNS (Speziale, 1998). However, this practice is not always possible, as the resolution of the mesh often limited by the available computing resources. The configurations and resolutions of meshes are carefully selected to simulate rotor-stator cavities, and a parameter, $Q_m = k/k_{total}$, has been defined to evaluate the adequacy of the mesh resolution. Here, $k_{total} = k + k_{sgs}$ is the total turbulent kinetic energy, where k and k_{sgs} are the resolved kinetic energy and subgrid-scale kinetic energy, respectively and they can be defined as

$$k = \frac{1}{2}(\overline{u'_r u'_r} + \overline{u'_\theta u'_\theta} + \overline{u'_z u'_z}), \tag{4.3a}$$

$$k_{sgs} = 1/2 tr(\boldsymbol{\tau_{sgs}}). \tag{4.3b}$$

The $tr(.)$ operation gives the trace of a tensor, and the resolved-scale fluctuation velocity field ($\boldsymbol{u}'$) is usually calculated by

$$\boldsymbol{u}' = \widetilde{\boldsymbol{u}} - \overline{\widetilde{\boldsymbol{u}}}, \tag{4.4}$$

where $\overline{\widetilde{\boldsymbol{u}}}$, $\widetilde{\boldsymbol{u}}$ are time-averaged filtered and instantaneous filtered velocity, respectively.

Figures 4.4 (a) & (b) show contours of Q_m in the midsection of r–z plane, for both $Re_\omega = 1 \times 10^5$ and 4×10^5 cases, and the most of the regions in the cross-section occupy Q_m values very close to unity. Figure 4.4 (c) presents frequency histogram of Q_m normalised by the total number of cells in the computational domain so that the height of each bar represents the percentage of cells belong to the corresponding bin of Q_m. As this histogram was constructed by considering the entire simulation domain, it shows a high percentage of cells in the simulations are $Q_m > 0.95$ for both the lower and higher Re_ω cases.
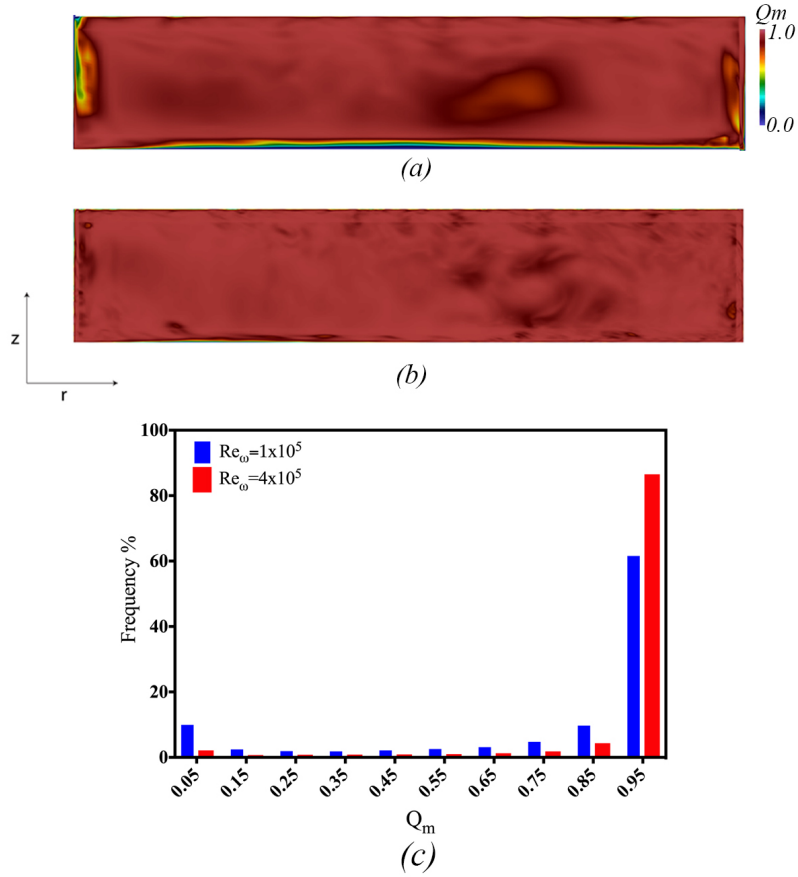
Fig. 4.4 Representation of Q_m as (a) contours of Q_m for $Re_\omega = 1 \times 10^5$, (b) contours of Q_m for $Re_\omega = 4 \times 10^5$, (c) normalised frequency histogram of Q_m.

For the presentation of the results, the radial and axial distances are non-dimensionalised as $r^* = \frac{(r-r_1)}{(r_2-r_1)}$ and $z^* = z/h$ respectively. The position $r^* = 0$ and $z^* = 0$ locates at the rotor hub corner of the rotor surface. For the sake of brevity, the filter notation $(\widetilde{(.)})$ is removed from the filtered velocity notations and henceforth, the instantaneous and time-averaged filtered velocity fields are denoted as $\boldsymbol{u} = (u_r, u_\theta, u_z)$ and $\boldsymbol{U} = (U_r, U_\theta, U_z)$, respectively. The time-averaged radial and tangential velocity components are non-dimensionalised as $U_r^*, U_\theta^* = \frac{U_r}{r\omega}, \frac{U_\theta}{r\omega}$. All the axial plots are extracted at the middle radial position $r^* = 0.65$ of the cavity, and at this particular location, finite cavity effects are minimal for both test cases. Further, all the axial profiles are averaged over the tangential direction (θ). The results present in this section are captured after several dozens of disk rotations, which is sufficient to pass the initial transient state of the simulations, and the mean (time-averaged) quantities are averaged over a couple of dozen of disk rotations.

4.3.1 The properties of the mean velocity profiles of the rotor-stator cavity boundary layers

Figure 4.5 shows the vector plot based on the instantaneous velocity of a typical rotor-stator cavity simulation in the r–z plane. Here, the near wall regions of the cavity tend to show their three-dimensional behaviour (see Figs. 4.5 (a) & (b)). However, the velocity vectors in the core region are mostly in the tangential direction. This core region separates the rotor and stator boundary layers and the vector plot of Fig. 4.5 suggests that the cavity is in the regime IV in the categorisation of Daily and Nece (1960). The fluid near the rotor boundary layer is flushed away toward the periphery of the disk ($U_r^* > 0$), where it eventually rises along the outer wall of the cylinder and the displaced fluid at the rotor is compensated with fluid suction from stator side. The stator boundary layer usually results in $U_r^* < 0$, and this inward radial flux is pushed toward the centre of the cavity, which leads the fluid to descend to the rotor boundary along the rotor hub.
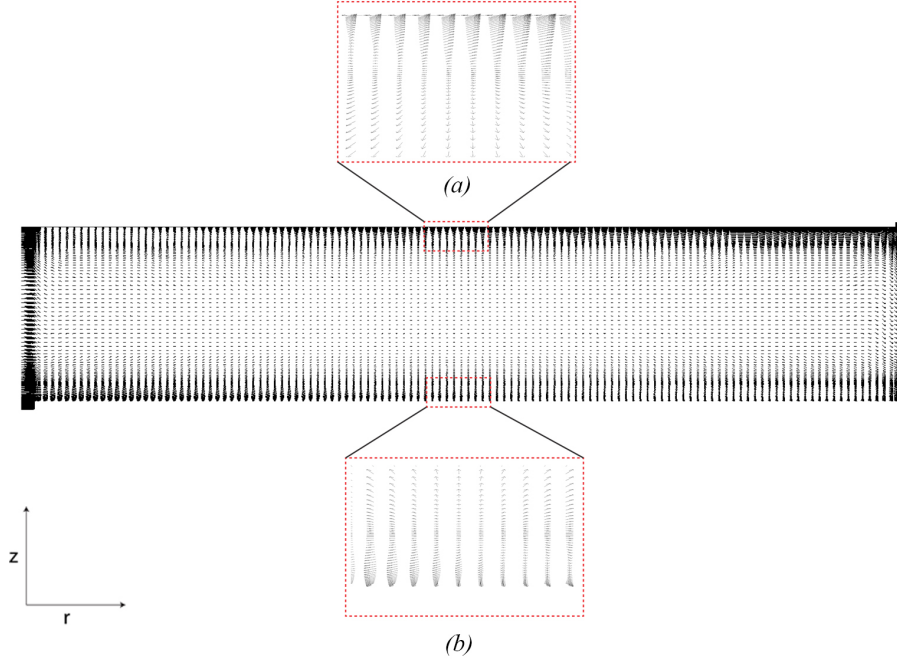
Fig. 4.5 The instantaneous velocity vector plot of the rotor-stator cavity in the r–z plane for $Re_\omega = 4 \times 10^5$, (a) at the rotor boundary layer, (b) at stator boundary layer.

Figure 4.6 shows the axial distributions of the mean radial and tangential velocity profiles for the Reynolds numbers, $Re_\omega = 1 \times 10^5, 4 \times 10^5$. The radial velocity profiles show an inflection point at the rotor layer, and then the velocity profiles reach zero in the core region. As described previously, radial velocity profiles are negative in the vicinity at the stator boundary layers, where they attain another inflection point. The tangential velocity profiles achieve their highest value at the rotor surface, and then the velocity profiles reduce toward the core region of the cavity, but the velocity profiles do not reach to zero, like in the von Kármán boundary layers.
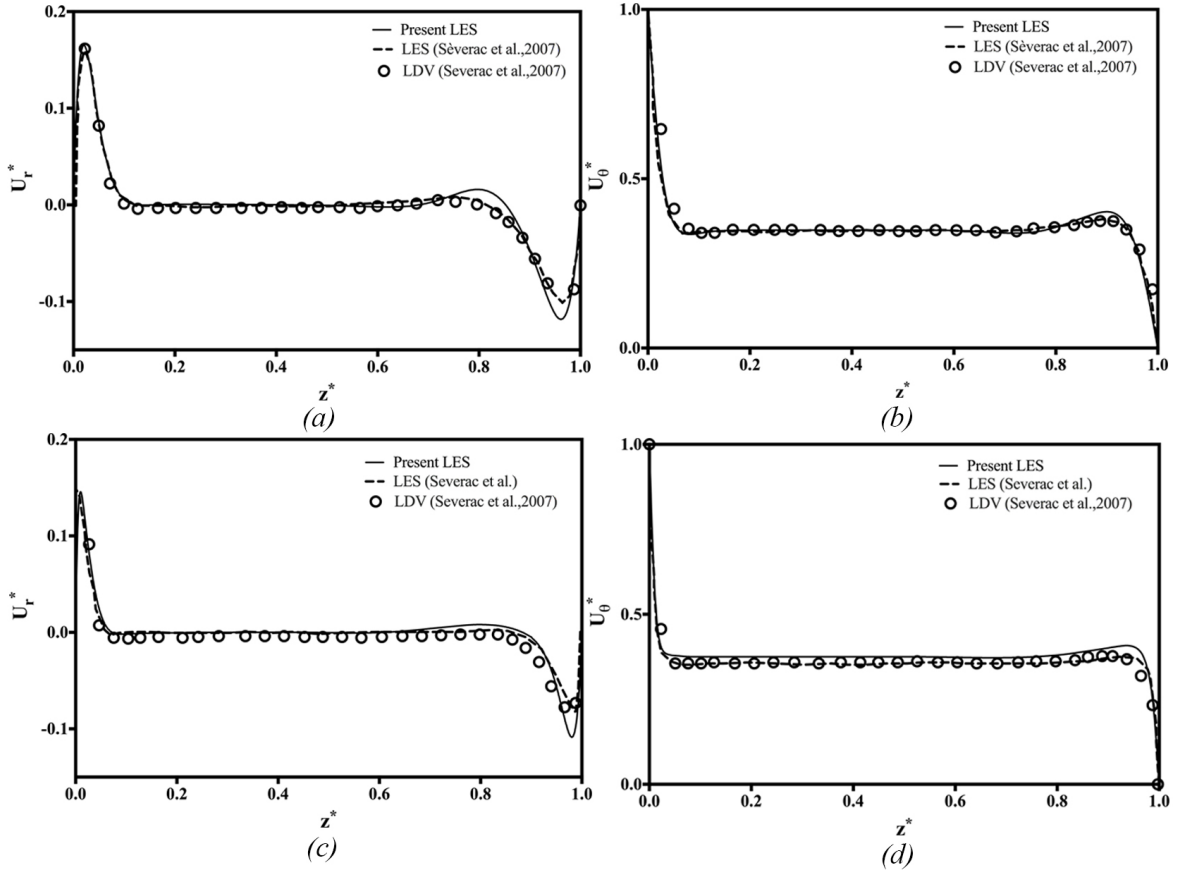
Fig. 4.6 The axial distributions of mean velocity fields, (a) radial velocity profiles at $Re_\omega = 1 \times 10^5$, (b) tangential velocity profiles at $Re_\omega = 1 \times 10^5$, (c) radial velocity profiles at $Re_\omega = 4 \times 10^5$, (d) tangential velocity profiles at $Re_\omega = 4 \times 10^5$.

The entrainment coefficient, $K = \frac{U_{\theta,core}}{U_{\theta,disk}}$, describes by the angular velocity (or tangential velocity) and it is an indication of the strength of the solid body rotation in the core region of the cavity. Figure 4.7 shows the radial distributions of K for the two Reynolds numbers of $Re_\omega = 1 \times 10^5$ and 4×10^5. The higher values of K are observed near $r^* = 0$, but these values are merely due to the angular motion of the rotor hub. The higher Reynolds number case achieves higher K values than the lower Reynolds number case, but in both cases, there are no steep variations in K with the local Reynolds numbers at the mid radial positions of the cavity. Usually, the value of K is below 0.5, which was obtained with a plain Couette flow (Séverac et al., 2007), and the current values of K at $r^* = 0.65$ are $K \approx 0.35$ for 1×10^5 and $K \approx 0.37$ for 4×10^5 and therefore follow this trend. When these values compared to the previous investigations, Cheah et al. (1994) have obtained $K \approx 0.35$ for a cavity with $G = 8$, $Re_\omega = 2.6 \times 10^5$, and for different configurations, Andersson and Lygren (2006) reported $K \approx 0.4$ for $G = 10$, $Re_\omega = 6.4 \times 10^5$ and $K \approx 0.47$ for $G = 15$, $Re_\omega = 1.6 \times 10^6$. Later,

Séverac et al. (2007) have obtained $K \approx 0.35$, and 0.36 values for the low and high Re_ω cases, which are identical configurations to the current investigation.
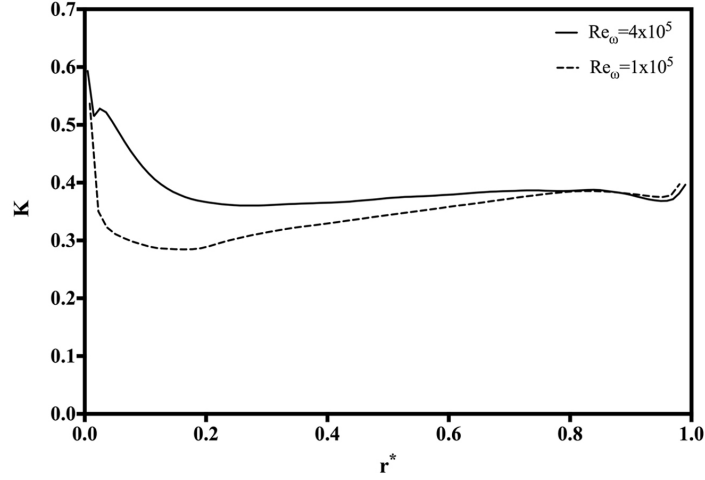
Fig. 4.7 A comparison of the radial distributions of the entrainment coefficients (K).

Figure 4.8 shows polar plots for the two test Reynolds numbers. The polar velocity plot is an alternative method of viewing the mean velocity fields. Near the rotor boundary layer ($U_\theta^* \to 1$), the present LES solutions are very much aligned with the von Kármán (1921) similarity solution, at both test Reynolds numbers. The velocity profile of the high Reynolds number case is more linear (flatter) near the $U_r^* \approx 0$ region when it compared to the low Reynolds number case and the similarity solution. This feature is more apparent in the velocity profile of Lygren and Andersson (2001), as it was captured at $Re_{\omega,local} = 4 \times 10^5$, and they called this as the characteristic "triangular form" of a three-dimensional turbulent boundary layer, due to the shape of the polar velocity profile.
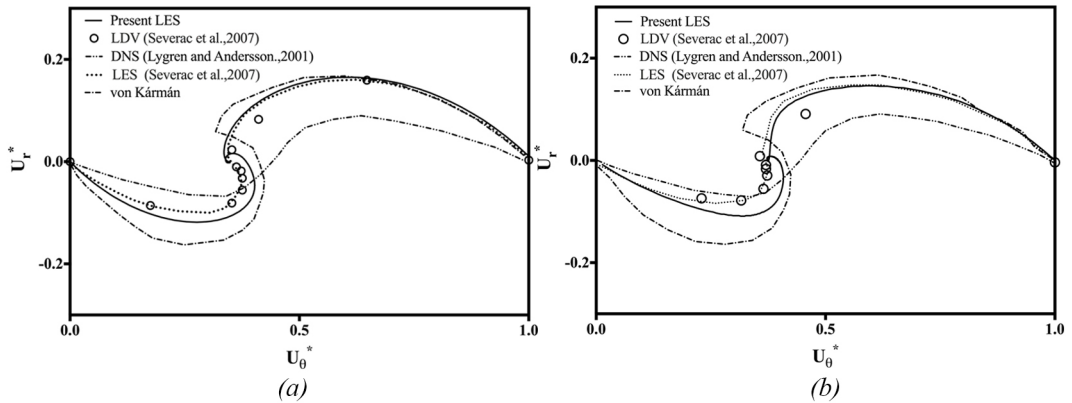
Fig. 4.8 The polar plots of time-averaged velocity components, (a) $Re_\omega = 1 \times 10^5$, (b) $Re_\omega = 4 \times 10^5$.

4.3.2 Turbulent properties of the rotor-stator cavity boundary layers

This section discusses the turbulent behaviour in the rotor and stator boundary layers of the cavity. Since the case $Re_\omega = 1 \times 10^5$ is limited to only to the stator boundary layer being turbulent, much of the discussion of this section focuses on the higher Reynolds number case, $Re_\omega = 4 \times 10^5$, in which the boundary layers are turbulent. Figure 4.9 shows the variation of relative tangential velocity, $u_{\theta,r} = (r\omega - U_\theta)$, against axial wall coordinates at $r^* = 0.65$ for rotor and stator boundary layers. Here, the velocities and wall distances are normalized by the friction velocity:

$$u_\tau = \left(((v\partial U_\theta)/\partial z)^2_{\text{wall}} + ((v\partial U_r)/\partial z)^2_{\text{wall}} \right)^{\frac{1}{4}}.$$

This inner scaling of the velocity profiles allows detailed comparisons of the laminar sublayer, buffer region and logarithmic layer of the velocity profiles. The laminar sublayer is a linear layer, and the rotor boundary follows this linearity up to $z^+ = 5.0$. It further extends with an approximate agreement to $z^+ \approx 8.0$, but after that, the agreement quickly deteriorates. The logarithmic layer starts to emerge at $z^+ = 10.0$, and the thin layer between the laminar sublayer and the logarithmic layer ($z^+ \approx 8.0$–10.0) can be identified as the buffer layer. The stator boundary layer shows the same trend, but the laminar sublayer is found only up to $z^+ \approx 5.0$, with the logarithmic layer starting at about $z^+ = 10.0$. The layer between these two regions defines the buffer layer $z^+ \approx 5.0$–10.0, which is broader than observed in the rotor boundary. A similar trend was observed by Séverac et al. (2007) except that they did not observe a buffer region in either boundary layers. The previous experimental results of Cheah et al. (1994) agree well within the laminar sublayers and the buffer regions, and the velocity profiles of Makino et al. (2015) show good agreement throughout the laminar sublayers and the buffer region of the boundary layers. To enable the quantitative comparison of the boundary layer profiles with these experimental and numerical results, all profiles are fitted to the well-known logarithmic velocity profile (Pope, 2000) by

$$u_{\theta,r}^+ = \frac{1}{\kappa} log_{10}(z^+) + B. \tag{4.5}$$

Here, κ is the von Kármán constant and B is the intersection, and the reference values of $\kappa \approx 0.4$ and $B = 5.5$ can be taken for a smooth-wall circular turbulent pipe flow (Schlichting et al., 1955). Table 4.2 shows a summary of configurations and a comparison of the gradient κ^{-1} and intersection values of the present LES with previous investigations when their respective velocity profiles are fitted to Eq. (4.5). The fitted values are within an acceptable range of both previous numerical and experimental results. However, the peak values of the velocity profiles do not agree well with either of the experimental investigations, which do

not agree with each other. This may be due to subtly different configurations and operational conditions between the two experiments and as compared to these simulations.

(a)   *(b)*
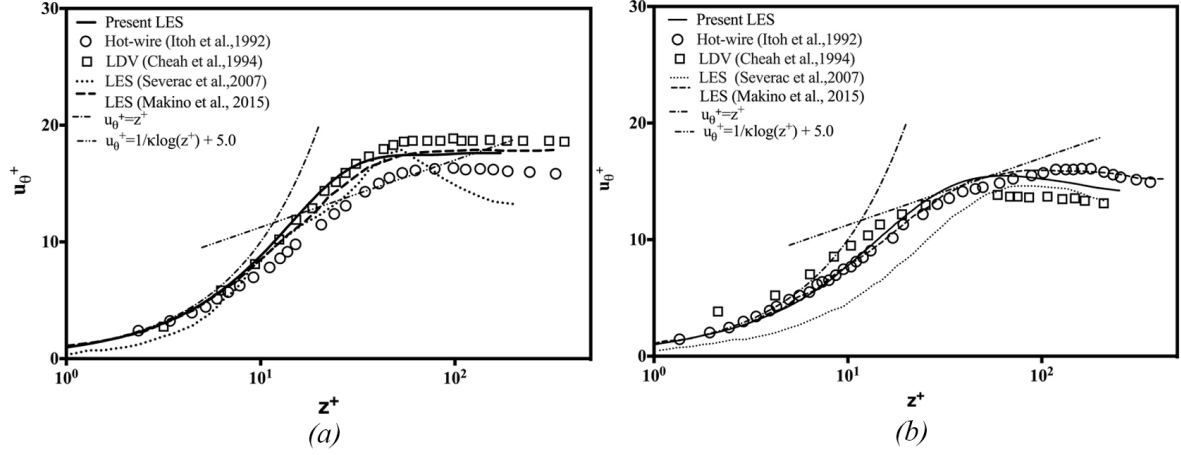
Fig. 4.9 The time-averaged tangential velocity profiles in the turbulent boundary layer at $Re_\omega = 4 \times 10^5$, (a) rotor boundary layer, (b) stator boundary layer.

Investigation	Method	$Re_{\omega,\text{local}}$	G	R_m	rotor		stator	
					κ^{-1}	B	κ^{-1}	B
Present	LES	2.2×10^5	0.2	1.8	14.9	-5.5	13.5	-5.6
Itoh et al. (1992)	Hot-wire	3.6×10^5	0.08	1.0	12.7	-5.2	11.3	-3.7
Cheah et al. (1994)	LDV	1.9×10^5	0.12	1.0	15.4	-6.5	9.4	-0.1
Makino et al. (2015)	LES	2.3×10^5	0.2	1.8	12.4	-3.6	12.5	-4.8
Séverac et al. (2007)	LES	4.1×10^5	0.2	1.8	14.0	-5.5	15.0	-10.8

Table 4.2 A comparison of different configurations of smooth rotor-stator cavities in previous numerical and experimental investigations, and the fitted κ and B values from the model in Eq. (4.5) for smooth turbulent rotor and stator boundary layers.

The resolved-scale Reynolds stress tensor components are calculated and normalised as $R_{\theta\theta} = \frac{\overline{u'_\theta u'_\theta}}{(r\omega)^2}$, $R_{rr} = \frac{\overline{u'_r u'_r}}{(r\omega)^2}$ and the velocity fluctuation components are defined by Eq. (4.4). The axial distances are measured from their respective boundary surfaces (e.g. $z^* = 0$ is the rotor surface in rotor distributions, and it represents stator surface in stator distributions). Figure 4.10 shows the tangential turbulence intensity $\sqrt{R_{\theta\theta}}$ against normalised axial distances. The axial locations of the peaks of the rotor and stator distributions are at $z^* = 0.013$, and $z^* = 0.018$ respectively. These values are well within the respective boundary layers of thickness $\delta = 2.5$ and $\delta = 2.4$ and the peak locations are well agreed with Makino et al. (2015)'s

investigation. Despite well-agreed peak locations, the current LES overestimates peak values by 13% in the rotor boundary layer and 14% in the stator boundary layer compared to Makino et al. (2015).
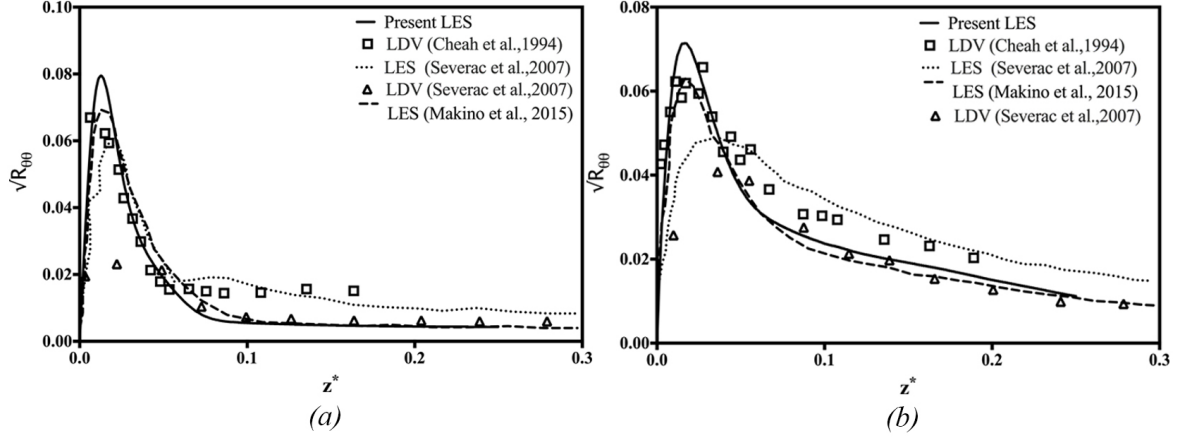
Fig. 4.10 The variation of tangential turbulence intensity component distributions in the axial direction at $Re_\omega = 4 \times 10^5$, (a) rotor boundary layer, (b) stator boundary layer.

Figure 4.11 shows radial turbulence intensity component $\sqrt{R_{rr}}$ versus axial distance. Similarly to the tangential turbulence intensity component, the peak locations of $\sqrt{R_{rr}}$ near the rotor and near the stator are inside the respective boundary layers, and they are at $z^* = 0.019$ and $z^* = 0.017$ for the rotor and stator boundary layers respectively. It is worth to mention that the peak value of $\sqrt{R_{\theta\theta}}$ at the rotor surface and the stator surface is over twice $\sqrt{R_{rr}}$ at the same locations. Séverac et al. (2007) also observed this tendency in their numerical investigation, but their experimental investigation has fairly equal turbulence intensity contributions $\sqrt{R_{rr}} \approx \sqrt{R_{\theta\theta}}$. They have suggested that this discrepancy is due to coarse meshing in the radial direction compared to the tangential direction and to the wall-normal direction.
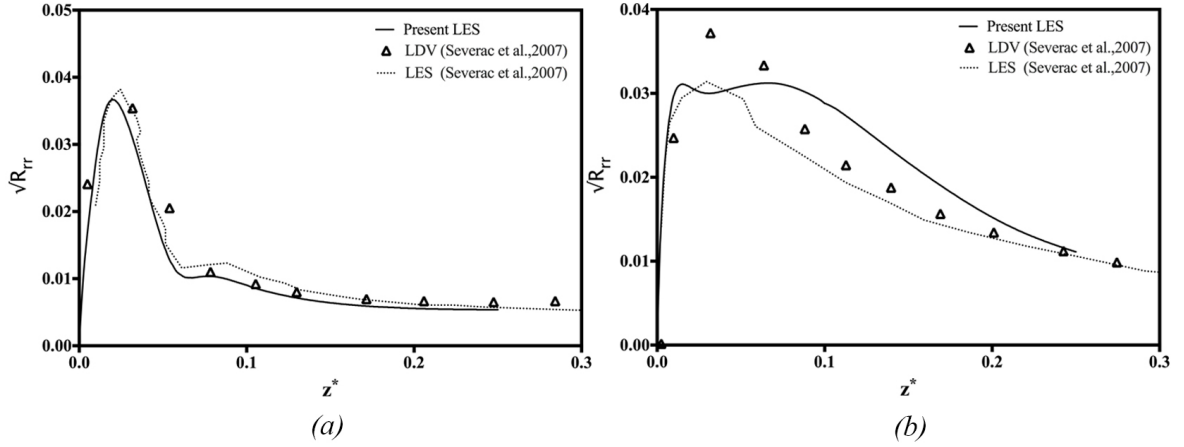
Fig. 4.11 The variation of radial turbulence intensity component distributions in the axial direction at $Re_\omega = 4 \times 10^5$, (a) rotor boundary layer, (b) stator boundary layer.

Even though the stator boundary layer transitions to turbulence at a lower Reynolds numbers than the rotor boundary layer, the peak values of the turbulence intensity contributions in the rotor boundary layers are higher than the corresponding values at stator boundary layer by 9% for the tangential component $\sqrt{R_{\theta\theta}}$ and by 6% for $\sqrt{R_{rr}}$.

4.3.3   The three-dimensional behaviour of rotor-stator boundary layers

The rotating disk boundary layers are one of the simplest examples of three-dimensional boundary layers and the vector plot of Fig. 4.5 provides visual evidence of the three-dimensionality of rotor and stator boundary layers. Apart from that, these boundary layers have several features that differentiate them from two-dimensional boundary layers. The following sections discuss these features.

In three-dimensional boundary layers, the direction of the mean velocity vector is not constant along the wall-normal direction (Séverac et al., 2007). Figure 4.12 shows the variation of the mean velocity angles $\left(\gamma_m = tan^{-1}(\frac{U_r}{U_\theta})\right)$ for rotor and stator boundary layer against the axial distance. Here, at axial distances up to $z^+ = 100$, both rotor and stator boundary layers show significant variations in mean velocity angles.

(a) *(b)*
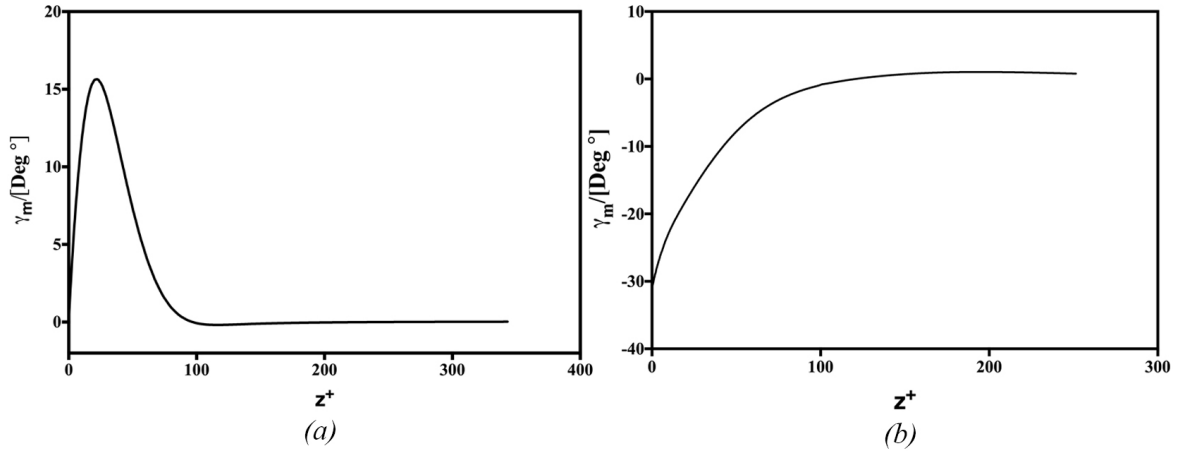
Fig. 4.12 The variation of mean velocity angles γ_m in the axial direction at at $Re_\omega = 4 \times 10^5$, (a) rotor boundary layer, (b) stator boundary layer.

Usually, the difference between the wall parallel turbulent shear stress angle $\left(\gamma_\tau = tan^{-1}\left(\frac{\overline{u'_r u'_z}}{\overline{u'_\theta u'_z}} \right) \right)$ and the mean gradient velocity angle $\left(\gamma_g = tan^{-1}\left(\frac{\partial U_r / \partial z}{\partial U_\theta / \partial z} \right) \right)$ is not zero for three-dimensional boundary layers (Séverac et al., 2007). Figure 4.13 shows the variation of the turbulent shear stress angle and of the mean gradient velocity angle in the axial direction for the rotor and stator boundary layers. At the surface of the rotor, the difference between the two angles is approximately $40°$, and the difference reduces to $28°$ at the stator boundary.

(a) *(b)*
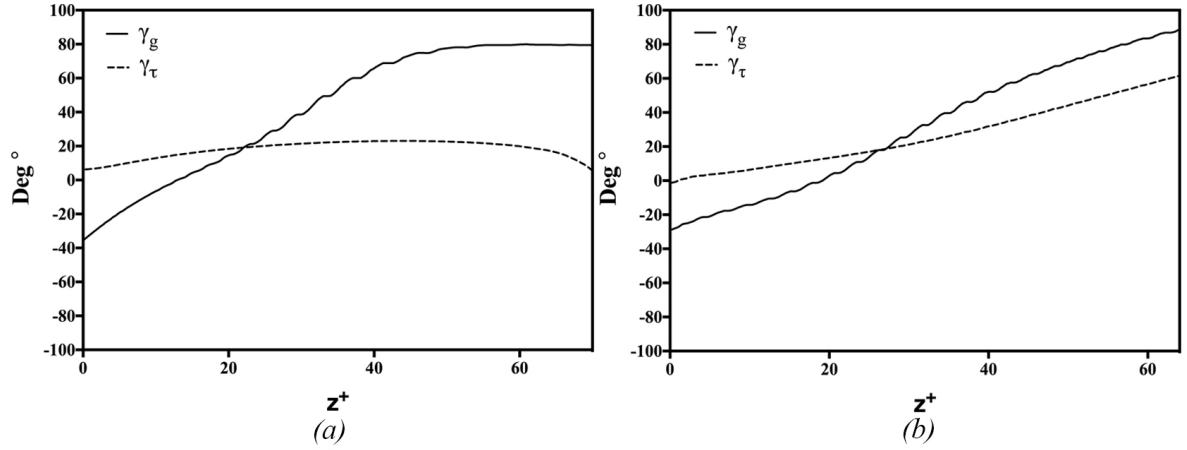
Fig. 4.13 The variation of turbulent shear stress angle (γ_τ) and mean gradient velocity angle in the axial direction at $Re_\omega = 4 \times 10^5$ (γ_g), (a) rotor boundary layer, (b) stator boundary layer.

86

The Townsend structure parameter (A_1) is an important parameter in turbulent boundary layers and it is defined as

$$A_1 = \frac{\sqrt{(\overline{u'_r u'_z})^2 + (\overline{u'_\theta u'_z})^2}}{2k}, \tag{4.6}$$

where k is the resolved turbulent kinetic energy defined in Eq. (4.3a), and the resolved fluctuation components can be obtained by Eq. (4.4). A_1 describes the efficiency of the process in turbulent kinetic energy extraction from the mean flow. For two-dimensional boundary layers, specifically in two-dimensional Couette flows, the structure parameter is usually around $A_1 = 0.15$. The previous investigations suggest that the structure parameters of the three-dimensional boundary layers are lower than this value, which indicates that the three-dimensional boundary layers are less efficient than their two-dimensional counterparts when extracting turbulent energy from the mean flow. Townsend structure parameter is defined as

Figure 4.14 shows axial distributions of the structure parameter in both the rotor and the stator boundary layers. The rotor boundary layer has its maximum value of $A_{1,max} = 0.068$ at $z^+ = 48$ and the stator boundary layer attains the value $A_{1,max} = 0.08$ at $z^+ = 58$, which is much lower than the value $A_1 = 0.15$ for the two-dimensional boundary layers. However, these axial distributions are lower than the previous LES investigation of Makino et al. (2015), but they are higher than the Séverac et al. (2007)'s LES investigation.
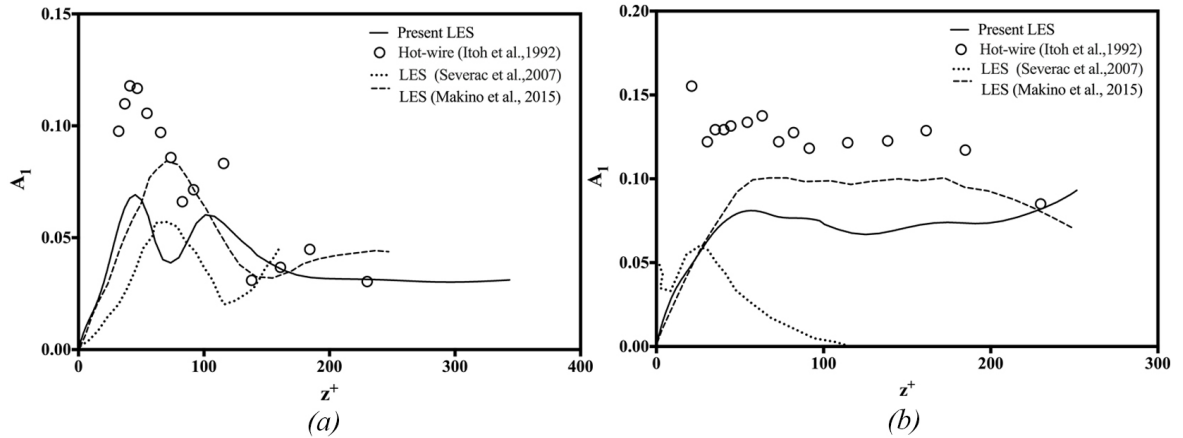
Fig. 4.14 The variation of Townsend structure parameter in the axial direction at $Re_\omega = 4 \times 10^5$, (a) rotor boundary layer, (b) stator boundary layer.

4.3.4 Flow visualisation

Flow visualisation provides a good aid to understand the flow structures and patterns in rotor and stator boundary regions. By well-resolved LES simulations, it is possible to visualise the instantaneous structures of the flow in details. Here, all the velocity contours are normalised by $U_{\theta,max} = r_2\omega$.

Figure 4.15 shows normalised instantaneous tangential velocity contours in the rotor boundary layer at $z^* = 0.025$. They are based on the instantaneous velocity of the last time step of the simulations. By comparing two boundary layers, it is clear that the lower Reynolds number case of $Re_\omega = 1 \times 10^5$ shows laminar behaviour compared to the higher Reynolds number case, $Re_\omega = 4 \times 10^5$. Regardless of the Reynolds number, both of these boundary layers show spiral arms near the rotor hub. It is thought that the occurrence of these spiral arms at the rotor hub provides a destabilisation effect on the rotor-stator cavity. However, even at the $Re_\omega = 4 \times 10^5$, the inner section of the rotor boundary layer is not fully turbulent, whereas, at the high radial locations, there are axisymmetric elongated structures, which is an indication of turbulent flow at high Reynolds numbers. In Séverac et al. (2007)'s investigation, a fully turbulent rotor boundary was achieved at $Re_\omega = 1 \times 10^6$.
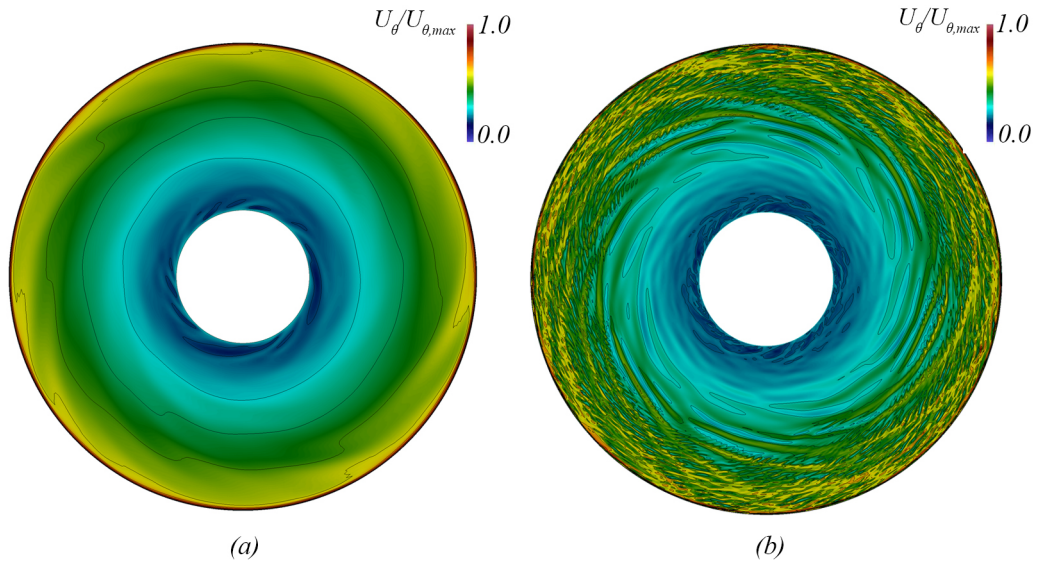
Fig. 4.15 Instantaneous normalised tangential velocity contours of the rotor boundary layer, at $z^* = 0.025$, (a) $Re_\omega = 1 \times 10^5$, (b) $Re_\omega = 4 \times 10^5$.

The stator boundary shows turbulent structures at a Reynolds number as low as $Re_\omega = 4.1 \times 10^4$ (Séverac et al., 2007). Figure 4.16 shows the instantaneous normalised tangential velocity (U_θ^*) in the stator boundary layer, at $z^* = 0.95$. As suggested by previous investiga-

tions, at the lower Reynolds number case of $Re_\omega = 1 \times 10^5$, the stator boundary layer shows transition patterns with small-scale turbulent structures at high radial positions. In the higher Reynolds number case $Re_\omega = 4 \times 10^5$, the stator boundary becomes turbulent, as evidenced by structures of small wave-numbers forming at all radial locations.

<div align="center">(a)</div>

<div align="center">(b)</div>
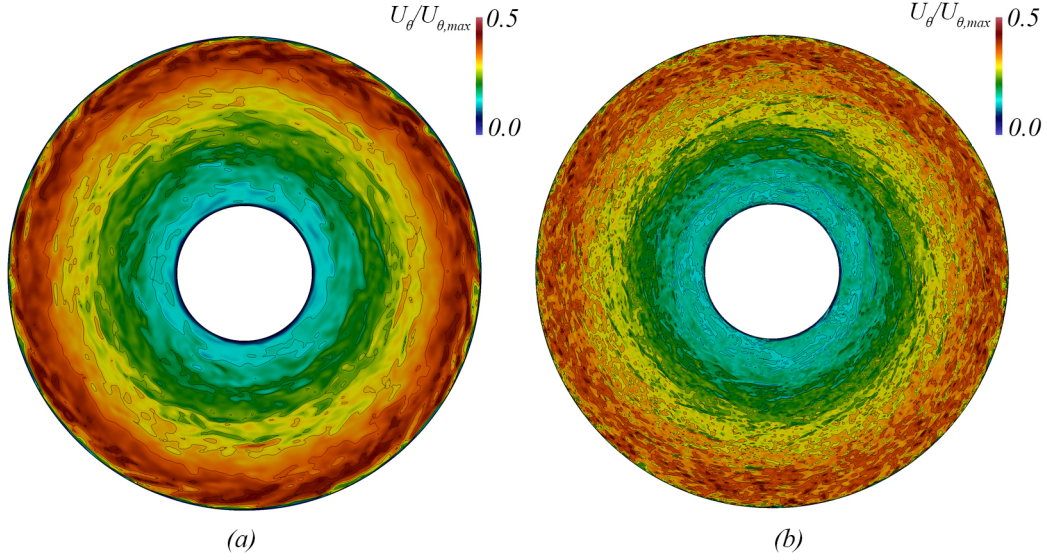
Fig. 4.16 Instantaneous normalised tangential velocity contours of the stator boundary layer, at $z^* = 0.95$, (a) $Re_\omega = 1 \times 10^5$, (b) $Re_\omega = 4 \times 10^5$.

Figure 4.17 shows the normalised axial velocity (U_z^*) distribution in the r–z plane of the mid-section of the cavity. This further confirms that at $Re_\omega = 1 \times 10^5$ the rotor boundary layer is free from vortices and, at $Re_\omega = 4 \times 10^5$, both boundary layers shows radial patterns of tangential vortices. The most disturbed position in the cavity appears to be located at the junction between the stator and outer wall of the cylinder. At both low and high Re_ω, the majority of upward mass transfer occurs along the outer wall, whereas downward mass transfer occurs along the inner rotor hub of the cavity.

The velocity contours are powerful tools to visualise flow fields, but there are more appealing methods to identify vortices in the flow field. The *Q-criterion* (Hunt et al., 1988) and The λ_2 *criterion* (Jeong and Hussain, 1995) are two such popular methods. This study adopts the λ_2 criterion to identify the vortices on the rotor-stator boundary layers of the cavity.

According to Jeong and Hussain (1995), a vortex is considered as a connected region with two negative eigenvalues of $S^2 + \Omega^2$ where $S = \frac{1}{2}(\nabla u + \nabla u^T)$ and, $\Omega = \frac{1}{2}(\nabla u - \nabla u^T)$ are the symmetric and antisymmetric parts of ∇u, respectively. Since the equation $S^2 + \Omega^2$ is symmetric, it has real eigenvalues (say $\lambda_1, \lambda_2, \lambda_3$). If these eigenvalues are ordered in,

(a)

(b)
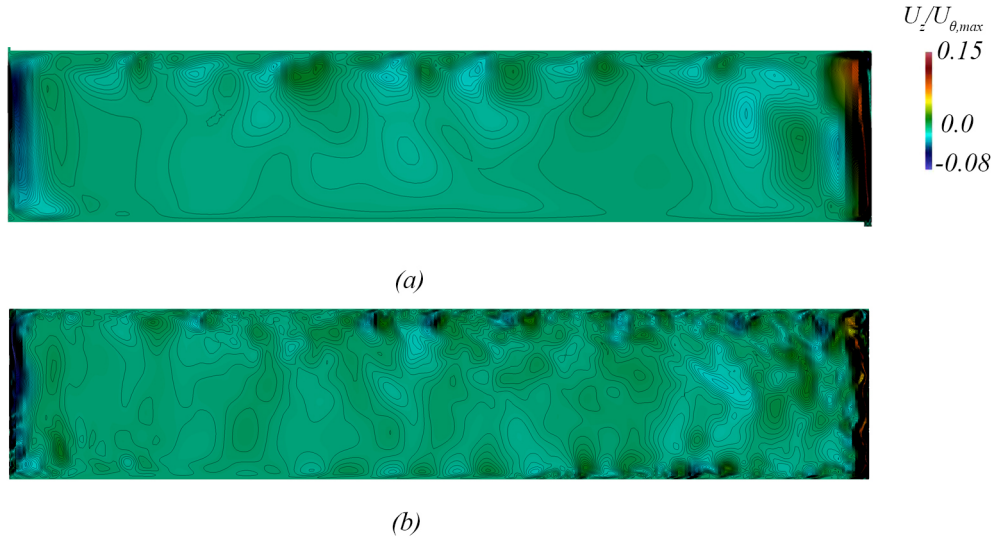
Fig. 4.17 Instantaneous axial velocity contours at the r–z plane, (a) $Re_\omega = 1 \times 10^5$, (b) $Re_\omega = 4 \times 10^5$.

$\lambda_1 \leq \lambda_2 \leq \lambda_3$ manner, then the condition for the vortex cores can be fulfilled by selecting the $\lambda_2 < 0$ in a connected flow region.

In practice, plotting the negative iso-surfaces of λ_2 in the rotor and stator boundary layers can identify vortex structures within them. Figure 4.18 is an iso-surface representation of negative λ_2 values that are extracted from the rotor boundary layers of $Re_\omega = 1 \times 10^5$ and 4×10^5. The colour scale of these figures does not correspond to the strength of the vortex cores, but it represents the magnitude of the local tangential velocity, which used in Fig. 4.16. At $Re_\omega = 1 \times 10^5$, some spiral patterns that start to emerge in the boundary layer, and unlike $Re_\omega = 4 \times 10^5$, there are no fine-scale structures toward the periphery of the disk. At $Re_\omega = 4 \times 10^5$ elongated spiral structures appeared close to the hub, then, as the local Reynolds number increases with increasing radius, the length of these structures increases around the rotor disk. At a local Reynolds number close to $Re_\omega = 4 \times 10^5$, these spiral patterns break down into fine-scale turbulent structures, which indicate the presence of a turbulent region. In this investigation, there are approximately 14–15 spiral arms around the disk boundary layer, and they incline $\varepsilon \approx -18°$ to the tangential direction. This is a quite good agreement with previous investigations, in which Makino et al. (2015) have reported approximately 16 spiral arms around the disk boundary layer with $\varepsilon \approx -16°$ and Serre et al. (2001) have observed 18 spiral arms with $-7.5° \leq \varepsilon \leq -20°$ in their DNS investigation. The characteristics of these spiral patterns are similar to Type II instability patterns, which is a viscous instability pattern that described in Serre et al. (2004). These instability patterns were previously observed in Ekman layers in the investigations by Faller and Kaylor (1966),

and Lilly (1966). Serre et al. (2001) explained that these patterns emerge as a result of stator layer instabilities, which propagate along the rotor hub to rotor boundary layer. Subsequently, Makino et al. (2015) purposed that these Type II structures are characteristic of a Streamline-Curvature instability (S-C instability), which is described in Itoh (1996).

The previous investigations of Séverac et al. (2007) demonstrated Type I instability, which consists of 19 spiral arms around the disk with an inclination of $\varepsilon \approx 18°$ to the tangential direction. Neither the current study nor Makino et al. (2015)'s investigation features an array of spiral arms with positive angles to the tangential direction, which are the characteristics of the Type I instability pattern. Hence, in this case, the transition to turbulence cannot be explained as a result of the Cross-Flow instability (C-F instability).

4.3.5 Transition to turbulence

Unlike single rotating disk boundary layers, a generally valid transition mechanism to turbulence for rotor-stator cavities is not available, due to the availability of many different types of rotor-stator cavities depending on G and R_m. A theoretical approach, such as linear stability theory, cannot be used readily because of the finite size of the rotor-stator cavities.
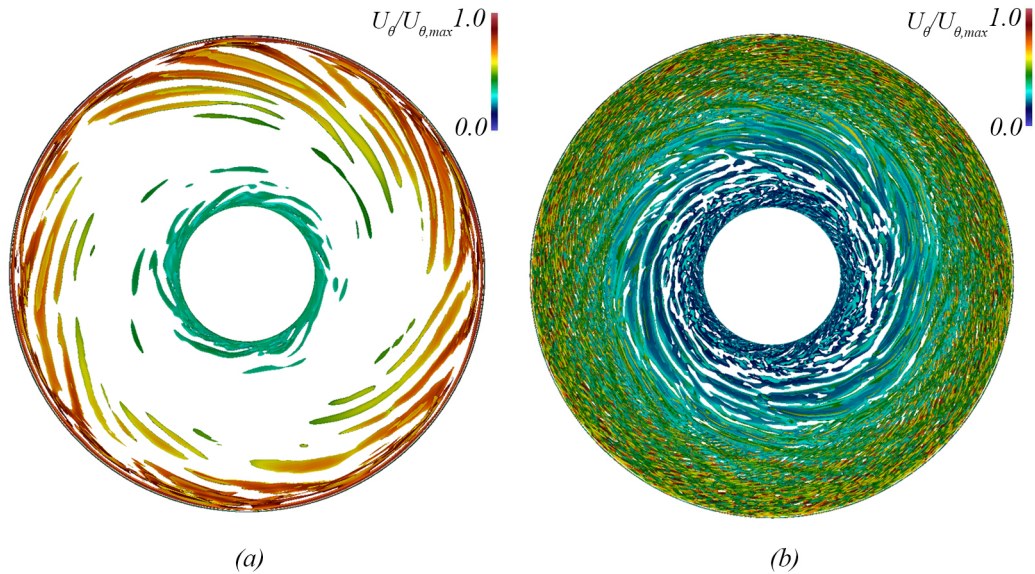
Fig. 4.18 Top view of λ_2=-2675 iso-surfaces of vortex structures in the rotor boundary layer, (a) $Re_\omega = 1 \times 10^5$, (b) $Re_\omega = 4 \times 10^5$.

Tuliszka-Sznitko et al. (2001) and Serre et al. (2004) have conducted a coupled theoretical and numerical study on instabilities in rotor-stator cavities. Both of these studies feature Type I and Type II instability patterns in DNS results, but absolutely unstable regions result

in the linear stability analysis. The numerical investigation of Serre et al. (2002) identified spiral structures in the turbulent Ekman layer, which they thought could relate to the absolute instability in the Ekman layer. Later, Séverac et al. (2007) confirmed the existence of Type I patterns in the Ekman layer.

Figure 4.18 suggests that the current study does not feature Type I patterns in the boundary layer. However, the results show similar features to the transition path proposed by Makino et al. (2015). The following sections discuss these features and the arguments presented by Makino et al. (2015).

The disturbance levels near the rotor boundary can be calculated by

$$Tu = \frac{\sqrt{\overline{u'_\theta u'_\theta}}}{U_{\theta,max}}, \quad (4.7)$$

where u'_θ is the zero time-mean fluctuation component of the tangential velocity resolved by LES as defined by Eq. (4.4). Figure 4.19 presents the radial distribution of the flow disturbances at a plane $z^* = 0.00875$, and $r^* = 0$ and $r^* = 1$ correspond to the rotor hub and the stator outer wall, respectively. The minimum of the radial distributions approximately 1.9%, which exceeds the range of $Tu = 0.5$–1% required for *Tollmien-Schlichting* waves to dominate the transition process in the two-dimensional boundary layers (Makino et al., 2015). Even though the S-C instability waves in the rotor boundary layers have a different mechanism than the Tollmien-Schlichting waves, Makino et al. (2015) argues that inflow disturbances from the stator could trigger S-C instability in the rotor boundary layer. As described previously, Serre et al. (2001) also suggested that the disturbance from stator boundary layer could be the reason for the Type II instability at the rotor boundary layers. However, according to the Faller (1991), several dominant modes of Type II or secondary instability should be present for the onset of turbulence.
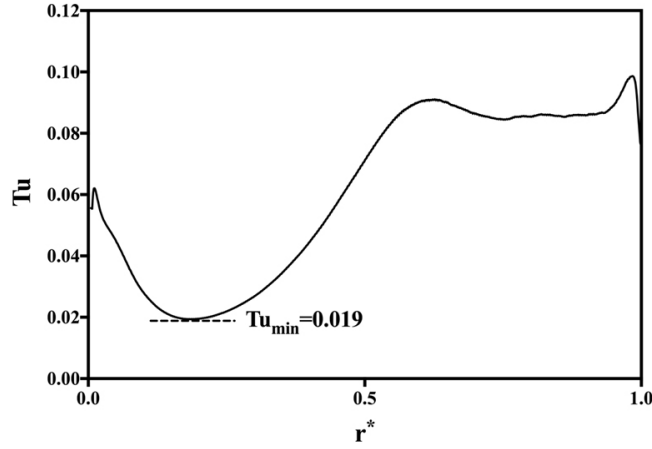
Fig. 4.19 The flow Tu levels based on, $z^* = 0.00875$ from the rotor boundary layer.

Figure 4.20 shows the time trace of tangential fluctuation component of tangential velocity, by Eq. (4.4), at three different monitoring positions (r^*, z^*)=(0.25,0.0125), (0.5,0.0125), (0.75,0.0125) in the rotor boundary layer. The two points closest to the rotor hub (see Figs. 4.20 (a) & (b)) display a lower frequency spectral context than $(r^*, z^*) = (0.75, 0.0125)$ that could be related to Type II structures. The time trace of $(r^*, z^*) = (0.75, 0.0125)$ high frequency spectral context that could be due to secondary instabilities.

Figure 4.21 shows the instantaneous wall-normal profiles of the resolved velocity component from LES across the same monitoring points of Fig. 4.20. These velocity distributions are shown in the form of instantaneous tangential velocity lag with respect to the rotating disk $u_\theta = (r\omega - u_\theta)$. The instantaneous velocity profile in low-speed and high-speed regions feature inflection points, where they are shown by the open circles in the figures, and Makino et al. (2015) argued that this type of velocity profile could lead to secondary instabilities in the boundary layer.

Figure 4.22 shows an iso-surface of the secondary instability pattern, which is captured before the turbulence break-down at the high Reynolds numbers. This indicates that the turbulent transition mechanism is similar to the mechanism (B) in Faller (1991)'s investigation, which was explained in page 12 of Section 2.2.
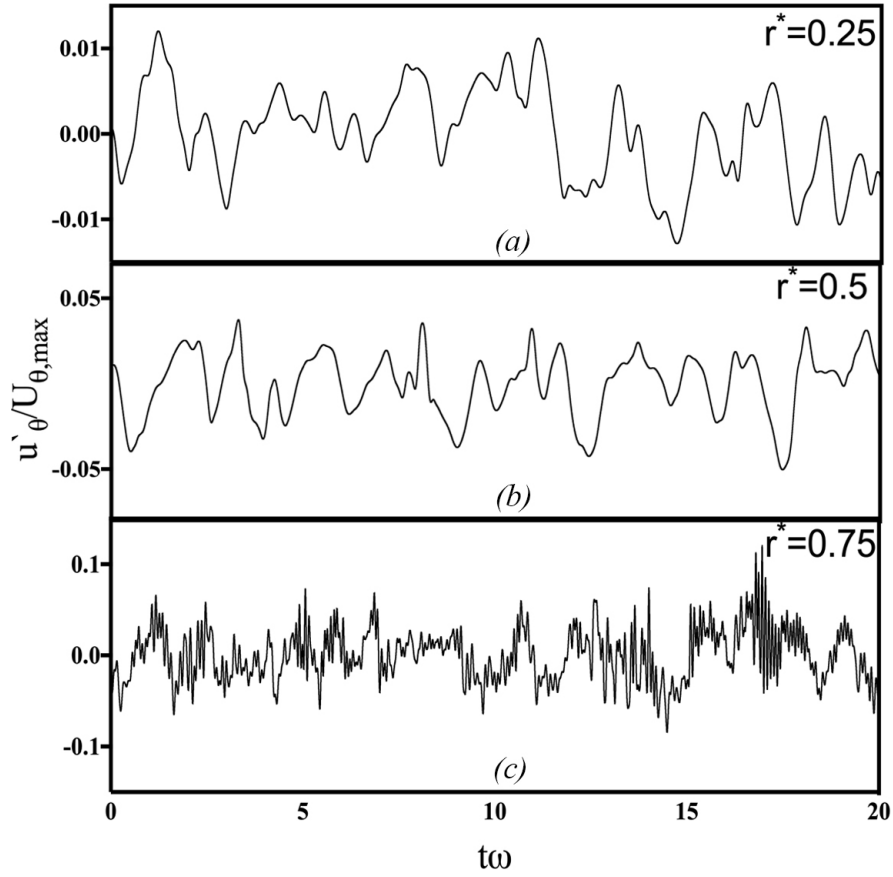
Fig. 4.20 The time trace of the resolved fluctuations of tangential velocity components at $z^*=0.0125$ and radial locations, (a) $r^*=0.25$, (b)$r^*= 0.5$, (c) $r^*= 0.75$.

(a)

(b)

(c)
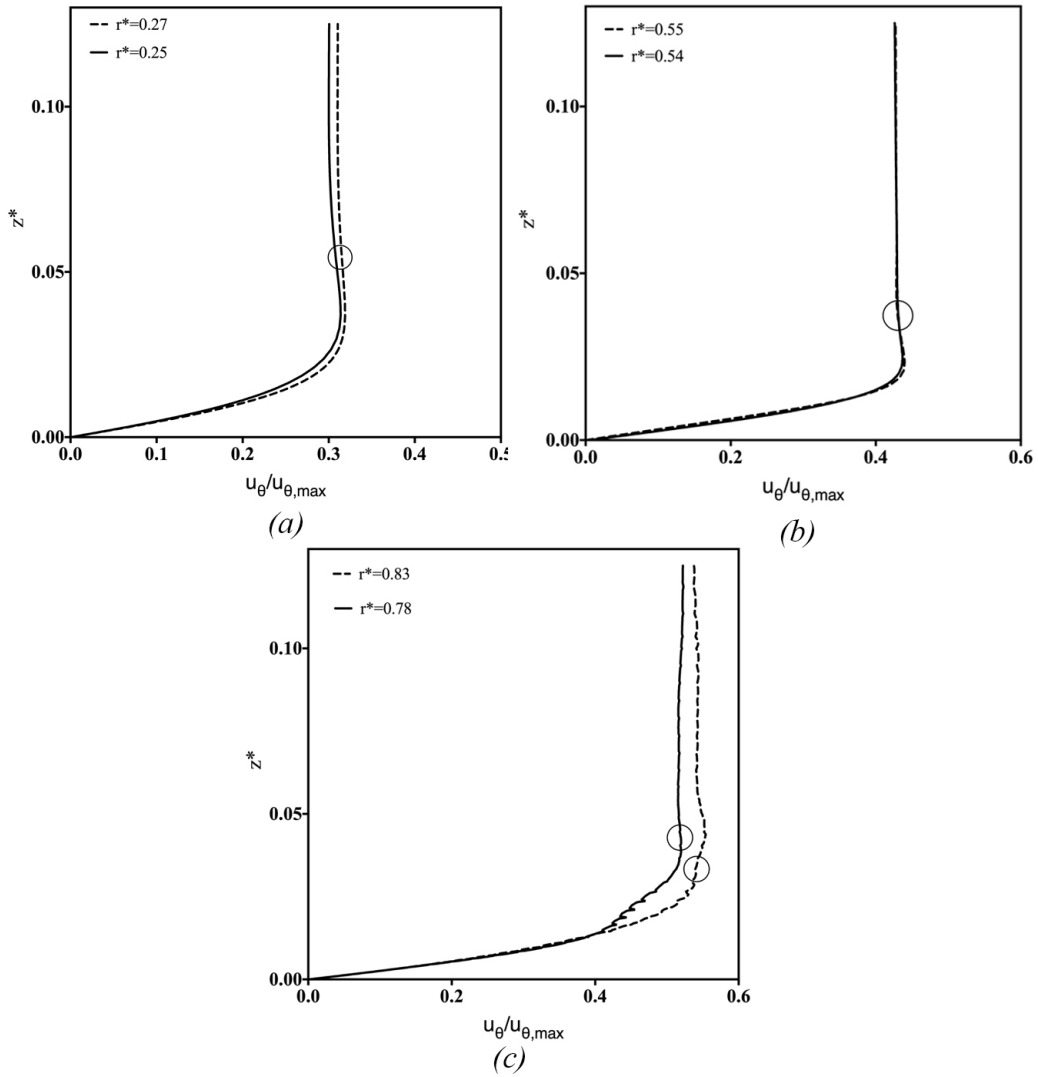
Fig. 4.21 Wall-normal profiles of the resolved instantaneous tangential velocity lag with respect to the rotating disk.

Riblets of secondary instability pattern
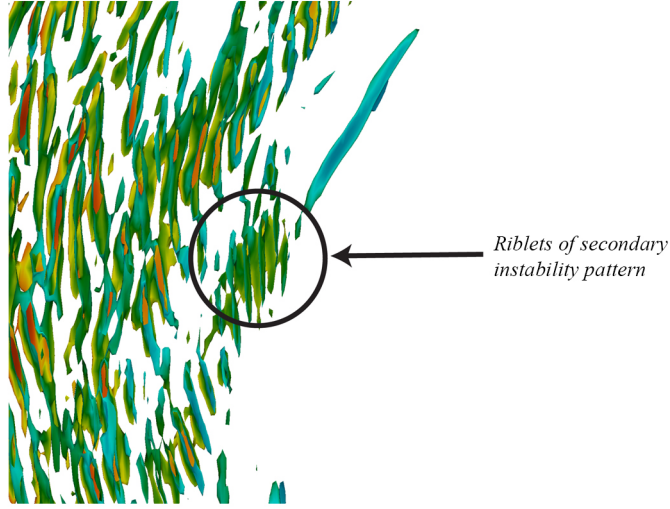
Fig. 4.22 The λ_2 iso-surfaces of secondary instability in the rotor boundary layer.

4.4 Summery and conclusions

This chapter provided the validation for the rotor-stator flow by LES based on the dynamic subgrid-scale method and a second-order accurate FVM. Two well documented Reynolds numbers, $Re_\omega = 1 \times 10^5, 4 \times 10^5$, were used for this purpose. At the $Re_\omega = 1 \times 10^5$, only the stator boundary layer is in the transitional-turbulent state, and the rotor boundary is mostly in the laminar region. At the Reynolds number $Re_\omega = 4 \times 10^5$, the stator boundary is turbulent, and the rotor boundary is in the transitional-turbulent state.

The mean velocity profiles of both simulations were validated against similar LES simulations by Séverac et al. (2007) and Makino et al. (2015). A similar approach has been followed to validate turbulent intensity profiles at higher Reynolds numbers. In all the cases, current simulations demonstrated a satisfactory agreement with previous investigations. Three-dimensionality of the of the boundary layer was confirmed by observing the axial variations in the Townsend structure parameter, turbulent shear angle and mean velocity gradient angles.

The tangential velocity and λ_2 contours visualised the vortex structures to evidence nature of the rotor and stator boundary layers. It confirmed that the rotor boundary layer is populated with 15 Type II instability patterns with $\varepsilon \approx -18°$ inclination to the tangential direction. However, no Type I instability was observed on the rotor boundary layer. This suggests

that transition could be initiated by the mechanism (B) in Faller (1991)'s investigation, as previously reported by Makino et al. (2015).

By observing the outcomes of this chapter, it can be concluded that the FVM methods are sufficient for conducting further simulations in rotor-stator flows, and the selected turbulent models and boundary conditions can reproduce close results to the previous experimental and numerical investigations. However, the current simulations do not produce any Type I instability pattern, which was previously found on an identical test case in Séverac et al. (2007).

Chapter 5

A qualitative assessment of roughness modelling on a rotor-stator cavity

5.1 Introduction

This chapter discusses the implementation and simulation of Busse and Sandham (2012)'s parametric force model on rotor-stator cavities. This method is suitable for representing various types of real-world rough surfaces, and the approach is adaptable in general-purpose CFD packages like OpenFOAM. In the current context, the roughness effects are only considered on the rotor boundary surface, and the stator boundary is modelled as a hydraulically smooth surface. The several test cases are simulated by adapting the parametric force model on rotor-stator cavities, which operate at Reynolds numbers of $Re_\omega = 1 \times 10^5$ and 4×10^5.

5.2 Parametric force model

As described in earlier Section 2.4, Busse and Sandham (2012)'s parametric force model accepts multiple parameters to represent the surface roughness in a wall. The force term is included in the Navier-Stokes equation, and Eq. (5.1) shows the expression for this parametric force:

$$F_i = -\alpha_i G(z, h_r)(u_i - u_{d,i})|u_i - u_{d,i}|. \tag{5.1}$$

Here, the parameters, α_i, $G(z, h_r)$, h, u_i and u_d are the roughness factor, the shape factor, the roughness height, the local flow velocity and the local disk surface velocity, respectively. The subscript $i = 1, 2, 3$ denotes the stream-wise, span-wise and the wall-normal directions, respectively. The difference between the disk velocity and the local fluid velocity gives the local relative velocity with respect to the disk surface. The quadratic term on the right-hand

side of the Eq. (5.1), $(u_i - u_{d,i})|u_i - u_{d,i}|$, is the roughness term, which emulates form drag effects. The roughness factor and the roughness term have dimensions of $[\text{L}^{-1}]$ and $[\text{LT}^{-1}]$ to achieve homogeneity in the Navier-Stoke Equations. The significance of the roughness factor, roughness height, and shape factor are discussed in the following sections.

5.2.1 Roughness factor

Roughness factor (α_i) can be interpreted as the density of the roughness elements, or frontal area per unit volume, as it holds the dimensions of line density $[\text{L}^{-1}]$. A sparse roughness has a lower value of α_i. Busse and Sandham (2012) have observed that the roughness function ($\Delta \boldsymbol{U}^+$) increases as α_i increase, but, after a certain threshold value of α_i, there may be a tendency to $\Delta \boldsymbol{U}^+$ decrease, which may be due to the shielding effects of the high-density roughness elements Jiménez (2004). Apart from this standard definition, α_i can be interpreted as the drag coefficient due to a roughness element, and this definition removes the requirement of an upper limit for α_i, as theoretical drag coefficients do not hold such a restriction.

$\boldsymbol{\alpha}$ is a vector, and the model requires defining its values in the stream-wise, span-wise, and wall-normal directions. For a rotor-stator flow configuration, it is more meaningful to define stream-wise, span-wise and wall-normal directions in a cylindrical coordinate system, therefore, $\boldsymbol{\alpha} = (\alpha_r, \alpha_\theta, \alpha_z)$, with α_r, α_θ and α_z the radial, tangential and wall-normal components represent the corresponding span-wise, stream-wise and wall-normal components of the roughness factor.

A suitable set of values of α_i can be used to represent a real rough wall, but these values are not intuitive, So DNS or experimental data of the equivalent surface is required to evaluate them. However, this step is beyond the scope of the current investigation, as the investigation focuses on the response from relative roughness effects on the rotor-stator boundary layers. Therefore, the following assumption was made to determine the values for

$$\alpha_i = \beta_k / k_r, \tag{5.2}$$

where k_r and β_k are the physical roughness height and a multiplicative constant, respectively. β_k is obtained using numerical adjustments, which require comparisons of the magnitude of the roughness term with other dominant terms in the Navier-Stoke equations. Then, the β_k values were fine tuned to minimise any shielding and wall shifting effects (Jiménez, 2004).

The range of values $\beta_k = 0.5 \times 10^{-3}$–$5.0 \times 10^{-3}$ have delivered satisfactory results in the current investigation. At a constant physical roughness height of $k_r = 1 \times 10^{-4}$ m, the selected range of β_k produces the range of dimensionless roughness factors $\alpha^* = \alpha h = 0.1$–$1.0$. The vector expression is selected as $\alpha_\theta^* = \alpha^*(0, 1, 0)$, so that the roughness effects are

only activated in the stream-wise direction (henceforth, the notation α^* will be used to denote the stream-wise component α_θ^* of the rotor-stator cavity simulations).

5.2.2 Roughness height and shape factor

Even though the roughness height and the shape factor are separate parameters, they related to each other. According to the Busse and Sandham (2012), the shape function determines the extent of roughness function toward the wall-normal direction (z) and it is usually associated with the roughness height parameter (h_r). An auxiliary parameter, $\eta_r(h_r)$, defines the relationship between the shape function and the roughness height.

The original study of Busse and Sandham (2012) defines six mathematical profiles as the shape functions, and each function has different mathematical properties. Three of them are polynomial based functions, and the rest of them are exponentially decaying functions.

1. **Polynomial functions:**

   - Box profile,

$$G(z,h_r) \begin{cases} 1 & z \le \eta_r(h_r), \\ 0 & z > \eta_r(h_r). \end{cases} \tag{5.3}$$

   - Triangular profile,

$$G(z,h_r) \begin{cases} 1 - \frac{z}{\eta(h_r)} & z \le \eta_r(h_r), \\ 0 & z > \eta_r(h_r). \end{cases} \tag{5.4}$$

   - Parabolic profile,

$$G(z,h_r) \begin{cases} \left(1 - \frac{z}{\eta(h_r)}\right)^2 & z \le \eta_r(h_r), \\ 0 & z > \eta_r(h_r). \end{cases} \tag{5.5}$$

2. **Exponential functions:**

$$G(z,h_r) = e^{-z/\eta_r(h_r)}. \tag{5.6}$$

3. **Gaussian profile:**

$$G(z,h_r) = e^{-z^2/\eta_r(h_r)^2}. \tag{5.7}$$

The exponential functions have different smoothness properties than the polynomial functions, since the exponential functions are infinitely differentiable (C^∞), whereas polynomial functions are smooth up to some extent, for example, the box profile is discontinuous itself (C^0), the triangular profile is discontinuous first derivative (C^1), and the parabolic profile is discontinuous at second derivative (C^2). Another property is that the polynomial functions become zero at finite z values, but negative exponential functions attain zero at $z \to \infty$, which is not compatible with physical roughness elements. Despite the asymptotic behaviour of these exponential functions, they attain a machine zero value at a very short distance in wall-normal direction, which is ideally equivalent to zero in the context of numerical simulations.

The significance of the roughness height h_r is explicit in the polynomial functions. In that $\eta_r(h_r)$ is the point where the corresponding profile vanishes and, as such, $\eta_r(h_r) = h_r$ for polynomial functions. This definition is not valid for exponential functions. Therefore, an expression for the $\eta_r(h_r)$ is obtained by the solution of

$$h_r = \frac{\int_0^\infty G(z, h_r)\, z \, dz}{\int_0^\infty G(z, h_r)\, dz}.\tag{5.8}$$

According to Eq. (5.8), there is no explicit relationship between physical roughness heights (k_r) and h_r. The k_r represents the extent of the roughness element in the flow field, but h_r describes the extent of the roughness effected region in the flow field. Increasing in a physical roughness height is typically expected to increase the roughness height parameter ($h_r \propto k_r$). Further, in the application considered this study, the threshold ratio $\delta_{99}/k_r > 40$ (critical blockage ratio) is not limiting the explicit roughness height parameter, yet it is important to maintain the roughness heights parameter in such a way that the effects of the roughness should not spread into the outer layer of the boundary layer.

Firstly, several test cases have been simulated with the box profile, and both tangential and radial velocity profiles of these test cases were affected by abrupt inflection points at the top end of the shape function. These inflection points may be a result of the discontinuity of the box profile. Hence, further tests were conducted with the Gaussian shape functions which act as smearing-out box profiles (Busse and Sandham, 2012). The Gaussian profile provides considerably smoother velocity profiles compared to box profiles, but determining $\eta_r(h_r)$ is not as straightforward as with a box profile. Substituting Eq. (5.7) in to the integral expression of Eq. (5.8) gives the following expression for

$$\eta_r(h_r) = h_r\sqrt{\pi}.\tag{5.9}$$

From Eqs. (5.8) & (5.9), the expression for the Gaussian profile is then given by

$$G(z, h_r) = e^{-z^2/h_r^2 \pi}. \tag{5.10}$$

Figure 5.1 shows the solutions of Eq. (5.9) for the two test cases of $Re_\omega = 1 \times 10^5$ and 4×10^5. The same h_r value has different effects depending on the inter-disk spacing of the cavity (h), therefore a dimensionless roughness height is defined as $h_r^* = h_r/h$.
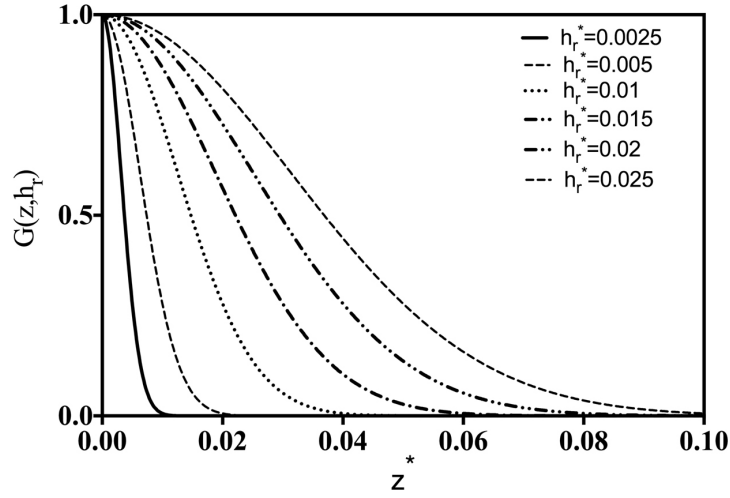
Fig. 5.1 Wall-normal extent of the numerical roughness layers at different h_r^* values.

5.3   Problem definition

The geometry and mesh are identical to the two Re_ω cases presented in Section 4.2.1. The governing equations are also similar to Eqs. (3.30) in Section 3.5.2, but here, the force term in Eq. (5.1) is added as a body force term to the momentum equation ($\widetilde{F_b} \neq 0$).

In this case, only the rotor surface is assumed as a rough wall. Hence, a particular numerical treatment only applies to the rotor boundary. All the other surfaces, including the hub, the outer sleeve, and the stator are assumed to be hydraulically smooth.

The same second-order accurate FVM based segregate solver is used in these simulations, and pressure-velocity coupling is achieved using the same non-iterative PISO algorithm. Despite the roughness effects on the rotor boundary, the turbulence model, the boundary conditions, and the operational conditions are the same as the respective smooth rotor cases, which were described in Sections 4.2.2 & 4.2.3. Further, all simulations are performed at $z_{max}^+ \leq 1.0$ and the time steps (Δt) have been chosen to satisfy $Co_{max} \leq 0.325$ condition.

Near the rotor, the force term is non zero, and the resulting force is defined by the Eq. (5.1). This selective forcing mechanism is enforced through a particular region called, the numerical roughness layer, which is a thin layer next to the rough wall. In this case, the numerical roughness layer is applied next to the rotor surface. This technique will subdivide the internal fluid region into three regimes. As shown in Fig. 5.2, these regimes can be described as follows:

1. The disk and hub: This is where the rotating boundary conditions are set according to Eq. (4.2).

2. Numerical roughness layer (yellow region): Here, a non-zero force ($\widetilde{F_b} \neq 0$) is applied as shown in Eq. (5.10). The thickness of this layer depends on the h_r^*.

3. Outside the roughness layer (blue region): In this region, the force term in Eq. (3.30b) is zero ($\widetilde{F_b} = 0$), and the governing equations are equivalent to the smooth case.
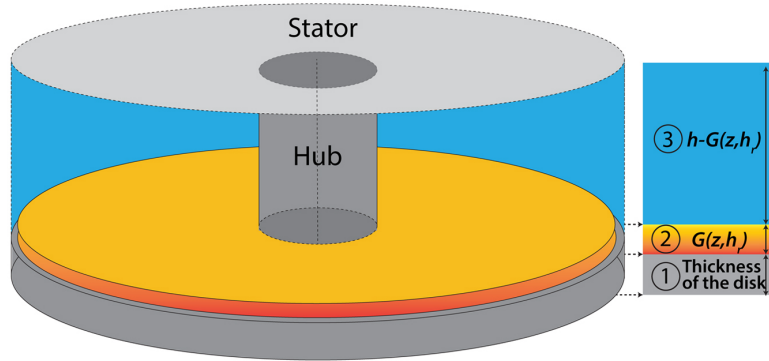
Fig. 5.2 An illustration of different regions in the current rotor-stator numerical simulation models with the parametric model to evaluate roughness effects.

5.4 Results and discussion

This section presents the flow predictions at $Re_\omega = 1 \times 10^5$ and 4×10^5 obtained with a modelled rough rotor. In consideration of the nature of the flow and the computational cost, the first part presents simulations at $Re_\omega = 1 \times 10^5$ that are used to describe the mean flow properties of the rotor and stator boundary layers under various model constants of h_r^*, α^*. The second half consists of comparatively few $Re_\omega = 4 \times 10^5$ simulations that describe the mean and turbulent flow properties of the rough rotor and smooth stator boundary layers.

Further, the initialisation condition and the simulation time of these simulations are selected similarly to the previous description in Section 4.3.

Table 5.1 summarises the parameters used in these two sections, and dimensionless terms, $\alpha^* = 0$ and $h_r^* = 0$ usually represent the corresponding smooth wall cases.

Re_ω	α^*	h_r^*	Shape function	h $[mm]$
1×10^5	0–1.0	0–0.025	Gaussian	20
4×10^5	0, 0.4	0, 0.00125, 0.00375	Gaussian	40

Table 5.1 The roughness modelling and geometric parameters use in the simulations.

All the test cases have a relatively low roughness level, $\Delta U^+ < 4.0$ (based on the shift in the mean velocity field) (Jiménez, 2004). It is important to recall that the model constants, h_r^*, and α^* have not been calibrated to represent any physical roughness condition, but they are assigned arbitrary values in these simulations. Still, these model constants enable to study the relative effects of a rough rotor wall by observing the shifts in flow field distributions relative to the previously validated flow fields of smooth rotor-stator simulations. In the future, these model constants can be replaced with experimental or DNS calibrated values to represent real-world rough surfaces.

As in Section 4.3, the radial and axial distances are normalised as $r^* = \frac{(r-r_2)}{(r_2-r_1)}, z^* = \frac{z}{h}$, and the velocity components are normalised as $U_r^*, U_\theta^* = \frac{U_r}{r\omega}, \frac{U_\theta}{r\omega}$, where the parameters $r_1, r_2, r, h, U_r, U_\theta$ are defined in Sections 4.2.1 & 4.3. Similar to Section 4.3, all the axial plots are extracted at the middle radial position of the cavity of $r^* = 0.65$. As described in Section 4.3, all the axial profiles are averaged over the tangential direction (θ), and the mean quantities are obtained by averaging them over a couple of dozen of disk rotations.

5.4.1 Boundary layer properties of the rough rotor and smooth stator at $Re_\omega = 1 \times 10^5$

Figure 5.3 shows the time-averaged axial profiles of the radial velocity components over the rotor. Fig. 5.3 (a) covers the range of $\alpha^* = 0.1$–1.0 at a constant $h_r^* = 0.005$, while Fig. 5.3(b) covers the range $h_r^* = 0.0025$–0.025 at a constant $\alpha^* = 0.2$.

By comparing Figs. 5.3 (a) & (b), they show that the h_r^* has a higher impact on the mean radial velocity profiles than α^*. Higher height parameter increases the peak value of the time-averaged radial velocity profiles and the these show a thicker profile compared to the
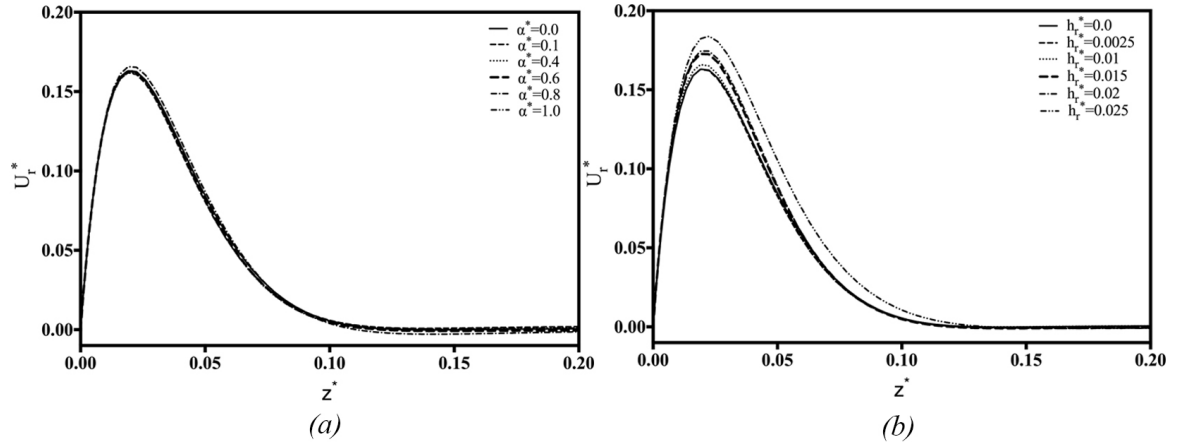
Fig. 5.3 A comparison of the time-averaged radial velocity profiles over the rotor for, (a) different α^* values, (b) different h_r^* values.
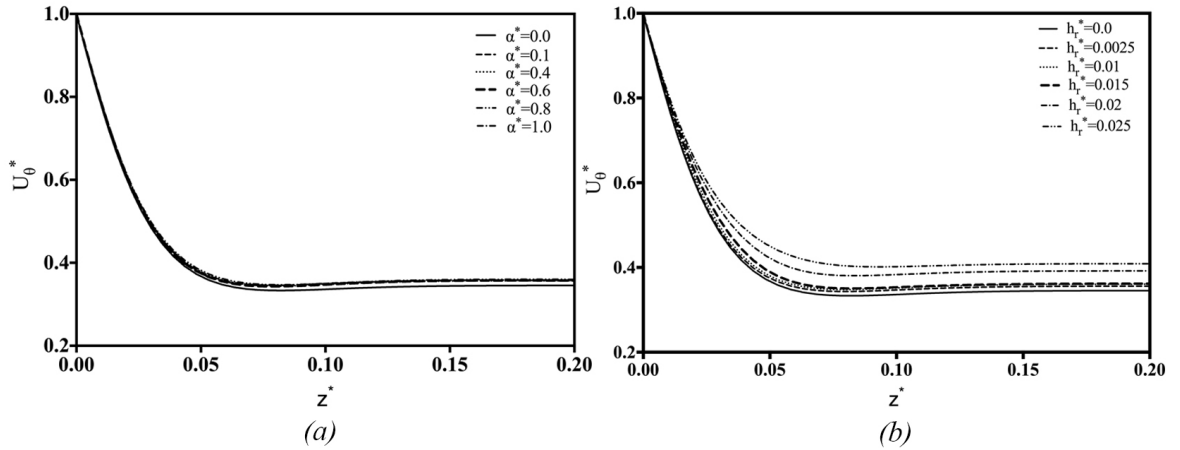
Fig. 5.4 A comparison of the time-averaged tangential velocity profiles over the rotor for, (a) different α^* values, (b) different h_r^* values.

smooth velocity profile ($h_r^* = 0, \alpha^* = 0$). Increasing α^* tends to reduce the profile thickness with a marginal decrease in its peak value (except for the highest α^* values).

Figure 5.4 shows the time-averaged tangential velocity profiles equivalent to the results described in Fig. 5.3. Figures 5.4 (a) & (b) show that increasing h_r^* and α^* tend to thicken the rotor boundary layers and increasing height parameter h_r^* has a higher effect on tangential velocity profiles.

Özkan et al. (2017) investigated the roughness effects on rotor-stator cavities using an FVM based RANS model with the Transition Shear-Stress-Transport turbulence model (TSST). They have imposed the roughness effects through the RANS rough wall function, as described in Section 2.4.3, The tangential velocity profiles in their investigation show

105

the same trend of a thickness profile with a higher modelled roughness. However, the radial velocity profile thickness was reported to reduce with diminished peak values, which contradicts with Fig. 5.3(b). Alveroglu et al. (2016) have investigated the effects of radially and azimuthally-anisotropic or isotropic roughness on BEK boundary layers and they have modelled the roughness using a partial slip method on the boundary. In this approach, radial velocity profiles of azimuthally-anisotropic roughness (radial grooves) in the Ekman layer show the same tendency as Fig. 5.3(b). This elucidates that the radial velocity profiles are more sensitive to the type of the roughness. Hence the disagreement with Özkan et al. (2017)'s radial profile could be due to a different type of roughness compare to the current model. The combined effects of the h_r^*, $\alpha^* = (\alpha_r^*, \alpha_\theta^*, \alpha_z^*)$ and the shape function are important factors to uniquely determine the type of the roughness so that the different combinations of these the parameters can model many different roughness types.

Simulations with numerical roughness layers higher than the model constants $\alpha^* = 0.4, h_r^* = 0.005$, can produce significant effects in the stator layer of the cavity. Figure 5.5 shows the wall-normal profiles of the time-averaged radial velocity for different α^* and h_r^* values. The profiles show that increasing α^* and h_r^* values increases the near-wall U_r^* minimum. The higher value of α^* and h_r^* tends to displace the U_r^* minimum toward the stator wall which is more evident in the simulations with higher roughness height values of Fig. 5.5(b).
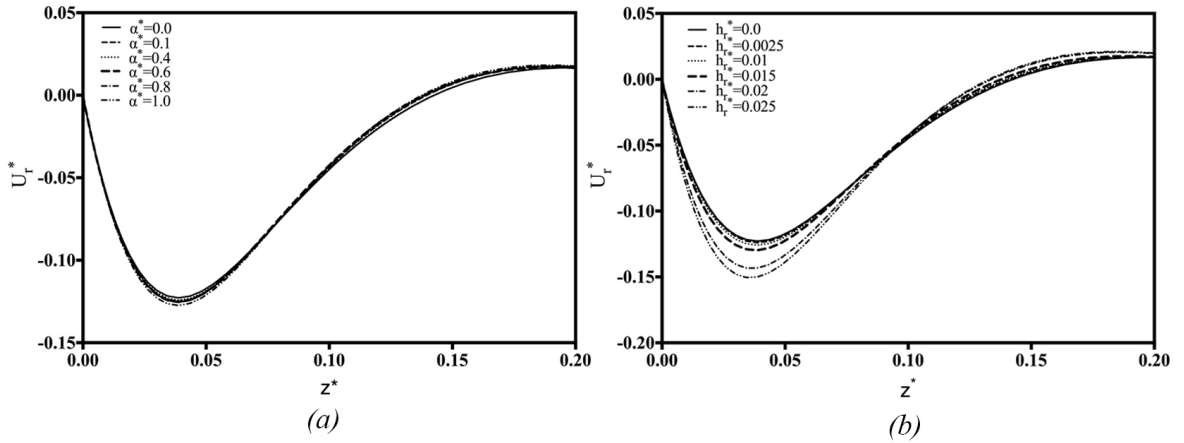
Fig. 5.5 A comparison of the wall-normal profiles of the time averaged radial velocity profiles over the stator for, (a) different α^*, (b) different h_r^* values.

A similar trend is observed for the wall-normal profiles of time-averaged tangential velocity, which are shown in Fig. 5.6. As the roughness effects increase, the near wall peak velocity moves closer to the wall.
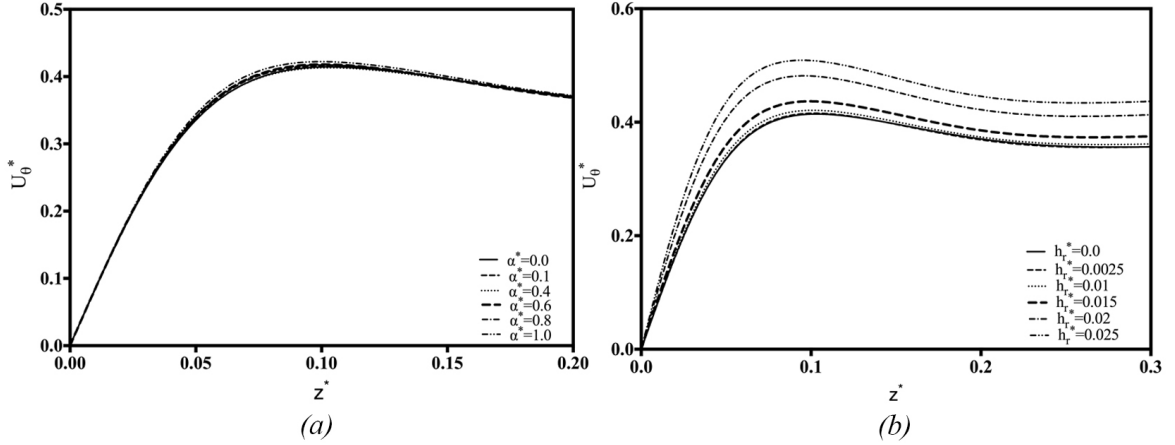
Fig. 5.6 A comparison of the wall-normal profiles of the time-averaged tangential velocity over the stator for (a) different α^* values, (b) different height values h_r^* values.

The changes in the velocity profiles across the boundary layers affect the integral properties in rotor-stator cavities, such as the displacement thickness (δ_1), momentum thickness (δ_2), and the shape factor (H). Equations (5.11)–(5.13) define these three quantities on the tangential velocity component of the rotor-stator boundary layers.

Displacement thickness :

$$\delta_1 = \int_0^\infty \left(1 - U_\theta^*(z)\right) dz. \tag{5.11}$$

Momentum thickness :

$$\delta_2 = \int_0^\infty \left(1 - U_\theta^*(z)\right) U_\theta^*(z) \, dz. \tag{5.12}$$

Shape factor :

$$H = \frac{\delta_1}{\delta_2}. \tag{5.13}$$

Figure 5.7 shows the variation of the azimuthal displacement thickness (δ_1) in the radial direction of the rotor boundary layer under different h_r^* and α^* values. In general, the displacement thickness δ_1 increases with the radius. For the simulated values of h_r^* and α^*, the average displacement thickness increases by up to 1.34% and 14.11% for the highest values of α^* and h_r^*, respectively.

Figure 5.8 shows the effects of modelled roughness on the radial distributions of the shape factor of the rotor boundary layer. The radial average of the shape factor increases by up to 1.49% and 16.14% for the cases of highest α^* and h_r^*, respectively compared to the $h_r^* = 0, \alpha^* = 0$ case. As observed in the displacement thickness distributions, the shape factor also depends on radial distances, and this is more noticeable in Fig. 5.8(b).

107
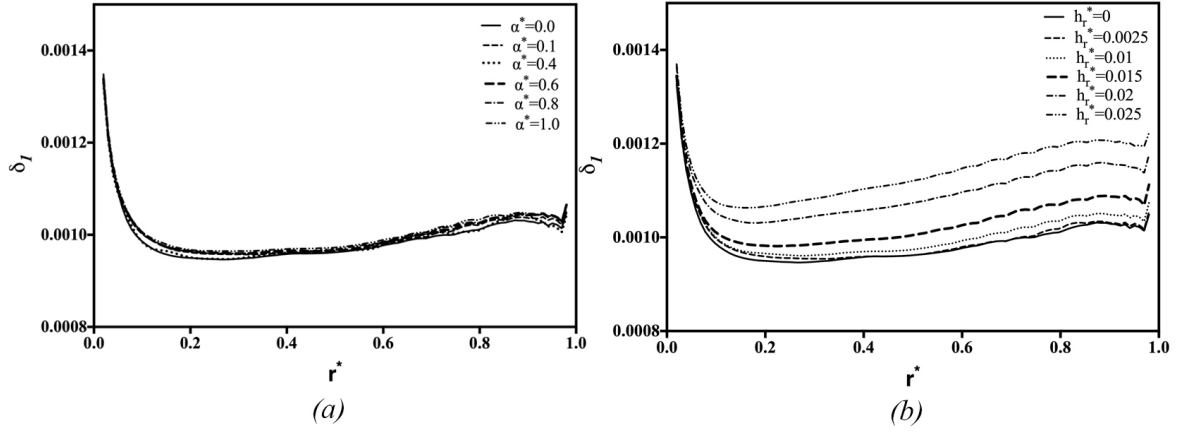
Fig. 5.7 A comparison of radial distributions of the displacement thickness (δ_1) on the rotor boundary layer under, (a) different α^* values, (b) different h_r^* values.
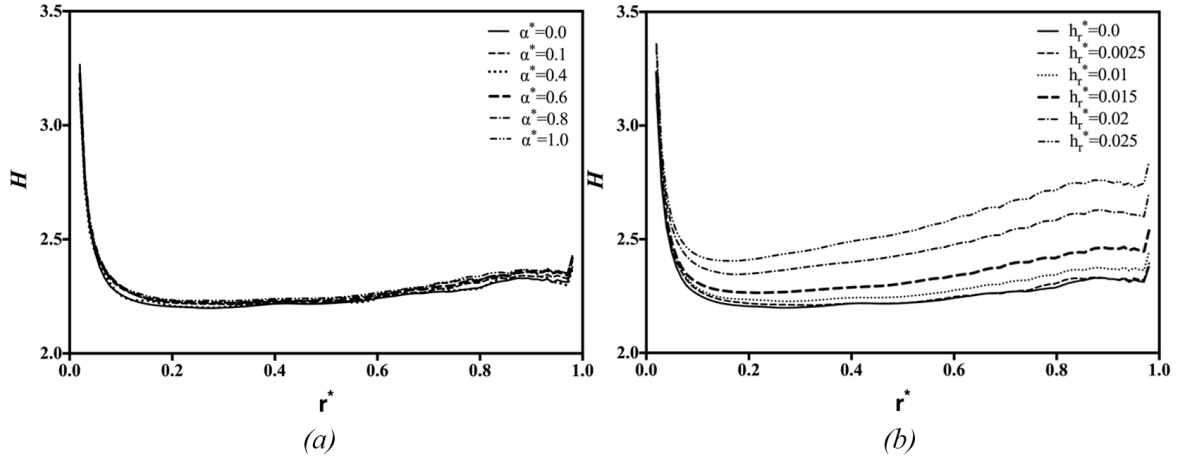

Fig. 5.8 A comparison shape factor (H) at the rotor boundary layer under, (a) different α^* values, (b) different h_r^* values.

Figures 5.9 & 5.10 show the displacement thickness and shape factor of the stator boundary layers and δ_1 and H follow similar trends as for the rotor boundary layers. The radial average of the displacement thickness δ_1 increases by 1.71% and 22.52% at the highest α^* and h_r^* values respectively, and the corresponding increments in the values of the shape factor are 0.97% and 14.70% for highest values of α^* and h_r^*, respectively.

Figure 5.11 shows the variation in the entrainment coefficient K defined in Section 4.3.1 under different h_r^* and α^* values. Increasing either α^* or h_r^* shows an increase in K, which is approximately $K \approx 0.35$ for a hydraulically smooth wall.

For Figs. 5.7 & 5.11, it is clear that modelled roughness on the rotor walls in the rotor-stator cavity gives higher displacement thickness and shape factors in the rotor boundary
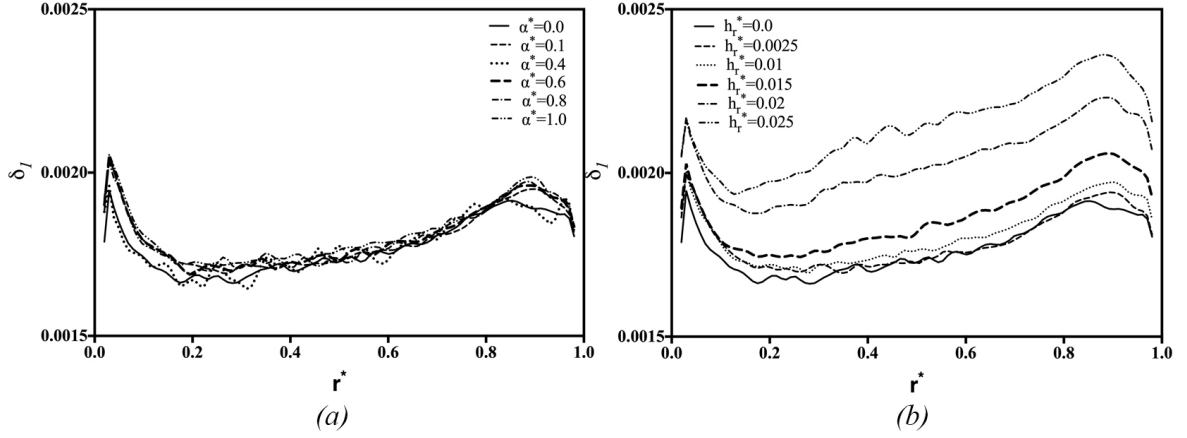
Fig. 5.9 A comparison of radial distributions of displacement thickness (δ_1) on the stator boundary layer under, (a) different α^* values, (b) different h_r^* values.
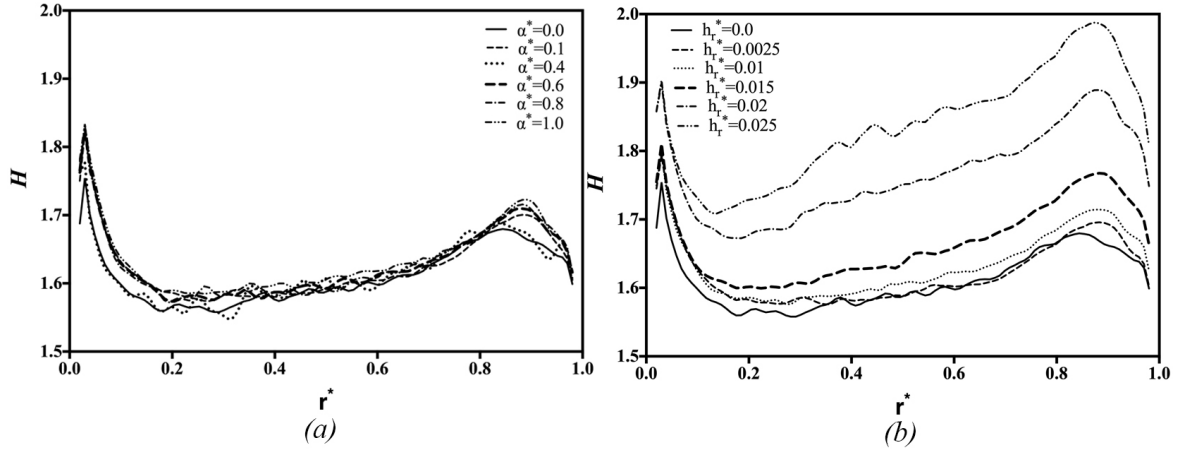
Fig. 5.10 A comparison of radial distributions of shape factor (H) on the stator boundary layer under, (a) different α^* values, (b) different h_r^* values.

layers. This is similar to what was observed by Schultz and Flack (2005) in their experiments in a flat plate boundary layer covered with uniform spheres and fine-scale grit roughness. Further, for the model constant combinations higher than $\alpha^* = 0.4, h_r^* = 0.005$, roughness effects also affect the stator boundary layer.

5.4.2 Boundary layer properties of the rough rotor and smooth stator at $Re_\omega = 4 \times 10^5$

In this section, the rotor-stator boundary layer properties are studied at $Re_\omega = 4 \times 10^5$. Two test cases have been simulated for $\alpha^* = 0.4$, and $h_r^* = 0.00125$ and 0.00375. The test cases
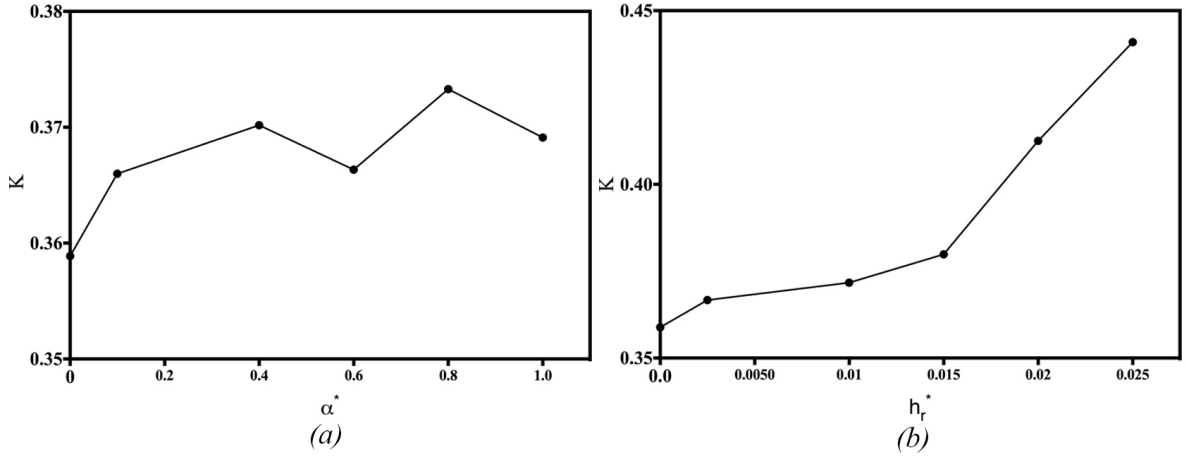
Fig. 5.11 The variation of the entrainment coefficient within the rotor-stator cavity for, (a) different α^* values, (b) different h_r^* values.

are labelled as Low ($h_r^* = 0.00125$) and High ($h_r^* = 0.00375$). The rough model parameters are lower than the α^* and h_r^* values tried at $Re_\omega = 1 \times 10^5$ in Section 5.4.1. This will help to achieve outer-layer similarity (see the description in page 21 of Section 2.4, and the explanations of Jiménez (2004)) and avoid distortion and abnormalities of the velocity profiles that might occur at higher Reynolds numbers.

Figure 5.12 shows turbulent boundary layers in the wall units as defined in Section 4.3.2, and as in Section 4.3.2, the velocity components and axial distances are normalized using the friction velocity (u_τ). As mentioned before, all the axial distributions are plotted at $r^* = 0.65$. Figure 5.12 uses the relative velocity $u_{\theta,r} = (r\omega - U_\theta)$ for the rotor and the absolute velocity U_θ for the stator and both of these quantities are labelled as u_θ^+ in figures. This is consistent with previous investigations including the investigation of Busse and Sandham (2012). The effects of the modelled roughness are visible on the rotor in Fig. 5.12(a) but not so on the stator, Fig. 5.12(b). This is not a surprise as the model constants, α^* and h_r^* have set to meet the outer-layer similarity conditions, which collapse the velocity profiles at the outer region in Fig. 5.12(a). A similar observation has been described in Ikeda and Durbin (2007)'s channel flow simulations, in which the turbulent channels have ribs transversely mounted on one side of the plane, while the surface of the other side of the channel is hydraulically smooth.
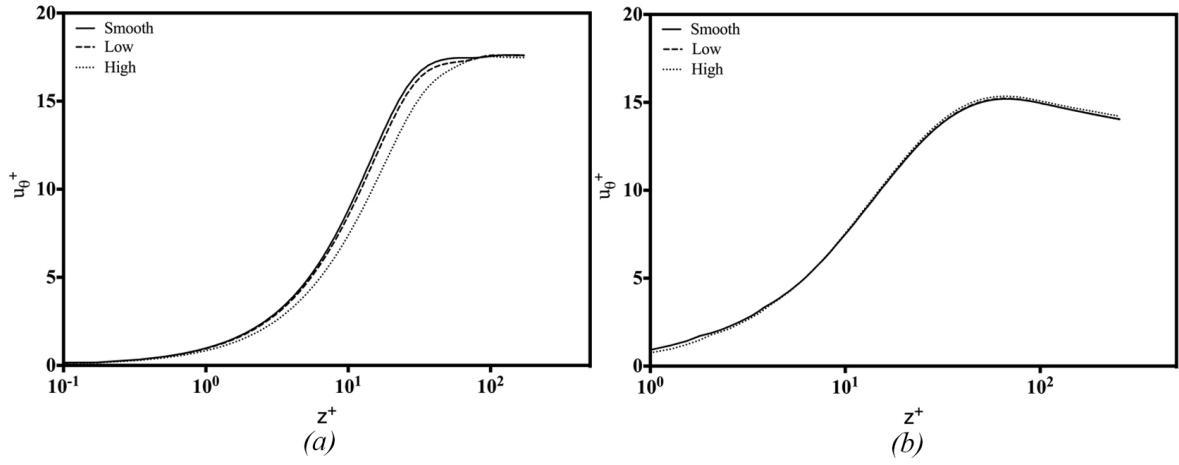
Fig. 5.12 Influence of rotor boundary roughness on time-averaged tangential velocity profiles, (a) relative velocity on rotor boundary layer, (b) absolute velocity stator boundary layer.

Figure 5.13 shows the wall-normal distributions radial LES resolved turbulence intensity component $\sqrt{R_{rr}}$ across the rotor and stator boundary layers. Increasing the rotor surface roughness result in a decrease in the near-wall peak values of $\sqrt{R_{rr}}$. This may be due to the damping nature of the roughness term in the momentum equation. A similar trend was observed in the previous experimental investigation of Krogstad et al. (2005), and in DNS investigations of Orlandi et al. (2003), Flores and Jimenez (2006) and Busse and Sandham (2012). Furthermore, Busse and Sandham (2012) reported the possibility of the peak $\sqrt{R_{rr}}$ moving closer to the wall with increasing wall roughness, but no evidence of this is found in the current predictions.
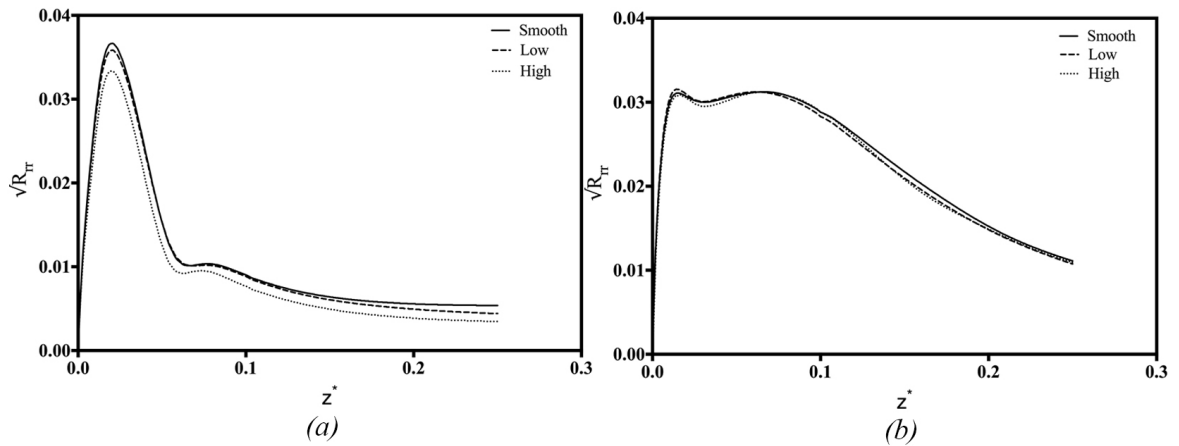
Fig. 5.13 Influence of rotor boundary roughness on radial turbulent intensity profiles, (a) rotor boundary layer, (b) stator boundary layer.

111

Figure 5.14 shows the wall-normal distributions of the tangential turbulence intensity component $\sqrt{R_{\theta\theta}}$. There is no evidence of any substantial rotor wall roughness effects on $\sqrt{R_{\theta\theta}}$ in the stator boundary layer (see Fig. 5.14(b)). In the rotor boundary layer, increasing the rotor wall roughness decreases the near-wall peaks, but these distributions evidence that the damping effects are less intense on $\sqrt{R_{\theta\theta}}$ than on $\sqrt{R_{rr}}$. The tangential component of the turbulent intensity near the rotor reduce over a much shorter axial distance than the radial component.
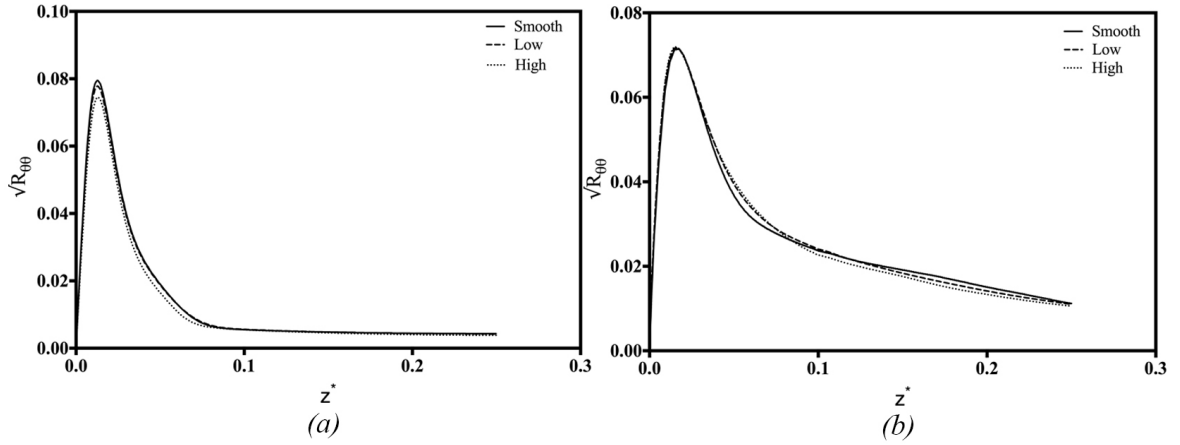
Fig. 5.14 Influence of rotor wall roughness on the tangential component of turbulence intensity, (a) rotor boundary layer, (b) stator boundary layer.

The above distributions of turbulence intensity components do not show the local Reynolds number dependency and the finite nature of the rotor-stator cavities as they have been constructed at the fixed radial location (or fixed Reynolds number) of the mid-section of the cavity, where effect from rotor hub and outer walls are minimum. The radial distributions of the turbulent quantities are used to understand the influence of the local Reynolds numbers and finite dimensions of the cavity. In addition to the turbulence intensity components discussed above, the turbulent kinetic energy is another important parameter, which gives a quantitative understanding of the mean kinetic energy associated with eddies in the turbulent flow and this analysis uses the resolved turbulent kinetic energy that is defined by Eq. (4.3a). For the sake of comparison, radial distributions of the turbulent intensities are constructed at two axial distances of $z^* = 0.0125$ and 0.04. The shorter distance is inside the numerical roughness layer (h_r^*), and the larger distance is just far enough from the rotor wall to be outside of the numerical roughness layer. This arrangement will provide an understanding of the behaviour of turbulent fluctuations inside and outside the numerical roughness layer.

Figure 5.15 illustrates turbulent kinetic energy distribution along the radial direction and it is normalised by $k_{disk} = 0.5U_{\theta,max}^2$. The kinetic energy radial distribution is lower

at the larger axial distance $z^* = 0.04$. At both $z^* = 0.0125$ and $z^* = 0.04$, the magnitude of the kinetic energy is fairly constant from the hub up $Re_{\omega,local} = 1.1 \times 10^5$, after, which there is a gradual increase in kinetic energy. The damping effects by the wall roughness also are apparent in these plots. As the local Reynolds number increases, the disparity between distributions marginally increases, which suggests that the roughness effects are pronounced at higher local Reynolds numbers. However, in both distributions at about $Re_{\omega,local} \approx 2.6 \times 10^5$–$3.0 \times 10^5$ region, there is a noticeable increase in kinetic energy due to the rough walls.

(a) *(b)*
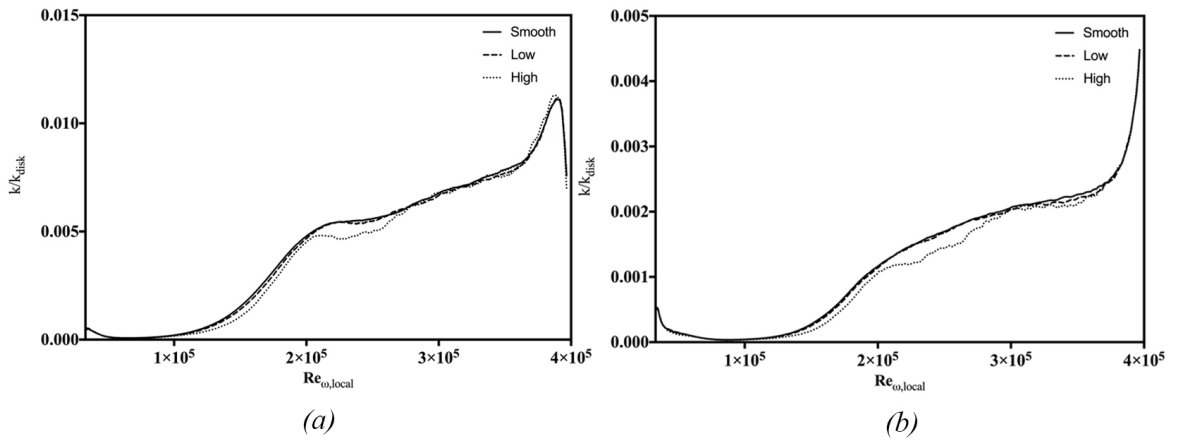
Fig. 5.15 Influence of rotor boundary roughness on turbulent kinetic energy distributions on radial direction, (a) at $z^* = 0.0125$, (b) $z^* = 0.04$.

Figures 5.16 & 5.17 illustrate the corresponding the radial and tangential turbulence intensity contribution at the same two axial locations. The tangential turbulence intensity component is considerably higher than its radial counterpart on both of these axial planes. These intensity distributions also show the damping effect due to the rough walls. The radial turbulence intensity component $\sqrt{R_{rr}}$ show the damping effect throughout the entire radial span, but the tangential intensities show $\sqrt{R_{\theta\theta}}$ values at high radial positions that are above the $\sqrt{R_{\theta\theta}}$ predicted with the hydraulically smooth wall. This could be the main contribution to the sudden increase in kinetic energy at the $Re_{\omega,local} > 2.6 \times 10^5$ in Fig. 5.15, and these observations above the rotor wall could be due to the finite nature of the cavity.
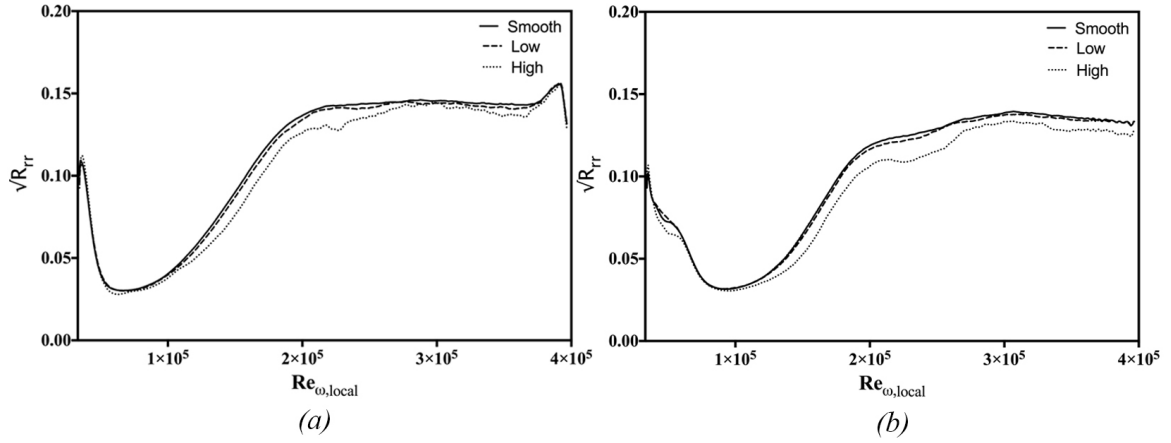
Fig. 5.16 Influence of rotor boundary roughness on the radial components of the turbulence intensity distribution in the radial direction, (a) at $z^* = 0.0125$, (b) $z^* = 0.04$.
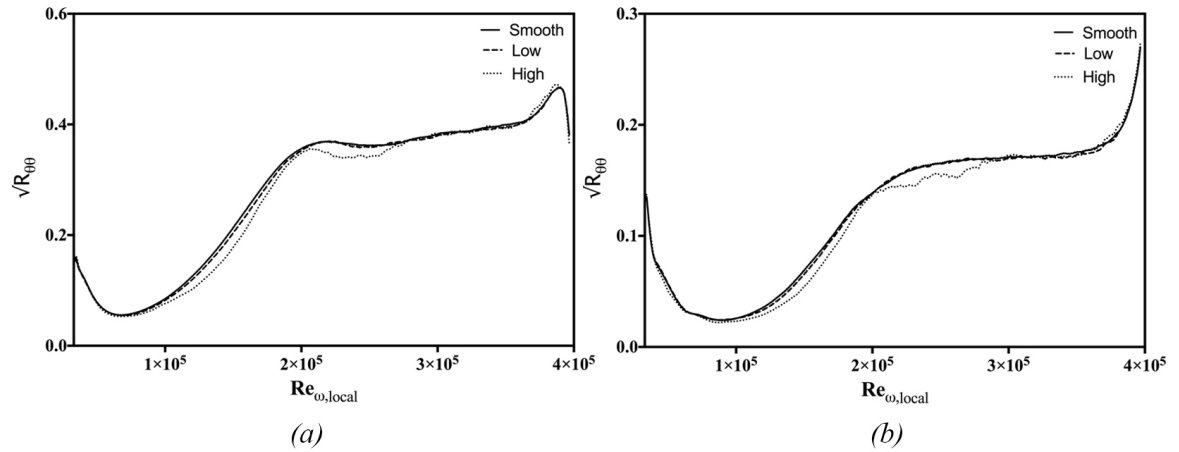
Fig. 5.17 Influence of rotor boundary roughness on the tangential components of the turbulence intensity distribution in the radial direction, (a) at $z^* = 0.0125$, (b) $z^* = 0.04$.

5.4.3 Flow visualisation

This section provides comparisons between velocity contours over the rough wall and over the hydraulically smooth rotor wall, in a rotor-stator cavity. The velocity contours are extracted from the higher Reynolds number cases of $Re_\omega = 4 \times 10^5$ to get the full perspective of both rotor and stator boundary layers. Here, all the velocity contours are normalised by the highest tangential velocity component value of the rotor $U^*_{\theta,max} = r_2\omega$.

Figure 5.18 shows the axial velocity contours predicted from rough and smooth wall cases on the r–z plane. There is no significant difference in the magnitude of the axial velocity components among the three cases. However, the inner regions of the stator boundary layer

114

of the test cases with a modelled rough rotor wall have more vortex structures compared to the hydraulically smooth wall cavity case. With a rough rotor wall, the structures in the core region and in the rotor boundary layer appear vertically elongated, and this is more apparent in the structures near the mid-radial positions of the rough rotor boundary layers. Another difference is that the upper junction between the stator layer and outer wall is more disturbed with a rough rotor wall, which implies convective transport of roughness effects to the stator even at the low roughness parameters $\alpha^* = 0.4$, $h_r^* = 0.00125$. This could be the reason for the high values of $\sqrt{R_{\theta\theta}}$ shown in Fig. 5.17(b). Further, for all the three cases shown in the figure, a train of vortices appears on the stator boundary, and these vortex patterns of Low and High rough cases spread more toward the lower Reynolds number regions of the stator boundary when they compared to the vortex pattern on the smooth case.
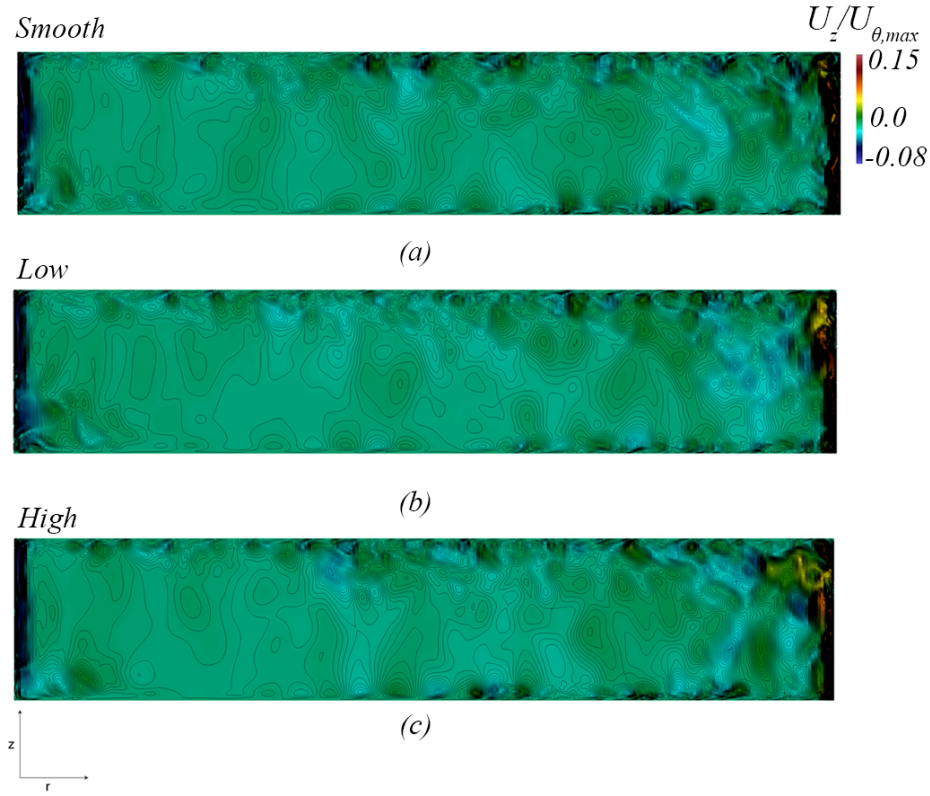
Fig. 5.18 Instantaneous axial velocity contours on the r–z plane for $Re_\omega = 4 \times 10^5$, (a) Smooth, (b) Low, (c) High.

Figure 5.19 illustrates the LES resolved instantaneous and time-averaged tangential velocity contours close to the rotor boundary layer. These contours have been extracted at the axial distances of, $z^* = 0.04$. The instantaneous velocity contours (see Figs. 5.19 (a),(b),(c)) predicted with a rough rotor wall show more energetic flow structures in the external portion

of the disk. In this region, the size of the structures gradually increases with increasing roughness. Close to the hub, a similar tread is present, but the effects are less significant.
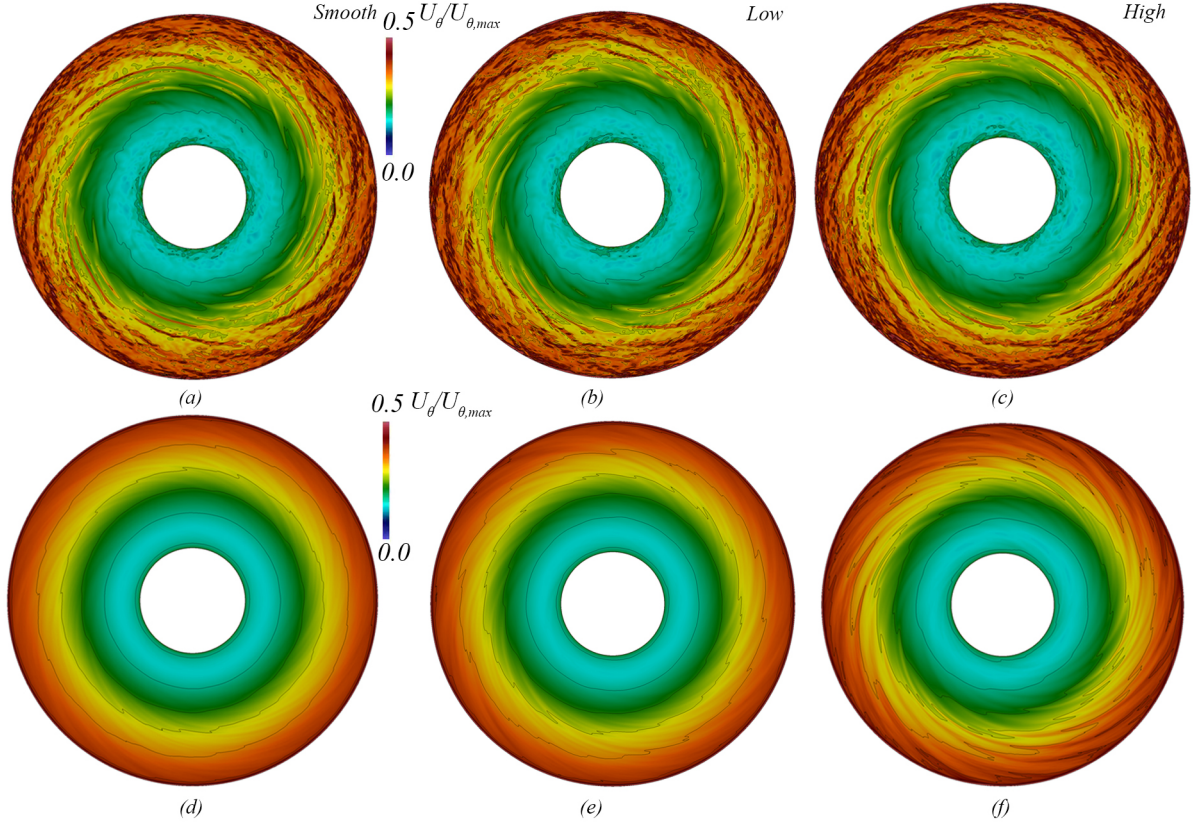
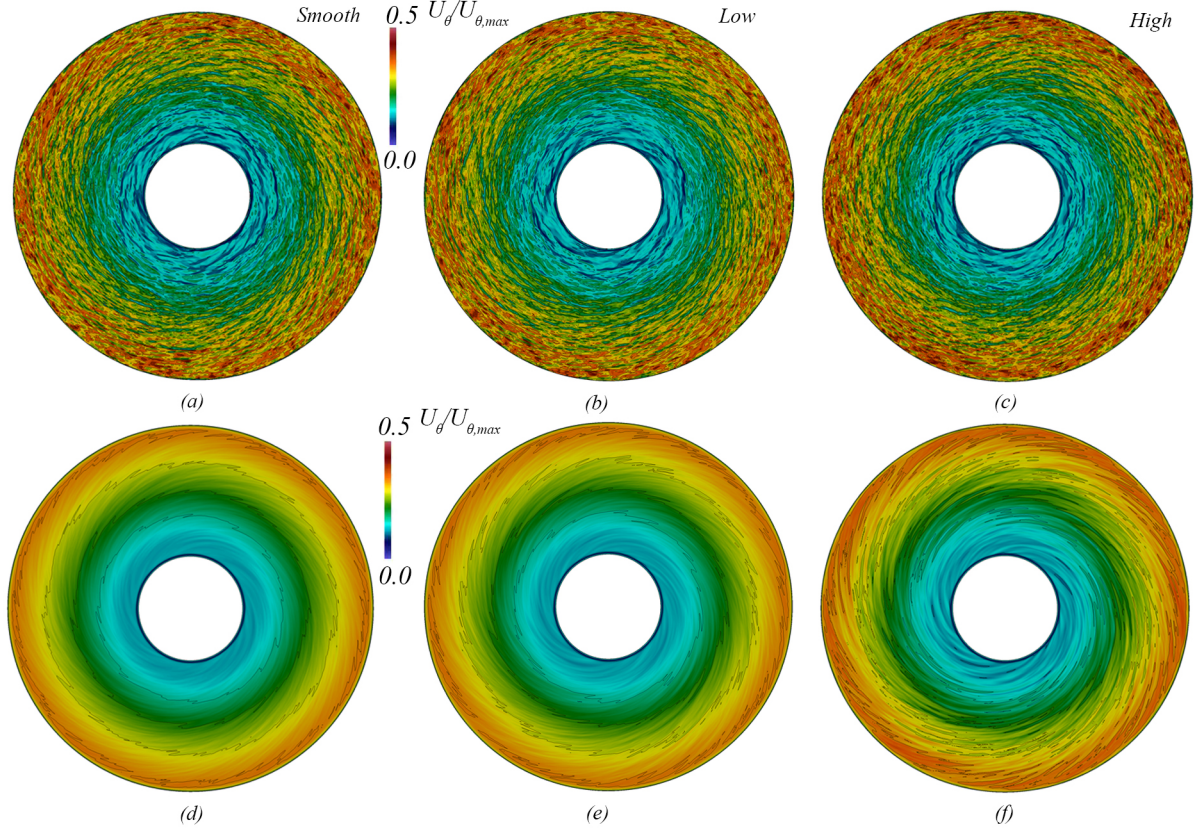Fig. 5.19 The tangential velocity contours near the rotor boundary layer, $z^* = 0.04$, instantaneous velocity contours, (a) Smooth , (b) Low, (c) High ; time-averaged velocity contours, (d) Smooth, (e) Low, (f) High.

Figures 5.19(d),(e),(f) show the corresponding time-averaged tangential velocity contours. These contours show large-scale spiral arms at in the external portions of the disk, but the velocity contours close to the hub are almost similar. This suggests that the structures in higher Reynolds number regions are more persistent compared to the structures in the mid and low Reynolds number regions.

Figure 5.20 shows the resulting instantaneous and time-averaged tangential velocity contours in the stator boundary layer. These contours are obtained at $z^* = 0.975$. The instantaneous tangential velocity contours above the stator show the same tread that was observed close to the rotor wall. In the outer disk region, the effects of roughness become more visible as the rotor wall roughness is increased. These effects are also present in the time-averaged velocity contours, but unlike in rotor boundary layer, these contours evidence that the disturbances spread into the inner regions of the cavity which are close to the hub.

This is no surprise as the stator boundary layer promotes radial flow toward the hub because of the favourable pressure gradients in the negative radial direction. These effects in the stator boundary layers could be the result of the disturbance propagation mechanism, which has explained in Fig. 5.18.

Fig. 5.20 The tangential velocity contours near the stator boundary layer, $z^* = 0.975$, instantaneous velocity contours, (a) Smooth, (b) Low, (c) High; time-averaged velocity contours, (d) Smooth, (e) Low, (f) High.

As explained in Section 4.3.4, the velocity contours across the full disk are sometimes unable to render the changes in fine structures. Hence, the λ_2 criterion is used to capture the fine-scale structures near the outer edge of the rotor boundary and Fig. 5.21 shows the λ_2 iso-surface representation of these structures at $z^* = 0.04$. These structures are captured at the same locations as Fig 5.19, and the same λ_2 colour scale is used for both hydraulically smooth and rough wall boundary layers. By observing the structures in both boundary layers, it is clear that the structures at the outer edge of the rough wall boundary are plumper than the hydraulically smooth wall counterparts. A similar observation is given in Busse and Sandham (2012).
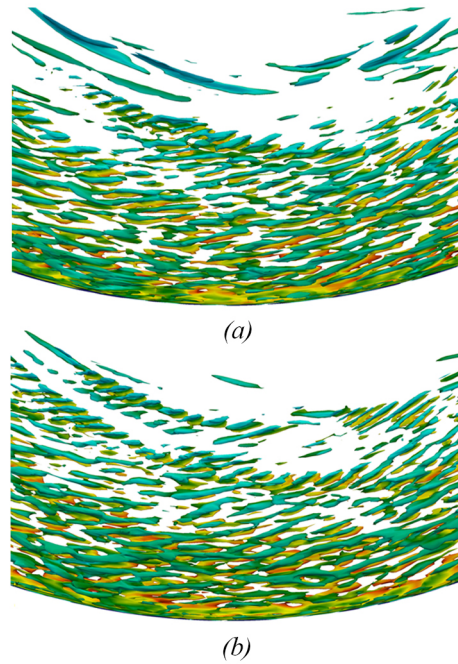
Fig. 5.21 The λ_2 iso-surfaces of vortex structures near the rotor boundary layer at $z^* = 0.04$, (a) Smooth, (b) High.

5.5 Summary and conclusions

This chapter discusses the modifications and applications of a parametric wall roughness model to represent rough rotor walls in rotor-stator cavities. Here, the roughness effects only apply to the rotor boundary layer and, in all cases, the stator boundary is modelled as a hydraulically smooth wall.

Busse and Sandham (2012)'s original work is based on standard channel flow calibration results, which consist of a stationary wall. Hence, suitable modifications were introduced to represent a rotating disk, which has a moving wall instead of a stationary wall. A set of simulations were run with numerically simulated rough rotor wall over the modelled roughness parameter space of α and h_r and the results are presented by their normalised values of $\alpha^* = 0.1$–1.0 and $h_r^* = 0.0025$–0.025.

Initial simulations were conducted at the low Reynolds numbers of $Re_\omega = 1 \times 10^5$. The mean velocity profiles at the rotor boundary showed an increase in the peak values at higher model constant values. Increasing the roughness height model constant h_r^* was found to be more significant than increasing the roughness factor constants (α^*). The model constant values higher than $h_r^* = 0.005$ show effects in the hydraulically smooth stator boundary

layer and these effects are more significance beyond $h_r^* = 0.01$. Corresponding changes in displacement thickness and shape factors were also predicted.

The second set of simulations ran at the higher Reynolds numbers of $Re_\omega = 4 \times 10^5$, and the wall roughness model constants were set over the narrow range of low values of $h_r^* = 0.00125$ and 0.00375 for $\alpha^* = 0.4$. The purpose of this was to study the turbulent properties under the roughness effects and achieve outer layer similarity. The time-averaged velocity profiles of turbulent boundary layers were obtained, and their tangential components were plotted in wall units. The time-averaged tangential velocity profiles at the rotor boundary show a reduction in the relative velocity profiles compared to the hydraulically smooth wall cases, but under these model constant values, the time-averaged tangential components at the stator boundary layer are unaffected. The peak values of both radial and tangential turbulent intensities of the rotor boundary layer decrease probably due to damping effects of the roughness terms, but the corresponding values at the stator boundary layer are relatively unaffected. The radial dependency on turbulent kinetic energy and turbulent intensities was also shown, and here tangential turbulent intensities are more disturbed at rough walls.

The flow visualisation was carried out to understand the changes in flow structures of the cavity under the influence of wall roughness. The structures were visualised from different viewpoints of the cavity. The side view shows that the upper junction between the stator wall and outer wall is more disturbed in the cavity with a rough rotor wall. The tangential velocity contours show the effects of modelled roughness near both rotor and stator boundary layers. The iso-surface visualisation near the rotor boundary shows a more enlarged vortex structure on rough wall layers.

These results show the general effects of rotor layer roughness on rotor-stator cavities. As a conclusion, even small amounts of roughness on the rotor layer can influence other parts of the cavity, and the bulk fluid transport through the outer wall enables this process.

Chapter 6

Numerical modelling of a nanofluid and its heat transfer in a rotor-stator cavity

6.1 Introduction

This chapter focuses on implementing numerical models to evaluate rotor-stator heat transfer with nanofluids. The numerical model uses the transport models discussed in Section 2.5.1, to evaluate nanofluid properties. These models are simulated with different volume fractions of Al_2O_3 nanoparticles.

The first half of the chapter discusses the preparation of computational models to simulate rotor-stator flows. The second half focuses more on discussing the outcomes of these models. The new models are validated with previous investigation results, and the effects of nanofluids on the flow and heat transfer aspects are elaborated and compared against the validated outcomes.

6.2 Problem definition

6.2.1 Geometric and numerical modelling

An identical geometry and mesh are used to the $Re_\omega = 1 \times 10^5$ configuration described in Table 4.1. For the sake of brevity, readers are referred to Section 4.2.1 for more details. Unlike in the previous simulation, in the current simulations, the orientation of the cavity is important, due to the buoyancy of the flow. The current configurations assume a top rotor and a bottom stator as shown in Fig. 6.1. However, in the physical mesh, the rotor is on the $z = 0$ plane and the required directional dependency is achieved by defining the gravitational vector $\mathbf{g} = (0, 0, 9.81)$.
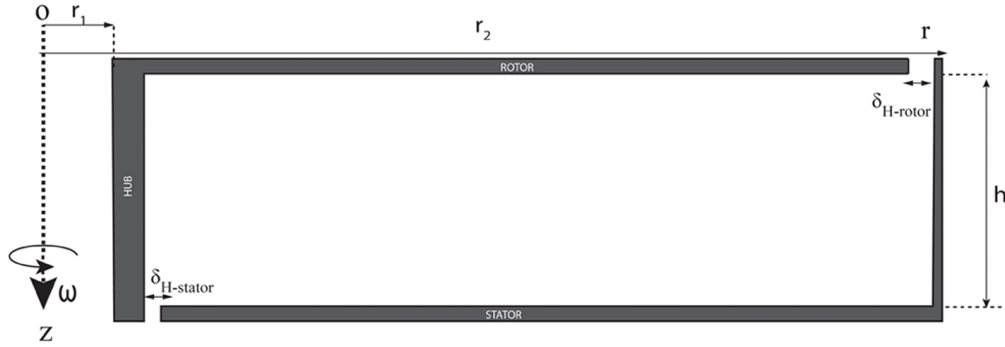
Fig. 6.1 The rotor-stator cavity use in the nanofluid heat transfer simulations.

For all the simulations conducted in this section, the subgrid-scale quantities are calculated using the WALE model (see Section 3.5.2.2) and the value of the subgrid-scale Prandtl number (Pr_{sgs}) is taken as 0.4 (Antonopoulos-Domis, 1981).

Two sets of simulations have been performed, using respectively, the single-phase (S_P) approach and the two-phase (T_P) approach (hereafter, S_P and T_P denote the single-phase and the two-phase model, respectively). The governing equations for S_P model were explained in Eqs. (3.39)-(3.41). The T_P model uses the mass, momentum and thermal transport equations described in Eq. (3.47)–(3.49) and an additional transport equation, Eq. (3.50), used to solve the volume fraction distributions of the nanoparticle phase. In both cases, the nanofluid thermal conductivity (k_{nf}) and viscosity (μ_{nf}) are calculated using the correlations given in Sections 2.5.1.2 & 2.5.1.1. Specifically, In this study, Maxwell's model in Eq. (2.1) and Brinkman (1952)'s viscosity model in Eq. (2.10) are used to calculate the values for k_{nf} and μ_{nf}.

Like in the previous chapters, all simulations are conducted using OpenFOAM, and a second-order accurate FVM based segregate solver is used for solving the system of equations. The pressure-velocity coupling is achieved using the non-iterative PISO algorithm, and all simulations are performed with $z_{max}^+ \leq 1.0$. The time steps (Δt) have been chosen to satisfy the condition $Co_{max} \leq 0.3$.

6.2.2 Boundary and operational conditions

In both S_P and T_P simulations, the same velocity and thermal boundary conditions are set. In all the rotating walls, the no-slip boundary condition, which is based on the relative velocity on the wall, is used. At the stator and outer walls, which are stationary walls, the velocity is

set to zero. The rotor and hub velocities are set by

$$\boldsymbol{u_{rotor}} = \omega \boldsymbol{r_p} \times \boldsymbol{I_{dir}}, \tag{6.1}$$

where $\boldsymbol{I_{dir}} = (0,0,1)$ and ω are the axial directional unit vector, and the $\boldsymbol{r_p}$ is the position vector for respective cell faces. The value for ω is set by $Re_\omega = 1 \times 10^5$. Constant temperature wall boundary conditions are used. The temperature values of the rotor and hub are 300 K, and the stator and the outer wall temperatures are set to 325 K.

The thermal Rossby number is defined as $B_{thermal} = \beta_{nf}(T_2 - T_1)$ (Tuliszka-Sznitko et al., 2009b) where T_2 and T_1 are stator and rotor temperatures and β_{nf} is the thermal expansion coefficient of the nanofluid that can be obtained using a weighted average method as shown in Eq. (3.46). The initial temperature and velocity values (i.e. temperature and velocity at $t = 0$) of all the simulations are set with 300 K and zero velocity conditions at everywhere in the computational domain.

Both S_P and T_P simulations require defining an initial nanoparticle volume fraction value (ϕ) to calculate nanofluid properties, and the set of initial values $\phi = 0, 0.02, 0.04, 0.2$ has been considered to conduct S_P and T_P simulations. The previous investigations of Bachok et al. (2011) and Turkyilmazoglu (2014) have used the volume fraction of $\phi = 0.2$ in their simulations and Turkyilmazoglu (2014) mentioned that the accumulation of nanoparticles is acceptable up to $\phi = 0.2$. In the case of the S_P simulation, the initial values of the volume fraction do not change with simulation time, and these values are a key factor in determining the nanofluid thermo-physical properties.

The volume fraction Eq. (3.50) determines the evolution in space and time of the ϕ field in T_P simulations. Apart from the initial values, T_P simulations require boundary conditions for the volume fraction equation, similar to other governing equations. The relevant boundary conditions at the walls are set as

$$\boldsymbol{j_p} = \boldsymbol{j_B} + \boldsymbol{j_T}, \tag{6.2}$$

$$\boldsymbol{j_p} = D_B \boldsymbol{\nabla} \phi + D_T \frac{\boldsymbol{\nabla} T}{T}. \tag{6.3}$$

The parameter $\boldsymbol{j_p}$ is the mass flux due to the Brownian and thermophoresis forces. By considering zero mass fluxes in the wall-normal directions, Eq. (6.3) becomes

$$\boldsymbol{\nabla} \phi . \boldsymbol{n} = -\frac{D_T \boldsymbol{\nabla} T}{D_B T} . \boldsymbol{n}. \tag{6.4}$$

Equation 6.4 can be used as a boundary condition at the wall boundaries of the simulations and the further simplification of the equation can be stated as

$$\left(\frac{\partial \phi}{\partial n}\right)_{\textbf{wall}} = \frac{D_T}{D_B T}\left(\frac{\partial T}{\partial n}\right)_{\textbf{wall}}, \tag{6.5}$$

which is valid on the wall boundaries.

All the simulations are performed by the thermo-physical properties of pure Al_2O_3 and water at ambient conditions and Table 6.1 shows thermo-physical properties of Al_2O_3 and water.

Property	Al_2O_3	Water
Density (ρ) [kgm^{-3}]	3970	996
Viscosity (μ) [kgm^{-1}s^{-1}]	N/A	8.93×10^{-7}
Heat capacity at constant pressure (c_p) [Jkg^{-1}K^{-1}]	880	4177
Thermal conductivity (k_f/k_{np}) [Wm^{-1}K^{-1}]	42	0.61
Diameter (d_p) [nm]	30	0.385
Thermal expansion coefficient (β_{therm}) [K^{-1}]	2.5×10^{-5}	2.1×10^{-4}

Table 6.1 Thermo-physical properties of the constituent materials.

6.3 Results and discussion

This section describes the momentum balance and heat transfer characteristics of rotor-stator cavities filled with Al_2O_3 based nanofluid using the S_P and the T_P transport models. Despite the model validation presents in previous chapters for $Re_\omega = 1 \times 10^5$ cases, a basic validation is repeated here due to new transport models and turbulence model that are used for the first time in this study. All lengths and velocities are shown normalised as Section 4.3.

The volume fraction of $\phi = 0.0$ represents a simulation of pure water without any nanoparticle constituents, but the value $\phi = 0.0$ may cause singularities in current numerical models. Hence, a small volume fraction value of, $\phi \approx 2 \times 10^{-5}$ is used to represent pure water. It is important to remember that the results from this simulation will be denoted as $\phi = 0.0$.

Figure 6.2 describes the time-averaged axial profiles of the tangential velocity components for the case of $\phi = 0.0$. For the current test cases, the radial position $r^* = 0.5$ is selected to plot the axial profiles and this radial position gives smoother velocity profiles than the radial position $r^* = 0.65$ for the $Re_\omega = 1 \times 10^5$ cases. All the axial plot are averaged over

the tangential direction as described in Section 4.3, and a couple of dozen disk rotations was sufficient to obtain the stationary time-averaged quantities. Both single-phase (S_P) and two-phase (T_P) models have similar radial and tangential velocity profiles, which is explained by the fact that as $\phi \to 0$ the T_P model asymptotes to the S_P model, and the models show similar values for the entrainment coefficient $K \approx 0.36$.
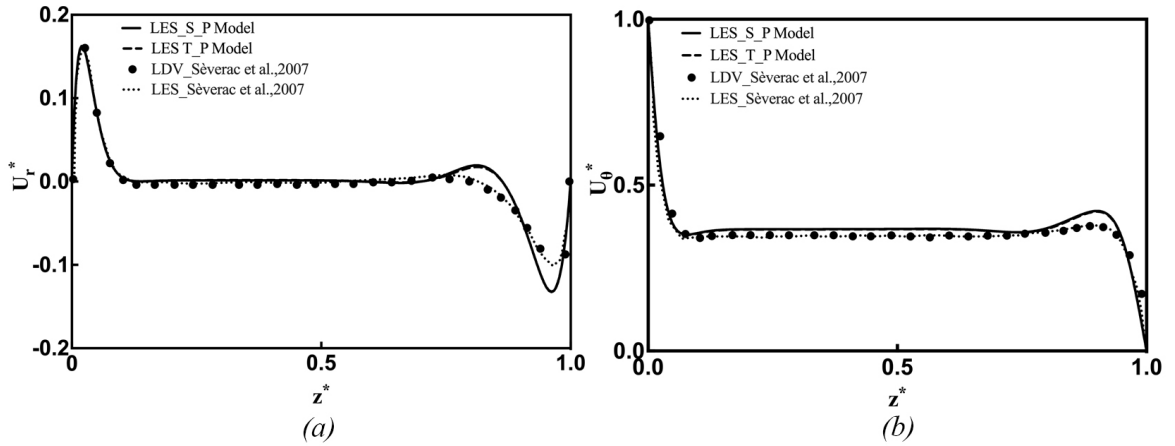

Fig. 6.2 The axial distributions of time-averaged velocity fields in pure water, $r^* = 0.50$, (a) radial velocity, (b) tangential velocity.

Figure 6.3 shows the time-averaged axial distributions of the radial and tangential turbulence intensity components. All the models underpredict the turbulence intensity level compared to the previous experiment results, but the locations of the peaks near the stator agree well with the experiment results. The damping effects in the predicted turbulence intensity components may be partially due to the small nanoparticles volume fractions present in the current simulations. The S_P and T_P simulations have very similar radial and tangential turbulence intensity profiles.

6.3.1 Momentum and heat transfer in a nanofluid filled rotor-stator cavity

This section describes the momentum and heat transfer characteristics of rotor-stator cavities filled with a nanofluid. Result are presented for the S_P model over the nanoparticle concentration range $\phi = 0, 0.02, 0.04, 0.2$.

Figure 6.4 shows time-averaged axial profiles of the radial velocity component through the rotor and stator boundary layers. At lower volume fractions, no significant changes can be observed in the boundary layers, but higher volume fractions, $\phi > 0.04$, tend to increase the radial velocity profile of the cavity.
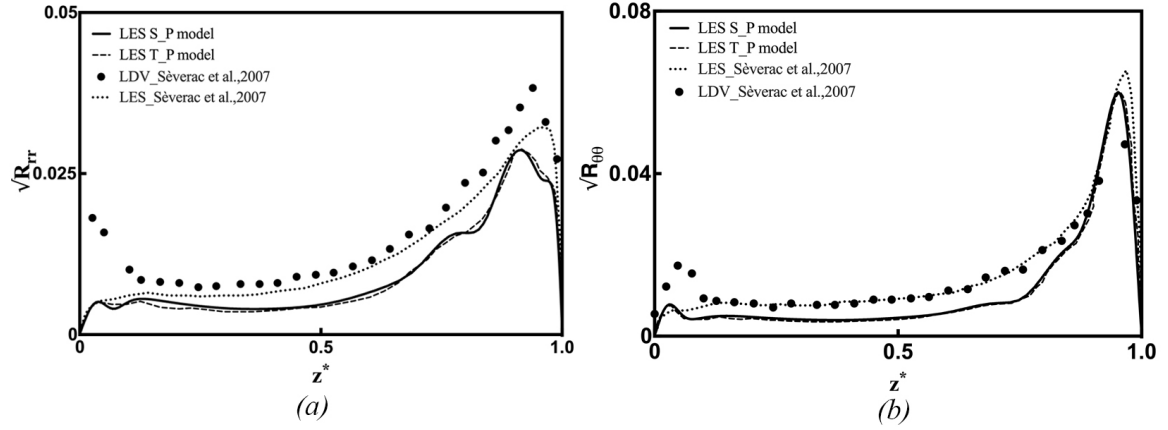
Fig. 6.3 A time-averaged axial profiles of the axial distributions of turbulence intensity fields in pure water, $r^* = 0.50$, (a) radial intensities, (b) tangential intensities.
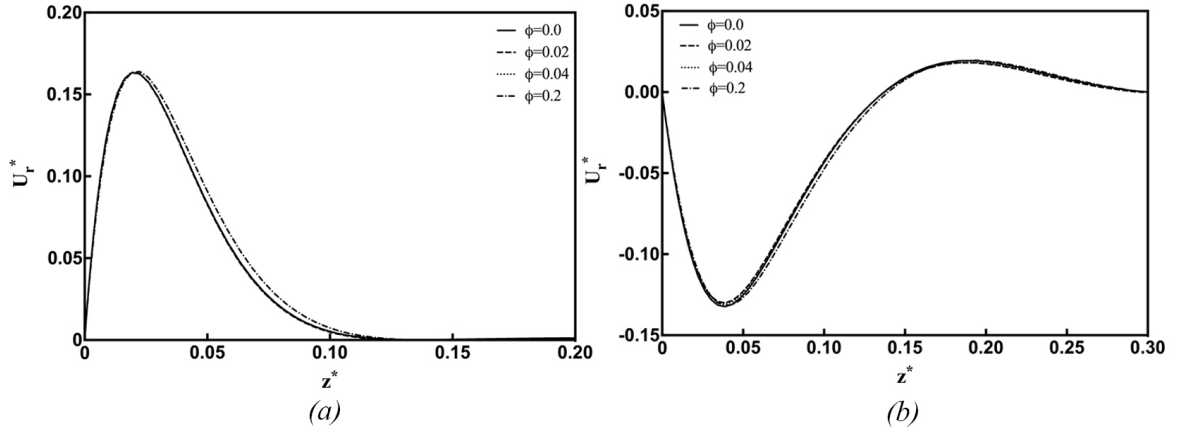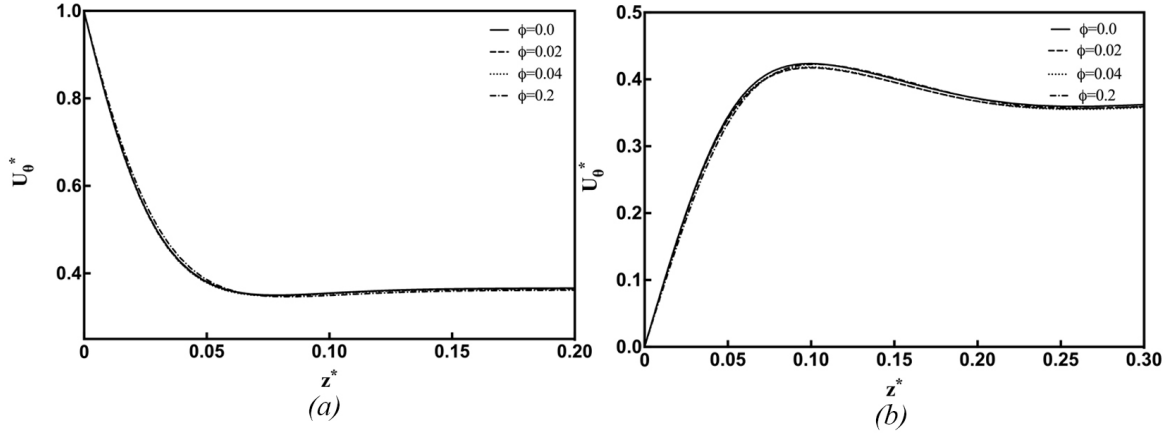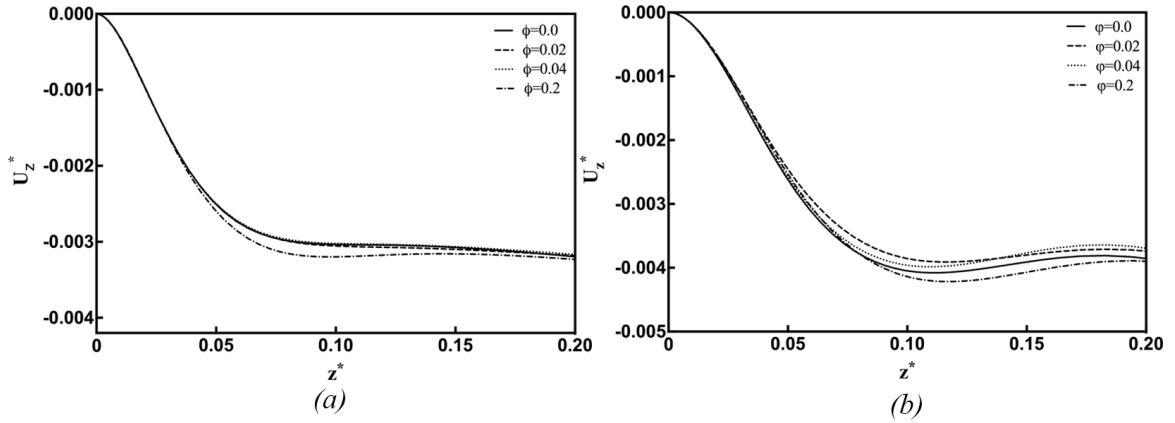

Fig. 6.4 A wall-normal profiles of time-averaged radial velocity components for different nanoparticle volume fractions, $r^* = 0.50$, (a) rotor boundary layer, (b) stator boundary layer.

In Fig. 6.5, a similar trend can be observed in the wall-normal profiles of tangential velocity through the rotor boundary layer, but the stator tangential velocity component is slightly reduced as a result of increased nanoparticle volume fractions.

The axial velocity distributions across the rotor and stator boundary layers are shown in Fig. 6.6. These distributions confirm higher U_z^* components (here, velocity components are negative) across both stator and rotor boundaries, as the concentration of the nanoparticle increases. These high values of negative U_z^* components can be explained as a result of mass continuity of the flow, in which a higher rate of fluid displacement in the radial and tangential directions often demands a higher rate of fluid from axial locations of the cavity to fill the gap. Figure 6.6(b) shows a similar trend in the stator boundary layer at $\phi = 0.2$ but this trend is less pronounced in the lower volume fraction cases. By intuition, a higher

125

Fig. 6.5 A wall-normal profiles of time-averaged tangential velocity component for different nanoparticle volume fractions, $r^* = 0.50$, (a) rotor boundary layer, (b) stator boundary layer.

axial inflow velocity component toward the rotor boundary may result in a higher axial outflow velocity component on the stator boundary and this is mostly the case for the infinite rotor-stator disk systems (i.e. derivatives of BEK boundary layers without outer walls and rotor hub). However, the rotor hub and the outer walls of a finite cavity often complicate the mass transfer process in the rotor-stator cavity, in which the bulk fluid motion (i.e. mass transfer) between the rotor and the stator boundary layers occurs through the rotor hub and outer walls.

Fig. 6.6 A wall-normal profile of the time-averaged axial velocity components for different nanoparticle volume fractions, $r^* = 0.50$, (a) rotor boundary layer, (b) stator boundary layer.

The previous investigation of Turkyilmazoglu (2014) explained the behaviour of the velocity components near a single rotating disk. His theoretical investigation confirms these observations in the time-averaged velocity components for the nanofluid with Al_2O_3

nanoparticles. Regardless of the volume fraction, the effects of nanoparticles on the time-averaged radial and tangential distributions are highly localised in the near wall areas, and the velocity distributions eventually collapse on each other, which results in identical behaviour in the core region of the cavity at all nanoparticle volume fractions tested.

Figure 6.7 show axial profiles of radial and tangential turbulence intensity components for different nanoparticle volume fractions at $r^* = 0.50$. Radial turbulence intensity distribution is more affected by the changes in volume fractions of the nanofluid. The tangential turbulence intensity distributions show some effects but to a less extent. At the highest volume faction value of $\phi = 0.2$, there is a visible reduction in the turbulence intensity $\sqrt{R_{rr}}$ near the walls and in the core region of the cavity in both radial and tangential distributions, but in the same models, nanoparticle volume fractions of $\phi = 0.02, 0.04$, show a subtle increase compared to pure water. In general, increasing the nanoparticle volume fractions is expected to result in higher turbulence intensities in rotor-stator cavities up to some extent. For instance, Hu et al. (2013) used an LES-Lagrangian based numerical investigation to study the transport properties of a nanofluid based on Cu, SiO_2 nanoparticles and they have observed that nanoparticles produce higher turbulence intensities at $\phi = 0.01$ compared to pure water simulations. Ghaffari et al. (2010) reported a reduction in the turbulence intensities, as the Grashof number (Gr) increases in their horizontal curved pipe simulations based on a two-phase modelling approach with slip velocities. Both of these examples have the bulk fluid flow in a streamline direction, but the rotor-stator flows have an induced type of fluid motion due to the rotation of the rotor.
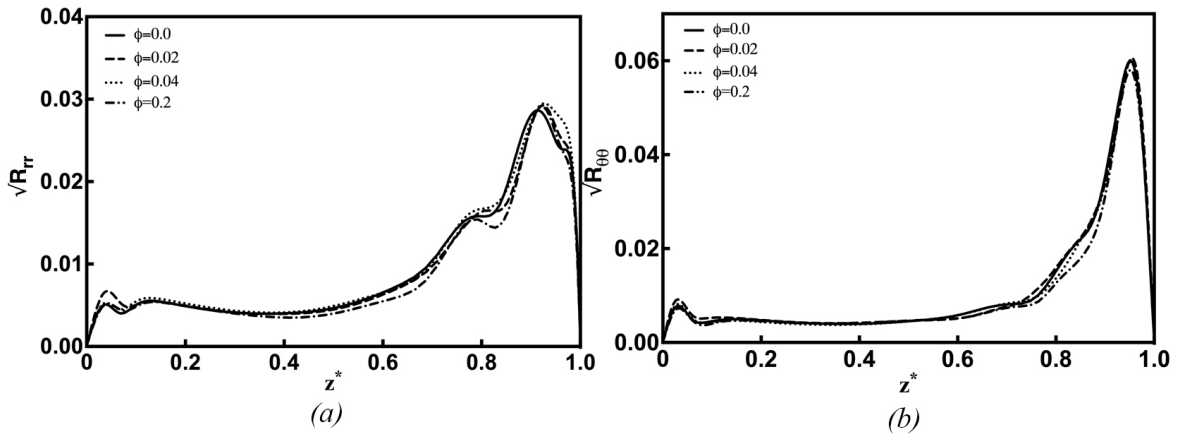

Fig. 6.7 A time-averaged axial profiles of turbulence intensity profiles for different nanoparticle volume fractions, $r^* = 0.50$, (a) radial turbulent intensities, (b) tangential intensities.

The time-averaged velocity and turbulence intensity distributions of the rotor-stator cavities have given evidence of the changes due to variations in nanoparticle volume fractions,

but in both cases, these changes are subtle (except Fig. 6.7(a)). Hence, they may not give significant contributions to the convective heat transfer process. These results suggest that the addition of nanoparticles to a base fluid has a less significant effect on momentum transport for rotor-stator applications, which is the primary motivation for using nanofluid in heat transfer applications instead of mixtures based on micro-sized particles. However, the current investigation only concerns Al_2O_3 nanoparticles, and the investigation of Turkyilmazoglu (2014) suggested that the other nanofluids based on nanoparticles, such as Cu, CuO, Ag, have more intense effects on momentum transport than the Al_2O_3 nanoparticles.

After discussing the momentum transport properties of rotor-stator cavities filled with Al_2O_3 based nanofluid, Fig. 6.8 describes the time-averaged axial profile of temperature at $r^* = 0.50$ under different volume fractions of nanoparticles. This shows that the test cases with higher volume fractions produce elevated temperature distributions, especially in the core region of the cavity. This initial result suggests that the rotor-stator cavities filled with the nanofluid may have superior heat transfer capabilities compared to conventional cavities filled with pure water.
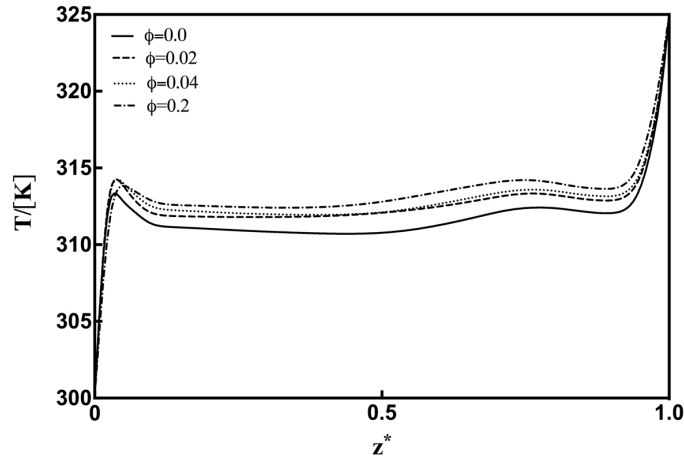
Fig. 6.8 A comparison of time-averaged temperature distributions for different nanoparticle volume fractions at $r^* = 0.50$.

6.3.2 Flow visualisation of rotor-stator cavities with nanofluid

This section aims to visualise the velocity and temperature distributions across axial and azimuthal planes through the rotor-stator cavities. Most of the contours presented in this section are instantaneous snapshots, which were taken at the last time step of the simulation. Usually, the velocity fields are normalised by the maximum disk velocity $U_{\theta,max} = r_2\omega$.

Figure 6.9 describes the normalised instantaneous axial velocity distributions in the r–z plane and they show a train of vortex structures initiated in the stator boundary. In rotor-stator cavities, fluid transfer between the rotor and stator boundary layers occur over the outer walls and the inner rotor hub of the cavity. The colder fluid flow in the rotor rises to higher z values, near the outer wall and hotter fluid near the stator is transported over the inner hub. This flow circulation process helps to accelerate the heat transfer between the two boundary layers of the cavity. The mean axial velocity profiles (not shown here) evidence that the velocity of the bulk fluid flows near the rotor hub and outer wall increases as the nanoparticle volume fraction increases.
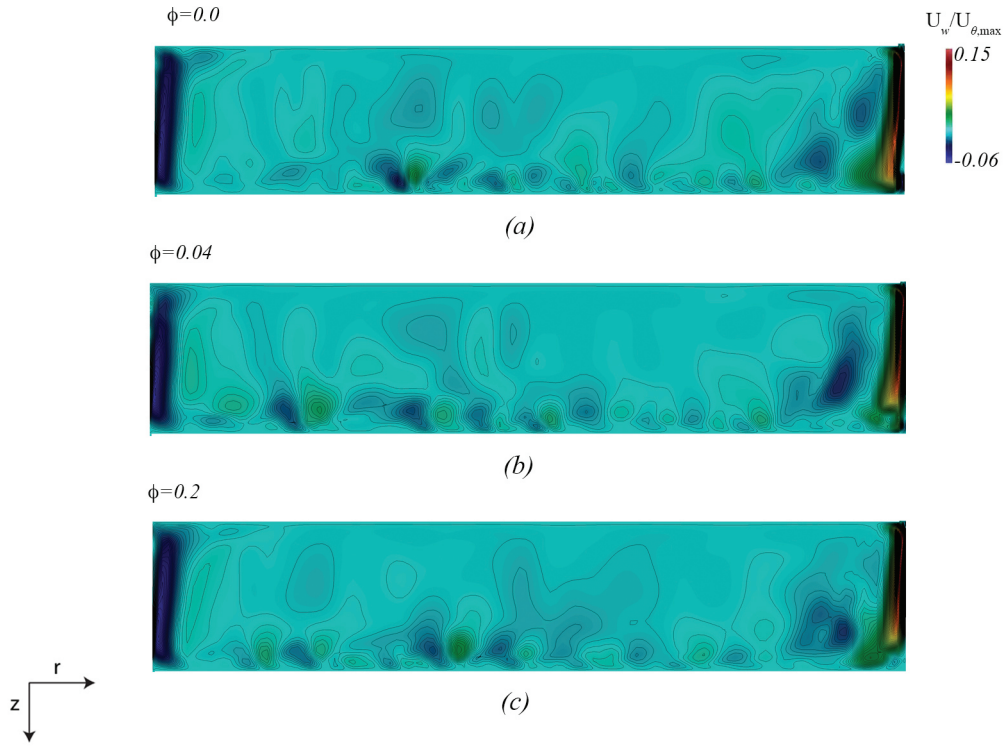
Fig. 6.9 Instantaneous normalised instantaneous axial velocity contours at the r–z plane, (a) $\phi = 0.0$, (b) $\phi = 0.04$,(c) $\phi = 0.2$.

For the sake of completeness, tangential velocity components at the rotor ($z^* = 0.025$) and stator ($z^* = 0.975$) boundaries for different volume fractions are shown in Fig. 6.11. As described in Section 6.3.1, higher volume fractions predicted to produce a marginal increase in the velocity components in the rotor boundary layer and a decrease in velocity in the stator boundary layer. Apart for nanofluid related effects, these boundary layers comply with the

typical behaviour of rotor-stator boundary layers at $Re_\omega = 1 \times 10^5$, in which rotor boundary layers are mostly laminar, while stator boundary layers show transient turbulent structures.
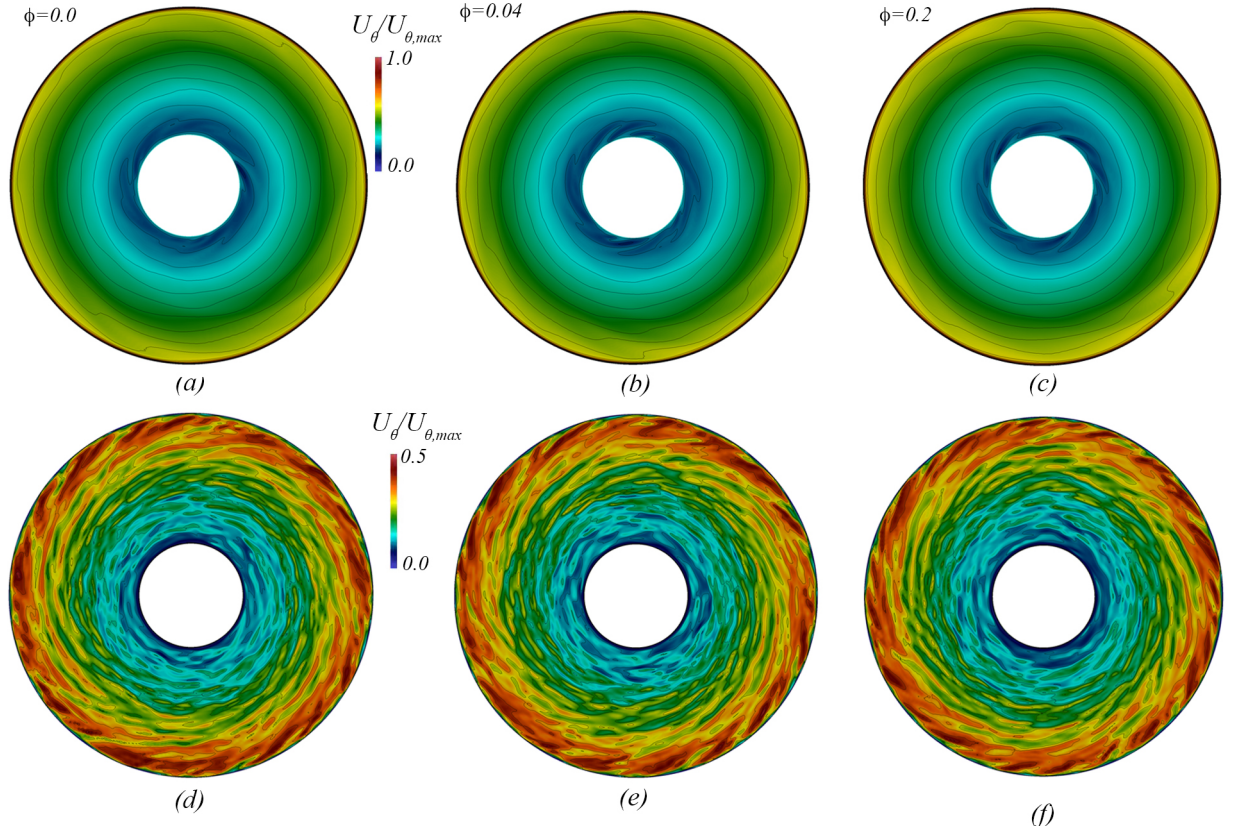

Fig. 6.10 Instantaneous tangential velocity contours at the rotor boundary, $z^* = 0.025$, (a) $\phi = 0.0$, (b) $\phi = 0.04$, (c) $\phi = 0.2$; at stator boundary, $z^* = 0.975$, (d) $\phi = 0.0$, (e) $\phi = 0.04$, (f) $\phi = 0.2$.

Figure 6.11 shows the temperature distributions at different volume fractions in the *r–z* plane. The central core region of the cavity has higher temperature values than the outer core region, in where heat distributes at a quicker rate due to the higher tangential velocity component and entrainment coefficients at these regions. As shown in the figures, the inner regions of the cavity consist the hot fluid streams that are flowing from the hot stator to the rotor side of the cavity, and this could be the main heat transport path between the stator and the rotor. The centrifugal motion of the rotating hub distributes hot fluid to the central regions of the cavity. The instantaneous temperature contours show that the cavities with higher nanoparticle volume fractions exhibit a greater spread in temperature distributions that featuring large-scale temperature extrusions near the rotor hub and stator.
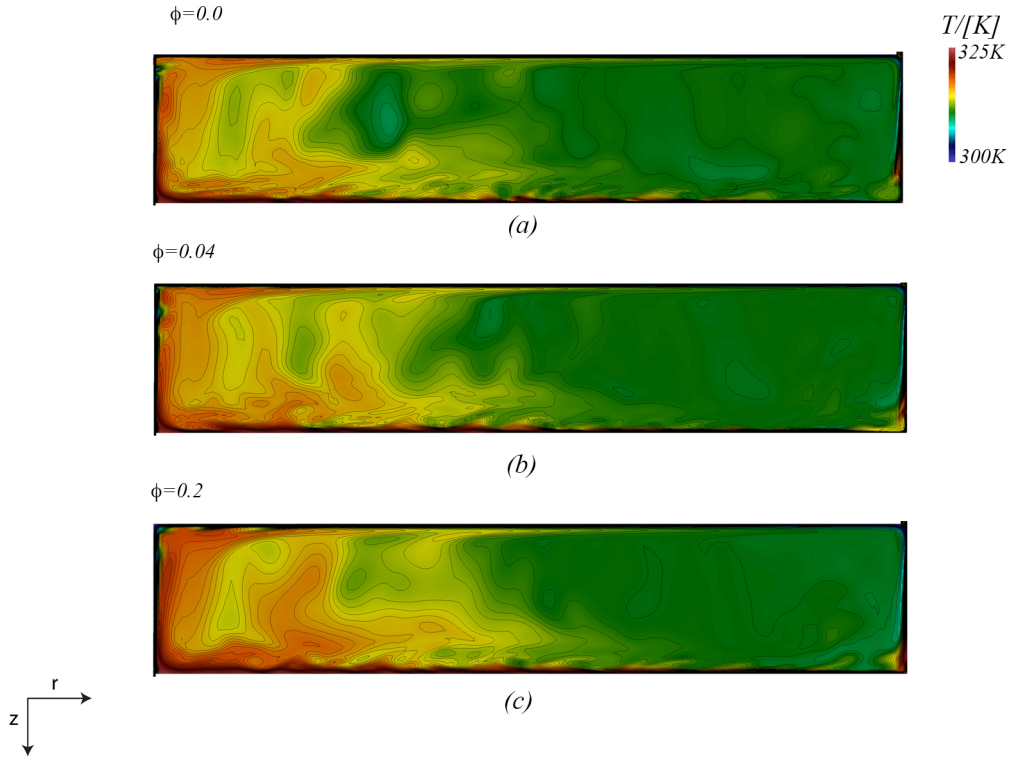
Fig. 6.11 Instantaneous temperature contours of S_P simulations at the r–z plane, (a) $\phi = 0.0$, (b) $\phi = 0.04$, (c) $\phi = 0.2$.

The axial plot temperature distributions over the rotor (leftmost column), mid-section (middle column) and stator (rightmost column) are shown in Fig. 6.12. These temperature contours show the role of rotor hub in funnelling of the temperature toward the outer regions of the cavity. At the rotor hub of the cavity, the coherent heat structures are located in the rotor and the mid-section contours, and the contours of the stator layer show more turbulent structures. Even though these structures are described as heat structures, they are indeed, the convective flow structures that were presented in Fig. 6.10. These structures play an important role in rotor-stator heat transfer by moving the hot fluid through the cavity. As explained before, increasing the volume fraction of nanoparticles has shown the greater spread of temperature distributions toward the central region of the cavity. However, increased nanoparticles concentrations cause a decrease in heat spread at the rotor (this is more visible in Fig. 6.12(g)) and a higher rate of bulk fluid flow along the rotor hub and outer walls could be the possible reason for this.
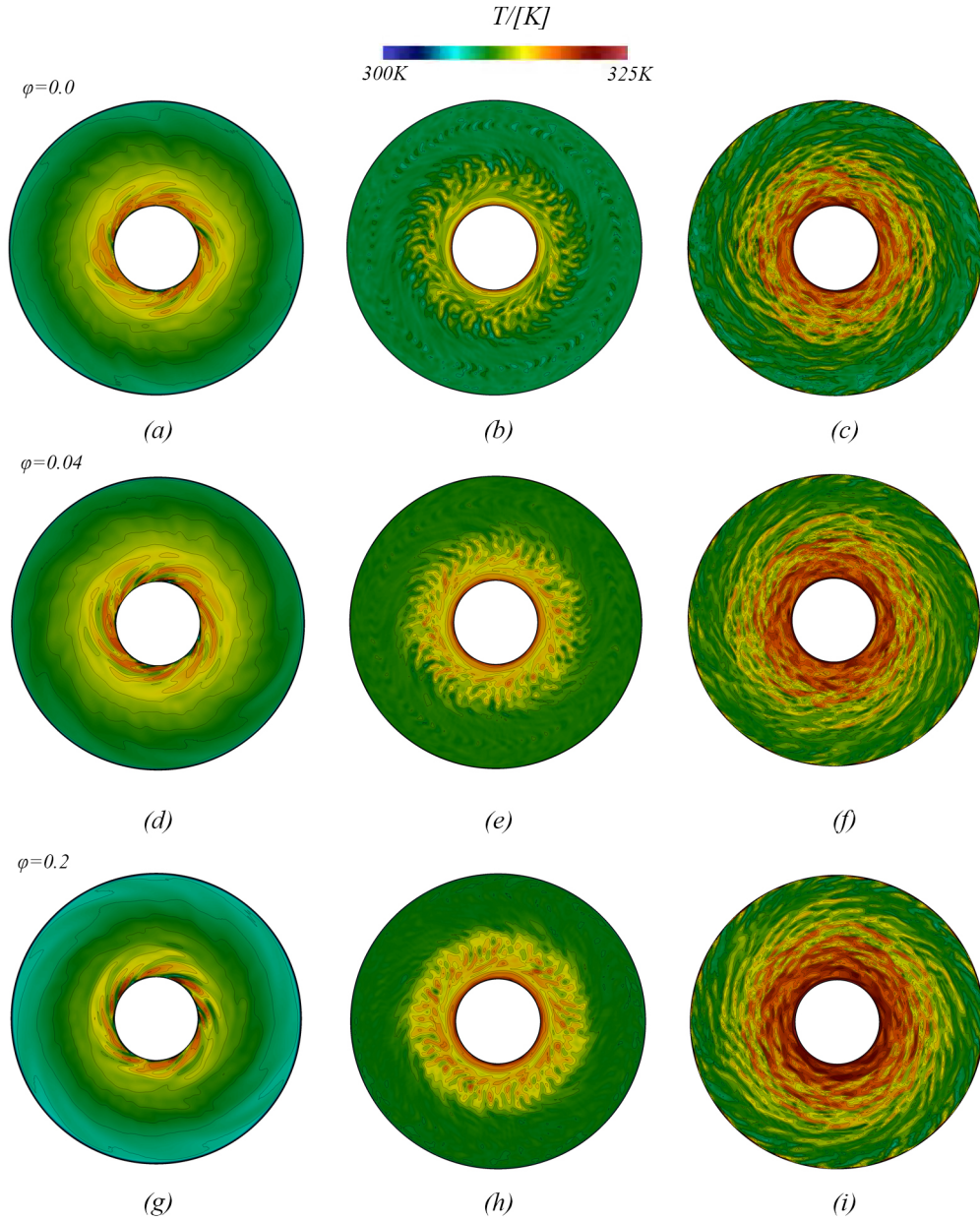
Fig. 6.12 Instantaneous temperature contours near the rotor boundary layer, (a) $\phi = 0.0$, (d) $\phi = 0.04$, (g) $\phi = 0.2$; at the mid-section, (b) $\phi = 0.0$, (e) $\phi = 0.04$, (h) $\phi = 0.2$; near the stator boundary layer, (c) $\phi = 0.0$, (f) $\phi = 0.04$, (i) $\phi = 0.2$.

Even though the nanofluid does not impose significant effects on the mean and turbulent structures of the rotor-stator cavities, their higher thermal conductivity may lead to a significant improvement in heat transfer rates.

6.3.3 Nanofluid heat transfer in rotor-stator cavities studied by a two-phase model

The main difference between S_P models and T_P models are that the latter may have a slip velocity between the nanoparticles and the base fluid, which results in different volume fractions inside the cavity, instead of time independent isotropic volume fraction. This may give different momentum and heat transfer characteristics with a T_P model that with a S_P model.

A set of T_P simulations starting from the same volume fractions of the S_P simulations were run. As shown in Figs. 6.2 & 6.3, there are just minor differences in the time-averaged velocity profiles and turbulence intensity profiles between the S_P and T_P simulations.

The time-averaged axial profiles of temperature at $r^* = 0.5$ in Fig. 6.13 show minor differences in the temperature distribution across the cavity, which indicates that the T_P modelling approach has slightly altered the underlying thermal transport mechanism of the rotor-stator cavity. The temperature distributions suggest that the T_P modelled flow has a lower core temperature compared to the S_P modelling approach, and at first glance, this suggests that the relative straight of thermophoresis forces overshadow the Brownian effects in heat transfer of rotor-stator cavities filled with a nanofluid. These facts motivate further investigation on to this matter.

Figure 6.14 shows the instantaneous temperature distributions in the r–z plane, and similarly to the S_P model predicts, the radial spread of the temperature increases with higher volume fractions.
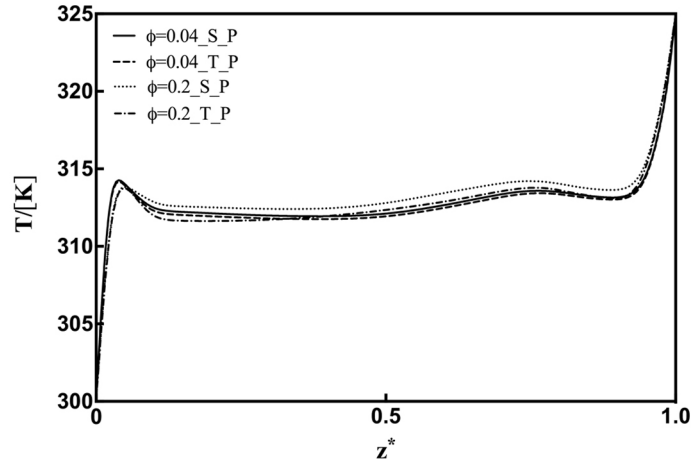
Fig. 6.13 A comparison of time-averaged temperature distributions in S_P and T_P simulation at $r^* = 0.50$.

The key difference between the S_P model and T_P models are that the latter allows nanoparticle slip velocity based on Brownian diffusion and thermophoresis effects, which results in non-uniform volume fraction distributions that are flow dependent. Figure 6.15 shows the instantaneous volume fraction distribution in the r–z plane for T_P model initialised by a uniform volume fraction of $\phi_{t0} = 0.2$ (this is denoted as inceptive volume fraction). The volume fraction distributions, which are obtained from the T_P model, are normalised by using the respective inceptive volume fraction value of the simulation to represent the distributions in terms of dimensionless volume fractions ($\alpha_n = \phi_{local}/\phi_{t0}$). These volume fraction contours show that the nanoparticles tend to aggregate just above the stator boundary layer and beside the rotor hub, where hot temperature occurs. The core region of the cavity is relatively unaffected, but other areas, which are occupied hot fluid, also have lower concentrations of nanoparticles. These observations suggest that the thermophoresis effects play a significant role in the heat transfer of rotor-stator cavities.
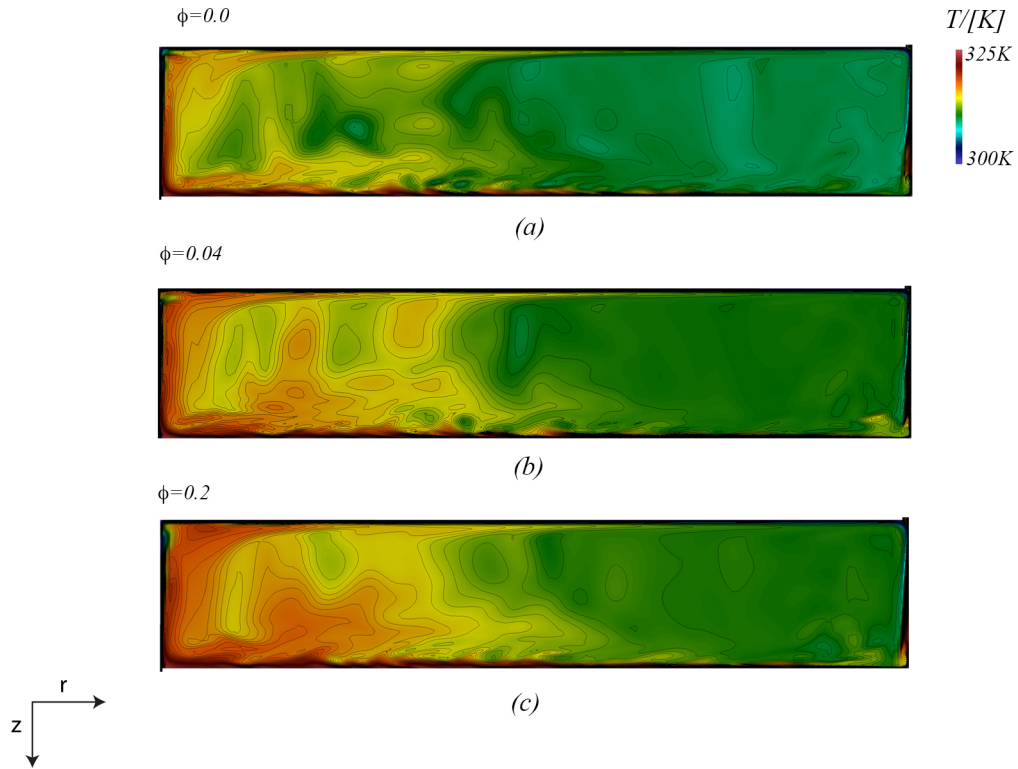
φ=0.0

(a)

φ=0.04

(b)

φ=0.2

(c)

T/[K]

325K

300K

Fig. 6.14 Instantaneous temperature contours of T_P simulations at the r–z plane, (a) $\phi = 0.0$, (b) $\phi = 0.04$, (c) $\phi = 0.2$.

α_n

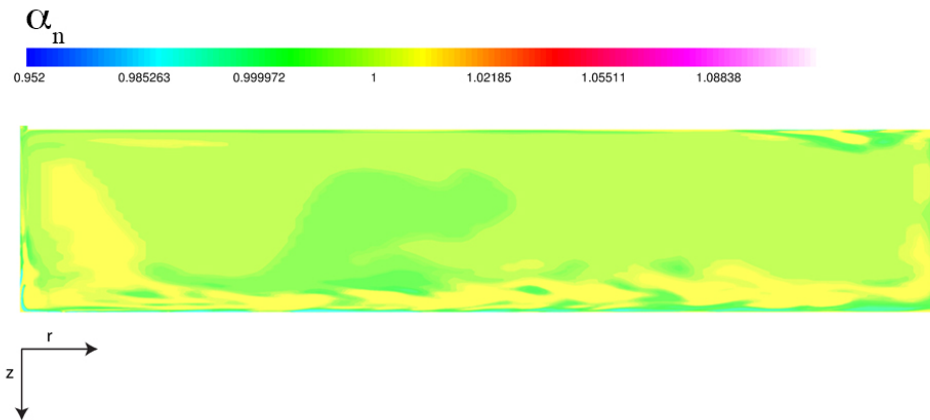0.952   0.985263   0.999972   1   1.02185   1.05511   1.08838

Fig. 6.15 Instantaneous normalised volume fraction (α_n) contours for a T_P simulation with $\phi_{t0} = 0.2$ at the r–z plane.

Figure 6.16 shows the instantaneous normalised volume fraction contour in the rotor and stator boundary layers. These contours are extracted from the laminar sublayer of the respective boundary layers. For both of these boundary layers, the areas with volume fraction below unity are marked by line contours. These contours evidence a higher concentration of nanoparticles on the rotor boundary layer (except for a very small area near the rotor hub) and a lower concentration of nanoparticles in the stator boundary layer. The axial outward displacement of the nanoparticles from the stator boundary layer is significant at higher radial positions, and the displaced nanoparticle fractions could result in the thick layer of nanoparticles above the outer region of the stator surface as shown in Fig. 6.15.

Figure 6.17 shows the instantaneous radial and axial profile of normalised volume fraction for the case of $\phi_{t0} = 0.2$ and all the profiles are averaged over the tangential direction. Figure 6.17(a) shows the variation of normalised volume fraction at the different radial positions. This suggests a higher nanoparticle concentration in the inner region of the rotor boundary layer and relatively low particle concentrations (but still higher than the uniform starting value of $\phi_{t0} = 0.2$) in the mid and outer region of the rotor boundary layer. The volume fractions in the core region of the cavity are nearly constant, $\alpha_n = 1$, and the stator boundary layer has lower nanoparticle concentrations of $\alpha_n < 1$ at the higher radial positions. Figure 6.17(b) further confirms the variations which have described above, and this suggests higher nanoparticle concentrations, $\alpha_n > 1$, in both rotor and stator boundary layers at radial locations lower than $r^* < 0.47$.

The above description suggests that the T_P simulations reported a reduction in nanoparticles volume fractions at the hot stator due to the thermophoresis effects and this could be a plausible reason for slightly lower mean temperature profiles for T_P models. The next section will attempt to obtain dimensionless instantaneous and mean heat transfer coefficients for both S_P and T_P model, which can provide a quantitative assessment on each case of S_P and T_P models.
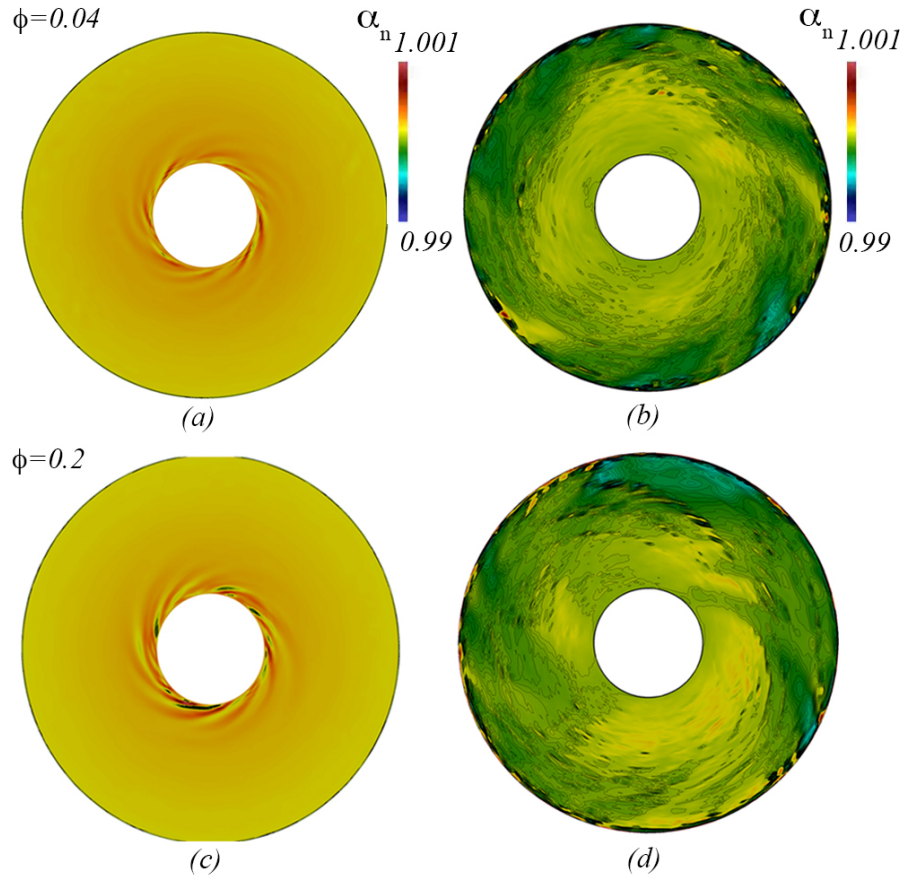
$\phi=0.04$

$\phi=0.2$

Fig. 6.16 Instantaneous normalised volume fraction contours for the T_P simulations at the rotor boundary layer (a) $\phi_{t0} = 0.04$, (c) $\phi_{t0} = 0.2$; stator boundary layer, (b) $\phi_{t0} = 0.04$, (d) $\phi_{t0} = 0.2$.
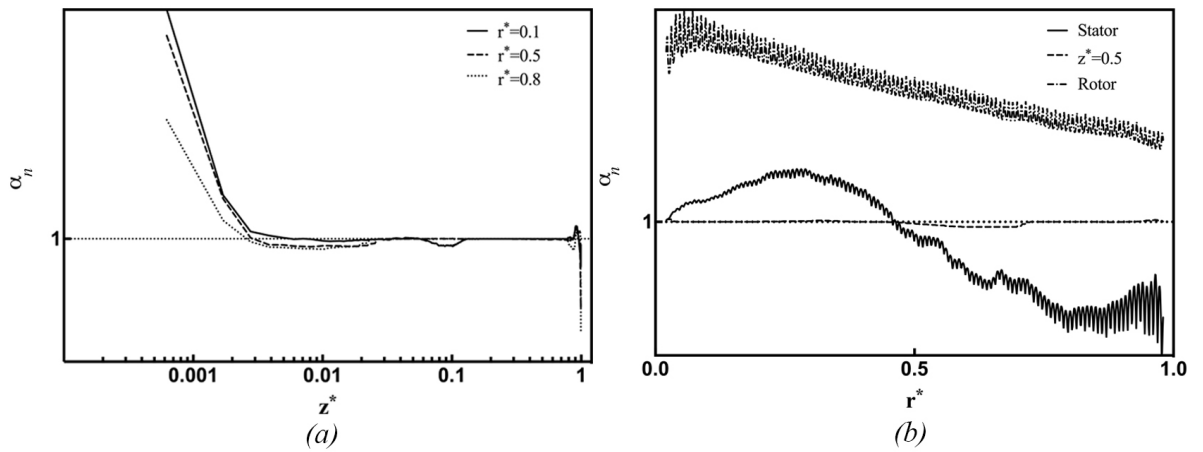

Fig. 6.17 Volume fraction distributions for $\phi_{t0} = 0.2$, (a) axial distributions at different radial positions, (b) radial distributions at the rotor boundary layer.

6.3.4 Nanofluid heat transfer coefficients in rotor-stator cavities

Nusselt numbers is a dimensionless parameter which is very important in heat transfer applications. It is often considered as a performance parameter to describe the effectiveness of the heat transfer process. In the current application, the local Nusselt number considers as a function of the local radius of the disk, and this is an indication of the overall convective heat transfer rate of a particular configuration. The previous investigations of Nikitenko (1963), Pellé and Harmand (2007) and Tuliszka-Sznitko et al. (2009*b*) studied the behaviour of the local Nusselt number in various rotor-stator flow configurations. In those investigations, they experienced a high dependency of the local Nusselt numbers with the local Reynolds numbers, which show that the local Nusselt number is sensitive to the local flow structures. For the rotor-stator flows, the local Nusselt number can be evaluated as

$$Nu_r = \frac{h_T r}{k_f},\qquad(6.6)$$

where, h_T, r and k_f represent the convective heat transfer coefficient, the local radius and the thermal conductivity of the fluid, respectively. Figure 6.18 shows the local Nusselt number distributions for both S_P and T_P simulations and they are evaluated at the stator boundary layer, which is the heat source of the current simulations. As shown in the mean temperature distributions of Fig. 6.13, the local Nusselt number increases as the volume fraction increases. However, at a given radial position, the local Nusselt number of each S_P simulation is marginally higher than their T_P counterparts, which can be explained by considering the displacement of nanoparticles due to the thermophoresis effects near the hot stator boundary layer. The correlation of local Nusselt number with the local radius of the disk (or Re_ω) can be described by the generalised model purposed by Nikitenko (1963) and it reads as

$$Nu_r = aRe^b_{\omega,local},\qquad(6.7)$$

where a and b are multiplicative and exponential constants respectively, and for the turbulent flow Nikitenko (1963) predicts the values $a = 0.0178$ and $b = 0.8$.

Table 6.2 shows the fitted values of a and b for the Nusselt number distributions shown above. As the nanoparticle volume fraction increases, the multiplicative constant decreases (for the T_P model a constant monotonically decreases), whereas the exponential constant b monotonically increases for both S_P and T_P models. Close observation of these constants suggests that at small radial positions (or $Re_{\omega,local}$) the Nu_r of pure water is greater than the Nu_r of nanofluid, which means the heat transfer rate of the pure water is higher than the nanofluid. Specifically, with nanofluid of volume fractions $\phi = 0.2$, Nu_r of pure water greater
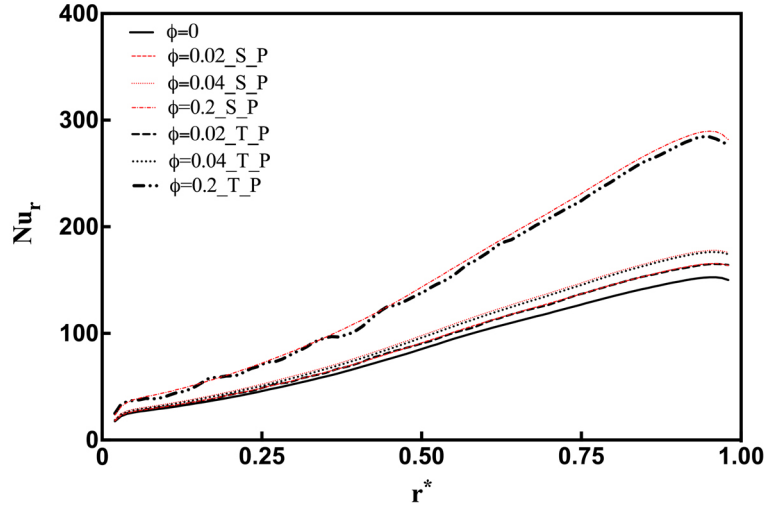
Fig. 6.18 A comparison of local Nusselt number distributions for S_P and T_P simulations at the stator boundary layer.

than the Nu_r of nanofluid at the local Reynolds numbers of $Re_{\omega,local} < 1000$. Similarly, the corresponding constant values for S_P and T_P models suggest that the heat transfer coefficients of T_P simulation should higher than its S_P counterpart at higher radial values. By considering the constant value initial volume fraction $\phi_{t0} = 0.2$, this occurs approximately the local Reynolds number of $Re_{\omega,local} = 3 \times 10^6$. According to the arguments made in Section 6.3.3, at higher local Reynolds numbers, nanoparticle displacement may be more significant, which results further decrease in heat transfer rates. Hence, the calculated values for these constants are only admissible for the considered Reynolds numbers region of $8 \times 10^4 < Re_{\omega,local} < 1 \times 10^5$.

The fourth column of Table 6.2 represents the mean Nusselt numbers of the stator,

$$\overline{Nu} = \frac{\int_{r_1}^{r_2} Nu_r 2\pi r \, dr}{\pi(r_2^2 - r_1^2)},$$

calculated based on the local Nusselt number distributions. Here, r_1 and r_2 are the inner radius and the outer radius of the cavity as shown in Fig. 6.1. The S_P and T_P simulations with the nanoparticle (inceptive) volume fractions of $\phi = 0.2$ show over 70% increase when them compared to the base simulation of $\phi_{t0} = 0$. In this case, the mean Nusselt number of the S_P simulation is about 4% higher than the similar T_P simulation. This observation agrees with the previous explanation about the thermophoresis effects on the nanoparticles near

ϕ	a	b	$\overline{Nu}$
0.0	0.0158	0.807	87.19
0.02 (S_P)	0.0144	0.822	93.25
0.02 (T_P)	0.0142	0.823	92.92
0.04 (S_P)	0.0155	0.822	100.23
0.04 T_P)	0.0132	0.834	98.54
0.2 (S_P)	0.0071	0.932	152.49
0.2 (T_P)	0.0063	0.940	148.57

Table 6.2 The fitted constant values of a and b for the model Eq. (6.7) and the mean Nusselt numbers $\overline{Nu}$.

a hot surface. However, the disparity between the S_P and the T_P simulations reduce as the nanoparticle volume fraction decreases.

6.4   Summary and conclusions

This chapter focused on the development and implementation of numerical models to evaluate rotor-stator cavities filled with a nanofluid. Two types of numerical models were used the S_P model and the T_P model. The first model is a single-phase transport model, in which the nanoparticle phase fraction is assumed constant throughout the simulation time. The second model allows for a slip velocity between the nanoparticles and the carrier phase, in which the Brownian diffusion and thermophoresis effects are considered to be the main cause of these slip velocities. The two models used Al_2O_3 nanoparticles with $t = 0$ volume fractions $\phi_{t0} = 0.02, 0.04, 0.2$, and in all the simulations, the operational Reynolds number is $Re_\omega = 1 \times 10^5$. The outcomes were compared to a pilot simulation with pure water in which a very small nanoparticle volume fraction of $\phi \approx 2 \times 10^{-5}$ was used for numerical stability purpose.

The velocity fields are very similar between the S_P and T_P models and time-averaged radial, tangential and axial velocity components of the rotor boundary layer tend to increase with higher nanoparticle concentrations. Similar observations have been made for the stator boundary layer, except the time-averaged tangential velocity components tend to decrease with higher nanoparticle volume fractions. In the current simulations, both radial and tangential turbulence intensities decreased under higher nanoparticle volume fractions. However, results show that the effects of nanoparticles on momentum transport are subtle.

Hence there would be no significant improvements in convective heat transport rates solely because of nanoparticle volume fractions.

Nevertheless, there were elevations in instantaneous and mean temperature in the cases with higher nanoparticle volume fractions. This is primarily because of the higher thermal conductivities of nanofluids. However, close observation on both S_P and T_P simulations showed that the S_P simulations have slightly elevated temperature distributions compared to their T_P counterparts. This can be explained by the displacement of the nanoparticles at the hot stator boundary, at which the thermophoresis forces are significant. This concludes that the thermophoresis forces are dominant over the Brownian forces. The local Nusselt number distributions have obtained for all the cases at the stator boundary, and they were compared with Nikitenko (1963)'s Nusselt number model described in Eq. (6.7). Further, the mean Nusselt numbers at the stator show up to 70% increase due to nanofluid.

Chapter 7

Simulation of particle dynamics inside a rotating chemical vapour deposition chamber

7.1 Introduction

This chapter is devoted to the application of the Lagrangian particles methods to evaluate the particle dynamics and deposition in a Rotating Chemical Vapour Deposition (RCVD) chamber, which is an interesting method that facilitates the forming of uniform film layers over a substrate. The method is widespread in the semiconductor manufacturing industry but even a small trace of particle contaminations inside the chamber could impact the purity of the film, which may cause a significant impact on the quality and usability of the end products.

The Lagrangian methods are capable of tracking individual particles inside the chamber but this may impose a high computational burden on a two-phase particle fluid simulation model if the particle phase consists of small particles (i.e. micro and nanoscale particles) in high volume fraction. Nevertheless, if the particle volume fractions are sufficiently small, the Lagrangian methods have a distinct advantage over Eulerian methods as they can track the path of each particle, which gives a profound understanding of particle dynamics in a fluid.

This section considers a trace of particles ($\alpha_p < 10^{-6}$), and in previous literature, the most of the contamination particles were found to be in micron and submicron scales (Otani et al., 1989; Pui et al., 1990; Gakis et al., 2015; Lee and Yook, 2015). The current study conducts a series of simulations to elaborate the dynamics and depositions of these particles near the stationary and rotating disks in a CVD chamber. As described in Section 2.6, the

Lagrangian particle tracking method (see Eqs. (2.18) & (2.19)) are combined with Lagrangian submodels to impose different forces and effects, such as turbulence of the carrier phase, the thermophoretic force, on the particles. The outcomes of this model are compared with the previous investigation of Chein and Su (2004), who conducted laminar axisymmetric simulations. The current investigation relaxes the laminar and axisymmetric flow assumptions by conducting the simulations under the fully three-dimensional and turbulent flow conditions. Further, the similarities and differences with previous literature are highlighted.

7.2 Problem definition

7.2.1 Geometric modelling

The geometrical model of the CVD chamber is shown in Fig. 7.1, and here, a simplified geometrical model is assumed by neglecting the central supporting shaft of the disk. The dimensions of the geometry are also proportional to Chein and Su (2004)'s investigation, but the present model is fully three dimensional compared to the original axisymmetric configuration. The inlet diameter is $2l$ and the outlet dimensions are identical to inlet dimensions. The diameter and thickness of the disk are $6l$ and $0.5l$ respectively. The disk is in the centre of the chamber. The height of the chamber section is $8l$ and its diameter is $10l$, to allow sufficient clearance between the disk and sidewall of the chamber.

7.2.2 Governing equations

Even though the flow is in a low Mach number region, a solver based on conservative form of the governing equations (i.e. Eqs. 3.2 (a) & (b) defined in Section 3.3) has been used to evaluate the carrier phase flow fields due to significantly high-temperature gradients, where the buoyancy effects may cause additional complexities in the flow field. Equations (3.5) is the energy equation, and all the governing equations are discretised using the FVM methods, which were described in Section 3.4.

All turbulent contributions from momentum and energy are evaluated using the RANS model, standard k-ε , which has described in Section 3.5.1.1. The size of the time step (Δt) is selected according to the $Co_{max} \leq 0.5$. In the current simulation model, a one-way coupling is assumed (see Section 2.6.7) between the continuum phase and the discrete phase. This assumption is valid for suspensions of small particles in low volume fractions ($\alpha_p < 10^{-6}$) and the interphase momentum and energy coupling terms have not been added to the momentum and energy equations.
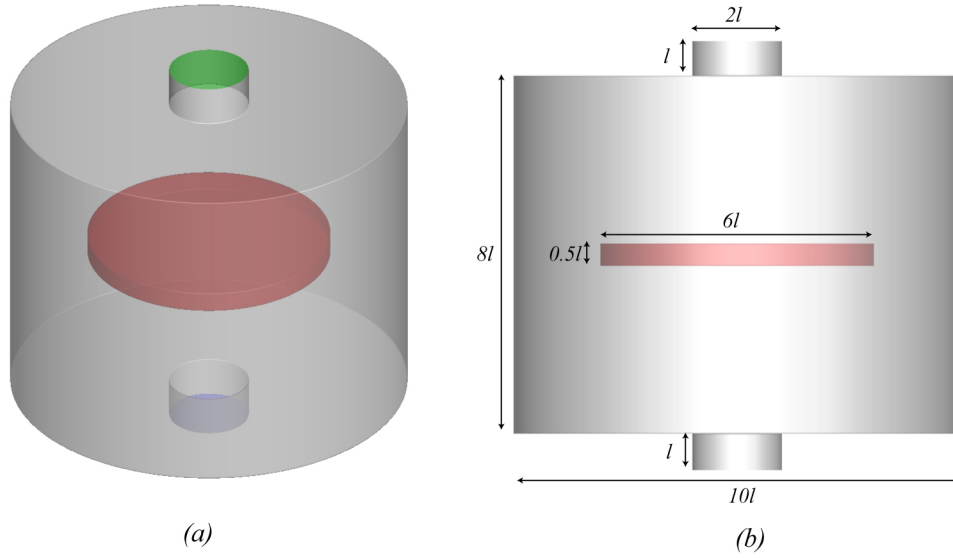
Fig. 7.1 Geometry of the CVD, (a) Isometric view of the geometry, (b) Side view of the geometry.

Hexahedral elements were used to discretise the computational domain into a finite number of volumes, and the finite distribution of volumes is shown in Fig. 7.2.
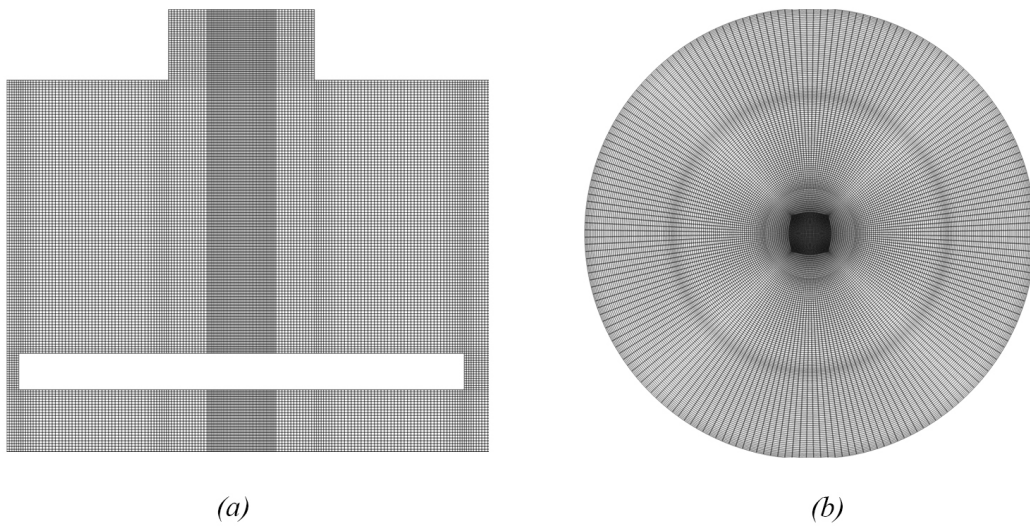

Fig. 7.2 Mesh of the CVD, (a) side view of the geometry, (b) top view of the mesh

144

7.2.3 Boundary and operational conditions

The inlet velocity profile is assumed and it is taken as the one-seventh power law profile (Prandtl, 1961, vol. II), which is a turbulent velocity profile assumed inside circular pipe flows (White, 1991). The expression for the one-seventh velocity profile can be taken as

$$u(R_r) = u_{max}\left[1 - \left(\frac{R_r}{R_2}\right)^{\frac{1}{7}}\right],\tag{7.1}$$

where R_r and R_2 are local radial location of the pipe plane and the radius of the pipe. Here, u_{max} is the centre line velocity and in current case, it is set to 1.0 ms^{-1}. The inlet Reynolds number is defined as the $Re_{in} = (2\rho u_{avg} R_2)/\mu$ for a circular pipe and the $u_{avg} = \frac{2n^2 u_{max}}{(n+1)(2n+1)}$ can be taken for the power law velocity profiles. The current case sets $n = 7$ to obtain the average velocity of the one-seventh power velocity profile and this gives the inlet Reynolds number $Re_{in} \approx 1550$. The no-slip boundary conditions are set to all the walls, and the rotating disk is based on rotating Reynolds number ($Re_{\omega} = (\rho \omega r_2^2)/\mu \approx 6 \times 10^4$).

Thermal boundary conditions are required to solve the energy equations, and for simplicity, the parameter $\Delta T = (T_{hot} - T_{cold})$ is defined to describe cases with different thermal boundary conditions. The T_{cold} and T_{hot} values are described in Table 7.1.

$T_{cold}/[\text{K}]$	300	300	300
$T_{hot}/[\text{K}]$	500	800	1200

Table 7.1 Thermal boundary conditions.

The current investigation considers two scenarios, T_{cold} = inlet, T_{hot} = disk and T_{cold} = disk, T_{hot} = inlet, where the former case defines positive ΔT values and latter defines the negative ΔT values on the CVD problem.

Inlet boundary conditions for the k and ε are set based on the turbulence intensity ($I = \frac{u_{rms}}{\bar{u}}$) at the inlet. Here, the turbulence intensity is taken as 4% from the average velocity (u_{avg}) and the fields, k and ε, are calculated as $k = \frac{3}{2}(u_{avg} I)^2$ and $\varepsilon = C_{\mu}^{3/4} k^{3/2}/l_t$, where $C_{\mu} = 0.09$ and $l_t = 0.42$ and k and ε set uniform across the inlet. Throughout this chapter, k and ε denotes the total turbulent kinetic energy and turbulent dissipation of the flow field, respectively and spatial and temporal variations of these fields can be obtained by solving Eqs (3.24) & (3.25). All the walls are treated with standard wall functions, which damp the turbulent components at the near wall areas.

The outlet pressure value set to atmospheric pressure (1×10^5 pa), which is also considered as the operating pressure of these simulations and all other outlet boundary conditions

are set to zero-gradient conditions ($\nabla \psi = 0$). The air is considered as the working fluid of the system, and the values $c_p = 1000$ J/kgK and $\mu = 1.8 \times 10^{-5}$ kg/ms are taken as the specific heat capacity at constant pressure and the dynamics viscosity respectively. To calculate effective thermal diffusivity (α_{eff}), turbulent Prandtl number (Pr_{tur}) is assumed as 1.0.

The dispersed particles are Silicon particles and these particles are assumed to be hard-spherical particles with density (ρ_d) 2330 kg/m^3. Particle injections are mostly done at the inlet boundary of the chamber using either patch injection or manual injections methods. The initial injection velocity always set to the local fluid velocity at the inlet.

7.3   Results and discussion

Two simulations are conducted with a rotating and stationary chemical vapour deposition chambers (hereafter, these denote as RCVD and SCVD), respectively. The following sections describe the carrier phase velocity and temperature fields for SCVD and RCVD cases followed by LPT simulation results.

7.3.1   Carrier phase flow and temperature patterns

Figure 7.3 shows axial and radial instantaneous velocity contours for stationary and rotating disk scenarios. In both cases, the flow enters through a sudden expansion section and it impinges on the disk, before leaving through a sudden contraction section at the bottom part of the chamber.

In the stationary disk simulations, the two recirculation zones appeared at the outer periphery and top of the disk. This observation agrees with the streamline patterns that were presented in Chein and Su (2004). However, there is another recirculation zone appearing below the disk, which may be a result of the relatively high inlet Reynolds number Re_{in} used in the current simulation. In the case with the rotating disk, the rotation severely affects the recirculation zones. Both circulation zones, which are near the disk periphery and at below the disk, elongate toward radial flow. Similar behaviours are shown in radial velocity contours of stationary and rotating disks. Further, Fig. 7.4 presents the vector plots of the instantaneous velocity fields in the stationary and rotating disks and these plots also confirm the existence of the circulations zones. By looking at the vector plots, the recirculation zones are more pronounced in the stationary disk case compared to the rotating disk, and the reason could be the strong three-dimensional behaviour of velocity fields of the rotating disk CVD. In von Kármán single rotation disk flows, there is an inward axial suction toward the disk

surface due to the disk rotation and this could initiate a reverse flow at the outlet of the chamber, but the current simulations do not show any sign of a reverse flow at the outlet.
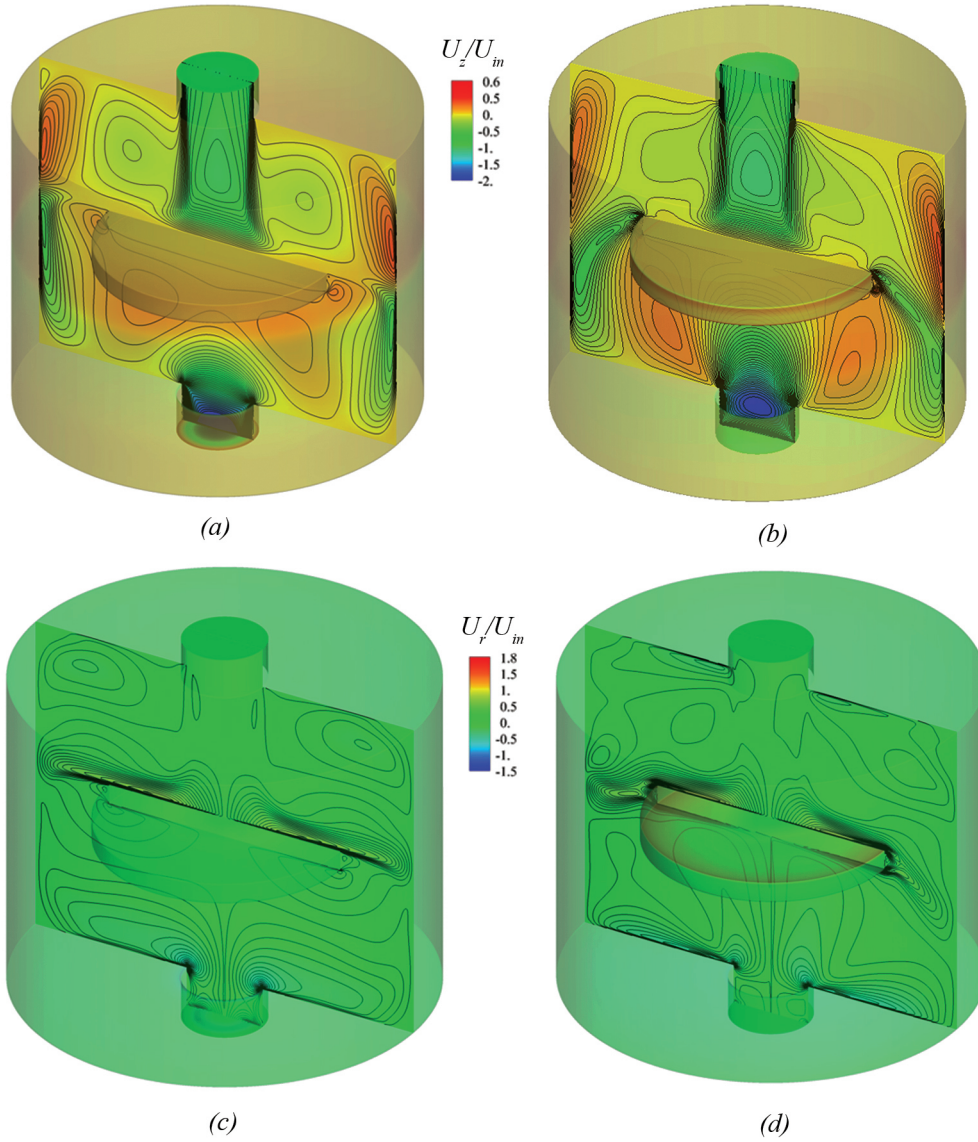

Fig. 7.3 Contours of instantaneous velocity components, (a) SCVD, axial velocity, (b) RCVD, axial velocity, (c) SCVD, radial velocity, (d) RCVD, radial velocity.

(a)   *(b)*

Fig. 7.4 Instantaneous velocity vector plot at $\Delta T = 200$ K, (a) SCVD, (b) RCVD.

Figure 7.5 shows the temperature distributions of the stationary and rotating disks for two isothermal disk temperature values of $T_2 = 500$ K, 1200 K, and in all the cases, the inlet air temperature is kept constant to $T_1 = 300$ K. In these cases, the corresponding ΔT values are 200 K, 900 K, respectively. Heat transfer in the stationary disk takes place by the diffusion and convection of the inlet gas flow, but the rotating disk adds an extra convective pumping due to the rotation of the disk. Hence, the RCVD is predicted to have an improved heat distribution across the top and the bottom portions of the disk, when it compares to the SCVD.

Figure 7.6 shows the fluid particle streamlines, which originate from the inlet of the CVD and these streamlines are generated using the carrier phase velocity fields. The streamline patterns evidence that the SCVD flow field is axisymmetric, whereas the corresponding streamlines for RCVD indicate a three-dimensional flow. This fact encourages to perform three-dimensional Eulerian-Lagrangian simulations to observe the dynamics and deposition of particles. The next section will discuss the results related to the particle tracking and depositions over the previously described carrier phase flow field.
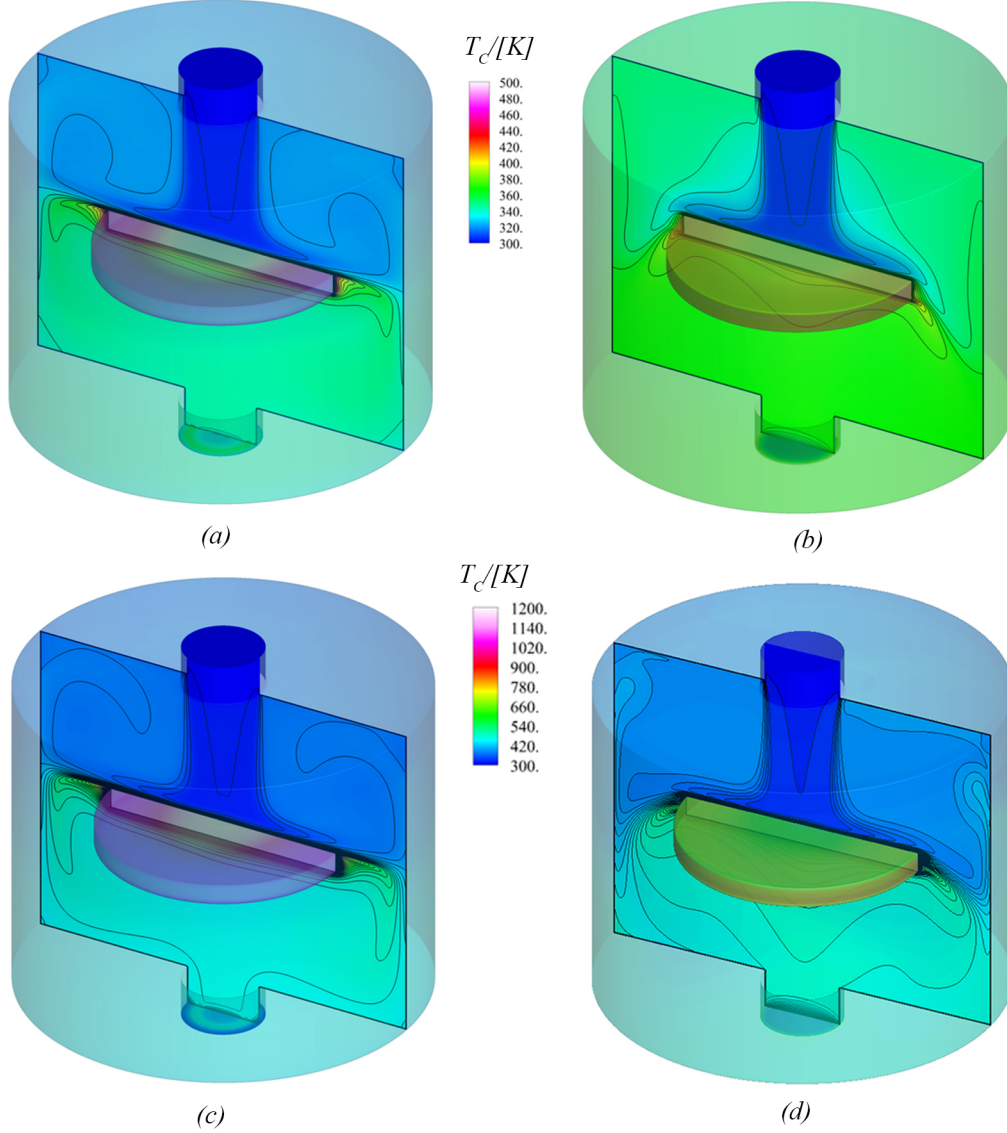
Fig. 7.5 Instantaneous Temperature Contours, (a) SCVD, $\Delta T = 200$ K, (b) RCVD, $\Delta T = 200$ K, (c) SCVD, $\Delta T = 900$ K, (d) RCVD, $\Delta T = 900$ K.

7.3.2 Particle phase dynamics and deposition

Lagrangian particle tracking (LPT) simulations were conducted for the test cases described in the Section 7.3.1. In each test case, 20,000 particles were injected within the first second of the simulation, and their behaviours, trajectories and deposition were observed throughout the entire simulation time, which is 40 seconds for the current study. By default, particle size distributions are selected as uniform particles in micron and submicron sizes with the diameters of 1 μm, 0.1 μm, 0.01 μm. In this section, the default forces, which are commonly

induced by particle motion, are used in LPT, and they are

$$\sum \boldsymbol{F}_{default} = \boldsymbol{F}_D + \boldsymbol{F}_L + \boldsymbol{F}_B + \boldsymbol{F}_G, \tag{7.2}$$

where $\boldsymbol{F}_D, \boldsymbol{F}_L, \boldsymbol{F}_B$ and $\boldsymbol{F}_G$ are the drag force, the lift force, the Brownian force, and the gravitational force, respectively. The thermophoretic forces are deferred to the next section. Apart from these forces, the particle turbulent dispersion effect, which was described in Section 2.6.5, is also added to the simulations. The set of simulations assumes that the rotor act as a perfect sink of particles. Unless otherwise mentioned, all the particle tracks, which are shown in this section correspond to $\Delta T = 200$ K.

(a)   *(b)*

(c)   *(d)*
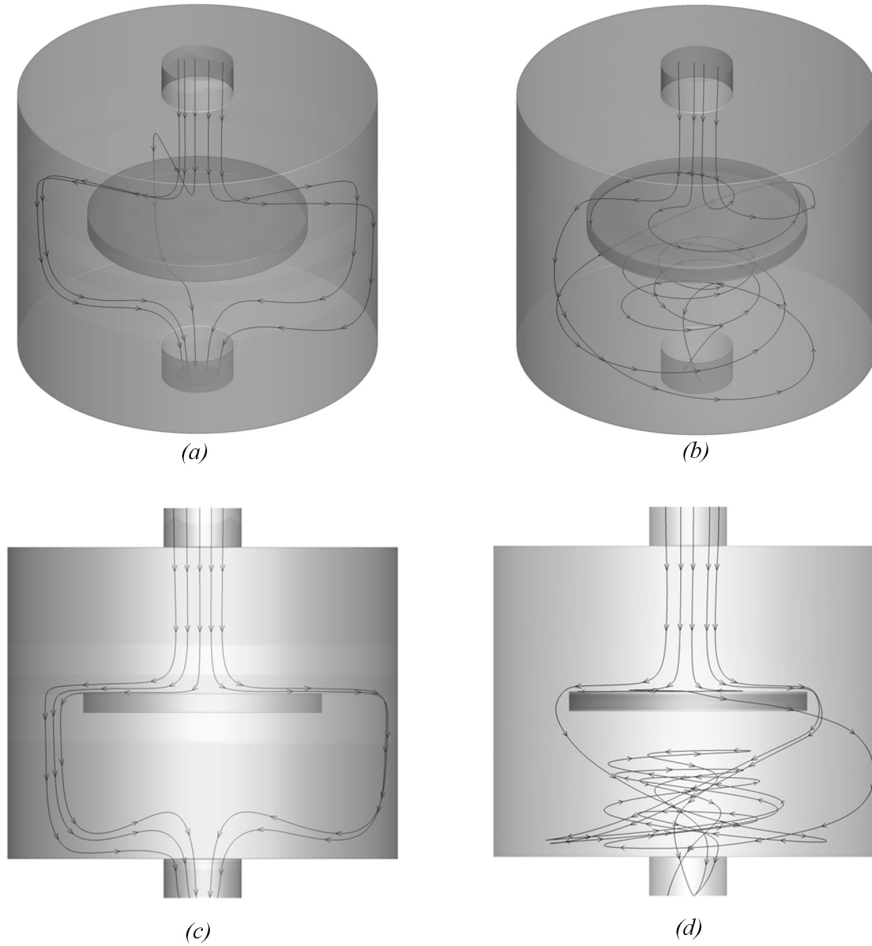
Fig. 7.6 Instantaneous streamlines at $\Delta T = 200$ K, (a) & (c) for SCVD, (b) & (d) for RCVD.

Figure 7.7 shows Lagrangian particle tracks for both SCVD and RCVD for different particle sizes. For the small particles, the particle tracks in the SCVDs tend to be axisymmetric (see Figs. 7.7(c) & (e)). Whereas, large particles are more likely to depart from the carrier

streamlines (see Fig. 7.7(a)). Due to the low Stokes number, small particles follow mean carrier flow more than the large particles. In both cases, either the particle is deposited, or it is swept into the circulation zones. Unlike in axisymmetric simulations, the particles that escape from top circulation zone are more likely to enter into the bottom circulation zone, but some particles are directly escaping to the outlet through the walls of the chamber. The particle tracks in the RCVD simulations are affected by the rotating motion of the disk and particles are usually driven by the centrifugal outflow of the disk. In these cases, the particles either deposit or circulate several times before escaping from the outlet.

Observing the particle track is a useful method to understand the behaviour of the particles in the flow field but this may not give the bulk transport features of the particles. Increasing the number of particles is a solution but in practise, this can quickly decline the readability of the particle tracking plots. The cell interpolation of Lagrangian properties provides a viable solution to this problem. The particle probability density (p_t) at a given time $t = t$ in a computational cell can be estimated by

$$p_t = \frac{c_i}{V_{Pi} \sum_{j=0}^{j=N_D} w_j},$$
(7.3)

where
c_i = Number of interactions of particles with the cell i until $t = t$.
V_{Pi} = Volume of the cell i.
w_i = Number of interactions of particles with the cell j until $t = t$.
N_D = Number of total cells at the computational domain.

By combining the p_t values of all the cells in the domain, the probability density contours of p_t can be constructed. For a typical LPT simulation, the p_t values vary between 0 and 10^5. Hence, the values of the contour plots were limited to the range 0 and 10^5, which are the lower limit and the upper limit of p_t. Then, normalisation is done by dividing the entire p_t field by 10^5, which can remove the volumetric dimension of Eq. (7.3). A better contrast of contour plots can be obtained by using decadic logarithmic values of normalised probability density p_t^* values $\left(log_{10}(p_t^*)\right)$ and the cells with zero p_t^* values were removed from the calculation as they cause singularities. The previous calculations confined the $log_{10}(p_t^*)$ values between -5 and 0 and these are the new lower and upper limits of the contours. These limits are labelled as "Low" and "High", which are more intuitive when reading the particle probability density contours. All the results presented here are obtained for $t = 40$ s. For the sake of brevity, p_{40}^* is simply represented as p^*. The mean disperse phase velocity vectors

151

are obtained similar to Eq. (7.3), but here, instead of the number of interactions, the particle velocity components are considered in the cell centres.

Figure 7.8 shows the probability density contours of particles with their mean dispersed phase velocity vector, which is an approximate continuous representation of the dispersed phase particle trajectories. The probability density is based on 20,000 particles inside the CVD. In these plots, low probability represents the leftmost ("Low") colours of the legend bar, and high probability density gets rightmost ("High") colours. The high probability density of the particles in a planar surface indicates that the majority of particles are moving in that plane or the particles have high resident time in that particular plane. For identical particle injection conditions for the SCVD and RCVD cases, the SCVDs obtain higher values for the probability density in a plane surface, as shown in Fig. 7.8(a). This indicates that the particle tracks of the SCVDs are planar for both top and bottom portions of the disk. The top part of the RCVDs are planar (see Fig. 7.8(b)) but the rotation motion of the disk more influences the bottom part of the chamber, at which particles may tend to follow non-planar tracks inside the chamber. Further, this observation has also appeared in the particle track plots of Fig. 7.7.

A performance metric, deposition efficiency $(DE\%)$, is defined as the percentage of particles that are deposited on the rotor surface and it given by

$$DE\% = \frac{\text{Number of particles deposited}}{\text{Total particles injected}} \times 100. \tag{7.4}$$

Figure 7.9 shows deposition efficiency for SCVD and RCVD for different particle sizes and the breakdown of contributions from each section of the disk to the total particle deposition. Here, the deposition efficiency does not primarily depend on the particle size but rotation effects add significant improvements to the particle deposition efficiencies. In both cases, the top surface of the disk attracts a high portion of deposited particles, which is anticipated because of direct interaction with the inflow particle stream and the strong upper circulation zone.
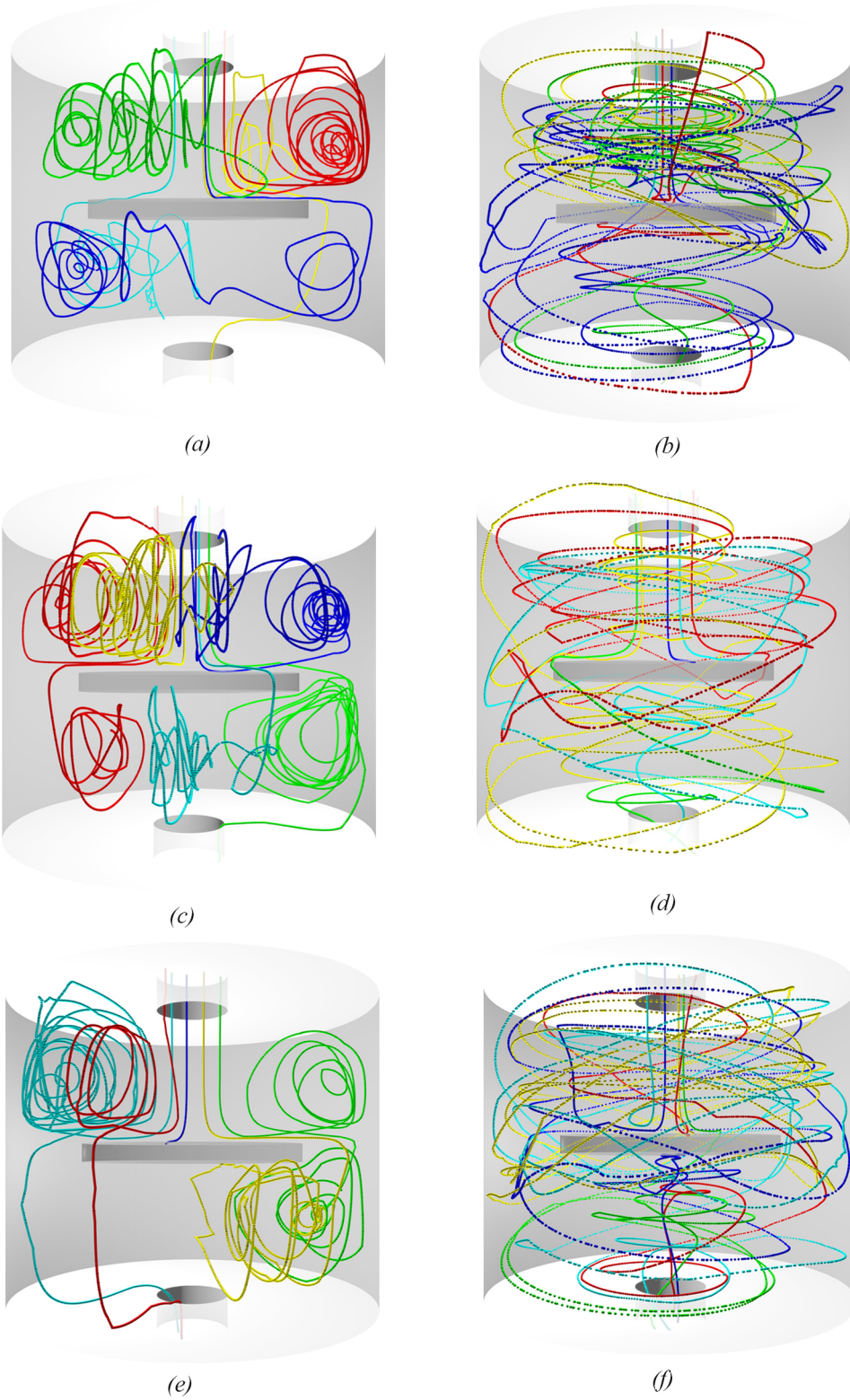
Fig. 7.7 Particle trajectories for default forces at $\Delta T = 200$ K, (a) SCVD, 1 μm, (b) RCVD, 1 μm, (c) SCVD, 0.1 μm, (d) RCVD, 0.1 μm, (e) SCVD, 0.01 μm, (f) RCVD, 0.01 μm.
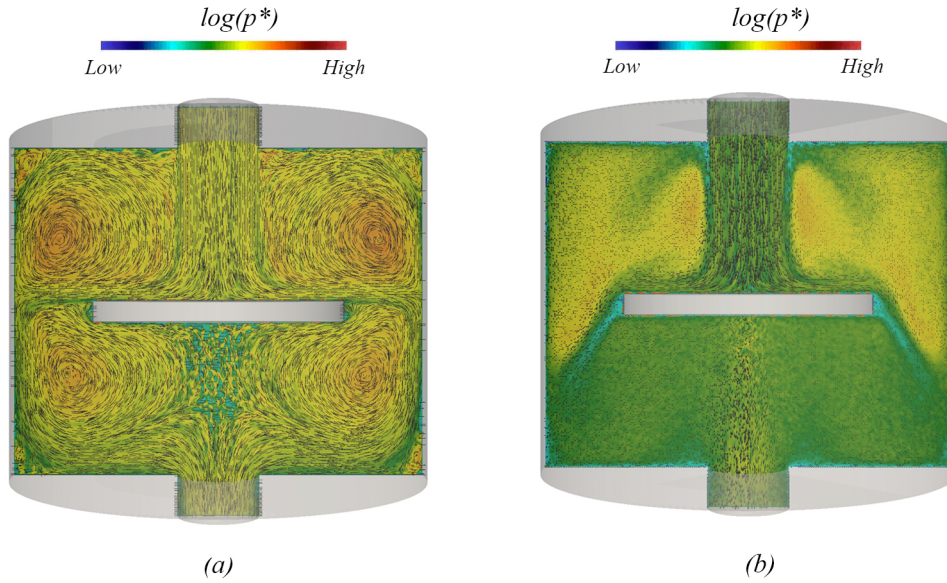
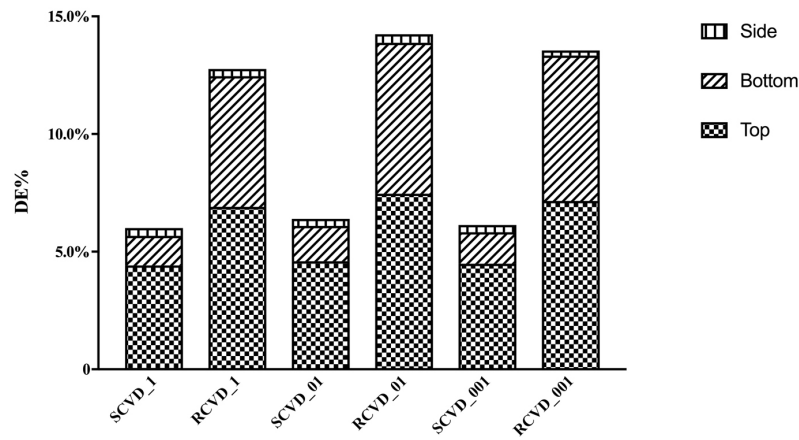Fig. 7.8 Probability of particles inside the CVD at $\Delta T = 200$ K, (a) SCVD, (b) RCVD.

Fig. 7.9 Breakdown of deposition contribution from each surface of the disk under default forces. (R)(S)CVD_D_ ΔT.

Even though the particle tracking did not include thermophoretic force, the deposition efficiency depends on the temperature of the disk. Figure 7.10 is the variation of the deposition efficiently with ΔT. Increasing the ΔT result in a decrease in the particle deposition efficiency. The observation may be described by the buoyancy effects in the vicinity of the hot surface, but no such strong buoyancy effect is captured in the current post-processing of the continuous phase results.
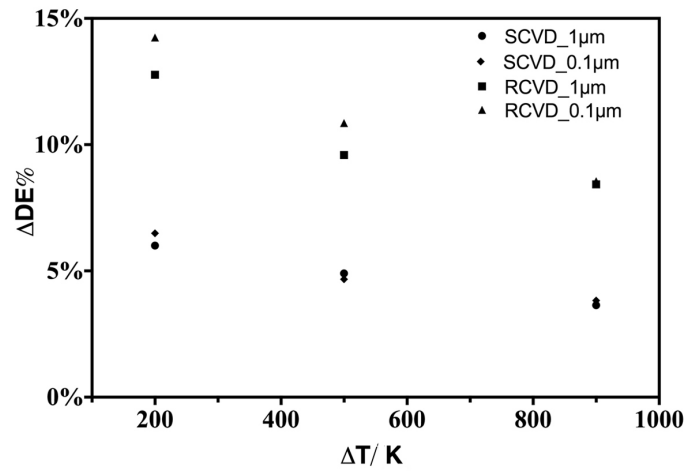
Fig. 7.10 Variation of deposition efficiencies with ΔT values for simulations with default forces.

7.3.3 Diffusion of submicron particles

In this investigation, Brownian effects and carrier phase turbulence are primary sources of diffusion for submicron particles. As described earlier, Ounis and Ahmadi (1990) have done an extensive review in this area and they concluded that the Brownian effects are negligible when compared to the carrier phase turbulent effects of the flow.

The several tests cases have been performed to ascertain the particle diffusion properties of these two sources. Figure 7.11 shows the three particle trajectories originated from the same point at the inlet (trajectories are shifted towered the left side for clarity), and these three tracks are enabled with different diffusion settings such as (1) no diffusion, (2) only Brownian diffusion, (3) only the turbulent diffusion. Once the simulation starts, it is clear that the trajectory with the turbulent diffusion (trajectory (3)) deviates from other two trajectories, but the trajectories (1) and (2) are visually identical.
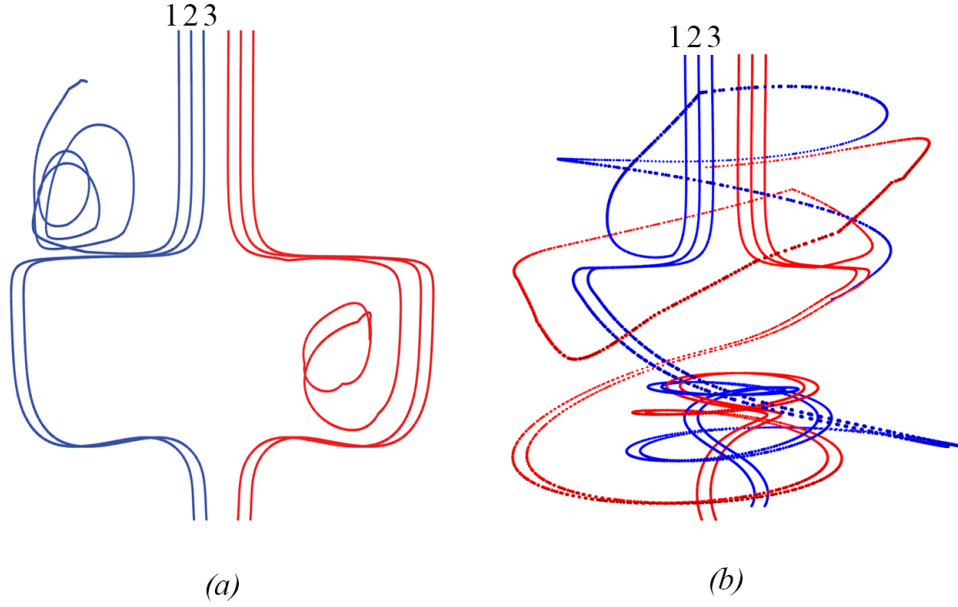
Fig. 7.11 Particle trajectories for particles initiate in the same position, d_p= 1 μm, (1) No diffusion, (2) Brownian diffusion only, (3) turbulent diffusion only; (a) SCVD, (b) RCVD.

Even though the Brownian diffusion does not show any deviation visually, the difference between the position vectors of the Brownian particle (r_{pB}) and non-Brownian particle(r_p)(see Fig. 7.12) evidence that these two particle trajectories are indeed non-identical. Further, the RCVD case shows a higher degree of particle deviation compared to the SCVD case.
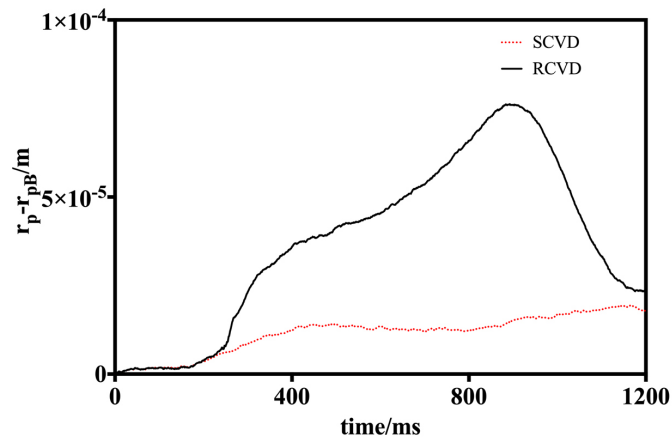
Fig. 7.12 Difference in particle position vectors in Brownian and non-Brownian particles.

156

Figure 7.13 shows the difference in Mean Squared Displacement (MSD) of the two particle trajectories ((1) and (2)) and the MSD is defined by

$$\mathrm{MSD} = \langle (\boldsymbol{r_p}(t) - \boldsymbol{r_p}(0))^2 \rangle, \tag{7.5}$$

where $\boldsymbol{r_p}(t)$ is the position vector of the particle at time $t = t$ and $\boldsymbol{r_p}(0)$ is the initial reference position of the particle at $t = 0$. The angle bracket indicates the averaging over the time series. MSD is an indication of magnitudes of the drift. In this case, RCVD shows a higher drift compared to the SCVD, and in both cases, the smaller particles obtain higher drift magnitudes than the larger particles.
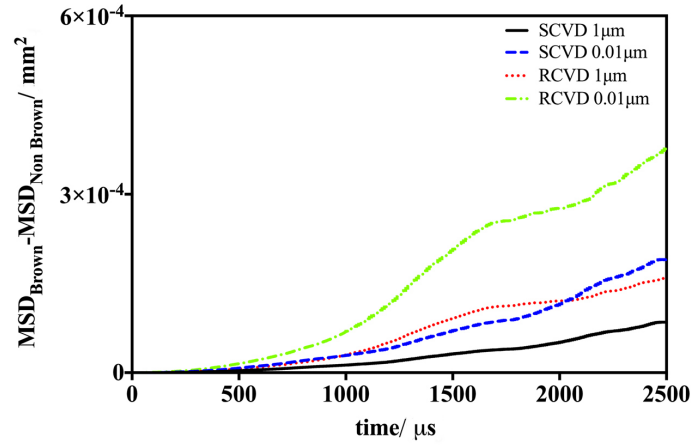
Fig. 7.13 Differences between MSD of Brownian motion and non-Brownian motion.

7.3.4 Effects of thermophoretic force on submicron particles under positive ΔT

A number of simulations with the same geometry and boundary conditions, as the Section 7.2.3, are performed, and the thermophoretic force is enabled to study the thermophoretic effects under positive ΔT values. Here, two different scenarios have been considered to conduct the simulations with thermophoretic effects. The first set of simulations consider the pure Brownian effects and the second set of simulations consider both Brownian and turbulent effects.

The simulations with pure Brownian condition help to understand the dynamics of particles without the direct influence of carrier phase turbulent effects. This will help to compare the current results with the outcomes of Chein and Su (2004)'s laminar axisymmetric

case. However, the instantaneous velocity and temperature fields of this study are derived from turbulent CFD simulations with different boundary conditions when compared to the previous investigation. For the sake of identification, pure Brownian simulations are denoted as f_B and simulations with turbulent effects are denoted as f_T.

Figures 7.14 (a),(b) & Figs. 7.15 (a),(b) show particle tracks for SCVD and RCVD cases with different particle sizes. The particle trajectories for higher ΔT values are not behaviourally different from particle trajectories for the $\Delta T = 200$ K case. The simulations with pure Brownian effects are more likely to follow the carrier fluid streamline and upward force. It appears to be that the thermophoretic forces near the rotor may not be sufficient to drive the particles to the upper circulation zone. However, superimposing the turbulent perturbations add significant randomness to the particle motion and the resulting motion is sufficient to drive the particles to the upper recirculation zones, which are less populated by particles in the simulations with pure Brownian effects (f_B).

There is a particle free zone in the vicinity of the hot disk. This particle free zone is notably evident in f_B type simulations, and particles with diameters 1 μm, 0.1 μm cannot penetrate through this particle free zone for both SCVD and RCVD simulations, which result in zero particle deposition efficiencies DE%=0 for the relatively larger particles. Still, some portion of smaller particles (0.01 μm) can penetrate through the free particle zone, but particle deposition efficiencies are extremely low compared to their non-thermophoretic counterparts as presented in Section 7.3.2. These observations agree with Chein and Su (2004)'s outcomes and the non-zero deposition efficiencies for smaller particles can be described by Brownian forces, which are more effective on smaller particles. By considering the outcomes of the f_B simulations, thermophoretic effect produces enough repulsive forces to drive the particles from the hot disk completely, but relatively strong Brownian effects on smaller particles allow a small portion of particles to deposit on the rotor.
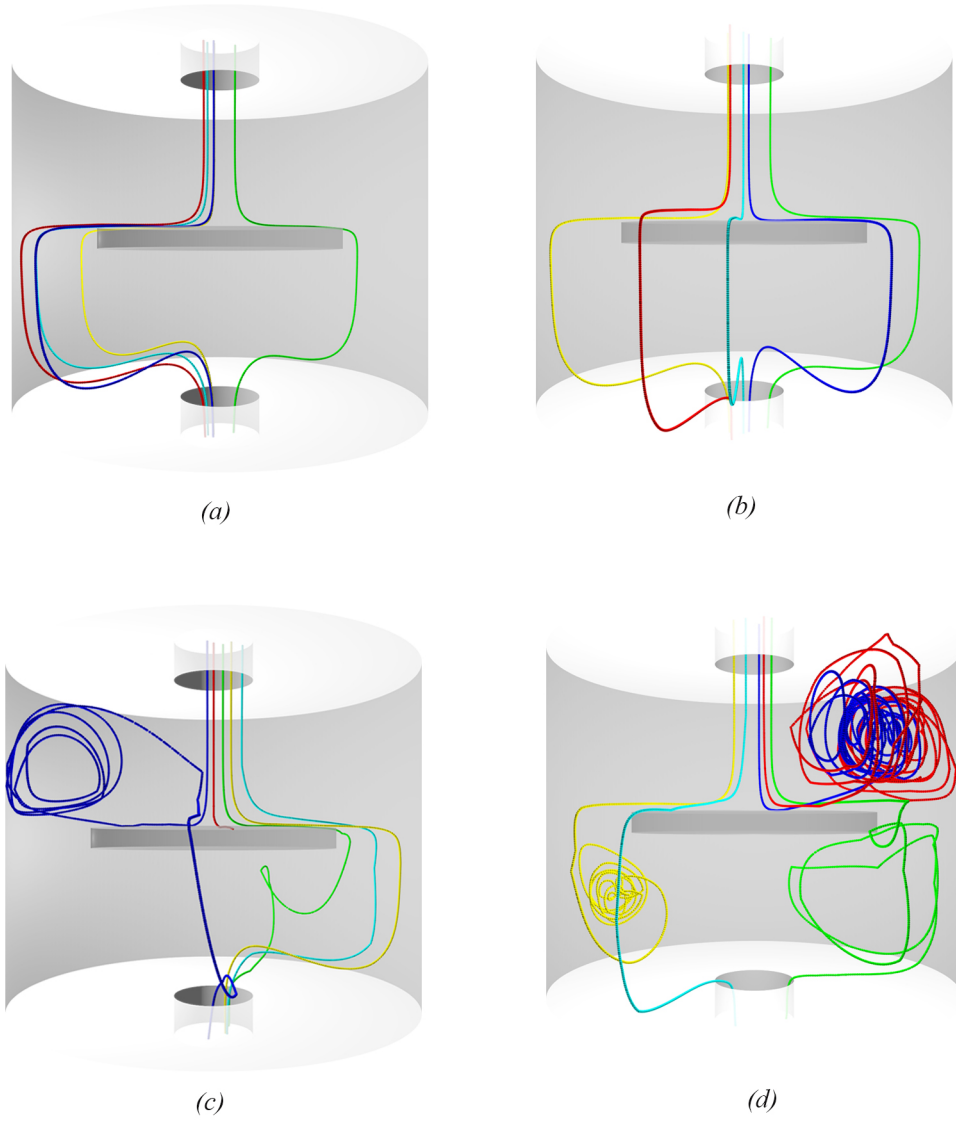
Fig. 7.14 particle trajectories under thermophoretic forces for SCVD with $\Delta T = 200$ K, (a) 1 μm, f_B, (b) 0.1 μm, f_B, (c) 1 μm, f_T, (d) 0.1 μm, f_T.
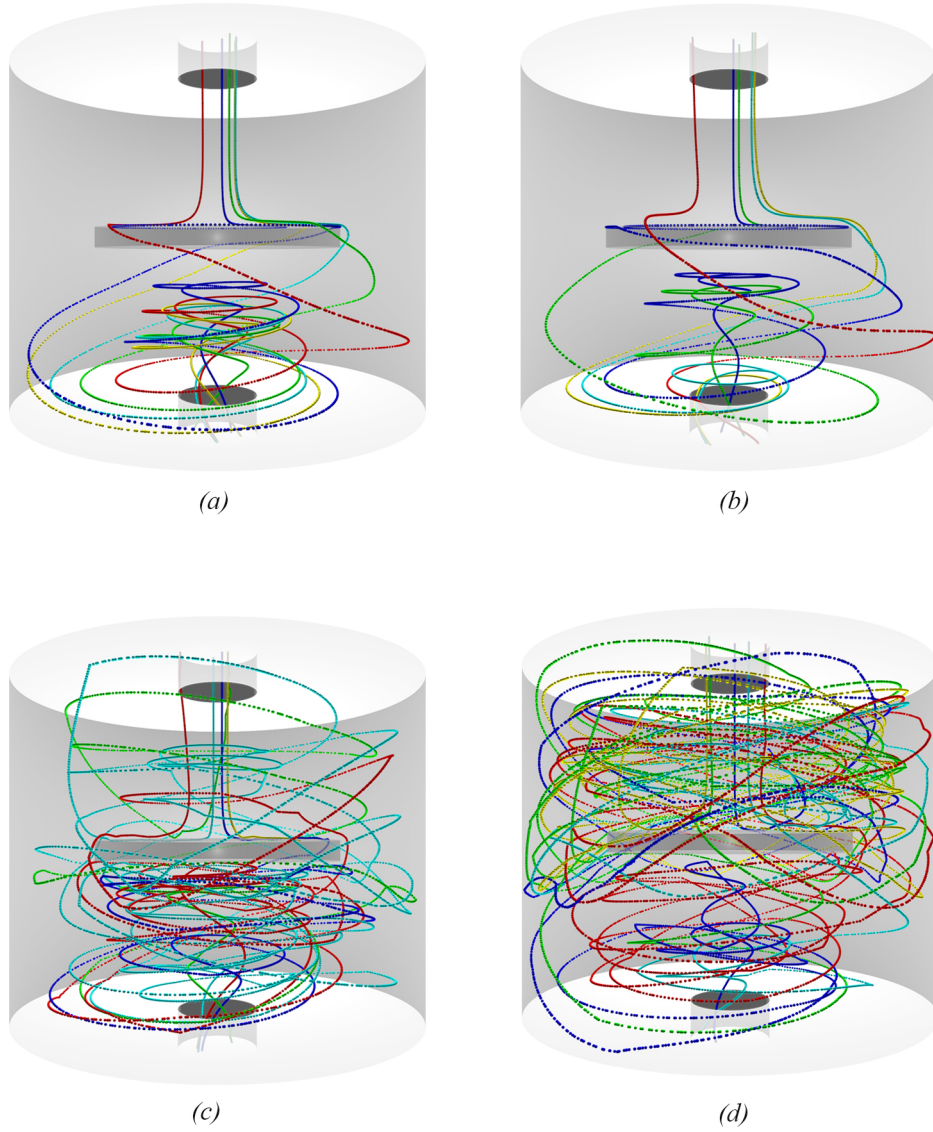
159

Fig. 7.15 Particle trajectories under thermophoretic effects for RCVD with $\Delta T = 200$ K, (a) 1 μm, f_B, (b) 0.1 μm, f_B, (c) 1 μm, f_T, (d) 0.1 μm, f_T.

As shown in Figs. 7.14 (c),(d) & 7.15 (c),(d), adding perturbation velocity components to the f_B simulations (called f_T simulations) creates a significant variability to particle tracks. This visual evidence suggests that the particle tracks are significantly influenced by the turbulent effects of the flow field. Despite the repulsive thermophoretic effects near the hot surface, f_T simulations show non-zero depositions efficiencies. Figure 7.16 shows the respective deposition efficiencies for both SCVD and RCVD for different ΔT values and particles sizes. In f_T simulations, the particle deposition efficiencies are similar to their

non-thermophoretic counterparts. An increase in ΔT values result in a reduction in deposition efficiency, but the observations may be due to the combined effects of thermophoretic forces and kinematic effects, as observed in Fig. 7.10.
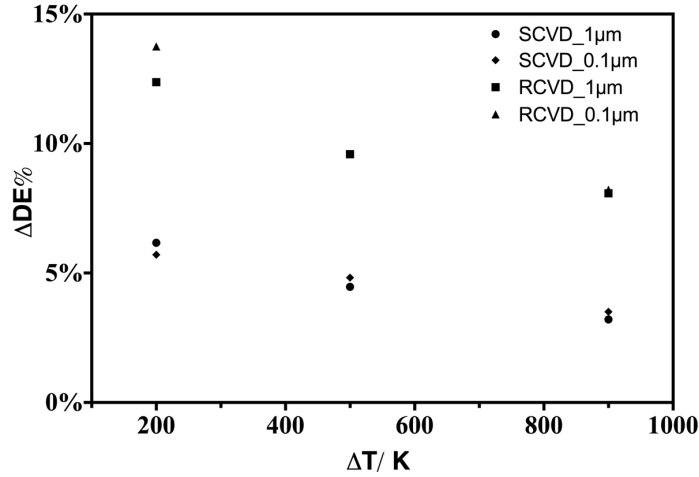

Fig. 7.16 Variation of deposition efficiencies with ΔT values, for f_T simulations.

Figure 7.17 shows the probability density distributions of the particles under positive ΔT values. Close observation of the probability density distributions for the f_B simulations shows that there is a thin layer of zero particle zone, which is often called as particle free zone (Chein and Su, 2004) located near the hot disk as shown in Fig. 7.17 (c) & (d). Figure 7.18 illustrates the breakdown of contributions from each section of the disk to total particle deposition under positive thermophoretic forces.

The above description reveals that the thermophoretic forces are significant only on pure Brownian motion simulations, but the turbulent diffusion of the carrier phase can suppress the thermophoretic forces. Therefore, the turbulent nature of carrier phase is an important factor to control the particle deposition uniformity.
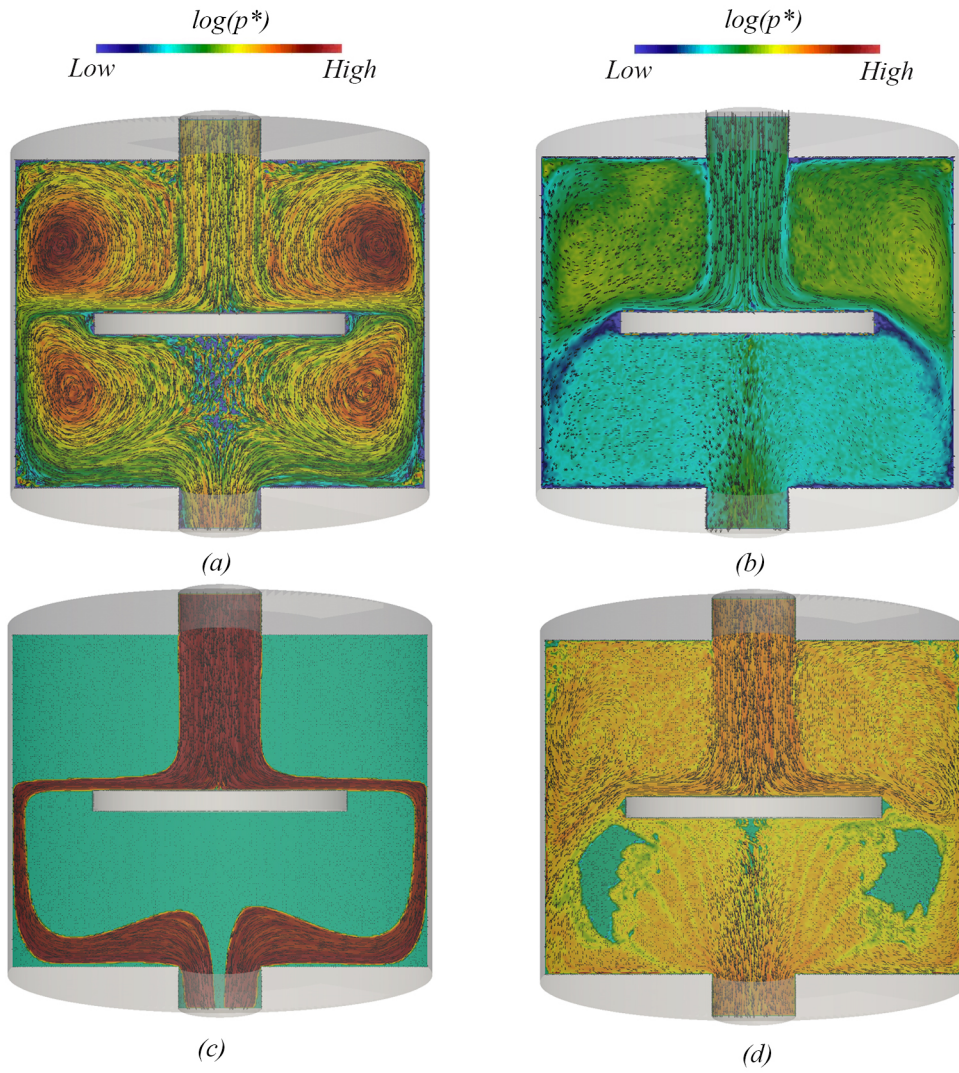
Fig. 7.17 Probability density of particles inside the CVD at $\Delta T = 900$ K, (a) SCVD, 1 μm, f_T, (b) RCVD, 1 μm, f_T, (c) SCVD, 1 μm, f_B, (d) RCVD, 1 μm, f_B.
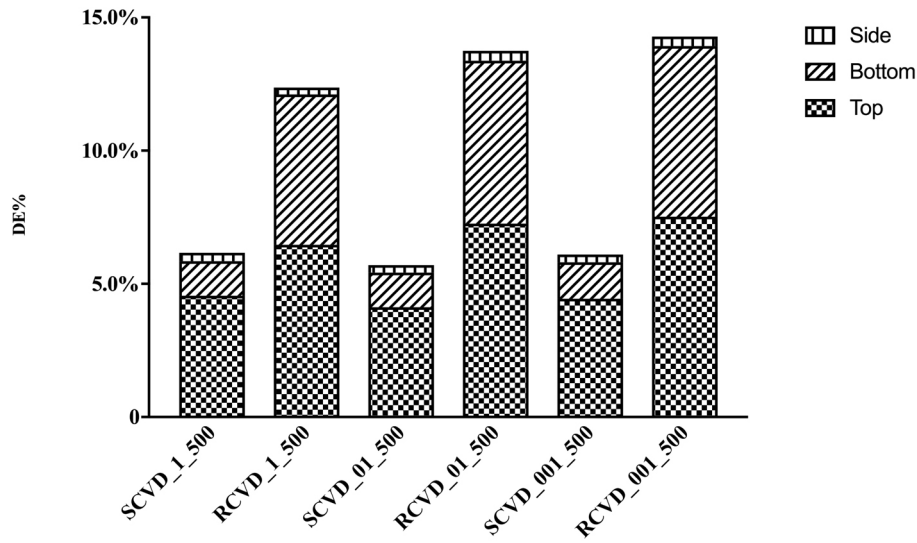
Fig. 7.18 Breakdown of deposition contribution from each surface of the disk under positive thermophoretic force. (R)(S)CVD_D_ΔT.

7.3.5 Effects of thermophoretic force on submicron particles under negative ΔT

The repulsive nature of the thermophoretic force is attributed to the positive ΔT values. However, imposing lower temperature on the disk surface than the inflow flow produces a negative ΔT value, which reverses the thermophoretic force to be an attractive force. In this case, the disk temperature is maintained at 300 K and the inflow temperature is varied to achieve ΔT values of -200 K, -500 K and -900 K. However, the modified temperature boundary conditions significantly alter the carrier phase flow field due to the strong buoyancy effects inside the chamber, and the difference is more pronounced for the cases of $\Delta T = -500$ K and -900 K.

Figure 7.19 shows the predicted RANS velocity vector plots for $\Delta T = -900$ K for both SCVD and RCVD cases. When they are compared to Fig. 7.4, the buoyancy effects have modified the upper and lower circulation zones for both SCVD and RCVD cases. The SCVD has two upper circulation zones, in which flow rotates clockwise and anti-clockwise, respectively. The lower circulation zones moved toward the central axis and their size is also smaller compared to the previous cases. The RCVD cases do not show any strong circulation zones, but upward movements of fluid are more apparent than in the SCVD modelled flow. Because of buoyancy effects, the size of the radial outflow stream near the disk surface of the RCVD appears smaller in the vector plot representation.

(a)   *(b)*

Fig. 7.19 Velocity vector plot for $\Delta T = -900$ K, (a) SCVD, (b) RCVD.

Figures 7.20 & 7.21 show the particle trajectories for SCVD and RCVD. They showed that at higher ΔT values, particle spread is more significant due to buoyancy effects. From a particle deposition perspective, buoyancy effects may act as an unfavourable effect, and this is more apparent when it compares the SCVD deposition efficiencies at $\Delta T = -200$ K and $\Delta T = -500$ K in Fig. 7.22. In these cases, $\Delta T = -500$ K has slightly lower deposition efficiency compared to $\Delta T = -200$ K, as the buoyancy effects overpower the thermophoretic attraction forces. At higher $\Delta T = -900$ K values, thermophoretic force overpowers the buoyancy effects to gain higher particle deposition efficiencies over its lower ΔT values. The red symbols denote the corresponding DE% of 1 μm particles for SCVD cases that were presented by Chein and Su (2004). These deposition efficiencies were obtained from their axisymmetric LPT simulations and the results show a clear pattern of a decrease in DE% as the Re_{in} increases. Compared to the current prediction, the DE% reported by Chein and Su (2004) is nearly six times higher than the DE% from the current study. However, the current $Re_{in} \approx 1550$ is over ten times higher than the highest Re_{in} condition of Chein and Su (2004)'s investigation and this could be a reason for the quantitative disagreement between the two results.
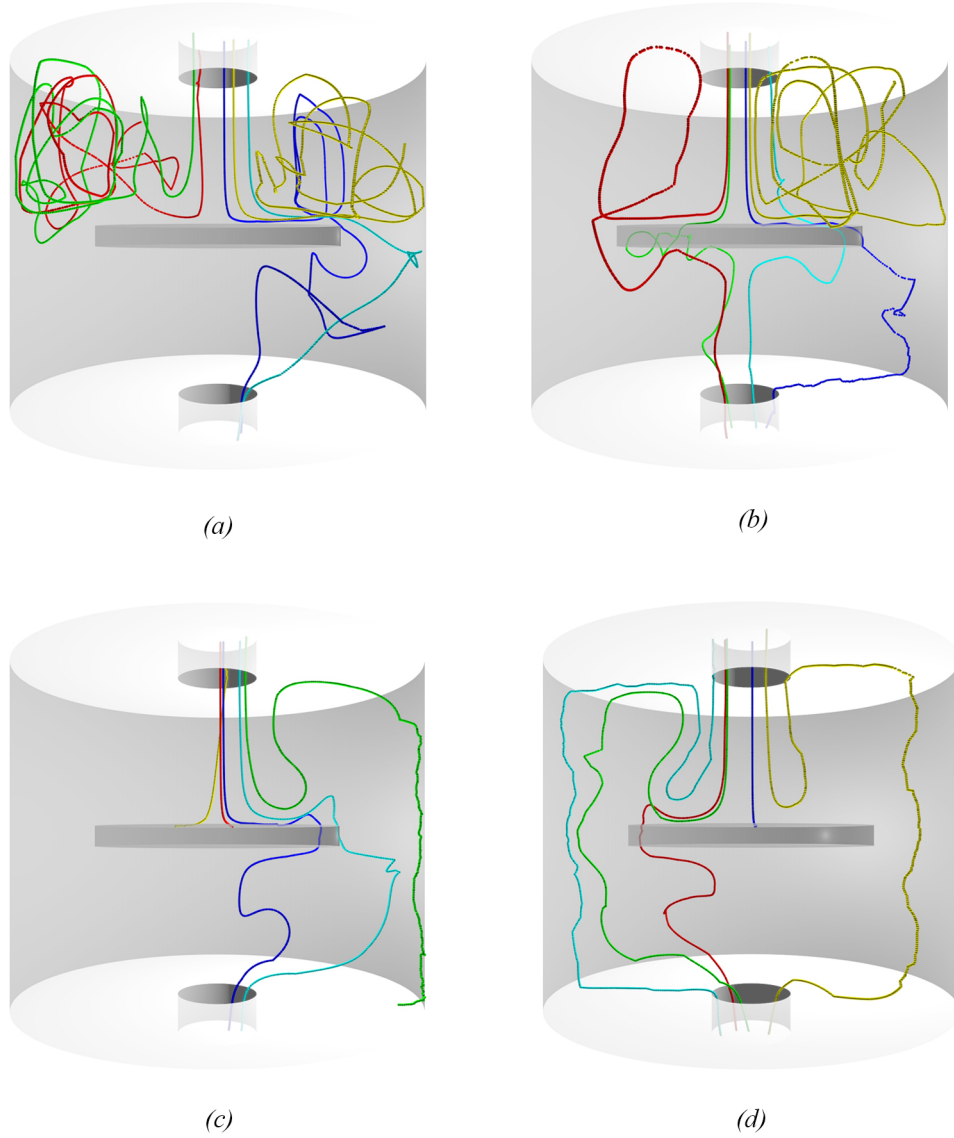
Fig. 7.20 Particle trajectories under thermophoretic effects for SCVD, (a) $\Delta T = -200$ K, $d_p = 1\mu$m, (b) $\Delta T = -200$ K, $d_p = 0.1$ μm, (c) $\Delta T = -900$ K, $d_p = 1$ μm, (d) $\Delta T = -900$ K, $d_p = 0.1$ μm.
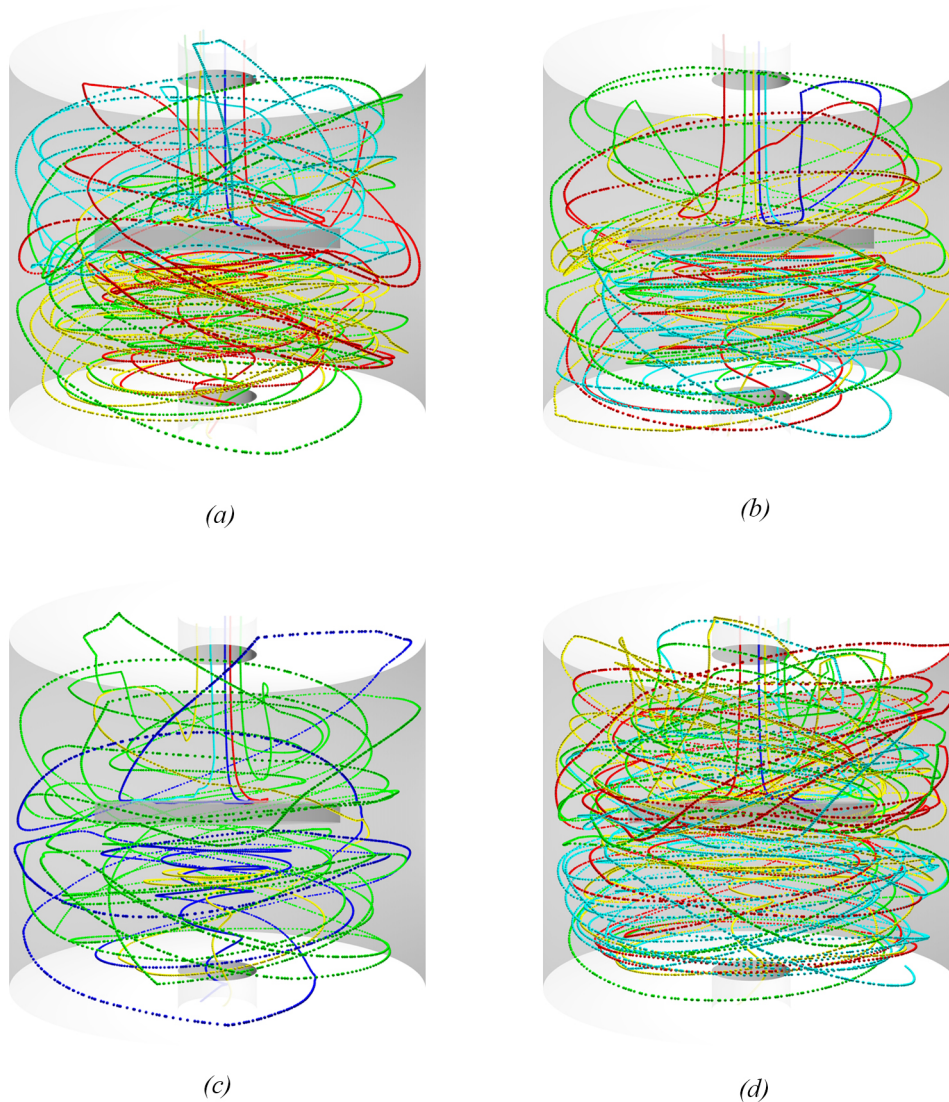
Fig. 7.21 Particle trajectories under thermophoretic effects for RCVD, (a) $\Delta T = -200$ K, $d_p = 1 \, \mu$m, (b) $\Delta T = -200$ K, $d_p = 0.1 \mu$m, (c) $\Delta T = -900$ K, $d_p = 1 \, \mu$m, (d) $\Delta T = -900$ K, $d_p = 0.1 \, \mu$m.
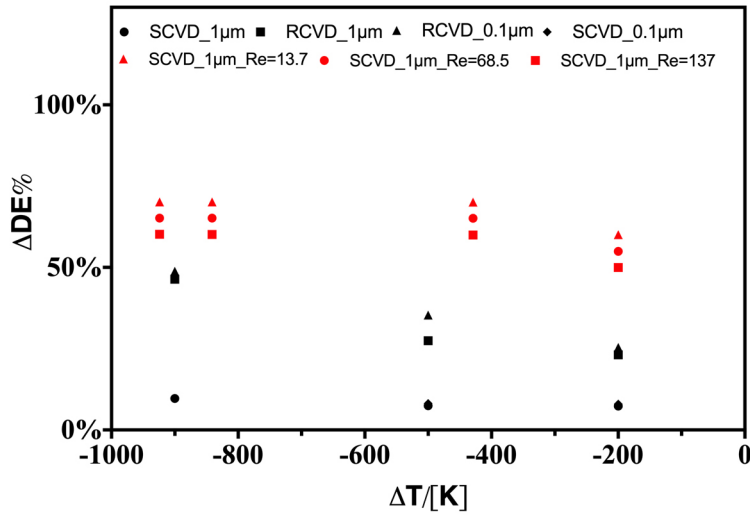
Fig. 7.22 Variation of deposition efficiencies with ΔT values for f_T simulations. (the black symbols represent the current simulation results and the red symbols represent results of Chein and Su (2004) for SCVD).

The RCVD models behave differently than the SCVD models, as they always tend to increase the deposition efficiencies under a high-temperature difference. High thermophoretic forces combined with decaying outward radial velocity component of the RCVDs always overpower the buoyancy effects, and notable improvements can be observed in deposition efficiencies.

According to Fig. 7.23, SCVDs attract significantly fewer particles at the bottom part of the rotor, in which the recirculation zones are relatively weaker, and this trend is even more noticeable toward the higher ΔT values. The particle depositions in RCVDs are more even between top and bottom portions of the disk when compare to the similar SCVD cases.
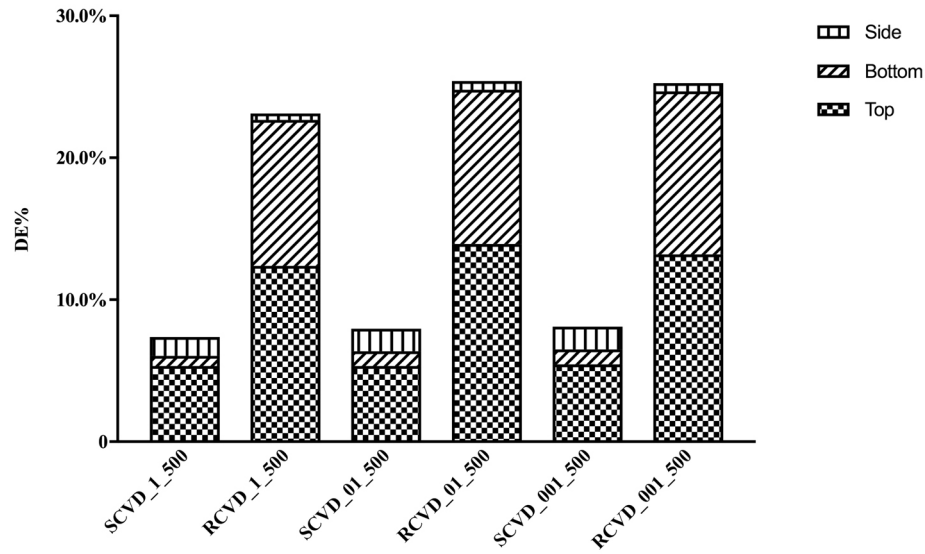
Fig. 7.23 Breakdown of deposition contribution from each element of the disk under negative thermophoretic force, (R)(S)CVD_D_ ΔT.

Here, the turbulence of the carrier phase improves the particle deposition efficiency significantly. In both SCVD and RCVD cases, turbulence in the carrier phase increases particle deposition by 25%–150% compared to non-turbulent LPT simulations. Figure 7.24 shows the particle probability contours and mean velocity vectors of both turbulent and non-turbulent LPT simulations for negative ΔT cases. The particles in the non-turbulent simulation follow the carrier phase path more, whereas turbulent effects agitated the particles into a less rectilinear motion, which creates more randomness in the particle tracks compared to non-turbulent simulations.
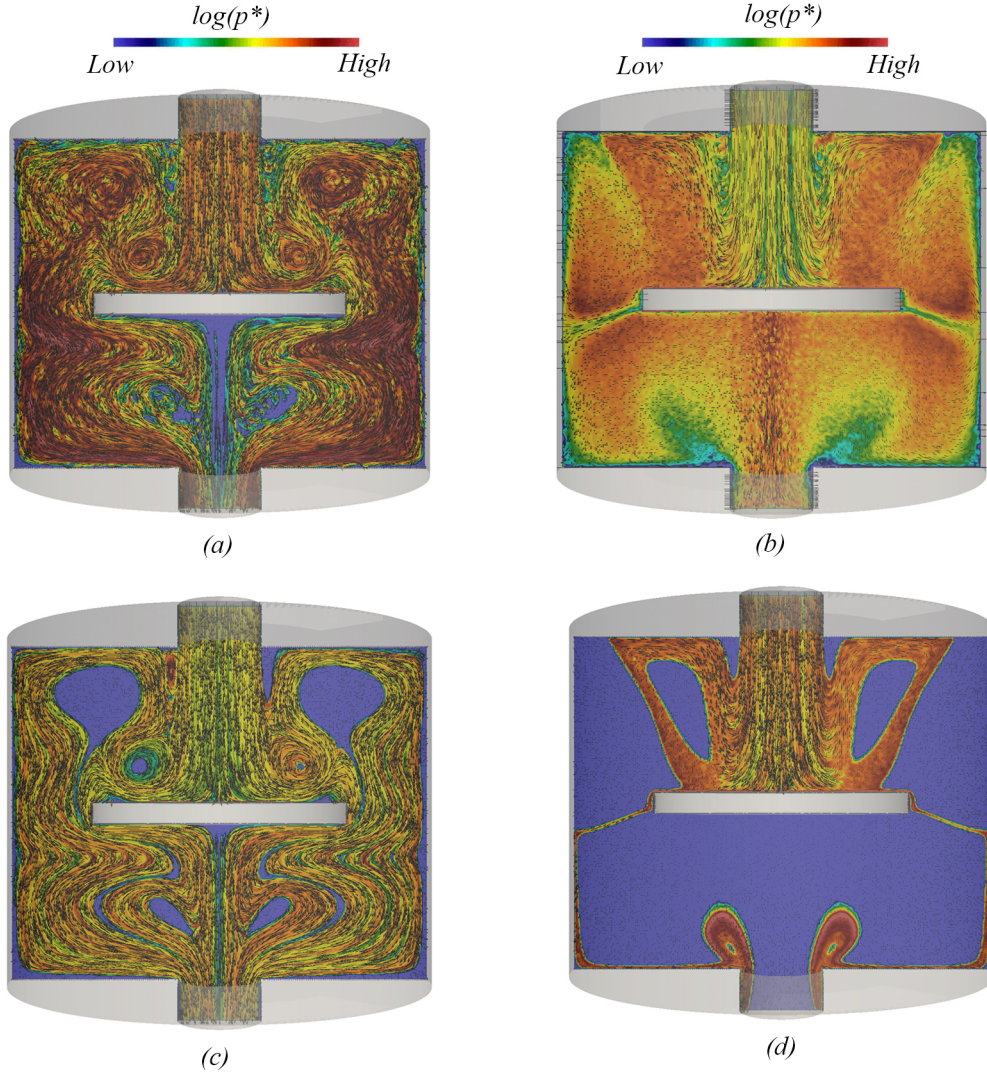
Fig. 7.24 Probability of particles inside the CVD at $\Delta T = -900$ K, (a) SCVD, 1 $\mu m, f_T$, (b) RCVD, 1 $\mu m, f_T$, (c) SCVD, 1 $\mu m, f_B$, (d) RCVD, 1 $\mu m, f_B$.

7.3.6 Effects of the injection location of the particles

The investigation is extended to ascertain the deposition efficiency with the initial particle injection location. In Fig. 7.25, the dotted areas show the injection locations of the particles and the central location represents approximately 8% of the total area of the inlet. The outer location is defined as the area outside of the central area, which is close to the periphery of the inlet. In both cases, 20,000 particles are injected through the respective locations, and the particle deposition is observed during the total simulation time.
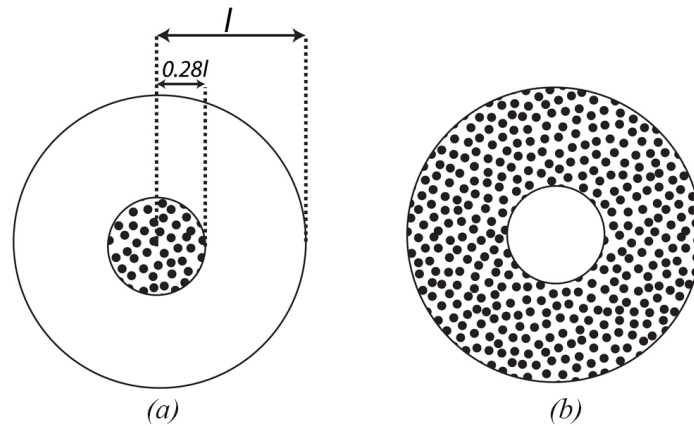
Fig. 7.25 Particle injection locations at the inlet, (a) central location, (b) outer location.

Figure 7.26 indicates that the particle deposition is highly depended on the initial injection location of the particles and the cases with the centre injections have higher deposition efficiencies over the outer injection locations. However, this figure shows that the particle deposition is uneven over the top and bottom surfaces of the disk.
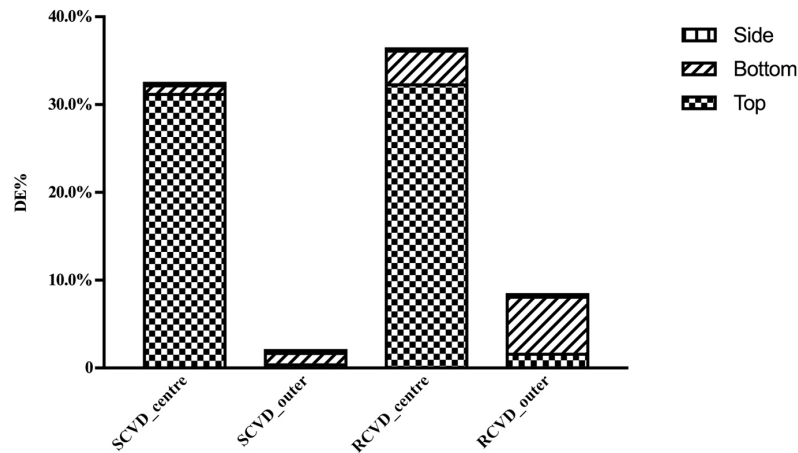
Fig. 7.26 Breakdown of deposition contribution from each surface of the element, (R)(S)CVD_D_Δ T.

By observation of Fig. 7.27, the centrally injected particles in SCVD and RCVD models are more likely to fall on the top surface of the disk, whereas outward injected particles are swept away with the radial outflow and show a considerable lack of deposition on the top surface of the disk. The starting injection locations are a convenient and effective strategy

to control the particle depositions but sometime it would be difficult to control the injection locations of the contamination particles.
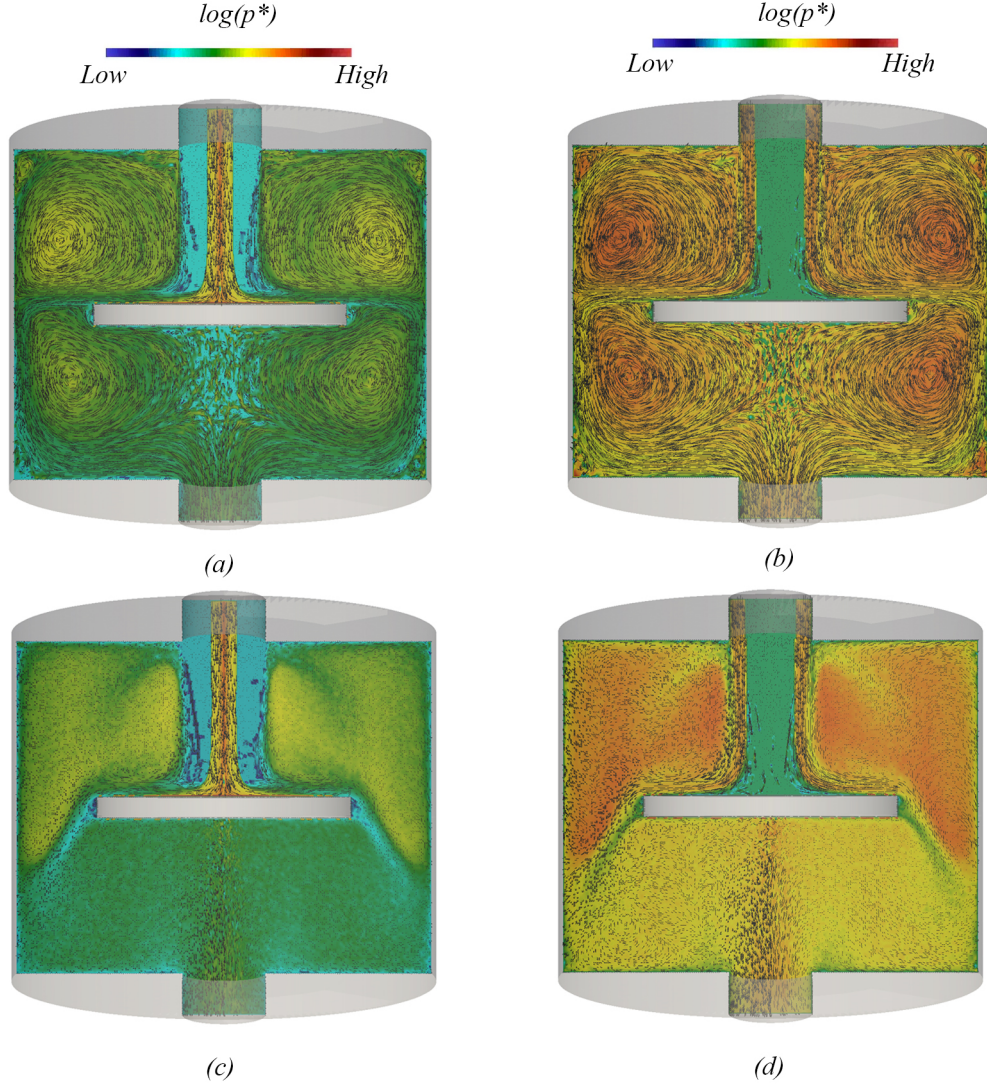
Fig. 7.27 Probability of particles inside the CVD at $\Delta T = 200$ K, (a) SCVD, centre location, (b) SCVD, outer location, (c) RCVD centre location, (d) RCVD outer location.

As shown in Fig. 7.4, a higher axial flow rate could result in strong outward flow toward the periphery of the disk, which could constrain the majority of particle deposition to a small stagnant region near the centre of the disk. Injecting the particles from the central location shown in Fig. 7.25(a) can significantly help the particles to have direct contact with the disk surface (see Fig. 7.27 (a)), whereas the particles injected though the outer location shown in Fig. 7.25(b) may be mostly entrained with the radial outward flow (see Fig. 7.27(b)). The injection location and the Re_{in} of the carrier flow field have a significant

influence on particle deposition efficiency. These reasons could partly explain the discrepancy in deposition efficiency with the previous investigation of Chein and Su (2004). However, more test cases under different flow conditions will be required to ascertain the exact reason for this difference.

7.4 Summary and conclusion

This chapter mainly discussed the particle dynamics inside RCVD chambers, and for the comparison, another identical configuration is considered without a rotating disk (SCVD). Here, a very low particle volume fraction enabled a one-way coupling between the particle phase and the carrier phase.

A series of test cases were modelled with the different temperature difference between the rotor and the inlet, $\Delta T = 200$ K, 500 K, 900 K, -200 K, -500 K, -900 K, for both RCVD and SCVD configurations. Then, the resulting velocity fields and temperature fields for the continuous carrier phase have been obtained using conventional Eulerian methods and the standard k-ε method was used to model the carrier phase turbulence. In all the cases, the inlet Reynolds number was $Re_{in} \approx 1550$. In general, the RANS velocity contours of the SCVD are axisymmetric, whereas RCVD velocity contours are three-dimensional, which shows greater mixing compared to the similar cases of SCVD.

The particles were selected in three different sizes of 1 μm, 0.1 μm, 0.01 μm, and in each size, 20,000 particles were injected within the first second of the simulation. Then, their behaviours were observed over the next 40 seconds.

Apart from the qualitative description of the particle path lines, a parameter, the deposition efficiency (DE%) is introduced (see Eq. (7.4)) to give a quantitative comparison between each case. The first stage does not consider the thermophoretic forces on particle phase simulations. This solution reveals that the particle paths in the SCVD case are axisymmetric compared to the corresponding simulations of the RCVD. Generally, RCVDs show higher DE% compared to SCVDs, and in all the cases, DE% drops with an increase in positive ΔT values.

The second stage considers the thermophoretic force in particle simulations. For all the positive ΔT values, this also shows similar behaviour to the above description, but there is a general drop in DE% because of the thermophoretic forces. In this case, turbulence in carrier phase plays a significant role in boosting DE%, and without these turbulent effects, there would be a zero DE%, which creates a particle free zone vicinity of the hot disk. The simulations with negative ΔT values create opposite the effect what was produced with a positive ΔT. In these cases, the thermophoretic force acts as an attractive force rather than

a repulsive force. However, the negative ΔT significantly modifies the carrier phase flow due to the strong buoyancy effect, which has adverse effects on DE% and this effect is more significant on the SCVD cases.

Generally, these three-dimensional simulations have a lower DE% than the two-dimensional simulations of Chein and Su (2004). The current simulations demonstrate that the rotating motion of the disk is very significant on particle depositions and particles are more evenly spread in RCVD cases compared to the similar SCVD cases. However, this check of uniformity is documented based on the difference between the deposition over the top and bottom surfaces of the disk. The uniformity of the coating over each surface is not documented. The turbulent carrier phase is also a significant factor in these simulations. The outcomes of this chapter can be used to promote or prevent particle depositions depending on the application requirements.

Chapter 8

Extended surface interactions on particle deposition

8.1 Introduction

Particle dynamics and deposition under different forces were considered in the preceding chapter, but an implicit assumption is made that the particles that touch the rotor are unconditionally deposited on the rotor. Under this assumption, the rotor is called as a perfect particle sink. As described in Section 2.6.8, many investigations (Xu et al., 1993; Xu and Willeke, 1993; Fergus, 2010) have revealed that the particle deposition can be complicated by particle bounce and resuspension, due to the complex particle-surface interactions at the surface.

Recent investigations in this area focus on the rebound and resuspension of nanoparticles due to the advancements of production processes that involve nanoscale particles. Nevertheless, according to the author's knowledge, currently, no investigation describes the effects and behaviours of submicron particles in a rotator-stator cavity (e.g. RCVD chambers) due to particle-surface interaction. Hence, this chapter considers an energy-based model that is particularly suitable for studying the rebound of micron-sized particles on the hard surfaces inside an RCVD chamber, which has a similar geometric configuration to one described in Chapter 7.

8.2 Modelling particle-surface interactions

The particle rebound model described here is based on the models of Xu and Willeke (1993) and Fergus (2010), but no plastic deformations and particle resuspension are considered in

the current investigation. Further, an assumption is made that the all the impacts are perfectly elastic.

If there are no chemical and electrical reaction between particle and surface, and the surface tension is negligible. The *Van der Waals forces* contribute to a significant portion of the surface adhesive energy between the particle and the surface (Tsai et al., 1990). A quantitative expression of surface adhesive energy per unit area is proposed by Derjaguin et al. (1994), and it is given as

$$\Delta \gamma_a = \frac{A_H}{12\pi\varepsilon_d^2}, \tag{8.1}$$

where

A_H = Hamaker constant.

ε_d = Adhesion distance ≈ 0.4 nm.

The value of the Hamaker constant (A_H) can be calculated by considering the respective Hamaker constants of particle, surface and fluid (say A_1, A_2, A_3) and this can be stated as

$$A_H = (\sqrt{(A_1 - A_3)}(\sqrt{A_2 - A_3}). \tag{8.2}$$

For a system with air as its working fluid, the Hamaker constant of the system (A_H) is reduced to the geometric mean of A_1 and A_2 $\left(\text{i.e.}\sqrt{A_1 A_2}\right)$, as A_3 can be neglected due to its small value ($\approx 4 \times 10^{20}$ J). A further assumption is made that the impacts of the particles do not exceed the elastic stress limit of the material of the particle and the corresponding elastic limiting velocity (V_y) is taken as

$$|V_y| = \left(\frac{2\pi}{3K_y}\right)^2 \left(\frac{2}{5\rho_p}\right)^{\frac{1}{2}} y_1^{\frac{5}{2}}, \tag{8.3}$$

where y_1 and ρ_p are the elastic stress limit and the density of the particle. K_y is a mechanical constant, which can be calculated using modulus of elasticity ($Y_{M,i}$) of the particle ($i = 1$) and surface ($i = 2$) materials and the expression reads as

$$K_y = \frac{4}{3\left[\left(\frac{1}{Y_{M,1}}\right) + \left(\frac{1}{Y_{M,2}}\right)\right]}. \tag{8.4}$$

According to Fergus (2010), the surface adhesive energy (E_a) is the sum of the surface energy (E_s) and the mechanical potential energy (E_m):

$$E_a = E_m + E_s. \tag{8.5}$$

The definitions of E_s and E_m are

$$E_s = \pi \left(\frac{G_c |\boldsymbol{F_s}|}{K_y} \right)^{\frac{2}{3}} \Delta \gamma_a, \tag{8.6}$$

$$E_m = |\boldsymbol{F_g}| \frac{\left(|\boldsymbol{F_s}|^{\frac{2}{3}} + 2|\boldsymbol{F_g}||\boldsymbol{F_s}|^{-\frac{1}{3}} \right)}{\left(2K_y^{\frac{2}{3}} G_c^{\frac{1}{3}} \right)}, \tag{8.7}$$

$$|\boldsymbol{F_s}| = |\boldsymbol{F_g}| + 3\pi \Delta \gamma_a G_c + \sqrt{(|\boldsymbol{F_g}| + 3\pi \Delta \gamma_a G_c)^2 - |\boldsymbol{F_g}|^2}, \tag{8.8}$$

where $|\boldsymbol{F_g}|$ and $|\boldsymbol{F_s}|$ are the gravitational force and the sum of the surface forces respectively. G_c is the contact geometric constant, with the zero-plastic deformation, $G_c = a_p$.

Figure 8.1 (a) & (b) show typical situations that might occur near the boundary of interest. The impact kinetic energy should be adequate to overcome the adhesive energy and the rest is released as rebound kinetic energy. If the inbound kinetic energy is below than adhesive energy, then the particle tends to stick on the surface. However, in practice, the particle may undergo a series of rebounds, as shown in Fig. 8.1(c), before it permanently sticks on the surface. The conditions for stick or rebound can be derived by considering a simple energy balance of the *particle-surface system* near the surface.
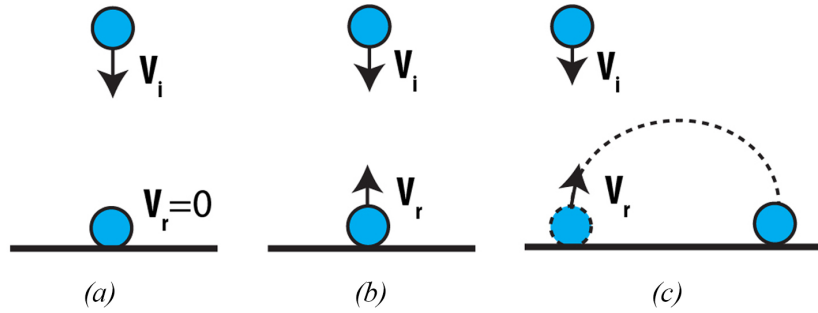

Fig. 8.1 A particle behaviour near a surface, (a) particle stick, (b) complete rebound of the particle, (c) rebound and stick.

By considering the conservation of energy,

$$\frac{1}{2} m_p |\boldsymbol{V_i}^2| = \frac{1}{2} m_p |\boldsymbol{V_r}^2| + E_a, \tag{8.9}$$

where, V_i and V_r are the relative impact and the relative rebound velocity with respect to the rotor, respectively. According to the Eq. (8.9), the rebound velocity can be calculated as

$$|V_r| = \sqrt{|V_i^2| - \frac{2E_a}{m_p}}. \tag{8.10}$$

The critical velocity ($|V_{cr}|$) is the impact velocity that is just enough to overcome the surface adhesive energy Therefore an expression for $|V_{cr}|$ can be obtained by setting $|V_r| = 0$ in Eq. (8.10) that given by

$$|V_{cr}| = \sqrt{\frac{2E_a}{m_p}} = \sqrt{\frac{2(E_s + E_m)}{m_p}}. \tag{8.11}$$

This criterion of Eq. (8.10) combines the two interactions *"Stick"* and *"Rebound"* depending on the values of $|V_{cr}|$ and $|V_i|$ and the following conclusions can be made:

- $|V_i| < |V_{cr}|$: particles tend to stick on the boundary where the particle velocity becomes zero.

- $|V_i| > |V_{cr}|$: particles rebound on the boundary and the collisions on the surface is assumed to be perfectly elastic.

8.2.1 Operation conditions for the simulations

This section uses the same continues phase fields of Section 7.2.3 to solve the particle phase equations. The particles are assumed to be spherical silicon particles with density (ρ_p) 2330 kg/m^3.

The particle-surface model that described in Eq. (8.11) implemented in the current LPT framework of OpenFOAM. To confirm the validity of the implementation and the applicability of this model on the RCVD applications, two test cases have been prepared under similar conditions described in Section 7.3.2. In these cases, an uniform particle distribution, which consists of 20,000 particles with different particle sizes ranging from $d_p = 0.001\ \mu$m–3.0 μm, is used (see Fig. 8.2). At the end of these simulations, the deposited particle distributions on the rotor surface have been obtained and they are compared with the corresponding particle distributions that are obtained using the standard LPT simulations, which do not use the particle-surface modelling feature. By comparing both types of simulation models, the net reduction of deposition efficiency due to particle-surface interactions ΔDE_{SI} is defined as

$$\Delta DE_{SI} = \frac{\text{depositions with S-I effects - depositions without S-I effects}}{\text{depositions without S-I effects}} \times 100, \tag{8.12}$$

where the notation "S-I" denotes particle-surface interaction and this notation will often appear in the upcoming figures and tables.
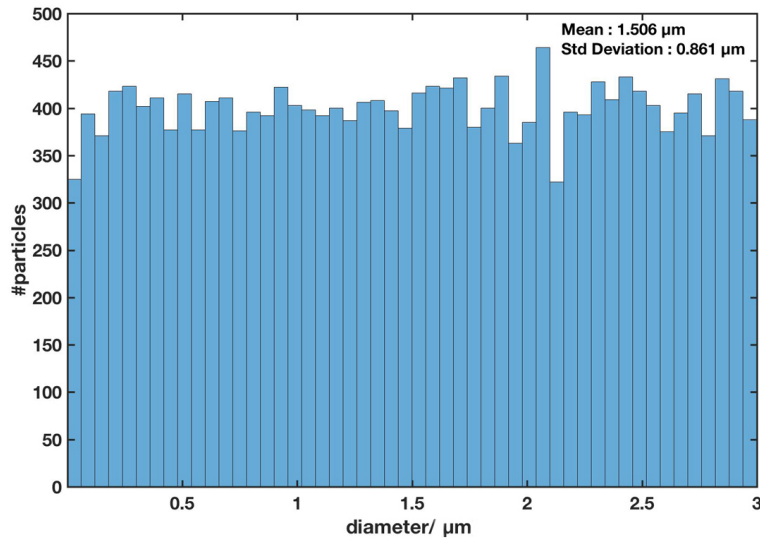

Fig. 8.2 Input uniform distribution at the start of the simulation.

Figure 8.3 (a) & (b) show the deposited particle distributions for SCVD and RCVD cases, and their mean diameters. When the mean diameters of the SCVD and RCVD cases are compared to the mean diameter of the input distribution, they are decreased by 9.01% and 15.60% for the respective cases of SCVD and RCVD. According to Section 7.3.2, the larger particles in the chemical vapour deposition chamber (for both SCVD and RCVD cases) tend to have lower DE% and this might result in lower mean diameters even without the particle-surface interaction effects. Hence, the net reduction of mean diameter (Δd_{mean}) is calculated in a similar fashion to the net reduction of deposition efficiencies (ΔDE_{SI}) as shown in Eq. (8.2).

By using particle deposition distributions of standard LPT simulations (as shown in Fig. 8.3 (c) & (d)), Δd_{mean} can be calculated. The mean particle diameters of SCVD and RCVD cases are reduced due to particle-surface interaction effects and the SCVD and RCVD cases report the values of Δd_{mean}= 7.5% and 6.6%, respectively. The particle distribution of the SCVD case shows a lower standard deviation value when it compares to the input particle distribution but this is slightly increased for the RCVD case. Further, the SCVD and RCVD cases show values of ΔDE_{SI}= 17.6% and 30.3%, respectively. These observations suggest that the particle-surface interaction could result in lower DE% for the larger particles.
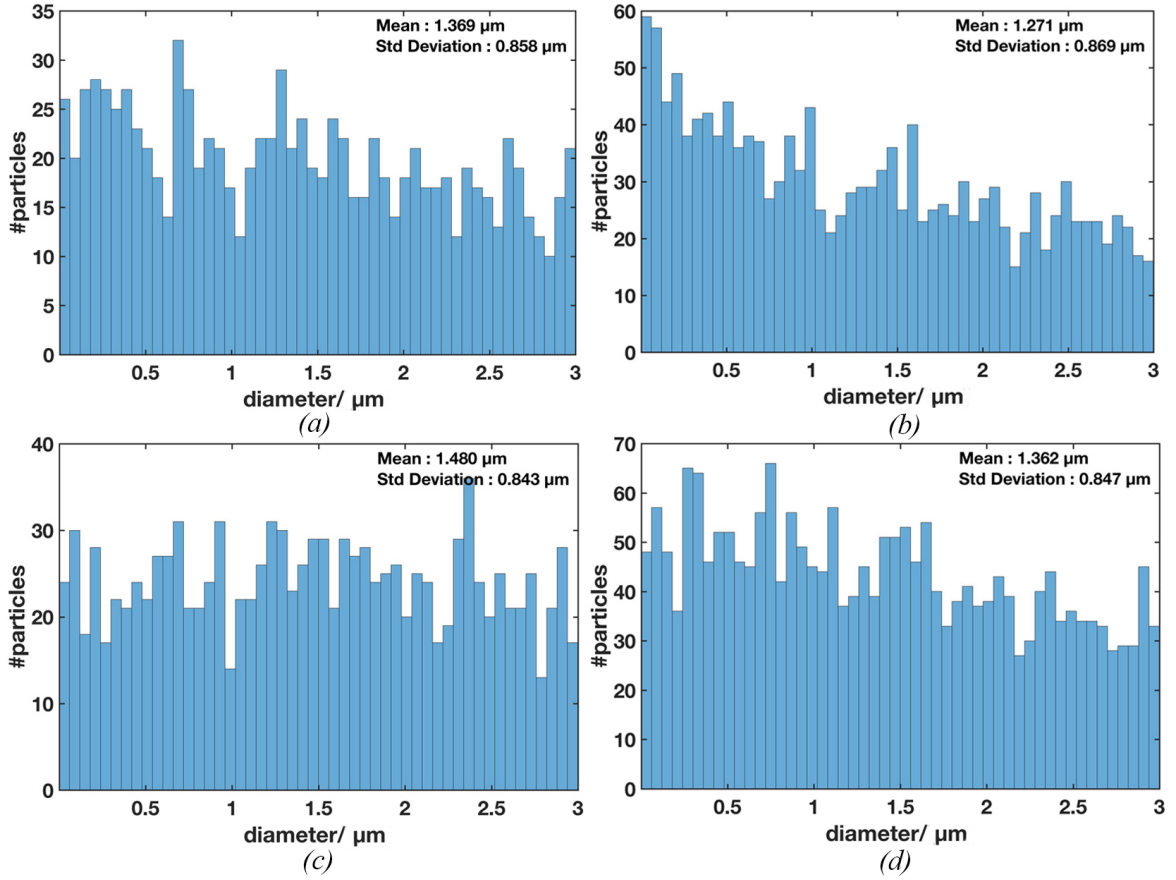
Fig. 8.3 Deposited particle distributions for the input uniform distribution of Fig. 8.2, (a) SCVD with S-I, (b) RCVD with S-I, (c) SCVD without S-I, (d) RCVD without S-I.

The above observations can be qualitatively explained by considering the variation of $|V_{cr}|$ with particle diameters that are shown in Fig. 8.4, which is constructed using Eq. (8.11). The particle depositions mostly depend on the $|V_{cr}|$ and $|V_i|$ values and the $|V_{cr}|$ is inversely proportional to the square root of the mass of the particles. Under this condition, a larger particle should have a sufficiently lower $|V_i|$ value (i.e. $|V_i| < |V_{cr}|$) for the deposition. Further, for a very small particle, the particle-surface interaction could be quite insignificant, as it might undergo an unconditional deposition due to large $|V_{cr}|$ value associated with it. However, this only explains the qualitative agreement of the model in the current application, and further investigations will be needed to obtain a quantitative agreement.

These arguments suggest that the particle size (or inertia) is a significant factor in determining particle-surface interactions and it should be in a correct range to observe effective particle depositions. Otherwise, particles may undergo unconditional rebound or depositions. By considering these facts, particle diameters are chosen to be 0.7 μm, 1 μm,

3 μm for the simulations. Figure 8.5 shows a typical deposition velocity distribution (this is equivalent to $|V_i|$) of 1 μm particles, for both SCVD and RCVD cases.
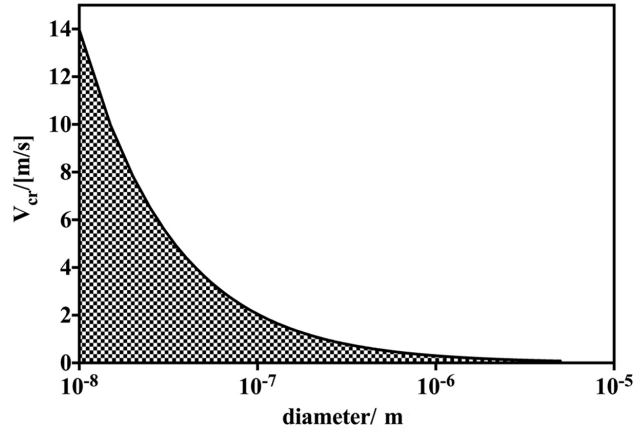
Fig. 8.4 Variation of $|V_{cr}|$ with the particle sizes.
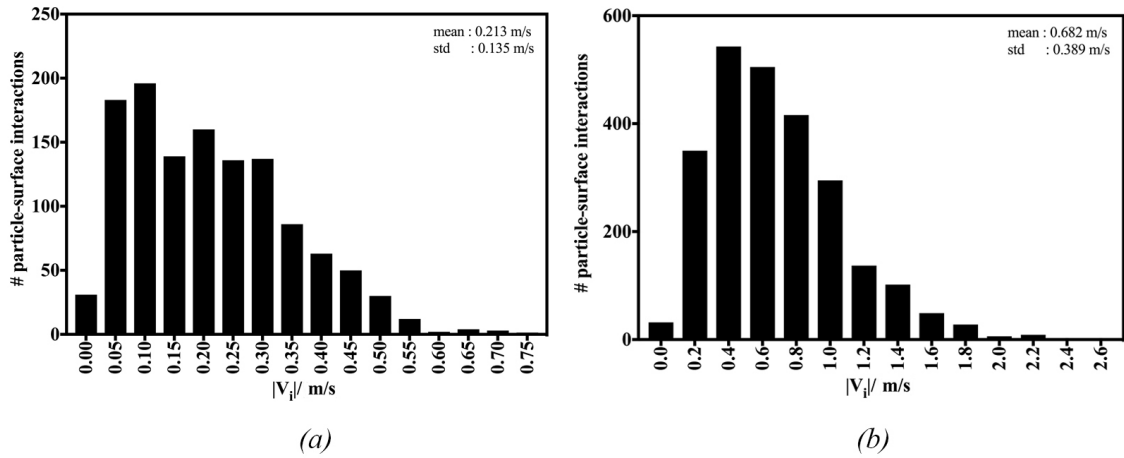
Fig. 8.5 Histogram of V_i for the particle diameter of 1 μm, (a) SCVD, (b) RCVD.

As in the simulations in Chapter 7, 20,000 particles are injected within the first second of the simulation, and the entire simulation is conducted for 40 seconds. For fixed particle sizes, uniform particle size distribution is used in the initial particle injection, and at a later stage, the *Rosin-Rammler* particle size distribution is used to study the particle deposition behaviour under various particle sizes.

8.3   Results and discussion

As in Chapter 7, the results are grouped into two sections based on the nature of the thermophoretic force upon the particles near the disk surface. Without any particle-surface interaction model turned on, the impacting particles are deposited, and other particles are eventually flushed out from the system. Regardless of the nature of the thermophoretic force, the particle-surface modelling enables new interaction types for impacting particles. As shown in Fig. 8.1, the impact can end up as a deposited particle on the surface, a complete rebound (this particle can either deposit again after a long interval or flush out from the system), a rebound-stick (rebound and stick take place within a short interval, by which bounced off particles re-impinge in a curved trajectory). Figure 8.6 illustrates these interaction types by the particle trajectories. Some particles are predicted to escape from the outlet without having any interaction with the disk surface. The subsequent sections will discuss the effects of particle-surface interactions concerning the nature of the thermophoretic force on the particles.

8.3.1   Particle-surface interactions under positive ΔT

Figure 8.7 illustrates typical particles trajectories inside the CVD. Particles tend to move to the recirculation zones shown in Figs. 7.3 & 7.4 of Chapter 7 by virtue of turbulent effects of the continuous phase. Following the same trend as in Chapter 7, particle trajectories for SCVD are two-dimensional, whereas the corresponding trajectories for RCVD are more three-dimensional. The larger particle trajectory is more independent than that of the smaller particles, which follow closely to the carrier phase fluid streamlines due to the comparatively low Stokes numbers.

(a)

(b)

(c)

(d)
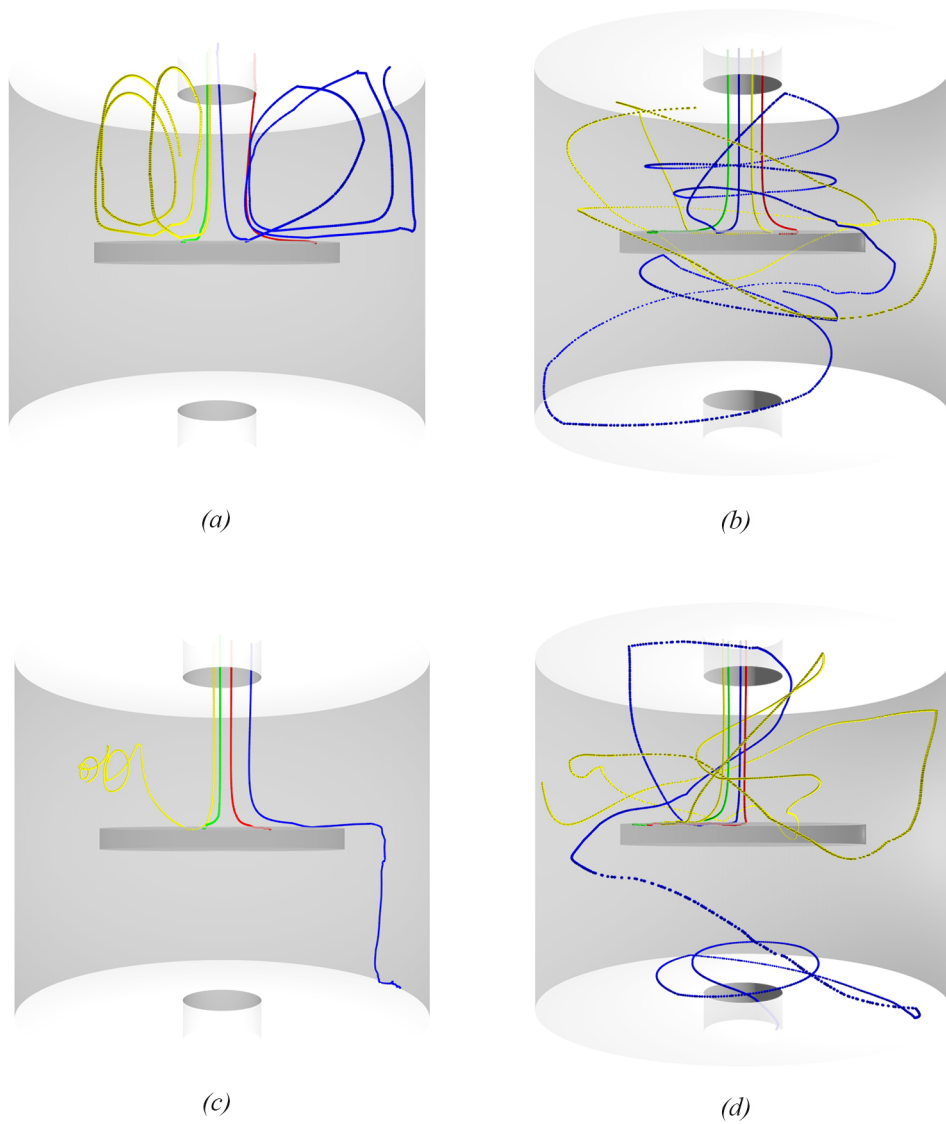
Fig. 8.6 Different interaction types of particle-surface interaction models 1 μm particles. (Blue): deposit, (green): complete rebound, (red): rebound-stick, (yellow): no interactions (a) SCVD, $\Delta T = 200$ K, (b) RCVD, $\Delta T = 200$ K, (c) SCVD, $\Delta T = 900$ K, (d) SCVD, $\Delta T = 900$ K.

182

(a)   *(b)*

(c)   *(d)*
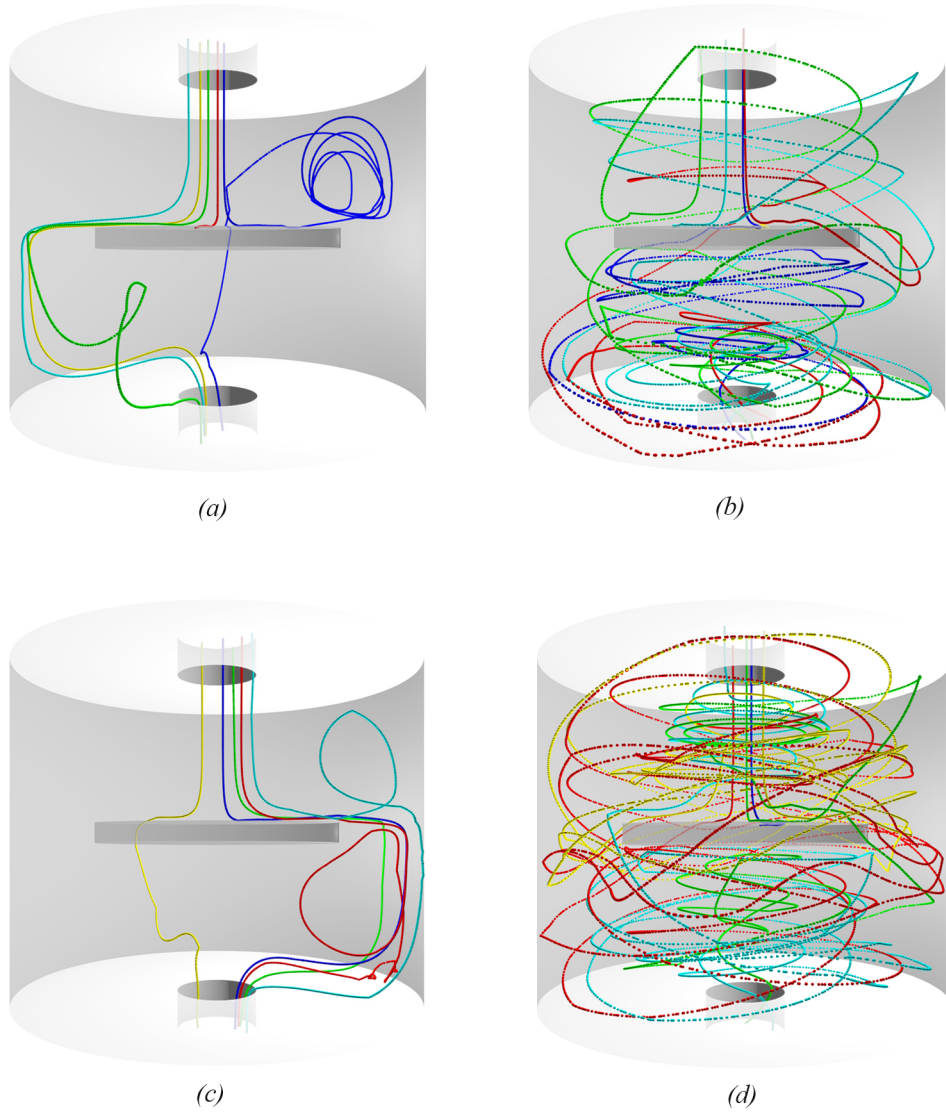
Fig. 8.7 Particle trajectories for $\Delta T = 200$ K. (a) SCVD, $d_p = 1 \ \mu$m, (b) RCVD, $d_p = 1 \ \mu$m, (c) SCVD, $d_p = 3 \ \mu$m, (d) RCVD, $d_p = 3 \ \mu$m.

Figure 8.8 shows the variation of V_i with the simulation time for SCVD. The red dotted line indicates the corresponding V_{cr} value for the given particle size. The particles below this line tend to deposit, while others bounce off. Particle-surface interactions are overwhelming during initial injection period of the particles. After that, these interactions are scattered throughout the entire simulation time. The small particles (1 μm) tend to be below the dotted red line, but the larger particles are relatively more populated above the critical line, which results in rebounds from the surface.

183
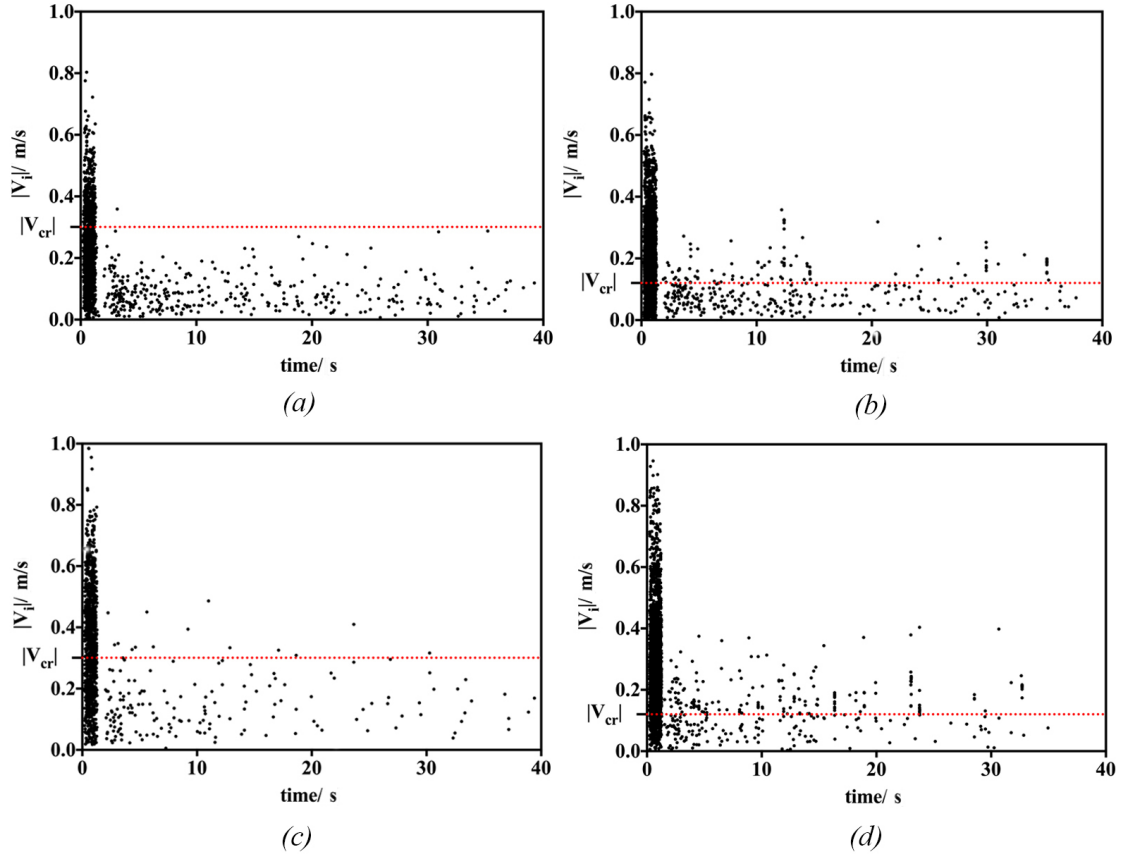
Fig. 8.8 The variation of V_i with the simulation time for SCVD cases, (a) $\Delta T = 200$ K, $d_p = 1$ μm, (b) $\Delta T = 200$ K, $d_p = 3$ μm, (c) $\Delta T = 900$ K, $d_p = 1$ μm, (d) $\Delta T = 900$ K, $d_p = 3$ μm.

The corresponding impact velocity plots for RCVD can show in Fig. 8.9. The interactions are widespread throughout the entire simulation time, though the most they registered as rebound interactions.

Fig. 8.9 The variation of V_i with the simulation time for RCVD cases, (a) $\Delta T = 200$ K, $d_p = 1$ μm, (b) $\Delta T = 200$ K, $d_p = 3$ μm, (c) $\Delta T = 900$ K, $d_p = 1$ μm, (d) $\Delta T = 900$ K, $d_p = 3$ μm.

Figure 8.10 indicates the variation of deposition efficiency with ΔT values for SCVD, and the efficiency usually decreases, as ΔT increases. This deposition efficiency prediction reconfirms that the smaller particles are less affected by effects of the particle-surface interactions.

According to the Fig. 8.11, the effects of particle-surface interactions are more pronounced in the RCVD case. The deposition efficiencies of RCVD are naturally improved compared to the SCVD case, and the lowest efficiency is predicted for larger particles.
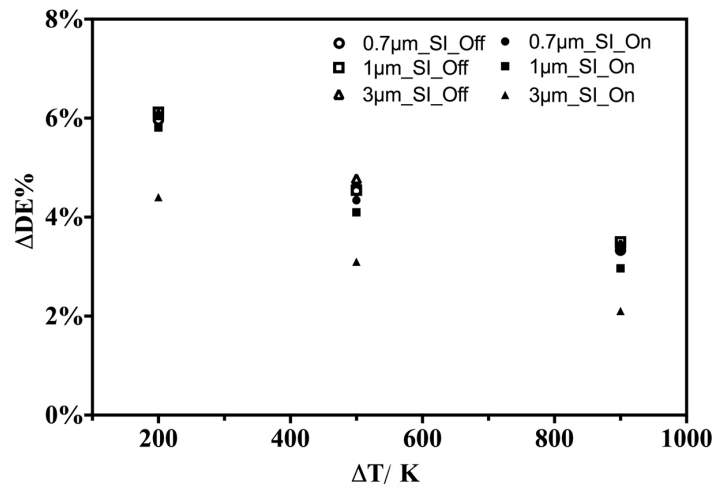
Fig. 8.10 Variation of deposition efficiencies with positive ΔT values for SCVD
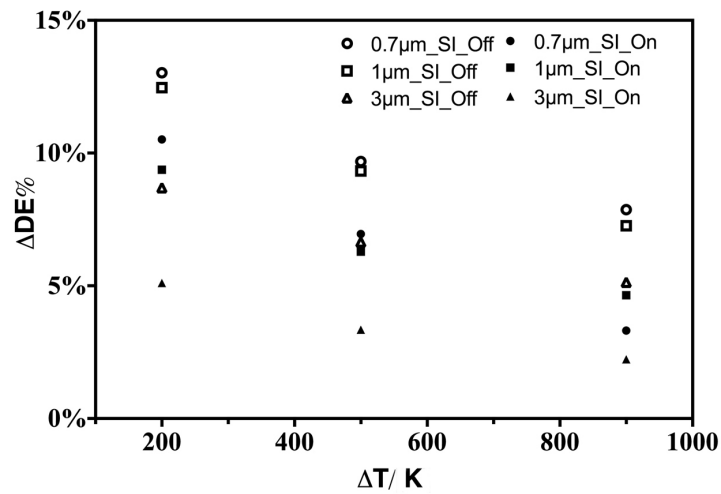
Fig. 8.11 Variation of deposition efficiencies with positive ΔT values for RCVD.

8.3.2 Particle-surface interactions under negative ΔT

As described in Chapter 7, the negative ΔT value attracts particles to the much colder disk surface, but the presence in buoyancy effects has a considerable influence on the particle deposition behaviour. Figure 8.12 shows a sample of the particle trajectories for the negative ΔT values. In the case of SCVD, the upward motion of particles is more apparent, whereas the rotating motion of the RCVD weakens the buoyancy effects.

186
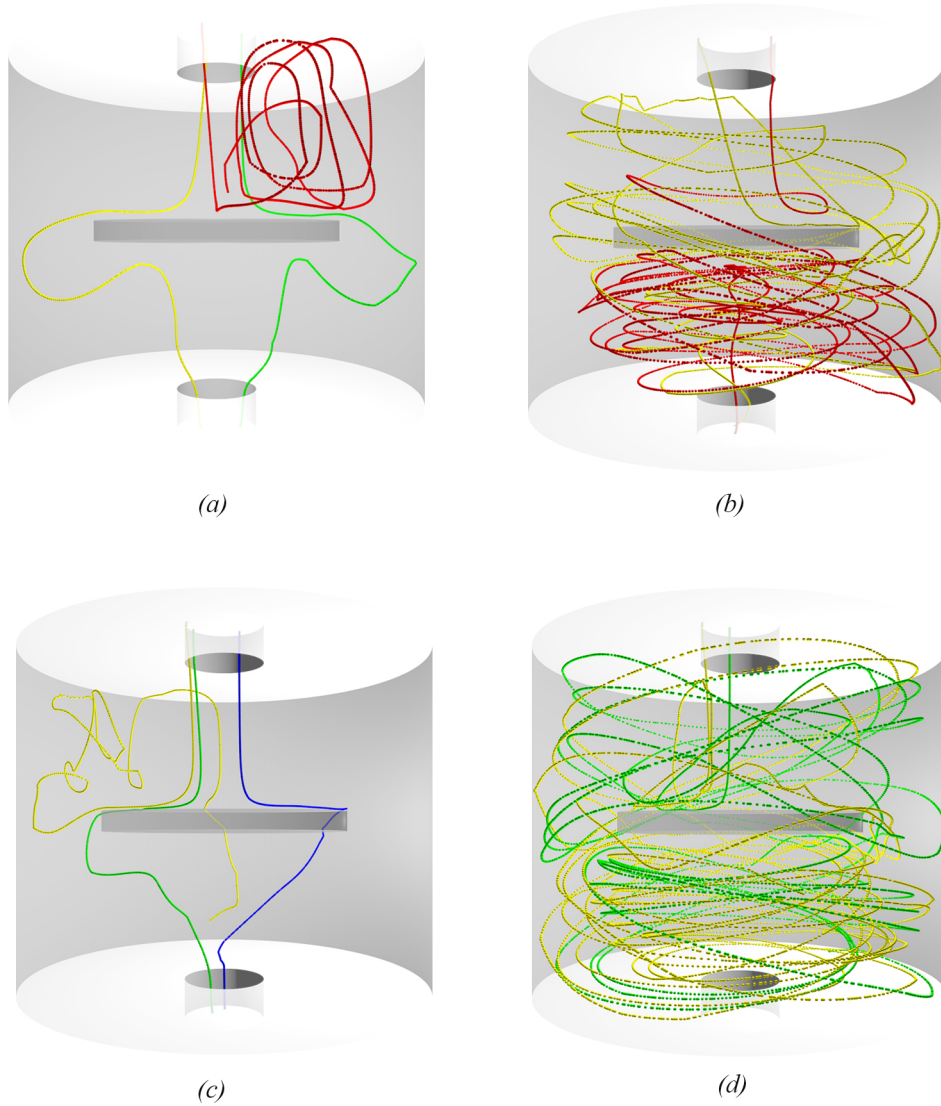
Fig. 8.12 Particle trajectories for $\Delta T = -200$ K, (a) SCVD, $d_p = 1$ μm, (b) RCVD, $d_p = 1$ μm, (c) SCVD, $d_p = 3$ μm, (d) RCVD, $d_p = 3$ μm.

Figure 8.13 shows the variation of $\boldsymbol{V_i}$ with the simulation time for the SCVD simulations, at a $\Delta T = -200$ K, the behaviour is similar to that with positive ΔT values in Fig. 8.8, but many of these interactions occur $\boldsymbol{V_i}$ at below the critical velocity value. At the more negative $\Delta T = -900$ K, particle-surface interactions are limited to approximately the first twelve seconds of the simulation, which could be an indication of strong buoyancy effects.
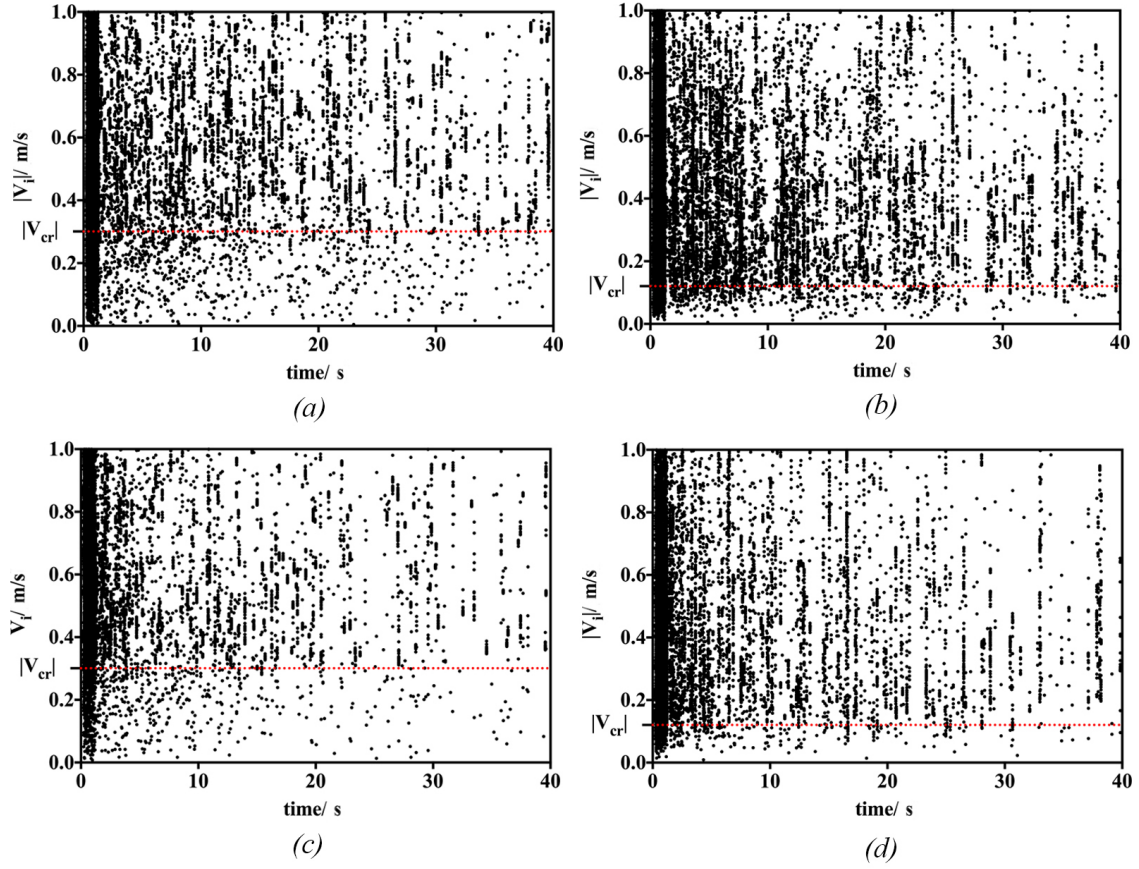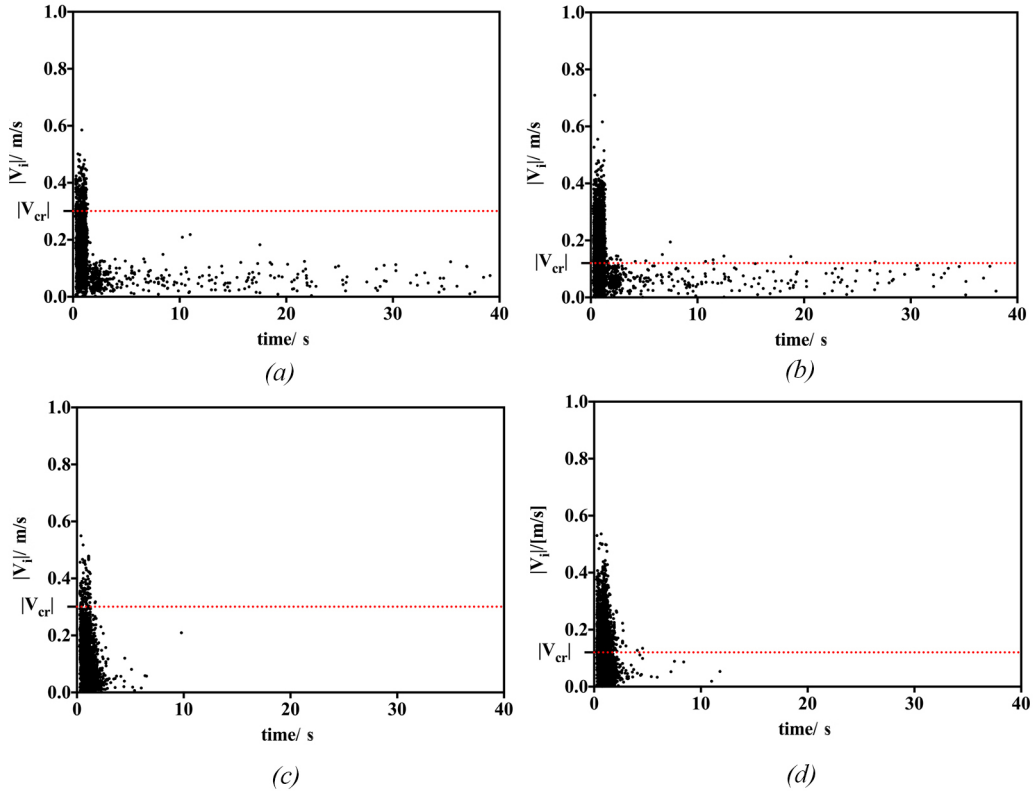
Fig. 8.13 The variation of V_i with the simulation time for SCVD cases, (a) $\Delta T = -200$ K, $d_p = 1$ μm, (b) $\Delta T = -200$ K, $d_p = 3$ μm, (c) $\Delta T = -900$ K, $d_p = 1$ μm, (d) $\Delta T = -900$ K, $d_p = 3$ μm.

Figure 8.14 shows the equivalent velocity distributions for RCVD. These diagrams do not indicate any substantial changes in impact velocity due to buoyancy effects that are driven by negative ΔT values compared to Fig. 8.9. However, the total number of particle-surface interactions have been increased in the negative ΔT cases when compared to positive ΔT cases of RCVD presented in Fig. 8.9. Hence, the attractive nature of thermophoretic forces are more apparent in RCVD cases, but the majority of registered interactions occurred above the critical velocity (V_{cr}), which result in rebound of particles on the surface.
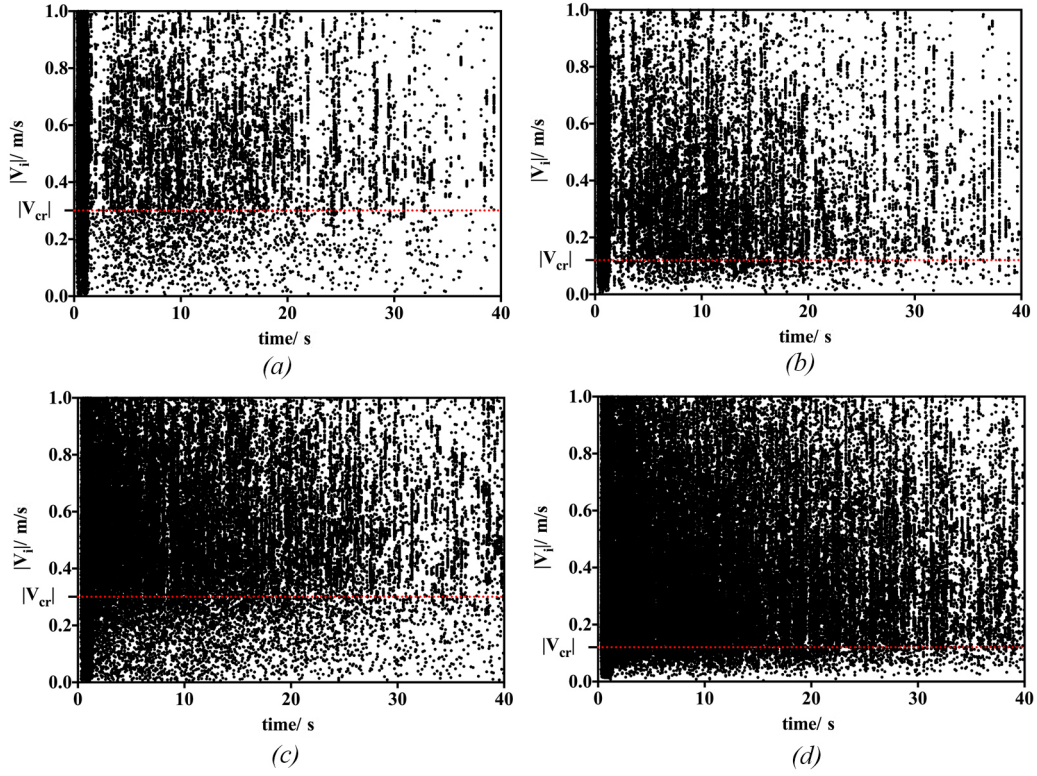
Fig. 8.14 The variation of V_i with the simulation time for RCVD cases, (a) $\Delta T = -200$ K, $d_p = 1\ \mu$m, (b) $\Delta T = -200$ K, $d_p = 3\ \mu$m, (c) $\Delta T = -900$ K , $d_p = 1\ \mu$m, (d) $\Delta T = -900$ K, $d_p = 3\ \mu$m.

According to Fig. 8.15, the deposition efficiency of SCVDs at $\Delta T = -500$ K is slightly lower compared to the $\Delta T = -200$ K due to the strong buoyancy effects, in which the attractive thermophoretic forces are not enough to overcome these buoyancy forces. However, at $\Delta T = -900$ K, the thermophoretic forces are strong enough, so the deposition efficiency is predicted to increase compared to the lower ΔT values. The largest particles are highly affected by the particle-surface interactions, which result in approximately a 1% drop in particle deposition efficiency.
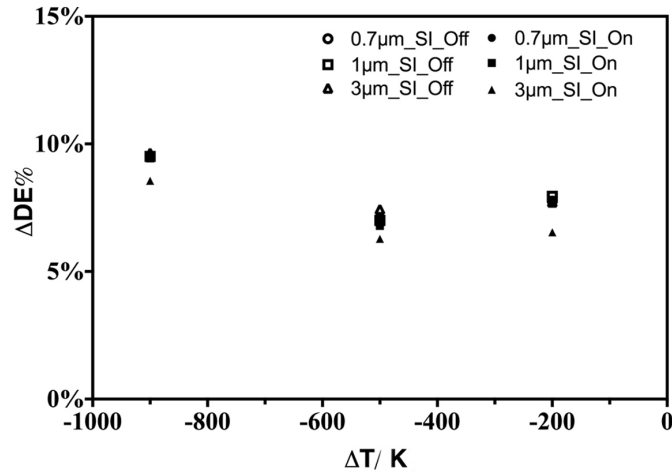
Fig. 8.15 Variation of deposition efficiencies with negative ΔT values for SCVD.

Figure 8.16 shows the corresponding deposition efficiency plots for RCVD cases, The deposition efficiency increases with increasing ΔT values. However, when compared to the SCVD counterparts, RCVDs are more affected by the particle-surface interaction, which is evidenced by the high rebounds recorded in Fig. 8.14 (c) & (d). Like the SCVD cases, the lowest particle deposition efficiencies is recorded with the largest particles. Apart from the particle size, the particle deposition efficiency in RCVDs depends on ΔT values, and higher ΔT values reducing the deposition efficiency. The actual values reside between 4%–5% compared to the 0.7 μm particles, 3 μm particles show a deposition efficiency drop for $\Delta T = -200$ K of 4%–5% for $\Delta T = -500$ K and of 13%–10% drop for $\Delta T = -900$ K. Even though the higher ΔT values give a higher penalty in terms of deposition efficiency, their efficiencies are still higher than the deposition efficiencies of lower ΔT values, which is preferable from a particle deposition perspective.
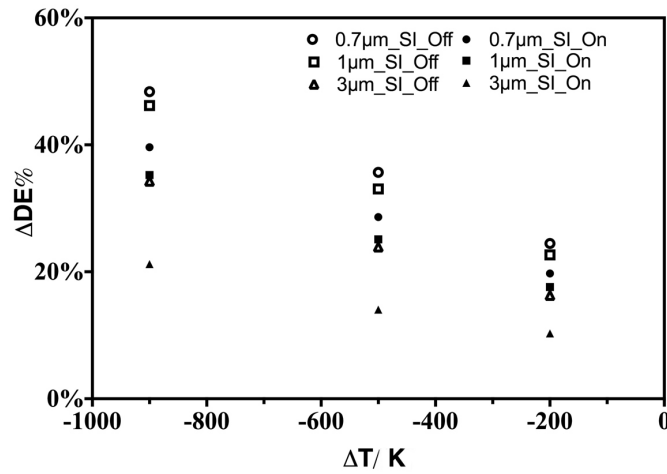
Fig. 8.16 Variation of deposition efficiencies with negative ΔT values for RCVD.

8.3.3   Particle-surface interactions with particle size distributions

In this section, the Rosin-Rammler particle size distribution, which is a widely used particle distribution in chemical engineering and pharmaceutical applications (Djamarani and Clark, 1997), has been used in the simulations, and the size distribution of deposited particles on the rotor are observed. Figure 8.17 shows the input particle size distribution, which has a mean value of 0.993 μm and a standard deviation of 0.323 μm. When analysing the particle depositions on the rotor, the respective particle deposition distributions for the "top", "bottom" and "side" surfaces of the rotor are considered. Further, radial dependency of the particle deposition distributions are studied by dividing the rotor into three concentric radial bands (say a_1, a_2 and a_3) as shown in Fig. 8.18. These radial bands have equal surface areas and they divide the entire rotor surface into three equal subsections (i.e. $a_1 = a_2 = a_3 = A_{disk}/3$), where A_{disk} is the surface area of the rotor.

191
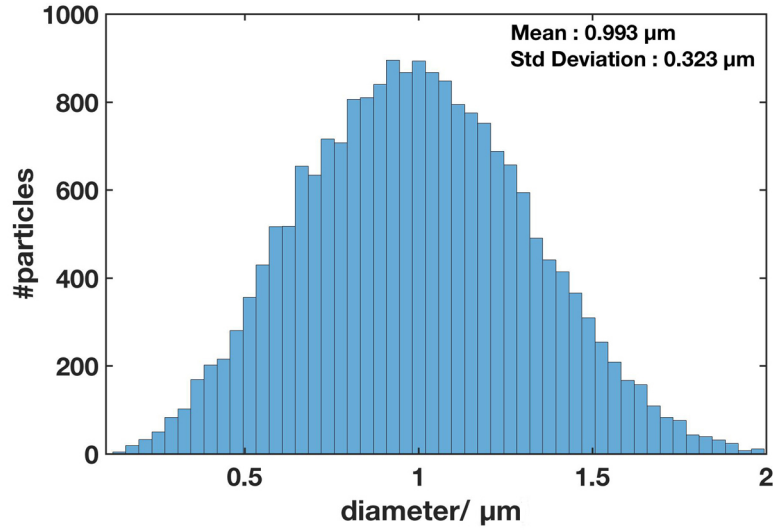
Fig. 8.17 Input Rosin-Rammler particle distribution at the start of the simulation.
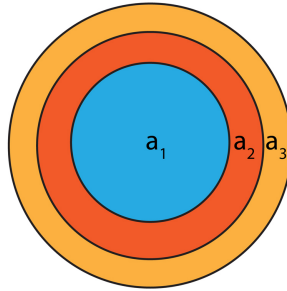
Fig. 8.18 The three bands of the disk, (a) a_1 central band, (b) a_2 middle band, (c) a_3 outer band.

Figure 8.19 (a) & (b) show the deposition distributions for the SCVD and the RCVD cases operate under $\Delta T = 200$ K condition, and three separate particle deposition distributions are derived to represent the top, bottom and side surfaces of the rotor. Figure 8.20 (a) shows that the majority of these depositions occur on the top surface of the rotor, at which the trend is common for both SCVD and RCVD cases but the RCVD case shows higher DE% on the bottom surface than the similar SCVD case. This deposition pattern may be due to the rotational motion of the disk and this attribute also appeared in Section 7.3.2, in which the rotor was assumed to be a perfect sink for all the inbound particles. Therefore, this is not a characteristic feature of particle-surface interactions. The SCVD and RCVD cases show overall reductions of $\Delta DE_{SI}= 17.1\%$ and 34.1%, respectively. The top surfaces show

the highest ΔDE_{SI} for both SCVD and RCVD cases and the values are 21.1% and 33.8%, respectively.

Fig. 8.19 The particle deposition histograms for positive thermophoretic forces $\Delta T = 200$ K, (a) particle distributions by the surface of the rotor for SCVD, (b) particle distributions by the surface of the rotor surfaces of RCVD, (c) particle distributions at different radial bands of SCVD, (d) particle distributions at different radial bands of RCVD.

Figure 8.19 (c) & (d) show the particle deposition distributions obtained for three radial bands. According to Fig. 8.20 (b), the central bands (a_1) of both SCVD and RCVD cases attract the majority of the particles inside the chamber, followed by the outer band (a_3). The middle band shows the lowest DE% in these cases. The middle band a_2 shows the highest $\Delta DE_{SI} = 25.3\%$ for the SCVD case, and the outer band a_3 shows the highest $\Delta DE_{SI} = 37.5\%$ for the RCVD case.

Fig. 8.20 Breakdown of deposition contributions for $\Delta T = 200$ K, (a) by the surfaces of the disk, (b) by the radial bands of the disk.

Table 8.1 shows mean diameters for the different deposition distributions that are shown in Fig. 8.19. In general, the side surface has the largest mean diameters for both SCVD and RCVD cases, and the lowest values reported on the top surface for both SCVD and RCVD cases. The top surface shows the highest Δd_{mean} for both SCVD and RCVD cases and their values are $\Delta d_{mean} = 2.5\%$ and 2.8%, respectively. The side surface shows a net increase in mean diameters (i.e. negative values for Δd_{mean}) by -3.9% for the SCVD and -4.5% for the RCVD. In the current simulations, the highest net increase in mean diameters reported on the bottom surface of the SCVD case, and the value is $\Delta d_{mean} = -6.5\%$. By comparing the mean diameter values in the radial bands, the central region of the disk (a_1) attracts heavier particles followed by outer region (a_3). The SCVD case shows the overall highest $\Delta d_{mean} = 9.29\%$ at the a_2 region, and the a_3 region reported the highest value of $\Delta d_{mean} = 7.46\%$ for the RCVD case.

Case	Surfaces / μm			Radial bands / μm		
	Top	Bottom	Side	a_1	a_2	a_3
SCVD S-I ON	0.963	1.017	1.027	0.496	0.205	0.28
SCVD S-I OFF	0.988	0.955	0.988	0.516	0.226	0.238
RCVD S-I ON	0.951	0.944	1.003	0.4	0.263	0.285
RCVD S-I OFF	0.979	0.97	0.959	0.392	0.264	0.308

Table 8.1 Mean particle diameters of surface and radial particle deposition distributions for SCVD and RCVD cases of $\Delta T = 200$ K.

Figure 8.21 (a) & (b) show the corresponding surface-particle distributions under the negative ΔT value. These particle deposition distributions confirm that the negative ΔT cases

only give minor characteristic changes in the deposition distributions. However, as expected, the attractive thermophoretic forces result in a higher overall deposition efficiency compared to the positive ΔT cases. The overall reductions reported as $\Delta DE_{SI} = 10.7\%$ and 24.6% for the respective SCVD and RCVD cases and these reductions are lower than the values reported for positive ΔT. Figure 8.22 (a) shows that the top surface is the highest impacted surface of the rotor due to the particle-surface interaction effects and the corresponding reductions for the top surfaces of the SCVD and RCVD cases are $\Delta DE_{SI} = 13.5\%$ and 29.1%, respectively. These net reductions on the top surfaces are slightly lower when they compared to the positive ΔT cases.
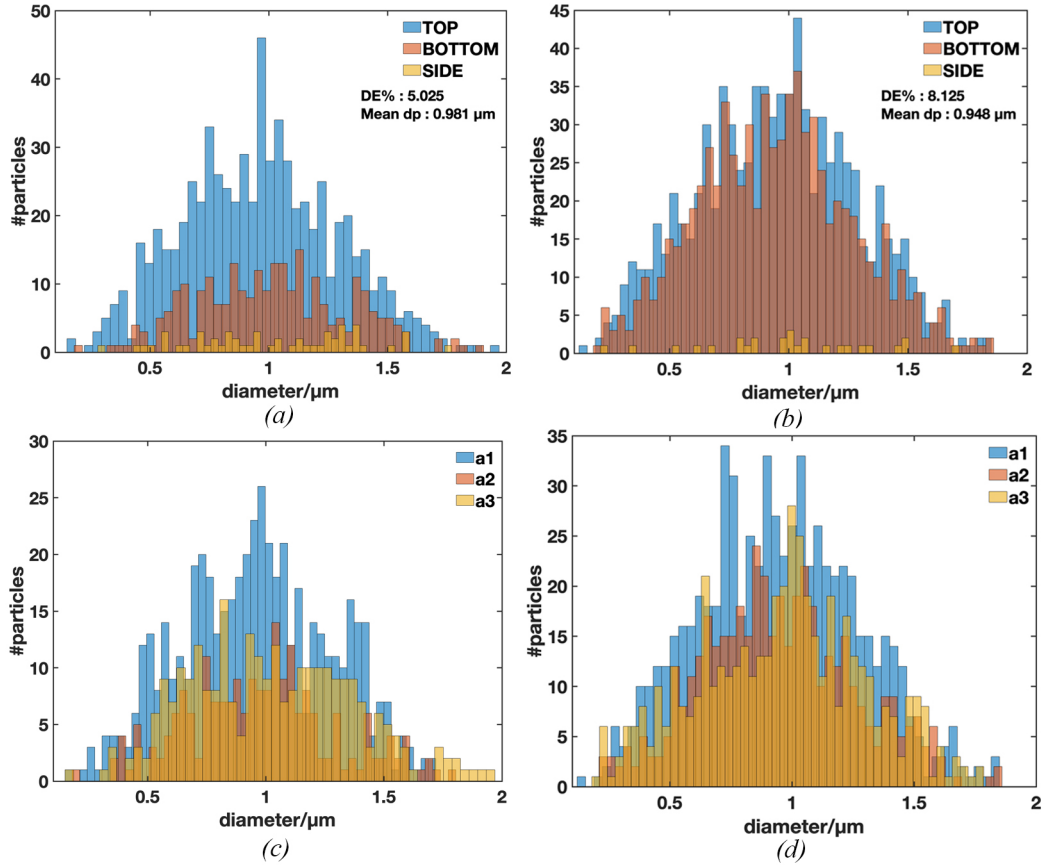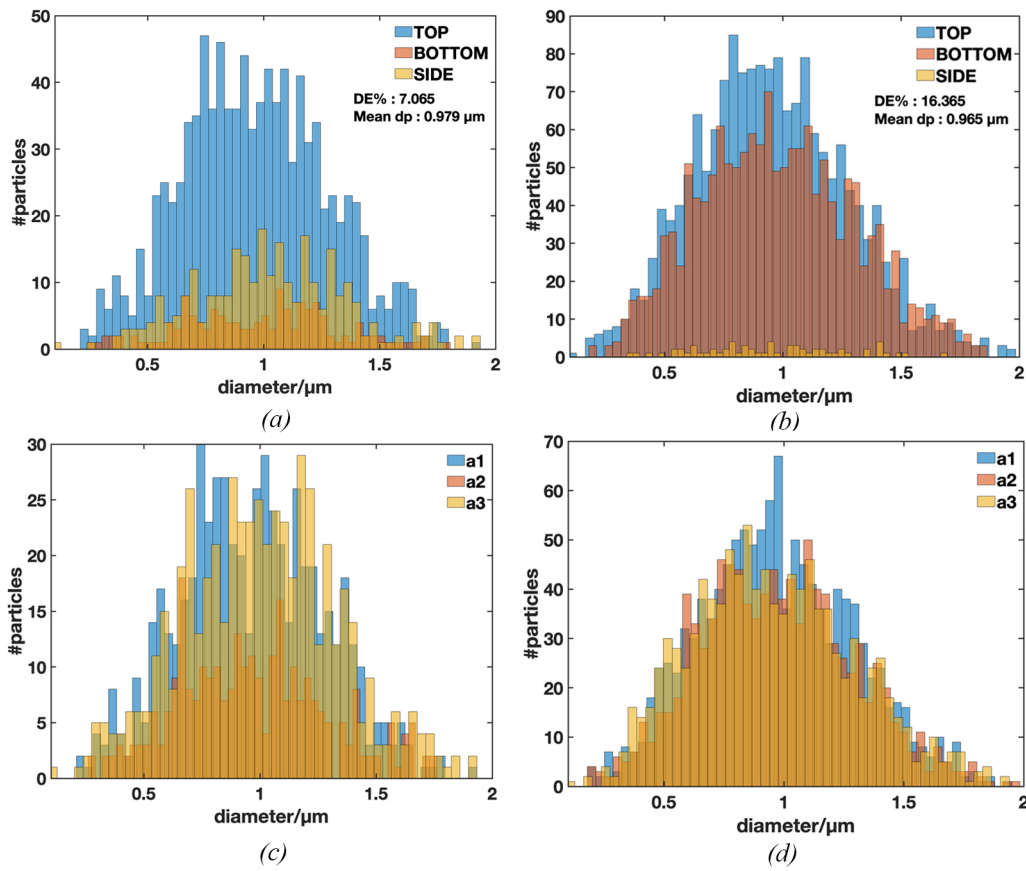

Fig. 8.21 The particle deposition histograms for negative thermophoretic forces $\Delta T = -200$ K, (a) particle distributions by the surface of the rotor for SCVD, (b) particle distributions by the surface of the rotor surfaces of RCVD, (c) particle distributions at different radial bands of SCVD, (d) particle distributions at different radial bands of RCVD.
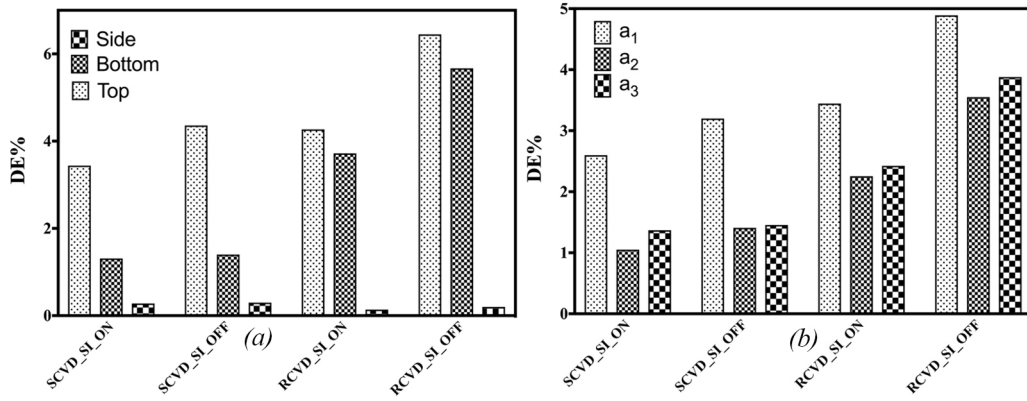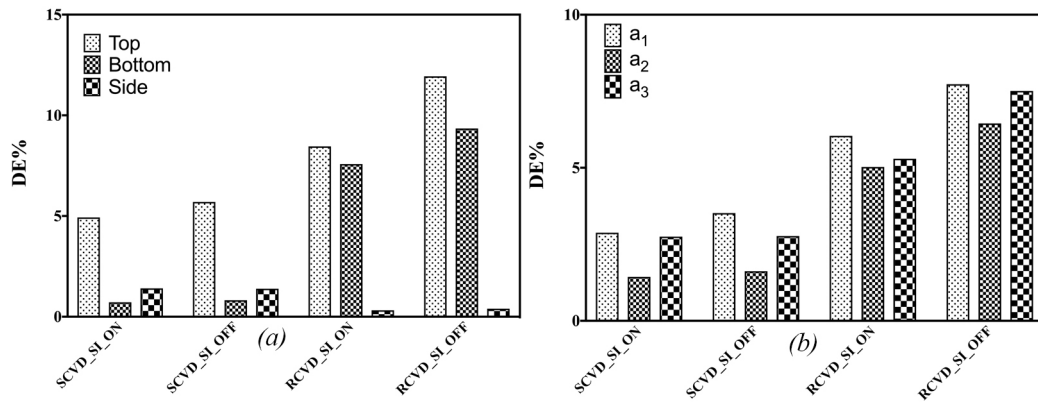
Fig. 8.22 Breakdown of deposition contributions for $\Delta T = -200$ K, (a) by the surfaces of the disk, (b) by the radial bands of the disk.

Figure 8.22 (b) shows the percentages of DE% by the radial bands and it shows that the a_1 region has the highest DE% followed by the a_3 region. Similar to positive ΔT cases, the a_2 region shows the lowest DE%. For the case of SCVD, the highest $\Delta DE_{SI} = 18.2\%$ reported at the a_1 region and the a_3 region reported the highest value of $\Delta DE_{SI} = 29.5\%$ for the RCVD case.

Table 8.2 shows the corresponding mean diameters for the different deposition distributions for the cases of negative ΔT. Similar to the positive ΔT cases, the top surface attracts heavier particles and the SCVD and RCVD cases reported the highest values of $\Delta d_{mean} = 2.6\%$ and 1.95%, respectively. Here, both bottom and side surfaces show a net increase in mean diameters and $\Delta d_{mean} = -2.5\%$ is the highest increase, which is reported on the bottom surface of the SCVD case. Similar to the positive ΔT case, heavy particles are deposited at the a_1 and a_3 regions. The SCVD case shows the highest $\Delta d_{mean} = 11.08\%$ in the a_1, and the a_3 region has the highest $\Delta d_{mean} = 7.2\%$ for the RCVD case.

Case	Surfaces / μm			Radial bands / μm		
	Top	Bottom	Side	a_1	a_2	a_3
SCVD S-I ON	0.965	0.985	1.026	0.393	0.197	0.390
SCVD S-I OFF	0.991	0.961	0.997	0.442	0.198	0.349
RCVD S-I ON	0.955	0.976	0.953	0.358	0.298	0.308
RCVD S-I OFF	0.974	0.969	0.941	0.349	0.290	0.332

Table 8.2 Mean particle diameters of surface and radial particle deposition distributions for SCVD and RCVD cases of $\Delta T = -200$ K.

8.4   Summary and conclusions

This chapter considers the particle-surface interaction in SCVD and RCVD simulations. For this chapter, silicon particles in three sizes have been chosen, $d_p = 0.7$ μm,1 μm,3 μm. The particle-surface interaction model is similar to the models described in the investigations of Xu and Willeke (1993) and Fergus (2010), but the current model is a more simplified version by assuming only right angle impacts and no resuspension of particles.

A series of numerical test cases have been prepared, similar to the previous chapter. The initial result suggests that larger particles tend to have lower DE% than the smaller particles under the same conditions. Further, this shows that the rotation of the disk substantially increases the particle-surface interactions, due to the high relative motion between the particle and the disk surface. The final section used a Rosin-Rammler particle distribution, which introduces a cluster of particles with different particle diameters ranging from $d_p = 0.1$ μm to 2 μm. The particle deposition frequency plots (histograms) are constructed to observe the particle deposition distributions. These frequency plots suggest that the thermophoretic and rotational effects are prominent factors in determining DE% of these cases.

This chapter reveals that the particle-surface interactions are more significant for heavier particles and this may decrease the effective deposition efficiencies. The RCVD cases showed higher effects than the similar SCVD case. The results of Section 8.3.3 show that the top surface was the most affected surface of the disk due to the particle-surface interaction effects, and the central (middle) one-third of the disk was more attracted by the heavier particles.

Chapter 9

Final remarks and future work

9.1 Conclusions

This study investigated mass, momentum and heat transfer properties of rotor-stator cavities using CFD methods. The entire investigation was conducted using OpenFOAM, which is a second-order accurate FVM solver. The rotor-stator cavities of $G = 0.2$ and $R_m = 1.8$ at operations Reynolds number of $Re_\omega = 1 \times 10^5$ and 4×10^5 were used to achieve the results.

Chapter 4 investigated the momentum transport properties of the rotor-stator cavities. This chapter concluded that the second-order FVM is accurate enough to conduct the engineering flow simulations on rotor-stator cavities, despite the fact that the overwhelming number of previous investigations adopted the higher-order methods. The mean velocity profiles and turbulent intensity profiles were validated against previous numerical and experimental results. The flow visualisations of rotor and stator boundary layers of $Re_\omega = 1 \times 10^5$ and 4×10^5 confirmed that the stator boundary layer attains turbulent behaviour at a much lower Reynolds number than the rotor boundary layer. At the higher Reynolds number of $Re_\omega = 4 \times 10^5$, 15 Type II spiral arms with a $\varepsilon \approx -18°$ inclination to the tangential direction were observed. Close observation of the inflow disturbance levels and instantaneous tangential velocity profile at the rotor boundary layer suggested that the possible turbulent transition mechanism could be the mechanism (B) in Faller (1991)'s investigation, which was also previously explained by Makino et al. (2015).

Then, the Busse and Sandham (2012)'s parametric model was used to represent surface roughness on rotor-stator cavities. For simplicity roughness was applied on the rotor boundary layer. Initially, a number of test cases in low Reynolds number $Re_\omega = 1 \times 10^5$ were considered for the range of normalised parametric model constants of $h_r^* = 0.0025$–0.025 and $\alpha^* = 0.1$–1.0. The results showed that the peak values of the rotor mean velocity profiles increase as the roughness effects increase The other boundary layer properties, such as dis-

placement thickness, shape factors, were affected by the roughness effects. If the roughness parameters are high enough (i.e. when the model constants higher than the $\alpha^* = 0.4$ and $h_r^* = 0.005$), these roughness effects on the rotor impose significant changes in time-averaged velocity, displacement thickness, shape factors profiles at the smooth stator. The entrainment coefficients of the rotor-stator cavities were increased due to the roughness on the rotor. These observations showed that the roughness layers on the rotor boundary layer could initiate non-localise effects in the cavity under the higher α^*, h_r^* values. Further, by considering these initial observations, it can conclude that h_r^* is a dominant factor than α^*. Hence, the controlling the thickness of the roughness layer (or the height of the discrete roughness element) is import to achieve the outer layer similarity of the rough boundary layers.

Next, at the higher Reynolds number of $Re_\omega = 4 \times 10^5$, the rotor boundary was simulated to investigate the effects of a rough rotor on turbulent properties of the rotor-stator cavities. Here, two test cases low ($h_r^* = 0.00125$) and high ($h_r^* = 0.00375$) have been considered and both of them have $\alpha^* = 0.4$. The peak values of both radial and tangential turbulence intensities of the rotor boundary decrease due to damping effects of the roughness terms, but the corresponding values at the stator layers are relatively unaffected due to the lower roughness effect on these simulations. Hence, in these test cases, time-averaged velocity profiles and turbulence intensity profiles suggest that the roughness effects are localised to the rotor boundary layer.

However, the flow visualisation evidenced that the upper junction between the stator layer and outer wall is more disturbed in rough wall cavities. The tangential velocity contours at away from the roughness layer showed effects of roughness in both the rotor and stator boundary layers. The iso-surface visualisation near the rotor boundary showed more enlarged vortex structure on rough wall layers. These results suggest the rotor-stator disk cavities are unstable even for small roughness effects and the outer wall is a way of rapid transporting these roughness effects from the rotor to the stator. Further, the high Re_ω case resulted in iso-surface visualisations near the rotor boundary with enlarged vortex structures on rough wall layers. As mentioned before, the test cases considered here were confined to relatively low h_r^* to values and no significant changes have been observed in turbulent transition properties.

Chapter 6 focused on heat transfer of rotor-stator cavities filled with nanofluids. The simulations were tested on rotor-stator cavities operating at $Re_\omega = 1 \times 10^5$, and nanofluid mixtures with, Al_2O_3 nanoparticle volume fractions, $\phi = 0.02, 0.04, 0.2$. For the simulations of the nanofluids, two transport models were adopted. The single-phase model (S_P) assumes homogeneous volume fractions throughout the simulations, and the two-phase model (T_P) imposed the slip velocity between the nanoparticles and the carrier phase, in which the

Brownian diffusion and thermophoresis effects are considered to be the cause of these slip velocities.

Both models suggested that the nanofluids have a minimal effect on momentum fields, but the instantaneous and mean temperature distributions show more significant changes in the cases with higher nanoparticle volume fractions due to the higher thermal conductivities of nanoparticles. The S_P models predicted a marginal increase in mean temperature compared to the same condition at T_P simulations. This can be explained by the displacement of nanoparticles at the hot stator boundary, at which the thermophoresis forces dominate over the Brownian forces. Further, the local Nusselt number and the mean Nusselt number distributions at the stator boundary have been obtained for all parameter and model cases and these distributions compared with a power law model. The model was found to hold at all volume fractions despite it arising from an experimental study of conventional fluid. The mean Nusselt numbers show 6%–70% increase due to the different nanoparticle volume fractions of $\phi = 0.02$–0.2. For the highest nanoparticle volume fraction $\phi = 0.2$, the mean Nusselt number of S_P simulation is 4% higher than the similar T_P simulation but the disparity is reduced as the nanoparticle volume fraction decreases. The results show that the nanoparticle suspension on a conventional fluid increases the effective heat transfer capabilities of the nanofluid mixture and the process does not impose a significant penalty on momentum transport properties, which is the main motivation of using the nanoparticles suspensions for the heat transfer applications over the microparticle suspensions.

Chapters 7 & 8 discussed the mass transfer aspects of rotor-stator flows. Here, instead of a rotor-stator cavity, a rotating chemical vapour deposition chamber (RCVD) has been used, which is an engineering application based on rotor-stator disks. A stationary disk chemical vapour deposition chamber (SCVD) was also simulated for the comparison purposes. The velocity fields of these two CVD obtained using FVM and the standard k-ε model, and submicron particle phase with particle diameters, $d_p =0.01, 0.1, 1.0 \ \mu$m simulated in a Lagrangian framework.

In all the test cases, RCVD showed higher particle deposition efficiencies (DE%) than the equivalent SCVD case, and some RCVD cases showed an over 8% increase in DE% over a similar SCVD case. For the SCVD cases, top surface attracted over 70% of total particle deposition but similar RCVD cases show more even particle distributions among the top and bottom surfaces.

The thermophoretic forces impose a significant effect on the particle phase and the positive thermophoretic forces, which acted as repulsive forces during the current cases, almost cease the particle deposition on the rotor, if the carrier phase turbulence effects are neglected. However, the carrier phase turbulence can subdue the positive thermophoretic

forces and restored the particle deposition on the rotor, but still, these cases showed decreased DE% when them compared to the cases without thermophoretic forces imposed. Further, the initial particle injection location at the inlet of the cavity has a significant effect on the DE%. If particles injections were concentrated in an inner central region (which was selected as 8% of the total area of the inlet) of the inlet, the SCVD case showed over ten times improvement of DE% compared to compared to the cases in which particle injections were more concentrated in an outer region of the inlet. The corresponding gain is less for RCVD but still, it showed over three times of an improvement of DE%.

The second part of these simulations considered the particle-surface interactions using an energy-based model near the rotor surface. The validation of this computational model was conducted using a uniform distribution that consisted of 20,000 Silicon particles with different particle diameters ranging from $d_p = 0.001$–$3.0\ \mu$m. Initial observations showed that the mean particle diameters of the deposition distributions are dropped by 7.5% and 6.6% for the SCVD and RCVD cases due to the particle-surface interaction effects.

Then, the Silicon particles of three different sizes, $d_p = 0.7\ \mu$m, $1.0\ \mu$m, $3\ \mu$m, were used. As observed before, the particle-surface interaction was more significant with the larger (heavier) particles, and it reduced the DE% of these particles. The thermophoretic and rotational effects are the prominent factors in determining DE% of these cases.

After the fixed size particle simulations, a Rosin-Rammler particle distribution, which has a mean diameter of 0.993 μm and 20,000 particles ranging from $d_p = 0.1$–$3\ \mu$m, was used during initial particle injection. The respective deposition distributions on the rotor showed that top surface attracted most particles and this surface reported the highest reductions in particle deposition of the rotor due to the particle-surface interactions for both SCVD and RCVD cases. By comparing the ΔDE$_{SI}$ of the SCVD and RCVD cases, it can see that RCVDs are more affected by particle-surface interactions, and they showed highest values of ΔDE$_{SI} = 34.1\%$ and 29.1% for the cases of positive thermophoretic force and negative thermophoretic force, respectively. The mean diameters of these distributions showed that the bottom surface attracts bigger particles than the top surface. As observed in the previous chapter, the central region of the disk (in this case, the central region located at the middle of the disk and it occupies 33.3% of the disk surface) has the highest DE% and the mean diameters of the particle distributions in this region relativity higher than the mid and outer regions of the disk.

Chapters 7 & 8 provided useful information on micron and submicron particle dynamics and their deposition behaviours under various flow and thermal conditions. In general, the rotation motion of the disk has the highest impact on the particle deposition followed by the carrier phase turbulence and the nature of the thermophoretic force. In practice,

contamination on the thin films can be avoided by maintaining slow rotation speeds of the disk and laminar status of the flow field. Under these conditions, a heated wafer can produce a particle free zone near the wafer surface, which can guarantee zero contamination depositions on the wafer. Further, particle-surface interaction modelling showed that the inertia of the contamination particles has an impact on their deposition efficiencies and the current simulation results showed that larger (or heavier) contamination particles are susceptible to rebound on the surface. However, the significance of this effect is secondary when it compared to the impacts of the disk rotation, turbulent and thermophoretic effects on the DE%.

These numerical simulations were able to shed some light on the engineering rotor-stator flows, which are relatively undocumented in previous investigations. However, the current simulations can be further improved to get the better results, or it can be re-run under the different configurations to get a different perspective on the result presented here. The following section discusses the potential future work on the current investigation.

9.2   Future work

This investigation was able to achieve many of its intended objectives by studying mass, momentum and heat transfer aspects of rotor-stator disk cavities. However, there is still room for improvements in the approaches used in this investigation.

Here, the roughness modelling was done through the uncalibrated model constants of Busse and Sandham (2012)'s parametric model. However, in future, an investigation can conduct with model constants that correlates with real-world rough surfaces. This can be extended to obtain roughness functions for rotor-stator cavities. The current investigation did not consider the influence of roughness on turbulent transitions aspects and further simulation data can be collected to study the properties of turbulent transition of rough rotor-stator cavities.

The heat transfer capabilities of rotor-stator cavities filled with nanofluid superior when it compares to a cavity filled with water. During the current investigations, the Reynolds numbers are limited to $Re_\omega = 1 \times 10^5$ due to time limitations. In the future, this can extend to cavities operate in higher Reynolds numbers, which could result in high levels of turbulence in the flow field. A similar approach can be considered to cavities with different aspect ratios (G) and curvatures (R_m). More investigations in this area can lead to a more refined Nusselt number correlation model that is suitable for studying the heat transfer in rotor-stator cavities due to nanofluids.

The Lagrangian particle tracking of RCVD chamber showed that the rotation of the disk highly influences the dynamics and depositions of the particles, and further, these simulations can be investigated in higher rotation rates of the disk. In the current investigation, the turbulence of the carrier phase was emulated by EIM method but the simulations can be significantly improved by using a DNS or high fidelity LES turbulent methods, which can provide instantaneous velocity fields of the carrier phase without relying much on the modelling aspects of the EIM model. These recommendations are valid for the particle-surface interactions simulations as well. Apart from that, the particle-surface modelling can be enhanced by considering the particle impacts with the incident angles less than 90° to the surface. Further, considering the particle resuspension into the flow field can result in more realistic simulation models.

References

Achenbach, E. (1974), 'Vortex shedding from spheres', *Journal of Fluid Mechanics* **62**(2), 209–221.

Alinia, M., Ganji, D. and Gorji-Bandpy, M. (2011), 'Numerical study of mixed convection in an inclined two sided lid driven cavity filled with nanofluid using two-phase mixture model', *International Communications in Heat and Mass Transfer* **38**(10), 1428–1435.

Alveroglu, B., Segalini, A. and Garrett, S. J. (2016), 'The effect of surface roughness on the convective instability of the BEK family of boundary-layer flows', *European Journal of Mechanics-B/Fluids* **56**, 178–187.

Amiri, A. E., Hannani, S. K. and Mashayek, F. (2006), 'Large-eddy simulation of heavy-particle transport in turbulent channel flow', *Numerical Heat Transfer, Part B: Fundamentals* **50**(4), 285–313.

Andersson, H. I. and Lygren, M. (2006), 'LES of open rotor–stator flow', *International journal of heat and fluid flow* **27**(4), 551–557.

Antonia, R. and Luxton, R. (1971), 'The response of a turbulent boundary layer to a step change in surface roughness Part 1. Smooth to rough', *Journal of Fluid Mechanics* **48**(4), 721–761.

Antonia, R. and Luxton, R. (1972), 'The response of a turbulent boundary layer to a step change in surface roughness. Part 2. Rough-to-smooth', *Journal of Fluid Mechanics* **53**(4), 737–757.

Antonopoulos-Domis, M. (1981), 'Large-eddy simulation of a passive scalar in isotropic turbulence', *Journal of Fluid Mechanics* **104**, 55–79.

Appelquist, E., Imayama, S., Alfredsson, P. H., Schlatter, P. and Lingwood, R. (2016), 'Linear disturbances in the rotating-disk flow: a comparison between results from simulations, experiments and theory', *European Journal of Mechanics-B/Fluids* **55**, 170–181.

Appelquist, E., Schlatter, P., Alfredsson, P. and Lingwood, R. (2015), 'Global linear instability of the rotating-disk flow investigated through simulations', *Journal of Fluid Mechanics* **765**, 612–631.

Aupoix, B. (2016), 'Revisiting the discrete element method for predictions of flows over rough surfaces', *Journal of Fluids Engineering* **138**(3), 031205.

Auton, T. (1987), 'The lift force on a spherical body in a rotational flow', *Journal of fluid Mechanics* **183**, 199–218.

Bachok, N., Ishak, A. and Pop, I. (2011), 'Flow and heat transfer over a rotating porous disk in a nanofluid', *Physica B: Condensed Matter* **406**(9), 1767–1772.

Bae, G.-N., Lee, C. S. and Park, S. O. (1994), 'Measurement of particle deposition velocity toward a horizontal semiconductor wafer by using a wafer surface scanner', *Aerosol science and technology* **21**(1), 72–82.

Bae, G.-N., Lee, C. S. and Park, S. O. (1995), 'Measurements and control of particle deposition velocity on a horizontal wafer with thermophoretic effect', *Aerosol science and technology* **23**(3), 321–330.

Batchelor, G. (1977), 'The effect of brownian motion on the bulk stress in a suspension of spherical particles', *Journal of fluid mechanics* **83**(1), 97–117.

Batchelor, G. K. (1951), 'Note on a class of solutions of the navier-stokes equations representing steady rotationally-symmetric flow', *The quarterly journal of mechanics and applied mathematics* **4**(1), 29–41.

Bhaganagar, K., Kim, J. and Coleman, G. (2004), 'Effect of roughness on wall-bounded turbulence', *Flow, turbulence and combustion* **72**(2-4), 463–492.

Bhattacharya, P., Saha, S., Yadav, A., Phelan, P. and Prasher, R. (2004), 'Brownian dynamics simulation to determine the effective thermal conductivity of nanofluids', *Journal of Applied Physics* **95**(11), 6492–6494.

Blackman, K., Perret, L., Calmet, I. and Rivet, C. (2017), 'Turbulent kinetic energy budget in the boundary layer developing over an urban-like rough wall using PIV', *Physics of Fluids* **29**(8), 085113.

Bödewadt, U. T. (1940), 'Die drehstr ömung über festem grunde', *ZAMM-Journal of Applied Mathematics and Mechanics/Zeitschrift für Angewandte Mathematik und Mechanik* **20**(5), 241–253.

Boussinesq, J. (1877), *Essai sur la théorie des eaux courantes*, Impr. nationale.

Breugem, W. and Boersma, B. (2005), 'Direct numerical simulations of turbulent flow over a permeable wall using a direct and a continuum approach', *Physics of fluids* **17**(2), 025103.

Brinkman, H. (1952), 'The viscosity of concentrated suspensions and solutions', *The Journal of Chemical Physics* **20**(4), 571–571.

Bruggeman, V. D. (1935), 'Berechnung verschiedener physikalischer Konstanten von heterogenen Substanzen. i. Dielektrizitätskonstanten und Leitfähigkeiten der Mischkörper aus isotropen Substanzen', *Annalen der physik* **416**(7), 636–664.

Buongiorno, J. (2006), 'Convective transport in nanofluids', *Journal of heat transfer* **128**(3), 240–250.

Burns, T., Davis, R. and Moore, E. F. (1997), 'Dynamical systems approach to particle transport modeling in dilute gas-particle flows with application to a chemical vapor deposition reactor', *Aerosol science and technology* **26**(3), 193–211.

Burry, D. and Bergeles, G. (1993), 'Dispersion of particles in anisotropic turbulent flows', *International Journal of Multiphase Flow* **19**(4), 651–664.

Busse, A. and Sandham, N. D. (2012), 'Parametric forcing approach to rough-wall turbulent channel flow', *Journal of Fluid Mechanics* **712**, 169–202.

Cheah, S., Iacovides, H., Jackson, D., Ji, H. and Launder, B. (1994), 'Experimental investigation of enclosed rotor-stator disk flows', *Experimental thermal and fluid science* **9**(4), 445–455.

Chein, R. and Su, T. (2004), 'Numerical modeling of particle dynamics in a cylindrical chamber containing a rotating disk', *Aerosol science and technology* **38**(3), 185–193.

Cheng, Y.-S. and Yeh, H.-C. (1979), 'Particle bounce in cascade impactors.', *Environmental Science & Technology* **13**(11), 1392–1396.

Choi, H., Moin, P. and Kim, J. (1993), 'Direct numerical simulation of turbulent flow over riblets', *Journal of fluid mechanics* **255**, 503–539.

Choi, S. U. and Eastman, J. A. (1995), Enhancing thermal conductivity of fluids with nanoparticles, Technical report, Argonne National Lab., IL (United States).

Clift, R. and Gauvin, W. (1971), 'Motion of entrained particles in gas streams', *The Canadian Journal of Chemical Engineering* **49**(4), 439–448.

Cobb, E. and Saunders, O. (1956), 'Heat transfer from a rotating disk', *Proc. R. Soc. Lond. A* **236**(1206), 343–351.

Crowe, C., Sommerfeld, M. and Tsuji, Y. (1998), 'Fundamentals of gas-particle and gas-droplet flows'.

Cui, J., Patel, V. C. and Lin, C.-L. (2003), 'Prediction of turbulent flow over rough surfaces using a force field in Large Eddy Simulation', *Journal of fluids engineering* **125**(1), 2–9.

Dahneke, B. (1971), 'The capture of aerosol particles by surfaces', *Journal of colloid and interface science* **37**(2), 342–353.

Dahneke, B. (1975), 'Further measurements of the bouncing of small latex spheres', *Journal of Colloid and Interface Science* **51**(1), 58–65.

Daily, J. W. and Nece, R. E. (1960), 'Chamber dimension effects on induced flow and frictional resistance of enclosed rotating disks', *Journal of basic engineering* **82**(1), 217–230.

Darcy, H. (1857), *Recherches expérimentales relatives au mouvement de l'eau dans les tuyaux*, Vol. 1, Mallet-Bachelier.

Das, S. K., Choi, S. U. and Patel, H. E. (2006), 'Heat transfer in nanofluids—a review', *Heat transfer engineering* **27**(10), 3–19.

Davies, C. (1945), 'Definitive equations for the fluid resistance of spheres', *Proceedings of the Physical Society* **57**(4), 259.

Davies, C. and Carpenter, P. W. (2003), 'Global behaviour corresponding to the absolute instability of the rotating-disc boundary layer', *Journal of Fluid Mechanics* **486**, 287–329.

Davis, R., Moore, E. and Zachariah, M. (1993), 'Numerical modeling of particle dynamics in a rotating disk chemical vapor deposition reactor', *Journal of crystal growth* **132**(3-4), 513–522.

De Angelis, V., Lombardi, P. and Banerjee, S. (1997), 'Direct numerical simulation of turbulent flow over a wavy wall', *Physics of Fluids* **9**(8), 2429–2442.

De Villiers, E. (2006), The potential of large eddy simulation for the modelling of wall bounded flows, PhD thesis, Imperial College of Science, Technology and Medicine, UK.

Deardorff, J. W. (1970), 'A numerical study of three-dimensional turbulent channel flow at large reynolds numbers', *Journal of Fluid Mechanics* **41**(2), 453–480.

Demirdžić, I., Lilek, Ž. and Perić, M. (1993), 'A collocated finite volume method for predicting flows at all speeds', *International Journal for Numerical Methods in Fluids* **16**(12), 1029–1050.

Derjaguin, B., Muller, V. and Toporov, Y. P. (1994), 'Effect of contact deformations on the adhesion of particles', *Progress in Surface Science* **45**(1-4), 131–143.

Dijkstra, D. and Van Heijst, G. (1983), 'The flow between two finite rotating disks enclosed by a cylinder', *Journal of Fluid Mechanics* **128**, 123–154.

Djamarani, K. and Clark, I. M. (1997), 'Characterization of particle size based on fine and coarse fractions', *Powder Technology* **93**(2), 101–108.

Eastman, J., Choi, U., Li, S., Soyez, G., Thompson, L. and DiMelfi, R. (1999), 'Novel thermal properties of nanostructured materials', *Materials Science Forum* **312-314**, 629–634.

Einstein, A. (1906), 'A new determination of molecular dimensions', *Ann. Phys.* **19**, 289–306.

Ekman, V. W. (1905), *On the influence of the earth's rotation on ocean-currents*, Almqvist & Wiksells boktryckeri, A.-B.,.

El Tahry, S. (1983), 'k-epsilon equation for compressible reciprocating engine flows', *Journal of Energy* **7**(4), 345–353.

Elena, L. and Schiestel, R. (1996), 'Turbulence modeling of rotating confined flows', *International Journal of Heat and Fluid Flow* **17**(3), 283–289.

Elghobashi, S. (1994), 'On predicting particle-laden turbulent flows', *Applied scientific research* **52**(4), 309–329.

Elkins, C. J. and Eaton, J. K. (2000), 'Turbulent heat and momentum transport on a rotating disk', *Journal of Fluid Mechanics* **402**, 225–253.

Esmen, N. A., Ziegler, P. and Whitfield, R. (1978), 'The adhesion of particles upon impaction', *Journal of Aerosol Science* **9**(6), 547–556.

Fallah, N., Bailey, C., Cross, M. and Taylor, G. (2000), 'Comparison of finite element and finite volume methods application in geometrically nonlinear stress analysis', *Applied Mathematical Modelling* **24**(7), 439–455.

Faller, A. J. (1991), 'Instability and transition of disturbed flow over a rotating disk', *Journal of Fluid Mechanics* **230**, 245–269.

Faller, A. J. and Kaylor, R. E. (1966), 'A numerical study of the instability of the laminar ekman boundary layer', *Journal of the Atmospheric Sciences* **23**(5), 466–480.

Fan, F. G. and Ahmadi, G. (1993), 'A sublayer model for turbulent deposition of particles in vertical ducts with smooth and rough surfaces', *Journal of Aerosol Science* **24**(1), 45–64.

Fan, L. S. and Zhu, C. (2005), *Principles of gas-solid flows*, Cambridge University Press.

Fedorov, B., Plavnik, G., Prokhorov, I. and Zhukhovitskii, L. (1976), 'Transitional flow conditions on a rotating disk', *Journal of Engineering Physics and Thermophysics* **31**(6), 1448–1453.

Fergus, A. (2010), The Integration of Bounce and Resuspension into a Lagrangian Simulation of Particle Movement., PhD thesis, National University of Ireland.

Ferziger, J. H. and Perić, M. (2002), *Computational Methods for Fluid Dynamics*, Springer Berlin Heidelberg.

Flores, O. and Jimenez, J. (2006), 'Effect of wall-boundary disturbances on turbulent channel flows', *Journal of Fluid Mechanics* **566**, 357–376.

Fuchs, N. (1964), 'The mechanics of aerosols', *Pagamon, New York* .

Fureby, C., Tabor, G., Weller, H. and Gosman, A. (1997), 'A comparative study of subgrid-scale models in homogeneous isotropic turbulence', *Physics of fluids* **9**(5), 1416–1429.

Gakis, G., Koronaki, E. and Boudouvis, A. (2015), 'Numerical investigation of multiple stationary and time-periodic flow regimes in vertical rotating disc CVD reactors', *Journal of Crystal Growth* **432**, 152–159.

Gallily, I. and La Mer, V. K. (1958), 'On the behavior of liquid droplets after impinging on solid surfaces', *The Journal of Physical Chemistry* **62**(10), 1295–1299.

Garrett, S. J. and Peake, N. (2002), 'The stability and transition of the boundary layer on a rotating sphere', *Journal of Fluid Mechanics* **456**, 199–218.

Garrett, S. and Peake, N. (2007), 'The absolute instability of the boundary layer on a rotating cone', *European Journal of Mechanics-B/Fluids* **26**(3), 344–353.

Gauthier, G., Gondret, P. and Rabaud, M. (1999), 'Axisymmetric propagating vortices in the flow between a stationary and a rotating disk enclosed by a cylinder', *Journal of Fluid Mechanics* **386**, 105–126.

Germano, M., Piomelli, U., Moin, P. and Cabot, W. H. (1991), 'A dynamic subgrid-scale eddy viscosity model', *Physics of Fluids A: Fluid Dynamics* **3**(7), 1760–1765.

Ghaffari, O., Behzadmehr, A. and Ajam, H. (2010), 'Turbulent mixed convection of a nanofluid in a horizontal curved tube using a two-phase approach', *International Communications in Heat and Mass Transfer* **37**(10), 1551–1558.

Ghasemi, B. and Aminossadati, S. (2010), 'Brownian motion of nanoparticles in a triangular enclosure with natural convection', *International Journal of Thermal Sciences* **49**(6), 931–940.

Gibson, M., Verriopoulos, C. and Vlachos, N. (1984), 'Turbulent boundary layer on a mildly curved convex surface', *Experiments in Fluids* **2**(1), 17–24.

Goodarzi, M., Safaei, M., Vafai, K., Ahmadi, G., Dahari, M., Kazi, S. and Jomhari, N. (2014), 'Investigation of nanofluid mixed convection in a shallow cavity using a two-phase mixture model', *International Journal of Thermal Sciences* **75**, 204–220.

Gosman, A. and Loannides, E. (1983), 'Aspects of computer simulation of liquid-fueled combustors', *Journal of energy* **7**(6), 482–490.

Gray, D. D. and Giorgini, A. (1976), 'The validity of the boussinesq approximation for liquids and gases', *International Journal of Heat and Mass Transfer* **19**(5), 545–551.

Gregory, N., Stuart, J. and Walker, W. (1955), 'On the stability of three-dimensional boundary layers with application to the flow due to a rotating disk', *Phil. Trans. R. Soc. Lond. A* **248**(943), 155–199.

Guha, A. (2008), 'Transport and deposition of particles in turbulent and laminar flow', *Annu. Rev. Fluid Mech.* **40**, 311–341.

Haider, A. and Levenspiel, O. (1989), 'Drag coefficient and terminal velocity of spherical and nonspherical particles', *Powder technology* **58**(1), 63–70.

Hamilton, R. L. and Crosser, O. (1962), 'Thermal conductivity of heterogeneous two-component systems', *Industrial & Engineering chemistry fundamentals* **1**(3), 187–191.

Harris, J., Thomas, P. and Garrett, S. (2013), On the stability of flows over rough rotating disks, *in* '42nd AIAA Fluid Dynamics Conference and Exhibit', p. 3075.

Hatschek, E. (1913), 'The general theory of viscosity of two-phase systems', *Transactions of the Faraday Society* **9**, 80–92.

Heris, S. Z., Esfahany, M. N. and Etemad, S. G. (2007), 'Experimental investigation of convective heat transfer of Al_2O_3/water nanofluid in circular tube', *International Journal of Heat and Fluid Flow* **28**(2), 203–210.

Hirsch, C. (1990), *Numerical computation of internal and external flows: volume 2: computational methods for inviscid and viscous flows*, Wiley & Sons.

Hu, C., Heng, P., Bai, M., Lv, J., Wang, Y. and Li, X. (2013), Numerical study of nanofluids flow characteristics using LES–Lagrange method and molecular dynamics simulation, *in* 'ASME 2013 4th International Conference on Micro/Nanoscale Heat and Mass Transfer', American Society of Mechanical Engineers, pp. V001T02A001–V001T02A001.

Hunt, J. C., Wray, A. A. and Moin, P. (1988), Eddies, streams, and convergence zones in turbulent flows, *in* 'Studying Turbulence Using Numerical Simulation Databases, 2'.

Ikeda, T. and Durbin, P. A. (2007), 'Direct simulations of a rough-wall channel flow', *Journal of Fluid Mechanics* **571**, 235–263.

Ingham, D. (1975), 'Diffusion of aerosols from a stream flowing through a cylindrical tube', *Journal of Aerosol Science* **6**(2), 125–132.

Inthavong, K., Mouritz, A. P., Dong, J. and Tu, J. Y. (2013), 'Inhalation and deposition of carbon and glass composite fibre in the respiratory airway', *Journal of aerosol science* **65**, 58–68.

Inthavong, K., Tian, L. and Tu, J. (2016), 'Lagrangian particle modelling of spherical nanoparticle dispersion and deposition in confined flows', *Journal of Aerosol Science* **96**, 56–68.

Inthavong, K., Tu, J. and Ahmadi, G. (2009), 'Computational modelling of gas-particle flows with different particle morphology in the human nasal cavity', *The Journal of Computational Multiphase Flows* **1**(1), 57–82.

Inthavong, K., Tu, J., Ye, Y., Ding, S., Subic, A. and Thien, F. (2010), 'Effects of airway obstruction induced by asthma attack on particle deposition', *Journal of Aerosol Science* **41**(6), 587–601.

Inthavong, K., Wen, J., Tu, J. and Tian, Z. (2009), 'From CT scans to CFD modelling–fluid and heat transfer in a realistic human nasal cavity', *Engineering Applications of Computational Fluid Mechanics* **3**(3), 321–335.

Issa, R. I. (1986), 'Solution of the implicitly discretised fluid flow equations by operator-splitting', *Journal of computational physics* **62**(1), 40–65.

Itoh, M., Yamada, Y., Imao, S. and Gonda, M. (1992), 'Experiments on turbulent flow due to an enclosed rotating disk', *Experimental thermal and fluid science* **5**(3), 359–368.

Itoh, N. (1996), 'Simple cases of the streamline-curvature instability in three-dimensional boundary layers', *Journal of Fluid Mechanics* **317**, 129–154.

Jasak, H. (1996), Error Analysis and Estimation for the finite volume method with applications to fluid flows, PhD thesis, Imperial College of Science.

Jensen, K. F., Einset, E. O. and Fotiadis, D. I. (1991), 'Flow phenomena in chemical vapor deposition of thin films', *Annual review of fluid mechanics* **23**(1), 197–232.

Jeong, J. and Hussain, F. (1995), 'On the identification of a vortex', *Journal of fluid mechanics* **285**, 69–94.

Jiménez, J. (2004), 'Turbulent flows over rough walls', *Annu. Rev. Fluid Mech.* **36**, 173–196.

Jordan, D. (1954), 'The adhesion of dust particles', *British Journal of Applied Physics* **5**(S3), S194.

Kármán, T. v. (1921), 'Über laminare und turbulente reibung', *ZAMM-Journal of Applied Mathematics and Mechanics/Zeitschrift für Angewandte Mathematik und Mechanik* **1**(4), 233–252.

Khanafer, K., Vafai, K. and Lightstone, M. (2003), 'Buoyancy-driven heat transfer enhancement in a two-dimensional enclosure utilizing nanofluids', *International journal of heat and mass transfer* **46**(19), 3639–3653.

Kobayashi, R., Kohama, Y. and Takamadate, C. (1980), 'Spiral vortices in boundary layer transition regime on a rotating disk', *Acta Mechanica* **35**(1-2), 71–82.

Kohama, Y. (1984), 'Study on boundary layer transition of a rotating disk', *Acta Mechanica* **50**(3-4), 193–199.

Koo, J. and Kleinstreuer, C. (2004), 'A new thermal conductivity model for nanofluids', *Journal of Nanoparticle Research* **6**(6), 577–588.

Koo, J. and Kleinstreuer, C. (2005), 'Laminar nanofluid flow in microheat-sinks', *International Journal of Heat and Mass Transfer* **48**(13), 2652–2661.

Kreiss, H.-O. and Parter, S. V. (1983), 'On the swirling flow between rotating coaxial disks: existence and nonuniqueness', *Communications on Pure and Applied Mathematics* **36**(1), 55–84.

Krieger, I. M. and Dougherty, T. J. (1959), 'A mechanism for non-newtonian flow in suspensions of rigid spheres', *Transactions of the Society of Rheology* **3**(1), 137–152.

Krogstad, P.-Å., Andersson, H., Bakken, O. and Ashrafian, A. (2005), 'An experimental and numerical study of channel flow with rough walls', *Journal of Fluid Mechanics* **530**, 327–352.

Kulkarni, D. P., Das, D. K. and Chukwu, G. A. (2006), 'Temperature dependent rheological property of copper oxide nanoparticles suspension (nanofluid)', *Journal of nanoscience and nanotechnology* **6**(4), 1150–1154.

Launder, B., Poncet, S. and Serre, E. (2010), 'Laminar, transitional, and turbulent flows in rotor-stator cavities', *Annual review of fluid mechanics* **42**, 229–248.

Launder, B. and Spalding, D. (1974), 'The numerical computation of turbulent flows', *Computer Methods in Applied Mechanics and Engineering* **3**(2), 269 – 289.

Lee, H. and Yook, S.-J. (2014), 'Deposition velocity of particles in charge equilibrium onto a flat plate in parallel airflow under the influence of simultaneous electrophoresis and thermophoresis', *Journal of Aerosol Science* **67**, 166–176.

Lee, M. and Yook, S.-J. (2015), 'Investigation of particulate contamination of heated wafers contained in a closed environment', *Journal of Aerosol Science* **88**, 148–158.

Lee, S., Choi, S.-S., Li, S. and Eastman, J. (1999), 'Measuring thermal conductivity of fluids containing oxide nanoparticles', *Journal of Heat transfer* **121**(2), 280–289.

Leonard, A. (1975), Energy cascade in Large-eddy simulations of turbulent fluid flows, *in* 'Advances in geophysics', Vol. 18, Elsevier, pp. 237–248.

Leonardi, S. and Castro, I. P. (2010), 'Channel flow over large cube roughness: a direct numerical simulation study', *Journal of Fluid Mechanics* **651**, 519–539.

Li, A. and Ahmadi, G. (1993), 'Computer simulation of deposition of aerosols in a turbulent channel flow with rough walls', *Aerosol Science and Technology* **18**(1), 11–24.

Li, A., Ahmadi, G., Bayer, R. G. and Gaynes, M. A. (1994), 'Aerosol particle deposition in an obstructed turbulent duct flow', *Journal of aerosol science* **25**(1), 91–112.

Lilly, D. (1971), 'Numerical simulation of developing and decaying two-dimensional turbulence', *Journal of Fluid Mechanics* **45**(2), 395–415.

Lilly, D. K. (1966), 'On the instability of ekman boundary flow', *Journal of the Atmospheric Sciences* **23**(5), 481–494.

Lingwood, R. (1996), 'An experimental study of absolute instability of the rotating-disk boundary-layer flow', *Journal of Fluid Mechanics* **314**, 373–405.

Lingwood, R. J. (1995), 'Absolute instability of the boundary layer on a rotating disk', *Journal of Fluid Mechanics* **299**, 17–33.

Lingwood, R. J. (1997), 'Absolute instability of the ekman layer and related rotating flows', *Journal of Fluid Mechanics* **331**, 405–428.

Liu, A. B., Mather, D. and Reitz, R. D. (1993), 'Modeling the effects of drop drag and breakup on fuel sprays', *SAE Transactions* pp. 83–95.

Liu, B. Y. and Ahn, K.-h. (1987), 'Particle deposition on semiconductor wafers', *Aerosol Science and Technology* **6**(3), 215–224.

Lygren, M. and Andersson, H. I. (2001), 'Turbulent flow between a rotating and a stationary disk', *Journal of Fluid Mechanics* **426**, 297–326.

MacInnes, J. and Bracco, F. (1992), 'Stochastic particle dispersion modeling and the tracer-particle limit', *Physics of Fluids A: Fluid Dynamics* **4**(12), 2809–2824.

MacKerrell, S. (1987), 'A nonlinear, asymptotic investigation of the stationary modes of instability of the three-dimensional boundary layer on a rotating disc', *Proc. R. Soc. Lond. A* **413**(1845), 497–513.

Magnus, G. (1861), 'A note on the rotary motion of the liquid jet', *Annalen der Physik und Chemie* **63**, 363–365.

Makino, S., Inagaki, M. and Nakagawa, M. (2015), 'Laminar-turbulence transition over the rotor disk in an enclosed rotor-stator cavity', *Flow, Turbulence and Combustion* **95**(2-3), 399–413.

Malik, M. R., Wilkinson, S. P. and Orszag, S. A. (1981), 'Instability and transition in rotating disk flow', *AIAA Journal* **19**(9), 1131–1138.

Mason, P. J. and Thomson, D. J. (1992), 'Stochastic backscatter in Large-eddy simulations of boundary layers', *Journal of Fluid Mechanics* **242**, 51–78.

Maxwell, J. C. (1881), *A treatise on electricity and magnetism*, Vol. 1, Clarendon press.

McLaughlin, J. B. (1993), 'The lift on a small sphere in wall-bounded linear shear flows', *Journal of Fluid Mechanics* **246**, 249–265.

Mei, R. and Klausner, J. (1994), 'Shear lift force on spherical bubbles', *International journal of heat and fluid flow* **15**(1), 62–65.

Mellor, G., Chapple, P. and Stokes, V. (1968), 'On the flow between a rotating and a stationary disk', *Journal of Fluid Mechanics* **31**(1), 95–112.

Meneveau, C. and Katz, J. (2000), 'Scale-invariance and turbulence models for Large-eddy simulation', *Annual Review of Fluid Mechanics* **32**(1), 1–32.

Millsaps, K. (1951), 'Heat transfer by laminar flow from a rotating plate', *Journal of the Aeronautical Sciences* **18**(5), 354–355.

Mittal, R. and Iaccarino, G. (2005), 'Immersed boundary methods', *Annu. Rev. Fluid Mech.* **37**, 239–261.

Miyake, Y., Tsujimoto, K. and Agata, Y. (2000), 'A DNS of a turbulent flow in a rough-wall channel using roughness elements model', *JSME International Journal Series B Fluids and Thermal Engineering* **43**(2), 233–242.

Morozov, A. N. and van Saarloos, W. (2007), 'An introductory essay on subcritical instabilities and the transition to turbulence in visco-elastic parallel shear flows', *Physics Reports* **447**(3-6), 112–143.

Morsi, S. and Alexander, A. (1972), 'An investigation of particle trajectories in two-phase flow systems', *Journal of Fluid mechanics* **55**(2), 193–208.

Mulhearn, P. (1978), 'A wind-tunnel boundary-layer study of the effects of a surface roughness change: rough to smooth', *Boundary-Layer Meteorology* **15**(1), 3–30.

Murshed, S. S. and Estellé, P. (2017), 'A state of the art review on viscosity of nanofluids', *Renewable and Sustainable Energy Reviews* **76**, 1134–1152.

Mushtaq, A. and Mustafa, M. (2017), 'Computations for nanofluid flow near a stretchable rotating disk with axial magnetic field and convective conditions', *Results in physics* **7**, 3137–3144.

Mustafa, M., Khan, J. A., Hayat, T. and Alsaedi, A. (2015), 'On Bödewadt flow and heat transfer of nanofluids over a stretching stationary disk', *Journal of Molecular Liquids* **211**, 119–125.

Nazridoust, K. and Asgharian, B. (2008), 'Unsteady-state airflow and particle deposition in a three-generation human lung geometry', *Inhalation toxicology* **20**(6), 595–610.

Nguyen, C. T., Roy, G., Gauthier, C. and Galanis, N. (2007), 'Heat transfer enhancement using Al_2O_3–water nanofluid for an electronic liquid cooling system', *Applied Thermal Engineering* **27**(8-9), 1501–1506.

Nicoud, F. and Ducros, F. (1999), 'Subgrid-scale stress modelling based on the square of the velocity gradient tensor', *Flow, turbulence and Combustion* **62**(3), 183–200.

Nikitenko, N. (1963), 'Experimental investigation of heat exchange of a disk and a screen', *J. Eng. Phys* **6**(6), 1–11.

Nikuradse, J. (1950), *Laws of flow in rough pipes*, National Advisory Committee for Aeronautics Washington.

Oliver, D. (1962), 'Influence of particle rotation on radial migration in the poiseuille flow of suspensions', *Nature* **194**(4835), 1269.

Orlandi, P., Leonardi, S. and Antonia, R. (2006), 'Turbulent channel flow with either transverse or longitudinal roughness elements on one wall', *Journal of Fluid Mechanics* **561**, 279–305.

Orlandi, P., Leonardi, S., Tuzi, R. and Antonia, R. (2003), 'Direct numerical simulation of turbulent channel flow with wall velocity disturbances', *Physics of Fluids* **15**(12), 3587–3601.

Oseen, C. W. (1927), 'Neuere methoden und ergebnisse in der hydrodynamik', *Leipzig: Akademische Verlagsgesellschaft mb H* .

Otani, Y., Emi, H., Kanaoka, C. and Kato, K. (1989), 'Determination of deposition velocity onto a wafer for particles in the size range between 0.03 and 0.8 μm', *Journal of aerosol science* **20**(7), 787–796.

Ounis, H. and Ahmadi, G. (1990), 'A comparison of brownian and turbulent diffusion', *Aerosol Science and Technology* **13**(1), 47–53.

Owen, J. (1994), Flow and heat transfer in rotating-disc systems, *in* 'ICHMT Digital Library Online', Begel House Inc.

Owen, J., Haynes, C. and Bayley, F. (1974), 'Heat transfer from an air-cooled rotating disk', *Proc. R. Soc. Lond. A* **336**(1607), 453–473.

Owen, J. and Roger, R. (1989), 'Flow and heat transfer in rotating-disc systems. volume I-rotor-stator systems', *NASA STI/Recon Technical Report A* **90**.

Özkan, M., Thomas, P., Cooper, A. and Garrett, S. J. (2017), 'Comparison of the effects of surface roughness and confinement on rotor–stator cavity flow', *Engineering Applications of Computational Fluid Mechanics* **11**(1), 142–158.

Patankar, S. and Spalding", D. (1972), 'A calculation procedure for heat, mass and momentum transfer in three-dimensional parabolic flows', *International Journal of Heat and Mass Transfer* **15**(10), 1787 – 1806.

Patel, H. E., Anoop, K., Sundararajan, T. and Das, S. K. (2006), A micro-convection model for thermal conductivity of nanofluids, *in* 'International Heat Transfer Conference 13', Begel House Inc.

Paw, U. and Tha, K. (1983), 'The rebound of particles from natural surfaces', *Journal of Colloid and Interface Science* **93**, 442–452.

Pellé, J. and Harmand, S. (2007), 'Heat transfer measurements in an opened rotor–stator system air-gap', *Experimental thermal and fluid science* **31**(3), 165–180.

Pendergrass, W. and Arya, S. (1984), 'Dispersion in neutral boundary layer over a step change in surface roughness—I. Mean flow and turbulence structure', *Atmospheric Environment (1967)* **18**(7), 1267–1279.

Peskin, C. S. (1977), 'Numerical analysis of blood flow in the heart', *Journal of computational physics* **25**(3), 220–252.

Poiseuille, J. (1841), 'Recherches sur le mouvement du sang dans les vein capillaires', *Mem. Acad. Roy. Sci* **7**, 105–175.

Poncet, S., Chauve, M.-P. and Schiestel, R. (2005), 'Batchelor versus stewartson flow structures in a rotor-stator cavity with throughflow', *Physics of fluids* **17**(7), 075110.

Poncet, S., Da Soghe, R. and Facchini, B. (2010), RANS modeling of flow in rotating cavity system, *in* 'V European Conference on Computational Fluid Dynamics'.

Poncet, S. and Serre, E. (2008), Large eddy simulation of non-isothermal turbulent rotor-stator flows, *in* 'The Twelfth International Symposium on Transport Phenomena and Dynamics of Rotating Machinery'.

Pope, S. B. (2000), *Turbulent Flows*, Cambridge University Press.

Prandtl, L. (1961), 'Collected works', *Tollmien, W., Schlicting, H., Go rtler, H.(Eds.). Springer, Berlin* .

Pui, D. Y., Ye, Y. and Liu, B. Y. (1990), 'Experimental study of particle deposition on semiconductor wafers', *Aerosol Science and Technology* **12**(4), 795–804.

Rajagopalan, S. and Antonia, R. (1982), 'Use of a quadrant analysis technique to identify coherent structures in a turbulent boundary layer', *The Physics of Fluids* **25**(6), 949–956.

Rao, A. and Whitby, K. (1977), 'Non-ideal collection characteristics of single stage and cascade impactors', *American Industrial Hygiene Association Journal* **38**(4), 174–179.

Rao, A. and Whitby, K. (1978), 'Non-ideal collection characteristics of inertial impactors—I. single-stage impactors and solid particles', *Journal of Aerosol Science* **9**(2), 77–86.

Raupach, M., Antonia, R. and Rajagopalan, S. (1991), 'Rough-wall turbulent boundary layers', *Applied mechanics reviews* **44**(1), 1–25.

Rebay, M., Kakac, S. and Cotta, R. M. (2016), *Microscale and Nanoscale Heat Transfer: Analysis, Design, and Application*, CRC Press.

Renardy, M., Renardy, Y. and Li, J. (2001), 'Numerical simulation of moving contact line problems using a volume-of-fluid method', *Journal of Computational Physics* **171**(1), 243–263.

Rogers, L. and Reed, J. (1984), 'The adhesion of particles undergoing an elastic-plastic impact with a surface', *Journal of Physics D: Applied Physics* **17**(4), 677.

Roscoe, R. (1952), 'The viscosity of suspensions of rigid spheres', *British Journal of Applied Physics* **3**(8), 267.

Rubinow, S. and Keller, J. B. (1961), 'The transverse force on a spinning sphere moving in a viscous fluid', *Journal of Fluid Mechanics* **11**(3), 447–459.

Rusche, H. (2003), Computational fluid dynamics of dispersed two-phase flows at high phase fractions, PhD thesis, Imperial College London (University of London).

Saffman, P. (1965), 'The lift on a small sphere in a slow shear flow', *Journal of fluid mechanics* **22**(2), 385–400.

Sagaut, P. (2006), *Large eddy simulation for incompressible flows: an introduction*, Springer Science & Business Media.

Schlichting, H., Gersten, K., Krause, E., Oertel, H. and Mayes, K. (1955), *Boundary-layer theory*, Vol. 7, Springer.

Schmitt, F. G. (2007), 'About boussinesq's turbulent viscosity hypothesis: historical remarks and a direct evaluation of its validity', *Comptes Rendus Mécanique* **335**(9-10), 617–627.

Schouveiler, L., Le Gal, P. and Chauve, M. (2001), 'Instabilities of the flow between a rotating and a stationary disk', *Journal of Fluid Mechanics* **443**, 329–350.

Schultz, M. P. and Flack, K. (2005), 'Outer layer similarity in fully rough turbulent boundary layers', *Experiments in Fluids* **38**(3), 328–340.

Scotti, A. (2006), 'Direct numerical simulation of turbulent channel flows with boundary roughened with virtual sandpaper', *Physics of Fluids* **18**(3), 031701.

Segré, G. (1961), 'Radial particle displacements in poseuille flow of suspensions', *Nature* **189**, 209–210.

Segré, G. and Silberberg, A. (1962), 'Behaviour of macroscopic rigid spheres in poiseuille flow part 2. Experimental results and interpretation', *Journal of fluid mechanics* **14**(1), 136–157.

Serre, E., Bontoux, P. and Launder, B. (2002), 'Direct numerical simulation of transitional turbulent flow in a closed rotor-stator cavity', *Flow, Turbulence and combustion* **69**(1), 35–50.

Serre, E., Bontoux, P. and Launder, B. (2004), 'Transitional-turbulent flow with heat transfer in a closed rotor-stator cavity', *Journal of Turbulence* **5**(8), 1–3.

Serre, E., Del Arco, E. C. and Bontoux, P. (2001), 'Annular and spiral patterns in flows between rotating and stationary discs', *Journal of Fluid Mechanics* **434**, 65–100.

Séverac, É., Poncet, S., Serre, É. and Chauve, M.-P. (2007), 'Large eddy simulation and measurements of turbulent enclosed rotor-stator flows', *Physics of Fluids* **19**(8), 085113.

Shchukin, V. and Olimpiev, V. (1975), 'Heat transfer of disc rotating in a housing with transitional and turbulent boundary layers', *Soviet Aeronautics* **18**, 105–110.

Silva, A. L. E., Silveira-Neto, A. and Damasceno, J. (2003), 'Numerical simulation of two-dimensional flows over a circular cylinder using the immersed boundary method', *Journal of Computational Physics* **189**(2), 351–370.

Sirivat, A. (1991), 'Stability experiment of flow between a stationary and a rotating disk', *Physics of Fluids A: Fluid Dynamics* **3**(11), 2664–2671.

Smagorinsky, J. (1963), 'General circulation experiments with the primitive equations: I. the basic experiment', *Monthly weather review* **91**(3), 99–164.

Smith, N. H. (1947), 'Exploratory investigation of laminar-boundary-layer oscillations on a rotating disk', *National Advisory Committee For Aeronautics* .

Speziale, C. (1998), 'Turbulence modeling for time-dependent RANS and VLES: a review', *AIAA journal* **36**(2), 173–184.

Stapleton, K.-W., Guentsch, E., Hoskinson, M. and Finlay, W. (2000), 'On the suitability of k–ε turbulence modeling for aerosol deposition in the mouth and throat: a comparison with experiment', *Journal of Aerosol Science* **31**(6), 739–749.

Stewartson, K. (1953), On the flow between two rotating coaxial disks, *in* 'Mathematical Proceedings of the Cambridge Philosophical Society', Vol. 49, Cambridge University Press, pp. 333–341.

Stokes, G. G. (1851), *On the effect of the internal friction of fluids on the motion of pendulums*, Vol. 9, Pitt Press Cambridge.

Subramanian, C. and Antonia, R. (1981), 'Effect of reynolds number on a slightly heated turbulent boundary layer', *International Journal of Heat and Mass Transfer* **24**(11), 1833–1846.

Sulaiman, D. R. (2011), 'Microprocessors thermal challenges for portable and embedded systems using thermal throttling technique', *Procedia Computer Science* **3**, 1023–1032.

Tadmor, E. (1989), 'Convergence of spectral methods for nonlinear conservation laws', *SIAM Journal on Numerical Analysis* **26**(1), 30–44.

Talbot, L., Cheng, R., Schefer, R. and Willis, D. (1980), 'Thermophoresis of particles in a heated boundary layer', *Journal of fluid mechanics* **101**(4), 737–758.

Tavener, S., Mullin, T. and Cliffe, K. (1991), 'Novel bifurcation phenomena in a rotating annulus', *Journal of Fluid Mechanics* **229**, 483–497.

Taylor, R., Coleman, H. and Hodge, B. (1985), 'Prediction of turbulent rough-wall skin friction using a discrete element approach', *Journal of Fluids Engineering* **107**(2), 251–257.

Townsend, A, A. (1976), *The structure of turbulent shear flow*, Cambridge and New York, Cambridge University Press, 1976. 438 p.

Tsai, C. J., Pui, D. Y. and Liu, B. Y. (1990), 'Capture and rebound of small particles upon impact with solid surfaces', *Aerosol Science and Technology* **12**(3), 497–507.

Tu, J., Yeoh, G. H. and Liu, C. (2007), *Computational fluid dynamics: A practical approach*, Elsevier Science & Technology.

Tuck, E. and Kouzoubov, A. (1995), 'A laminar roughness boundary condition', *Journal of Fluid Mechanics* **300**, 59–70.

Tuliszka-Sznitko, E. and Majchrowski, W. (2010), 'LES and DNS of the flow with heat transfer in rotating cavity', *Computational Methods in Science and Technology* **16**(1), 105–114.

Tuliszka-Sznitko, E., Majchrowski, W. and Kiełczewski, K. (2011), Heat transfer in rotor/stator cavity, *in* 'Journal of Physics: Conference Series', Vol. 318, IOP Publishing, p. 032022.

Tuliszka-Sznitko, E., Majchrowski, W. and Kiełczewski, K. (2012), 'Investigation of transitional and turbulent heat and momentum transport in a rotating cavity', *International Journal of Heat and Fluid Flow* **35**, 52–60.

Tuliszka-Sznitko, E., Soong, C.-Y., Serre, E. and Bontoux, P. (2001), 'Instability of the non-isothermal flow between a rotating and a stationary disks', *Task Quarterly* **5**(4), 557–566.

Tuliszka-Sznitko, E., Zielinski, A. and Majchrowski, W. (2009*a*), Large eddy simulation of non-isothermal flow in rotor/stator cavity, *in* 'Ichmt Digital Library Online', Begel House Inc.

Tuliszka-Sznitko, E., Zielinski, A. and Majchrowski, W. (2009*b*), 'LES of the non-isothermal transitional flow in rotating cavity', *International Journal of Heat and Fluid Flow* **30**(3), 534–548.

Turkyilmazoglu, M. (2014), 'Nanofluid flow and heat transfer due to a rotating disk', *Computers & Fluids* **94**, 139–146.

van Sint Annaland, M., Deen, N. and Kuipers, J. (2005), 'Numerical simulation of gas bubbles behaviour using a three-dimensional volume of fluid method', *Chemical Engineering Science* **60**(11), 2999–3011.

Versteeg, H. K. and Malalasekera, W. (2007), *An introduction to computational fluid dynamics: the finite volume method*, Pearson Education.

Verzicco, R., Mohd-Yusof, J., Orlandi, P. and Haworth, D. (2000), 'Large eddy simulation in complex geometric configurations using boundary body forces', *AIAA journal* **38**(3), 427–433.

Wallace, J. M. (2016), 'Quadrant analysis in turbulence research: history and evolution', *Annual Review of Fluid Mechanics* **48**, 131–158.

Wang, L. P. and Stock, D. E. (1992), 'Stochastic trajectory models for turbulent diffusion: Monte carlo process versus markov chains', *Atmospheric Environment. Part A. General Topics* **26**(9), 1599–1607.

Whitaker, S. (1996), 'The forchheimer equation: a theoretical development', *Transport in Porous media* **25**(1), 27–61.

White, F. M. (1991), 'Viscous fluid flow, 1991', *MacGraw, New York* pp. 335–393.

Wilkinson, S. P. and Malik, M. (1985), 'Stability experiments in the flow over a rotating disk', *AIAA journal* **23**(4), 588–595.

Wu, X. and Squires, K. D. (2000), 'Prediction and investigation of the turbulent flow over a rotating disk', *Journal of Fluid Mechanics* **418**, 231–264.

Xu, M. and Willeke, K. (1993), 'Right-angle impaction and rebound of particles', *Journal of aerosol science* **24**(1), 19–30.

Xu, M., Willeke, K., Biswas, P. and Pratsinis, S. E. (1993), 'Impaction and rebound of particles at acute incident angles', *Aerosol science and technology* **18**(2), 143–155.

Xuan, Y. and Li, Q. (2003), 'Investigation on convective heat transfer and flow features of nanofluids', *Journal of Heat transfer* **125**(1), 151–155.

Yan, Y., Li, X. and Tu, J. (2016), 'Effects of passenger thermal plume on the transport and distribution characteristics of airborne particles in an airliner cabin section', *Science and Technology for the Built Environment* **22**(2), 153–163.

Ye, Y., Pui, D., Liu, B., Opiolka, S., Blumhorst, S. and Fissan, H. (1991), 'Thermophoretic effect of particle deposition on a free standing semiconductor wafer in a clean room', *Journal of Aerosol Science* **22**(1), 63–72.

Yook, S.-J., Asbach, C. and Ahn, K.-H. (2010), 'Particle deposition velocity onto a face-up flat surface in a laminar parallel flow considering brownian diffusion and gravitational settling', *Journal of Aerosol Science* **41**(10), 911–920.

Zhao, B. and Chen, J. (2006), 'Numerical analysis of particle deposition in ventilation duct', *Building and Environment* **41**(6), 710–718.

Zhao, B., Zhang, Y., Li, X., Yang, X. and Huang, D. (2004), 'Comparison of indoor aerosol particle concentration and deposition in different ventilated rooms by numerical method', *Building and Environment* **39**(1), 1–8.

Zoueshtiagh, F., Ali, R., Colley, A., Thomas, P. J. and Carpenter, P. W. (2003), 'Laminar-turbulent boundary-layer transition over a rough rotating disk', *Physics of Fluids* **15**(8), 2441–2444.